



MONASH University

**Mechanistic Subtleties in the Voltammetry of
Polyoxometalates**

By:

Md Anisur Rahman

A thesis submitted to the Faculty of Science, Monash University, in fulfilment
of the requirements for the degree of Doctor of Philosophy.

School of Chemistry
Monash University
Australia

April 2020

Copyright notice

© The author 2020.

I certify that I have made all reasonable efforts to secure copyright permissions for third-party content included in this thesis and have not knowingly added copyright content to my work without the owner's permission.

Table of Contents

Table of contents	I
Abstract	III
Declaration	V
Acknowledgements	IX
Symbols	X
List of Figures	XII
Chapter 1. Introduction	1
1.1 Polyoxometalates	1
1.1.1 Varieties of Polyoxometalates	1
1.1.2 Applications of Polyoxometalates	4
1.1.3 Fundamental aspects of Polyoxometalates Electrochemistry	7
1.2 Introduction to Electrochemistry	9
1.2.1 The Electrochemical Cell	10
1.2.2 Faradaic and Non-faradaic current	13
1.2.3 Introduction to Electrode Reactions	14
1.2.3.1 Mass Transport	15
1.2.3.2 Butler-Volmer Theory of Electrode Kinetics	17
1.2.3.3 Conventional Method for Electrode Kinetic Measurements	18
1.2.4 Bulk Electrolysis	20
1.3 Spectroelectrochemistry	22
1.4 AC Voltammetry	23
1.5 Electron Paramagnetic Resonance Spectroscopy	29
1.6 Research Objectives	32
Chapter 2. Modelling Limitations Encountered in the Thermodynamic and Electrode Kinetic Parameterization of the α -[S ₂ W ₁₈ O ₆₂] ^{4-/5-/6-} Processes at Glassy Carbon and Metal Electrodes	42
Chapter 3. Identification of Mechanistic Subtleties that Apply to Voltammetric Studies at Boron Doped Diamond Electrodes: The α -[S ₂ W ₁₈ O ₆₂] ^{4-/5-/6-} Processes	68

Chapter 4. Electrode Material Dependence, Ion-Pairing and the Progressive Increase in Complexity of the α -[S ₂ W ₁₈ O ₆₂] ^{4-/5-/6-/7-/8-/9-/10-} Reduction Processes in Acetonitrile Containing [n-Bu ₄ N][PF ₆] as the Supporting Electrolyte	115
Chapter 5. Thermodynamics, Electrode Kinetics and Mechanistic Nuances Associated with the Voltammetric Reduction of Dissolved [n-Bu ₄ N] ₄ [PW ₁₁ O ₃₉ {Sn(C ₆ H ₄)C \equiv C(C ₆ H ₄)(N ₃ C ₄ H ₁₀)}] and a Surface Confined Diazonium Derivative	170
Chapter 6. Electrochemical and EPR Spectroscopic Characterisation of Two Electron Reduced Fe(III) and One Electron Reduced Zn(II), Cu(II) and Co(II) Functionalized Vanadium Polyoxometalates	225
Chapter 7. Conclusions and Future Works	254

ABSTRACT

The electrode kinetics of a series of Dawson and Kegging polyoxometalates (POMs) have been studied quantitatively by Fourier transform alternating current (FTAC) voltammetry. Both heuristic and computer-assisted automated data analysis protocols were employed to analyse the FTAC voltammetric data presented in Chapter 2 to Chapter 5 in acetonitrile containing [*n*-Bu₄N][PF₆] as the supporting electrolyte at glassy carbon (GC), boron doped diamond (BDD), gold (Au) and platinum (Pt) electrodes. Reversible potentials (E^0), heterogeneous electron-transfer kinetics (k^0) and charge transfer coefficients (α) based on Butler-Volmer theory were estimated by computer-assisted automated method and results compared with values initially derived from the heuristic approach to check the fidelity of these form of data analysis. Apparently, data analysis method dependent electrode kinetic parameters were observed when there are departures from the ideality in theory-experiment comparisons. In all cases, the electrode kinetics at GC were faster than at Au which in turn were faster than at a Pt electrode. The first α -[S₂W₁₈O₆₂]^{4-/5-} process was always kinetically faster than the second α -[S₂W₁₈O₆₂]^{5-/6-} process at all electrodes except at BDD, where the first process was slower than the second one. Some other non-idealities were also encountered, such as harmonic and concentration dependent electrode kinetics. Detailed investigation reveals that they originate from the graphite sp² carbon impurity.

Progressive departures in experimental versus simulated data comparisons were found in the α -[S₂W₁₈O₆₂]⁴⁻ and K^W_{Sn}[N₃C₄H₁₀]⁴⁻ reduction processes that occur at more negative potentials. Ion-pairing between oxidised or reduced POMs and the electrolyte cation ([*n*-Bu₄N]⁺), surface accumulation of POM reduced species and large double-layer capacitance effects at potentials near the solvent limit may induce non-idealities such as asymmetry in the

reduction and oxidation components. The comparatively slower electrode kinetics found for reduction of $\text{K}^{\text{W}}_{\text{Sn}}[\text{N}_3\text{C}_4\text{H}_{10}]^{4-}$ as compared to $\alpha\text{-}[\text{S}_2\text{W}_{18}\text{O}_{62}]^{4-}$ might be due to the long organic side chain hindering the approach of the monomeric electroactive POM to the electrode surface. Kinetic and thermodynamic dispersion present in the heterogeneous $\text{K}^{\text{W}}_{\text{Sn}}[-]^{4-}$ -grafted electrode are probable causes of non-ideality detected in the surface confined voltammetry of this material.

In chapter 6, electron paramagnetic resonance (EPR) data suggest that the electrons added to $[\text{Fe}^{\text{II}}\text{ClIV}^{\text{V}}_{12}\text{O}_{32}\text{Cl}]^{4-}$ and $[\text{Cu}^{\text{II}}(\text{MeCN})\text{V}^{\text{V}}_{12}\text{O}_{32}\text{Cl}]^{3-}$ upon reductions reside on the Fe and Cu in a $\text{Fe}^{\text{III/II}}$ and $\text{Fe}^{\text{II/I}}$ and $\text{Cu}^{\text{II/I}}$ based process, respectively. On the other hand, the electron was delocalised onto the V framework during the one electron reduction of $[\text{Zn}^{\text{II}}\text{ClIV}^{\text{V}}_{12}\text{O}_{32}\text{Cl}]^{4-}$. In the case of reduction of $[\text{Co}^{\text{II}}(\text{MeCN})\text{V}^{\text{V}}_{12}\text{O}_{32}\text{Cl}]^{3-}$, the added electron at least partially resides on V.

Declaration

This thesis is an original work of my research and contains no material which has been accepted for the award of any other degree or diploma at any university or equivalent institution and that, to the best of my knowledge and belief, this thesis contains no material previously published or written by another person, except where due reference is made in the text of the thesis.

Signature:

Print Name:

Date:

General Declaration

Monash University

Declaration for thesis based or partially based on conjointly published or unpublished work

In accordance with Monash university Doctorate Regulation 17.2 Doctor of Philosophy and Research Master's regulations the following declarations are made:

I hereby declare that this thesis contains no material which has been accepted for the award of any other degree or diploma at any university or equivalent institution and that, to the best of my knowledge and belief, this thesis contains no material previously published or written by another person, except where due reference is made in the text of the thesis.

This thesis includes 1 original paper published in peer-reviewed journals and 4 unpublished publications. The main theme of this thesis is detection of thermodynamic and electrode kinetic nuances associated with POMs electrochemistry. The experiment design, electrochemical measurements, data analysis and manuscript preparation of all the papers in the thesis were the principle responsibility of myself, the student, working within the school of Chemistry under the supervision of Dr. Jie Zhang and Professor Alan M. Bond.

The inclusion of co-authors reflects the fact that the work came from active collaboration between researchers and acknowledges input into team-based research.

In all chapters in the thesis, my contribution to the work involved the following:

Thesis Chapter	Publication Title	Status	Nature and % of student contribution	Co-author name(s) Nature and % of Co-author's contribution*	Co-author(s), Monash student Y/N*
2	Modelling Limitations Encountered in the Thermodynamic and Electrode Kinetic Parameterization of the α -[S ₂ W ₁₈ O ₆₂] ^{4-/5-/6-} Processes at Glassy Carbon and Metal Electrodes	Publish-ed	60% Concept and collecting data and writing first draft	Jiezhen Li and Si-Xuan Guo 10% manuscript input, Gareth Kennedy 5% data analysis, Tadaharu Ueda 5% production of compound and manuscript input, Jie Zhang 10% concept design and manuscript input. Supervision Alan M. Bond 10% concept design and manuscript input. Supervision	N N N N N

3	Identification of Mechanistic Subtleties that Apply to Voltammetric Studies at Boron Doped Diamond Electrodes: The α -[S ₂ W ₁₈ O ₆₂] ^{4-/5-/6-} Processes	In preparation	65% Concept and collecting data and writing first draft	Julie Macpherson 15% manuscript input, Jie Zhang 10% concept design and manuscript input. Supervision Alan M. Bond 10% concept design and manuscript input. Supervision	N N N
4	Electrode Material Dependence, Ion-Pairing and the Progressive Increase in Complexity of the α -[S ₂ W ₁₈ O ₆₂] ^{4-/5-/6-/7-/8-/9-/10-} Reduction Processes in Acetonitrile Containing [<i>n</i> -Bu ₄ N][PF ₆] as the Supporting Electrolyte	Publish-ed	80% Concept and collecting data and writing first draft	Jie Zhang 10% concept design and manuscript input. Supervision Alan M. Bond 10% concept design and manuscript input. Supervision	N N
5	Thermodynamics, Electrode Kinetics and Mechanistic Nuances Associated with the Voltammetric Reduction of Dissolved [<i>n</i> -Bu ₄ N] ₄ [PW ₁₁ O ₃₉ {Sn(C ₆ H ₄)C≡C(C ₆ H ₄)(N ₃ C ₄ H ₁₀)}] and a Surface Confined Diazonium Derivative	Publish-ed	60% Concept and collecting data and writing first draft	Si-Xuan Guo 5% experimental input, Maxime Laurans and Guillaume Izzet 5% manuscript input, Anna Proust 10% production of compound and manuscript input, Jie Zhang 10% concept design and manuscript input. Supervision Alan M. Bond 10% concept design and manuscript input. Supervision	N N N N N
6	Electrochemical and EPR Spectroscopic Characterisation of Two Electron Reduced Fe(III) and One Electron Reduced Zn(II), Cu(II) and Co(II) Functionalized Vanadium Polyoxometalates	In preparation	60% Concept and collecting data and writing first draft	Stephen Best 10% experimental input and data analysis, John Boas 5% data interpretation, Carsten Streb 5% production of compound Jie Zhang 10% concept design and manuscript input. Supervision Alan M. Bond 10% concept design and manuscript input. Supervision	N N N N N

**If no co-authors, leave fields blank*

I have renumbered sections of submitted or published papers in order to generate a consistent presentation within the thesis.

Student name:

Student signature:

Date:

I hereby certify that the above declaration correctly reflects the nature and extent of the student's and co-authors' contributions to this work. In instances where I am not the responsible author, I have consulted with the responsible author to agree on the respective contributions of the authors.

Main Supervisor signature:

Date:

Acknowledgements

I would like to acknowledge all the people I have met during my long PhD journey because they made me realise the importance of communication and teamwork and the exchange of ideas, which broadened my understanding of every aspect of research.

Firstly, I would like to convey my cordial gratitude to my supervisors, Associate Professor Jie Zhang and Professor Alan M. Bond. Their endurance, inspiration, and continuous guidance throughout my PhD study helped me to conduct the laboratory experiments, interpret the findings and finally write up the thesis.

I would like to acknowledge my graduate study committee members, Professor Douglas Macfarlane, Professor Bart Follink, and Dr. David Turner, for their valuable suggestions.

I would like to acknowledge Professor Tadaharu Ueda, Kochi University Japan, Professor Anna Proust, Sorbonne Université, France, and Professor Carsten Streb, Ulm University Albert-Einstein-Allee, Germany, for their kindness synthesising and supplying the chemicals used in this thesis work. I would like to thank Dr. John Boas and Dr. Stephen P. Best for their help in analysing the electron paramagnetic resonance spectroscopic data.

I would like to thank all my group members, especially Dr. Jiezhen Li and Dr. Si-Xuan Guo, for their comments and guidance.

I would like to acknowledge the Endeavour Postgraduate Scholarship, Australia, which provides my tuition fees and living allowances. I also want to acknowledge Monash University for giving me the opportunity to study here.

Finally, I would like to thank my parents and wife for their mental support and encouragement, which helped me to fulfil my dream.

Symbols

Symbol	Meaning	Usual Unit
A	electrode area	cm^2
β	Bohr magneton	$9.274 \times 10^{-28} \text{ J G}^{-1}$
C	concentration	mM or mol cm^{-3}
C_{dl}	double layer capacitance	F
D	diffusion coefficient	$\text{cm}^2 \text{ s}^{-1}$
E	applied potential on electrode versus a reference	V
ΔE	amplitude in AC voltammetry	mV
E^0	standard potential	V
$E^{0'}$	reversible potential of an electrode	V
E_p^{ox}	oxidation peak potential	V
E_p^{red}	reduction peak potential	V
ΔE	voltammetric peak-to-peak separation	V
F	Faraday's constant	$96,485 \text{ C mol}^{-1}$
f	(a) F/RT	V^{-1}
	(b) frequency	Hz
h	Planck constant	$6.626 \times 10^{-34} \text{ J-s}$
I	current	A
I_p^{ox}	peak oxidation current	A
I_p^{red}	peak reduction current	A
J_i	flux of species i	$\text{mol s}^{-1} \text{ cm}^{-2}$
k^0	standard heterogenous rate constant	cm s^{-1}
n	number of electrons	
Q	charge	C
R	universal gas constant	$\text{J mol}^{-1} \text{ K}^{-1}$
R_c	compensated resistant	Ω
R_s	uncompensated resistant	Ω
R_u	total resistant	Ω
T	absolute temperature	K
t	time	s

V	volume	cm^3
ν	frequency of photon	Hz
	Linear potential scan rate	V s^{-1}
λ	wavelength	nm
Ψ	dimensionless kinetic parameter	

Lists of Figures

- Figure 1.** Polyhedra structure of most prominent POM archetypes- (a) Keggin, (b) Wells–Dawson, (c) Anderson, (d) Lindquist and (e) Preyssler. 2
- Figure 2.** Structure of Mo-blue and Mo-brown species 4
- Figure 3.** Electrocatalytic oxidation of dimethyl sulfoxide and benzylic alcohol using (a) $[\text{PW}_{11}\text{O}_{39}\text{Ru}^{\text{III}}(\text{H}_2\text{O})]^{4-}$ and (b) $[\text{PW}_{11}\text{O}_{39}\text{Cr}^{\text{III}}(\text{H}_2\text{O})]^{4-}$ as oxidative electro-catalyst, respectively. 4
- Figure 4.** DC cyclic voltammograms obtained at a scan rate of 0.100 Vs^{-1} for reduction of $\alpha\text{-}[\text{S}_2\text{W}_{18}\text{O}_{62}]^{4-}$ in CH_3CN (0.50 M of $[n\text{-Bu}_4\text{N}][\text{PF}_6]$) at a GC macro disc electrode. 8
- Figure 5.** DC cyclic voltammograms obtained at a scan rate of 0.100 Vs^{-1} for the reduction of $[\text{FeClV}_{12}\text{O}_{32}\text{Cl}]^{4-}$ in CH_3CN (0.10 M of $[n\text{-Bu}_4\text{N}][\text{PF}_6]$) at a GC macro disc electrode. 9
- Figure 6.** An example of an electrochemical cell consisting Zn metal and Ag wire covered with AgCl immersed in a ZnCl_2 electrolyte solution. 10
- Figure 7.** Schematic depiction of a three-electrode electrochemical cell. 11
- Figure 8.** Schematic illustration of a three-electrode electrochemical cell as a potentiostat. 12
- Figure 9.** Representation of (a) reduction and (b) oxidation of species, A, in an electrochemical cell under condition of cyclic voltammetry. 12
- Figure 10.** The Schematic current-potential curve obtained at a Hg electrode in the cell $\text{Hg}/\text{H}^+, \text{Br}^- (1 \text{ M})/\text{AgBr}/\text{Ag}$, showing the limiting processes: proton reduction at a negative potentials and mercury oxidation at positive potential. 14
- Figure 11.** Pathway of electrode reaction 15
- Figure 12.** Types and effects of mass transport. a) Planar diffusion and b) Radial diffusion. 16
- Figure 13.** A diagram displaying a) the applied potential on working electrode and b) a cyclic voltammogram for a simple one-electron oxidation process. The symbols used in the diagram are as follows: t = time, E = potential, Red = reduced form, Ox = oxidised form, E_p^{ox} = peak oxidation potential, E_p^{red} = peak reduction potential, I_p^{ox} = peak oxidation current and I_p^{red} = peak reduction current. 18
-

Figure 14. Typical cells for bulk electrolysis, (a) Undivided cell for controlled-potential separations and electro-gravimetric analysis at a solid cathode. (b) Undivided cell for coulometric analysis at mercury cathode with a silver anode. (c) Three-compartment cell, with ground-glass joints, for coulometric and voltammetric vacuum line studies.	20
Figure 15. Steady-state current-potential curves obtained at different times during the course of a controlled-potential bulk electrolysis experiment undertaken at a controlled $E = E_c$ for an irreversible process.	21
Figure 16. Total coulombs (Q) passed (total electric charge) plotted versus time	21
Figure 17. Illustration of Transmittance	23
Figure 18. Reduction spectroelectrochemistry of 3,4,7,8-tetramethyl- 1,10-phenanthroline in DMF	23
Figure 19. A schematic representation of the FTACV waveform	25
Figure 20. A schematic representation of the data analysis protocols employed in FTACV	25
Figure 21. Heuristic comparison of simulated (red line) and experimental (blue line) AC voltammetric data for the α -[S ₂ W ₁₈ O ₆₂] ^{4-/5-/6-} processes, obtained with 2.5 mM α -[S ₂ W ₁₈ O ₆₂] ⁴⁺ in CH ₃ CN (0.5 M [<i>n</i> -Bu ₄ N][PF ₆]) at an Au electrode. Amplitude, $\Delta E = 80$ mV, frequency, $f = 27.01$ Hz and scan rate, $\nu = 0.067$ Vs ⁻¹ . (a) DC component, (b-g) 1 st to 6 th harmonic components. $R_u = 195 \Omega$, $D = D = 2.9 \times 10^{-6}$ cm ² s ⁻¹ , $C_{dl}(c_0, c_1, c_2, c_3, c_4) = 34.9, -25.6, 20.5, 97.8, 58.5 \mu\text{F cm}^{-2}$.	27
Figure 22. a) Heuristic and (b) computer-assisted comparison of simulated (red) and experimental (blue) AC voltammetric data	29
Figure 23. a) Angular momentum of unpaired electron and b) energy orientations of magnetic moment $\bar{\mu}$ with respect to the magnetic field B_0 .	30
Figure 24. Induction of the spin state energies as a function of the magnetic field B_0	30
Figure 25. EPR spectrum	31

Chapter 1: Introduction

1.1 Polyoxometalates:

Polyoxometalates (POMs) represent a vast series of anionic, cluster-like inorganic metal oxide compounds [1]. Generally, POMs exist as polyoxoanions anions with multiple non-oxo atoms such as early d^0 and d^1 transition metals (e.g. V, Nb, Mo, Ta, W) and p-block elements (e.g. B, Si, P, As) which are joined together by shared oxygen atoms. The transition metals, especially V, Mo, and W, produce a large variety of clusters identified as heteropoly salts [2-5], isopolyanions [6-9] or POMs [10, 11]. Berzelius [12] is credited for the preparation of the first polyoxometalate, which is now recognised as the dodecamolybdophosphate anion, $[\text{PMo}_{12}\text{O}_{40}]^{3-}$ although its structure was uncharacterised for more than 100 years [13] until the advancement of the X-ray diffraction technique. In the early days of polyoxometalate synthesis, little progress was observed in the characterisation and applications of POMs. Nevertheless, in the last few decades, with the advent of modern technologies to aid synthesis and characterisation, significant progress has been made regarding their molecular science in chemistry [14-22], physics [23, 24], biology, medicine [25-31], and materials science [32-40].

1.1.1 Varieties of Polyoxometalates:

A large number of polyoxometalates have been synthesised, and are classified under the following archetypes: Keggin, Wells–Dawson, Anderson, Lindqvist and Preyssler (see Figure 1).

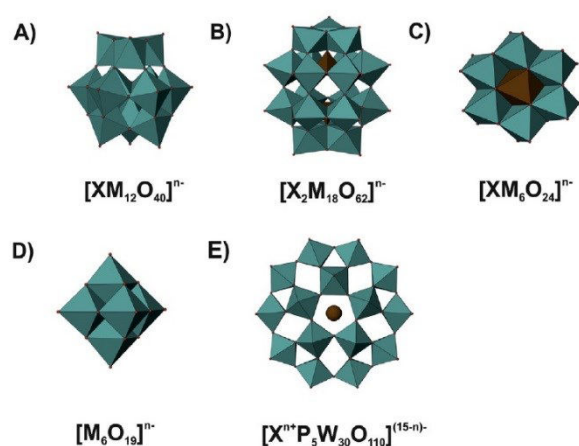


Figure 1. Polyhedra structure of common POM archetypes- (a) Keggin, (b) Wells–Dawson, (c) Anderson (d) Lindqvist and (e) Preyssler. Taken from ref. [41]

In summary, isopolyoxoanions $(M_mO_y)^{n-}$ and heteropolyoxoanions $(X_xM_mO_y)^{n-}$ are the two general POMs formulas, where M and X represent the addenda atom and heteroatom [42], respectively. The above-mentioned archetypes belong to one of the two general formulas.

Isopolyoxoanions:

Isopolyanions consist of single transition metals such as Mo, W and V, with heteroatoms though other elements may be present as ligands. Lindqvist (Figure 1d) [43–47], $[M_6O_{19}]^{n-}$ (M = Nb, Ta, Mo, V and W) is the most symmetrical and best-known structure of the isopolyoxoanions family. In the Lindqvist octahedral geometry [48], six metal atoms are arrayed by six reactive terminal oxygen atoms located at the centre.

Heteropolyoxoanions:

Heteropolyoxoanions are those consisting of clusters of fused MO_6 octahedra enfolded around a tetrahedron having a main group element or occasionally a transition metal [49]. Among these, Keggin [50] and Wells–Dawson [51] classes have been extensively investigated. The Keggin configuration shown in Figure 1a is the structural form of the α -Keggin isomer, which

has a standard formula of $[XM_{12}O_{40}]^{n-}$, where P, Si, As or B etc. are the heteroatom (X) and vanadium, molybdenum, tungsten etc. act as the addenda atom (M). X-ray diffraction was used by Keggin to determine the structure of α -Keggin anions in 1933 [13]. Different orientations of the $\{M_3O_{13}\}$ building blocks in the Keggin structure give rise to five different Keggin isomers [41] known as α , β , γ , δ and ϵ .

The unification of two curtailed $[XM_9O_{34}]^{n-}$ Keggin fragments by sharing of six oxygen atoms results in the Wells–Dawson structure $[X_2M_{18}O_{62}]^{n-}$ [52] (Figure 1b) which is closely related to the Keggin structure. Lacunary POMs are formed when a new transition metal replaces one or more addenda atoms in the Keggin and Wells–Dawson structure.

Hasenknopf et al. [53] reported the first preparation of an Anderson polyoxoanion, which was subsequently fully established by the method of synthesis developed by Song et al. [54-58] In the Anderson structure, the octahedral central atom is bounded by a loop of six coplanar MO_6 octahedra sharing edges $[XM_6O_{24}]^{n-}$ POM (Figure 1c). The fusion of five PW_6 units forming a crown gives Preyssler polyoxoanion $[X^{n+}P_5W_{30}O_{110}]^{(15-n)-}$ structure (Figure 1e).

Apart from the above mentioned two general categories of isopolyoxoanions and heteropolyoxoanions, there are other categories named the Mo-blue and Mo-brown species which were first reported by Scheele in 1783 [59]. Müller et al. [60] first revealed the structural identity POM type in 1995. These researchers then synthesised and characterised the ring-shaped $\{Mo_{154}\}$ (shown in Figure 2) which was the first of the Mo-blue sub-category. The first member of the Mo-brown sub-category is the spherical shaped $\{Mo_{132}\}$ [61] which exhibits higher reducing power than the Mo-blue species.

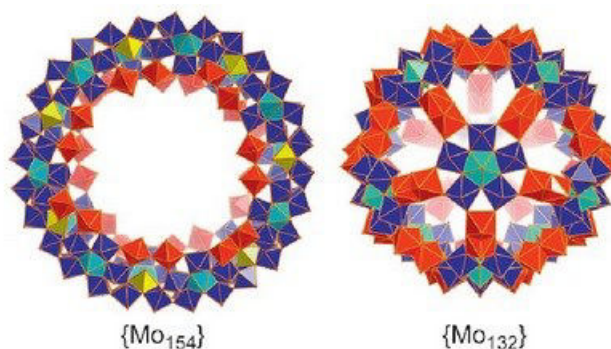


Figure 2. Structure of Mo-blue and Mo-brown species [62]

1.1.2 Applications of Polyoxometalates:

The availability of POMs with different sizes, structure, elemental composition and redox potentials leads to a wide range of applications including the following-

1.1.2.1 Oxidative catalysis

Recent studies on POMs based on transition and earth-scarce metals have provided efficient synthetic molecular systems for homogeneous catalysis. Transition metal (e.g. Ru, Cr, Mn) substituted heteropolyanions can be used as homogeneous oxidative electro-catalysts (Figure 3) in both organic and aqueous phases [63, 64]. According to Nadjo et al., Dawson-type mixed heteropolyanions can be used for the oxidation of NADH [65, 66].

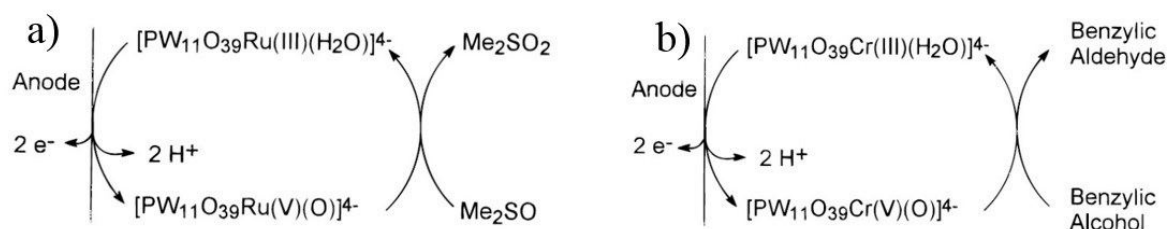


Figure 3. Electrocatalytic oxidation of dimethyl sulfoxide and benzylic alcohol using (a) $[\text{PW}_{11}\text{O}_{39}\text{Ru}^{\text{III}}(\text{H}_2\text{O})]^{4-}$ and (b) $[\text{PW}_{11}\text{O}_{39}\text{Cr}^{\text{III}}(\text{H}_2\text{O})]^{4-}$ as oxidative electrocatalyst, respectively. [64]

POMs can encapsulate and protect the active sites of water oxidation catalysts (WOCs) [67] due to their oxygen-enriched surface which provides stable inorganic arrangements and contains dynamic transition metal ion centres comprising cobalt, iridium or ruthenium. POMs are soluble and stable in aqueous and non-aqueous solvents [68], and oxidatively resistant as metals are held in their highest oxidation state and hydrolytically stable over wide pH ranges. Because of these properties, POMs show promise as catalysts for water oxidation [16, 69, 70].

1.1.2.2 Reductive catalysis:

Reduced heteropolyanions may be the product of the series of reversible one- and two-electron reduction heteropolyanion reactions which can be used as reductive electrocatalysts by (i) homogeneous dissolution in the electrolyte solution and (ii) attachment to an electrode surface.

i) *Electrocatalysts in Homogeneous Solution:*

Keggin type (α -[SiW₁₂O₄₀]⁴⁻) heteropolyanions can undergo four one-electron transfer reduction processes, which produce active one, two, three and four-electron reduced species. The two- and four-electron reduced compounds can catalyse the hydrogen evolution reaction [71, 72], while the first one-electron-reduced species is active for oxygen reduction [73]. However, nitrite reduction [74] in acidic solution is influenced by the first and third reduced compound. The one electron reduced form of the *Dawson-type* ([P₂W₁₈O₆₂]⁶⁻) heteropolyanion can act as a reductive catalyst for nitrite reduction [75] in an aqueous solution at pH <3. Transition metal-substituted heteropolyanions also can be used as electrocatalysts for reduction. Transition metals (Fe, Ru etc.) can favour reductive catalysis and are not deactivated during repetitive cycling of potential between their oxidised and reduced forms.

ii) *Heteropolyanions attached to the electrode surface:*

Sometimes reductive catalysis effectiveness can be amplified by the attachment of heteropolyanions to the electrode surface. For example an enhanced reduction rate of chlorate can be achieved by immobilisation of $[\text{PMo}_{12}\text{O}_{40}]^{3-}$ into the poly (4-vinylpyridine/1, 12-dibromododecane) matrix [73].

However, numerous shortcomings, such as some transition metals being non-abundant, do not provide cost-effective catalysis and may produce toxic effects, thus minimising their use in the industrial sector. The modern era demands the development catalysts based on period four earth-abundant transition metals (Fe, Co, Cu, etc.) that are ecologically benign. Nevertheless, few first-row transition metals containing POMs display water oxidation catalysis.

1.1.2.3 Sensing:

POMs can undergo fast and reversible multi-electron transfer redox conversions with minimal fundamental modification [76]. POM structure can be modified and perfected by adding or altering the hetero-atoms and addenda atoms into the structural framework [77-79]. The stable redox chemistry of POMs makes them attractive, selective and long-lived compounds for sensing applications. Reduction of the POMs causes an increase in negative charge, which raises the basicity of the POM anion. Concomitant protonation of the reduced species makes the POM redox properties pH sensitive. This allows POMs to be used as electrochemical probes to survey micro-environmental effects by using POM-functionalized electrodes as pH sensors [80].

1.1.2.4 Medicine:

POM-protein/enzyme interactions, combined with protein precipitation power and cellular POM penetration, create considerable opportunities in medical science, specifically in antiviral, antibacterial and antitumour research [81].

Penetration of polytungstoantimoniate ($[\text{NaSb}_9\text{W}_{21}\text{O}_{86}]^{18-}$) into C3HBI fibroblast cells was evidenced by Raman spectroscopy [82], photonic microscopy and X-ray fluorescence. The existence of heteropolytungstate ($[\text{Co}_4(\text{H}_2\text{O})_2(\text{PW}_9\text{O}_{34})_2]^{10-}$) inside the cellular membrane of human peripheral blood mononuclear cells was probed by scanning proton microprobe [83].

The antiviral activity of POMs (e.g., polytungstosilicate) against the murine leukemia sarcoma virus [84] was reported in 1971. Polytungstoantimoniate showed antiviral activity against murine leukemia sarcoma, rabies, rhabdovirus and Epstein-Barr virus [85-88].

A few reports have highlighted the anticancer activity of POMs. Anticancer activity against human colon cancer [89] and carcinoma of the intestinal tract [90] were evidenced by the use of $[\text{NH}_3\text{Pr}^i]_6[\text{Mo}_7\text{O}_{24}]$ in combination with phosphotungstic acid, phosphomolybdic acid or caffeine. β -lactam antibiotics showed enhanced antibacterial activity against resistant strains of bacteria when jointly used with polyoxotungstates [91].

1.1.3 Fundamental Aspects of Polyoxometalates Electrochemistry:

Extensive work has emphasised the importance of POM redox chemistry. For this reason, the electrochemical behaviour of POMs provides key knowledge related to their applications. The electrochemistry of POMs has been studied extensively – mainly Dawson and Keggin categories such as $[\text{P}_2\text{W}_{18}\text{O}_{62}]^{4-}$, $[\text{S}_2\text{W}_{18}\text{O}_{62}]^{4-}$, $[\text{PW}_{12}\text{O}_{40}]^{4-}$, $[\text{SiW}_{12}\text{O}_{40}]^{4-}$, $[\text{SiMo}_{12}\text{O}_{40}]^{4-}$, $[\text{Cu}(\text{MeCN})\text{V}_{12}\text{O}_{32}\text{Cl}]^{3-}$ and $[\text{Co}(\text{MeCN})\text{V}_{12}\text{O}_{32}\text{Cl}]^{3-}$ [92].

Typically, POMs display a series of chemically reversible one or two electron transfer redox conversion processes [93-95] with minimal structural modification. These electron transfer properties can be modified by varying the hetero-atoms and addenda atoms in the structure.

Dawson- Archetype POMs $[X_2M_{18}O_{62}]^{n-}$:

This study selected DC cyclic voltammograms at a scan rate of 0.100 V s^{-1} for the reduction of $\alpha\text{-}[S_2W_{18}O_{62}]^{4-}$ in acetonitrile (CH_3CN ($0.50 \text{ M } [n\text{-Bu}_4\text{N}][\text{PF}_6]$)) as a prototype for the electrochemistry of Dawson-type POMs. Six well defined reduction processes are found at a glassy carbon (GC) electrode (see Figure 4 and detailed descriptions in Chapter 2 and the references [96, 97]). The reversible potentials for these processes are -0.22 , -0.59 , -1.16 , -1.54 , -2.00 and $-2.35 \text{ V vs. F}^{0/+}$.

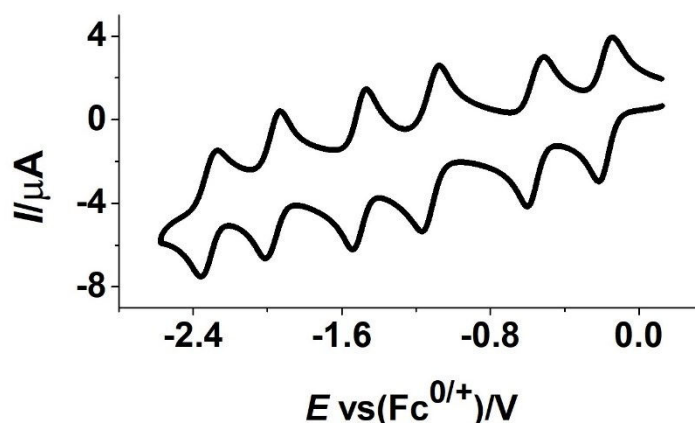
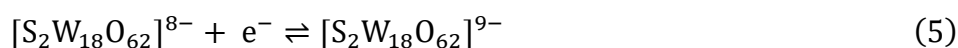
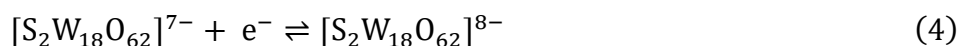
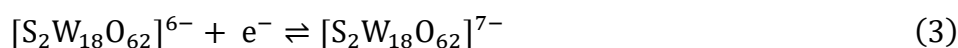
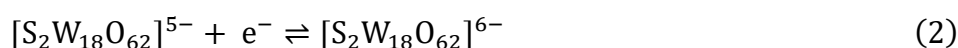
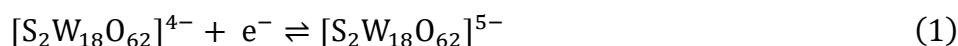
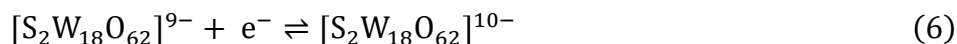


Figure 4. DC cyclic voltammograms obtained at a scan rate of 0.100 Vs^{-1} for reduction of $\alpha\text{-}[S_2W_{18}O_{62}]^{4-}$ in CH_3CN (0.50 M of $[n\text{-Bu}_4\text{N}][\text{PF}_6]$) at a GC macro disc electrode.

A negative shift in reversible potential was found when the supporting electrolyte ($[n\text{-Bu}_4\text{N}][\text{PF}_6]$) decreased from 0.50 to 0.10 M [96]. The electron transfer processes in Figure 4 are summarised in Equations 1 to 6 as follows:





Keggin- Archetype POMs $[XM_{12}O_{40}]^{n-}$:

The DC cyclic voltammetry for the reduction of $[FeClV_{12}O_{32}Cl]^{4-}$ in CH_3CN containing 0.10 M $[n-Bu_4N][PF_6]$ was selected as a prototype for the electrochemistry of Keggin-type POMs. $[FeClV_{12}O_{32}Cl]^{4-}$ exhibits three reduction processes at GC electrode (see Figure 5 and Chapter 6 of the thesis).

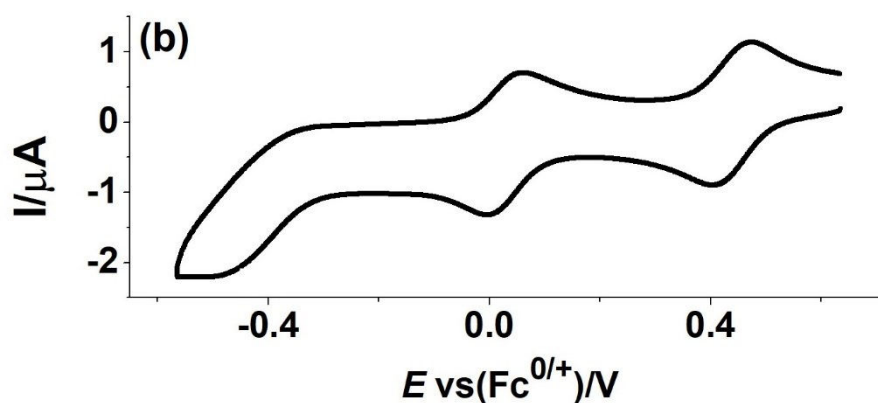


Figure 5. DC cyclic voltammograms obtained at a scan rate of 0.100 Vs^{-1} for the reduction of $[FeClV_{12}O_{32}Cl]^{4-}$ in CH_3CN (0.10 M of $[n-Bu_4N][PF_6]$) at a GC macro disc electrode.

1.2 Introduction to Electrochemistry:

Electrochemistry is the branch of chemistry that considers the relationship between electrical and chemical effects in an electrochemical reaction. Electrochemists are interested in thermodynamic and kinetic parameters that describe an electrochemical reaction. They are also concerned about the charge transportation at the electrode/electrolyte interfaces when potential is applied. The charge is transported through the electrolyte and electrode phases by the movement of ions and electrons, respectively.

1.2.1 The Electrochemical Cell:

Two independent half reactions occur at the two electrode/electrolyte interfaces present in a typical electrochemical cell (see Figure 6). Commonly, electrochemists are interested in the reaction that occurs at the working electrode (WE) with a reference electrode being used to standardise the other half of the cell reaction. In Figure 6, the reaction $Zn^{2+} + 2e^{-} \rightarrow Zn$ (metal) may be of interest with the Ag/AgCl reaction $Ag(\text{metal}) + Cl^{-} \rightleftharpoons AgCl + e^{-}$ being a reference reaction.

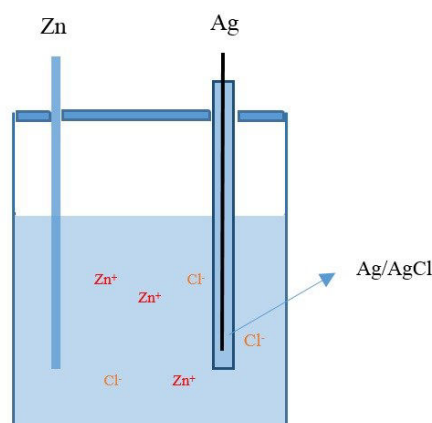


Figure 6. An example of an electrochemical cell consisting of Zn metal and Ag wire covered with AgCl immersed in a $ZnCl_2$ electrolyte solution. [98]

Two-electrode, three-electrode and four-electrode cell setups are available for electrochemical measurements [99, 100]. The three-electrode cell arrangement (see Figure 7) is discussed here as this is the only used cell setup in this thesis. The working electrode (WE), reference electrode (RE), and counter electrode (CE) make up the modern three electrode system. The working electrode is where the reaction of interest occurs in an electrochemical cell [98, 101, 102]. The WE is arranged in conjunction with a CE and a RE in a three-electrode cell system. The WE could be employed as a cathode or anode depending on whether a reduction or oxidation reaction occurs at this electrode. Usually, solid metals (e.g. platinum, gold), liquid metals (e.g.

mercury, amalgams), semiconductors (e.g. indium-tin oxide, silicon) and carbon (e.g. graphite, glassy carbon, boron doped diamond) are used as the working electrode. A half-cell with constant and well-known potential is used as a RE. Examples of internationally recognised and widely used REs are the standard hydrogen electrode (SHE), saturated calomel electrode (SCE) and silver/silver chloride Ag/AgCl. Since the current in a three-electrode electrochemical cell will flow through a counter electrode (CE), its surface area needs to be larger than that of the WE. The CE should be non-reactive regarding the reaction of interest at the WE and is usually made from Pt, Au, graphite or GC and often separated from the WE compartment by a salt bridge.

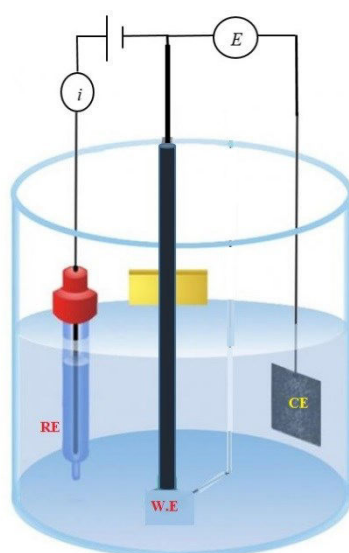


Figure 7. Schematic depiction of a three-electrode electrochemical cell.

The ohmic potential drop (iR_s , where i is the current flowing between WE and CE and R_s is the solution resistance) is the main problem with a two-electrode cell setup, and this is minimised by using a three electrode electrochemical cell [103-106]. In the three-electrode electrochemical cell arrangement, uncompensated resistance (R_u) and compensated resistance (R_c) (see Figure 8) jointly constitute the total resistance (R_s). R_c is not included in the potential

measurement and one can minimise this R_u by having only a small distance between the WE and RE.

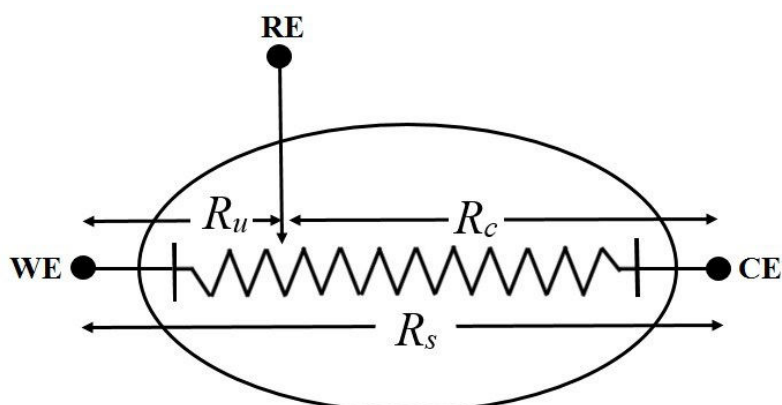


Figure 8. Schematic illustration of a three-electrode electrochemical cell as a potentiostat.

[102]

An external power supply controls the potential of the WE related to the fixed RE potential. The electrochemical reaction of interest can occur in the WE electrode/electrolyte interface when a suitable potential (E) is applied [98]. A reduction current (see Figure 9a) is evident when a sufficiently negative potential is applied. In this case, electrons within the working electrode are excited to a sufficiently high level of energy so they can be transferred into vacant electronic states on electroactive species in the solution or adhere to the surface of the electrode.

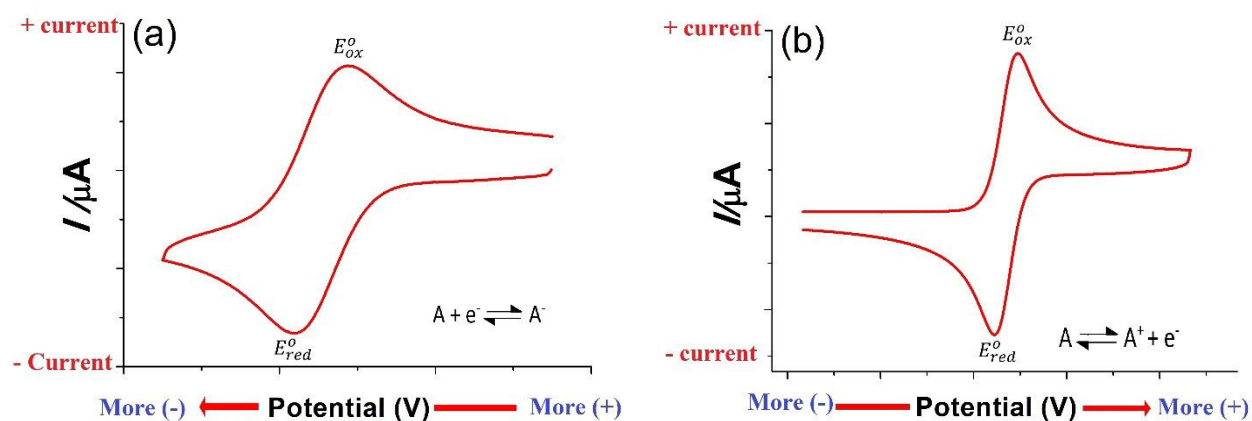


Figure 9. Representation of (a) reduction and (b) oxidation of species, A, in an electrochemical cell under condition of cyclic voltammetry.

Similarly, an oxidation current (see Figure 9b) is evident with the level of energy of electrons lowered by applying a more positive potential. In this instance, electrons on electroactive species in the solution with favourable energy will transfer to the electrode. Overall, the path direction of the electron's movement can be reversed with a variation of the applied potential. Hence, the working electrode can act as a cathode and anode in reduction and oxidation reaction, respectively.

1.2.2 Faradaic and Non-Faradaic Currents:

Faradaic and non-faradaic currents are derived from faradaic and non-faradaic processes, respectively, that occur at the WE. The former arises from reactions in which electrons (charges) are transferred across the electrode–electrolyte (solution) interface; this is called a faradaic current since it is governed by Faraday's law. Under some potentials in an electrochemical cell, the electrode-electrolyte interface does not display any significant charge-transfer reactions (e.g. between 0 and -0.8 V vs. AgBr in Figure 10). Other processes such as adsorption and desorption also can occur and change the structure of the electrode-solution interface depending on the potential and solution composition. Such processes are called non-faradaic processes. Faradaic processes are the primary interest in the study of an electrode reaction. Nevertheless, since faradaic and non-faradaic processes take place in an electrochemical experiment, both must be included in the electrochemical data analysis of charge transfer and associated reactions.

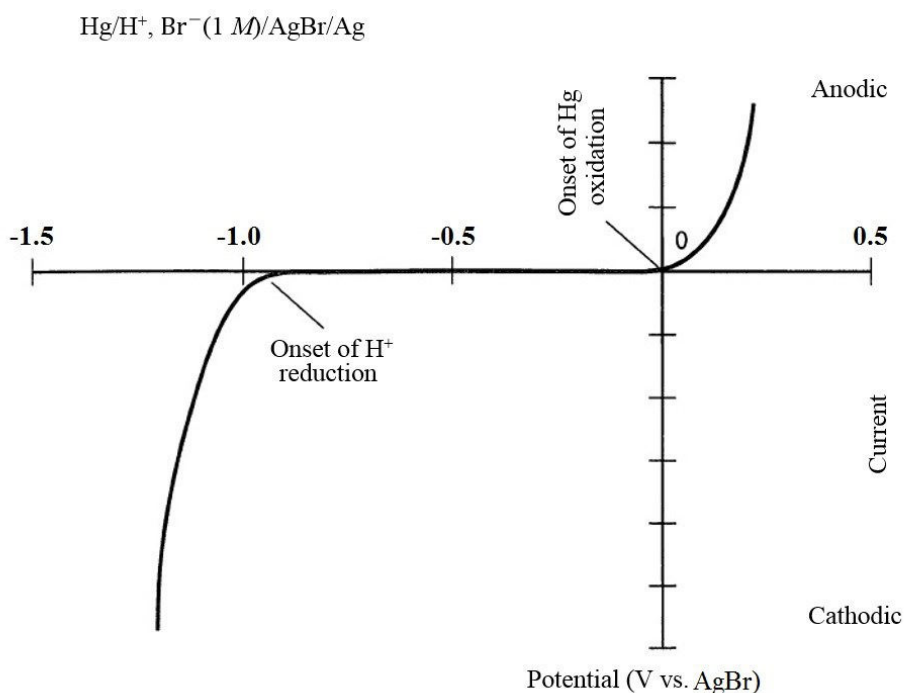


Figure 10. The schematic current-potential curve obtained at a Hg electrode in the cell Hg/H⁺, Br⁻ (1 M)/AgBr/Ag [98], showing the limiting processes: proton reduction at a negative potential and mercury oxidation at a positive potential.

1.2.3 Introduction to Electrode Reactions:

The kinetics of an electrode reaction $O + ne^- \rightleftharpoons R$, where O and R represent the oxidised and reduced form in solution are governed by the rates of the following processes:

- 1) Mass transfer (e.g., of reactant O from the bulk solution to the electrode surface and product R from the electrode surface to the bulk solution).
- 2) Electron transfer at the electrode surface.
- 3) Chemical reactions associated with electron transfer. For example, protonation in homogeneous processes and catalytic reaction in heterogeneous process on the electrode surface.
- 4) Other surface reactions, such as adsorption and desorption.

The simplest reactions involve just three simple steps: i) the mass transfer of a reactant to the electrode surface; ii) heterogeneous electron transfer involving non adsorbed species; iii) mass transfer of the product to the bulk solution. In a complex reaction (see Figure 11), chemical reactions may proceed or follow the electron transfer and modification of the electrode surface by adsorption or desorption may also be present.

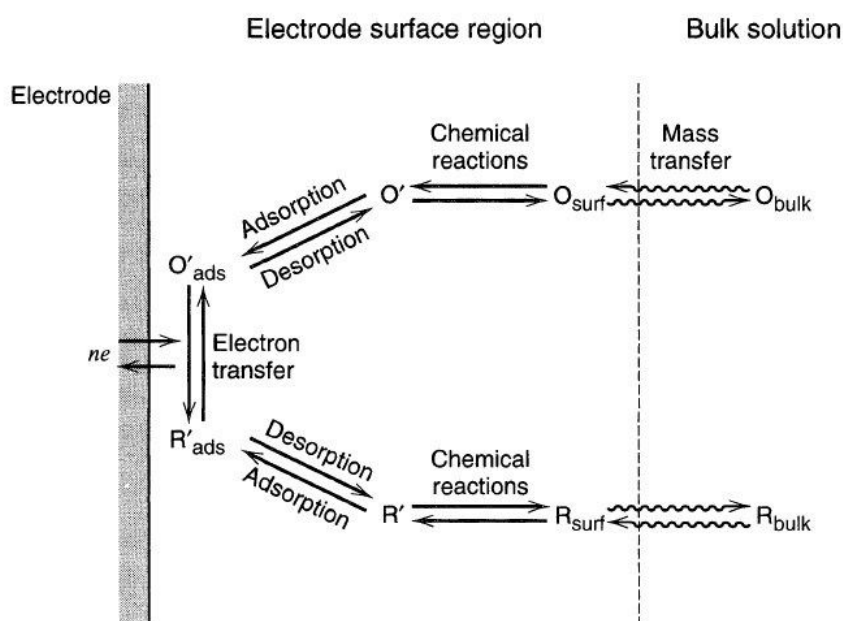


Figure 11. Pathway of electrode reaction [98]

1.2.3.1 Mass Transport:

Movement of material from one location in solution to another is defined as mass transport. Mass transport is governed by either electrical or chemical potential (concentration gradient) or external forces. One dimensional mass transfer to an electrode is governed by the Nernst-Planck equation and written as follows:

$$J_i(x) = -D_i \frac{\partial C_i(x)}{\partial x} - \frac{z_i F}{RT} D_i C_i \frac{\partial \Phi(x)}{\partial x} + C_i v(x) \quad (7)$$

where $J_i(x)$ is the flux of species i ($\text{mol s}^{-1}\text{cm}^{-2}$) at distance x from the surface, D_i is the diffusion coefficient ($\text{cm}^2 \text{s}^{-1}$), $\partial C_i(x)/\partial x$ is the concentration gradient at distance x , $\partial\Phi(x)/\partial x$ is the potential gradient, z_i and C_i are the charge (dimensionless) and concentration (mol cm^{-3}) of species i , respectively, and $v(x)$ is the velocity (cm s^{-1}) with which a volume element in solution moves along the axis.

There are three forms of mass transport [98]:

- a) **Migration:** In this class of mass transport, charged species move from one place to another by the influence of a gradient of electrical potential.
- b) **Diffusion:** In diffusion, species are keen to flow from a region of higher to lower concentration meaning that the concentration gradient plays a vital role.
- c) **Convection:** In this mode of mass transport, an external force is applied to facilitate the transport of species. The external force could be convection created by stirring, laminar flow, turbulent flow etc.

Planar (linear) diffusion: In this diffusion mode, mass transport takes place in one dimension at all points to the electrode surface. This diffusive layer is thin compared to the radius of the electrode. This type of diffusion usually occurs with either macro electrodes or electrodes behaving as macro electrode. Transient cyclic voltammogram obtained with planar diffusion (see Figure 12a).

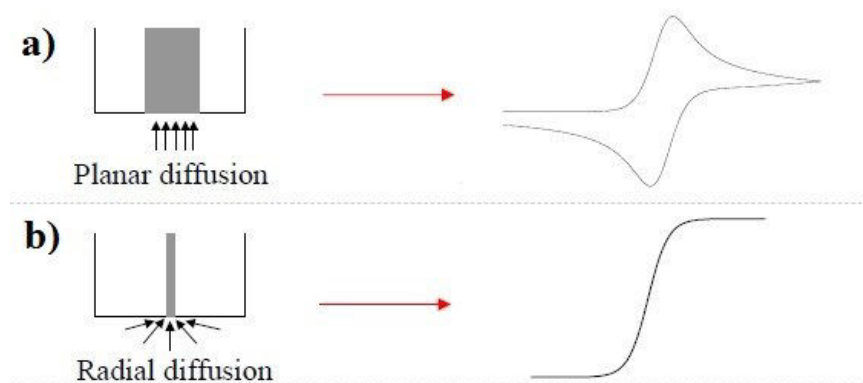
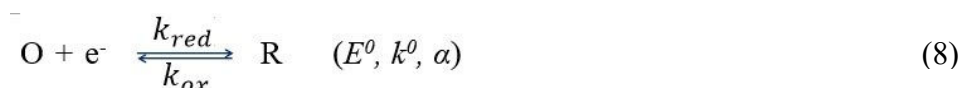


Figure 12. Types and effects of mass transport. a) Planar diffusion and b) Radial diffusion.

Spherical (radial) diffusion: This form of diffusion can take place either with a microelectrode or a macro electrode accompanied by an applied external force (e.g., convection by rotation). Mass transport takes place in multi dimensions at the electrode surface, and the thickness of the diffusive layer will be greater than the radius of the electrode (see Figure 12b). Either transient or steady-state voltammograms may be observed depending on the electrode's size or experimental time scale [107-110].

1.2.3.2 Butler-Volmer Theory of Electrode Kinetics:

The empirical Butler–Volmer (BV) [111, 112] theory used to model the electrode kinetics in this thesis is widely used in electrochemistry to describe both dissolved state and surface-confined electron transfer processes and can be used to predict the potential dependence of the electron transfer kinetics. Equation 8 represents a simple one-electron solution-based reduction process where O and R represent the oxidised and reduced forms of the POM.



According to the Butler-Volmer theory

$$i = F A k^0 [C_O(0, t) e^{-\alpha f(E-E^0)} - C_R(0, t) e^{(1-\alpha)f(E-E^0)}] \quad (9)$$

In Equation 9, F is the Faraday constant, A is the electrode area and $f = F/RT$, R = universal gas constant and T = temperature in Kelvin. More generally, the concentration is expressed as $c_O(x, t)$ and $c_R(x, t)$ for O and R, respectively, where x represents the distance from the surface at time t . Hence the surface concentrations given in Equation 9 are $c_O(0, t)$ and $c_R(0, t)$.

For reversible processes, the electrochemical reactions are governed by the equilibrium conditions within experimental uncertainty, so that voltammetric characteristics are governed solely by the Nernst relationship (Eqn. 10).

$$E = E^0 - \frac{RT}{F} \ln \frac{c_R(0,t)}{c_O(0,t)} \quad (10)$$

where E = applied potential and E^0 = standard potential.

1.2.3.3 Conventional Method for Electrode Kinetic Measurements

Cyclic voltammetry:

For years, many electrochemistry areas have extensively used the popular and simple cyclic voltammetry (CV) [98] as an electroanalytical technique. The basic principle for DC cyclic voltammetry is to apply a ramped (or staircase) potential to the working electrode and measure the resulting current as a function of applied potential (Figure 13a). Figure 13b represents a simple one electron oxidation process for redox active species present in solution.

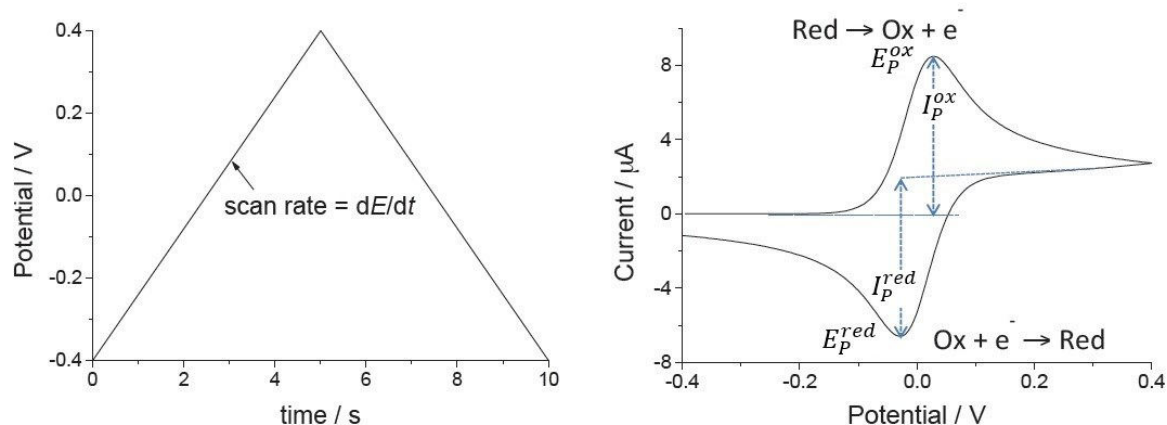


Figure 13. A diagram displaying a) the applied potential on working electrode and b) a cyclic voltammogram for a simple one-electron oxidation process [113]. The symbols used in the diagram are as follows: t = time, E = potential, Red = reduced form, Ox = oxidised form, E_p^{ox} =

peak oxidation potential, E_p^{red} = peak reduction potential, I_p^{ox} = peak oxidation current and I_p^{red} = peak reduction current.

One can extract the standard rate constant of a quasi-reversible process in cyclic voltammetry (Figure 13b) by using the simple Nicholson method [114] where only the peak-to-peak separation $\Delta E_p = (E_p^{red} - E_p^{ox})$ is required. According to this theory, ΔE_p is a function of dimensionless kinetic parameter Ψ (Table 1). Determination of the kinetic parameter can be done by using the value of Ψ in Equation 11. Assuming similar diffusion coefficient values for both oxidised (D_O) and reduced (D_R) gives $\{(D_O/D_R)^{\alpha/2} \cong 1\}$, which symbolises Equation 11.

$$\Psi = \frac{(D_O/D_R)^{\alpha/2} k^0}{(\pi D_O \nu F/RT)^{1/2}} \quad (11)$$

Table 1.1: Variation of ΔE_p with ψ at 25 °C [114]

Ψ	ΔE_p (mV)
20	61
7	63
6	64
5	65
4	66
3	68
2	72
1	84
0.75	92
0.5	105
0.35	121
0.25	141
0.10	212

Uncompensated resistance may increase the ΔE_p value and hence give the false impression of a diminished rate constant, as the Nicholson method [114] does not consider this feature during

calculations. Computer programs like DigiSim [115, 116] and MECSim include the uncompensated resistance effect in the comparison of experimental and theoretical voltammograms.

Steady-State Voltammetry:

Steady state voltammetry obtained with ultra-microelectrodes (UMEs) and a rotating disc electrode (RDE) favour the study of facile electrode kinetics, as this approach offers the advantages of the absence of a double layer charging current and reduced potential drop. In the steady-state method, the difference between two quartile potentials, $|E_{3/4} - E_{1/4}|$ can be used to measure the kinetic parameters.

1.2.4 Bulk Electrolysis:

Bulk electrolysis (BE) is an electrochemical approach where a controlled parameter (either potential or current) is applied to a specially designed electrochemical cell (see Figure 14) to change the redox level (either reduced or oxidised) of the species of interest. Depending on the approach, this method is also known as controlled potential coulometry or potentiostatic coulometry [98, 101, 102, 117, 118].

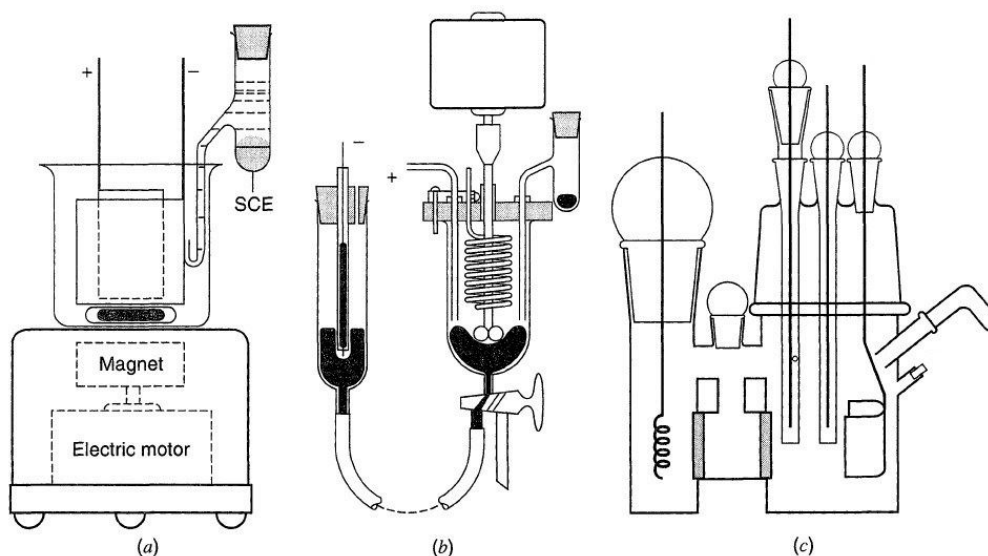


Figure 14. Typical cells for bulk electrolysis, (a) Undivided cell for controlled-potential separations and electro-gravimetric analysis at a solid cathode. [119] (b) Undivided cell for coulometric analysis at mercury cathode with a silver anode. [120] (c) Three-compartment cell, with ground-glass joints, for coulometric and voltammetric vacuum line studies. [121]

Controlled Potential Method:

Constant potential (E) is applied to a large surface area working electrode and current (i) is monitored over time (t). In the case where O is bulk electrolysed to R ($O + ne \rightarrow R$) then the bulk concentration (C_o^*) decreases with the time of electrolysis as in the $i - E$ plot shown in Figure 15.

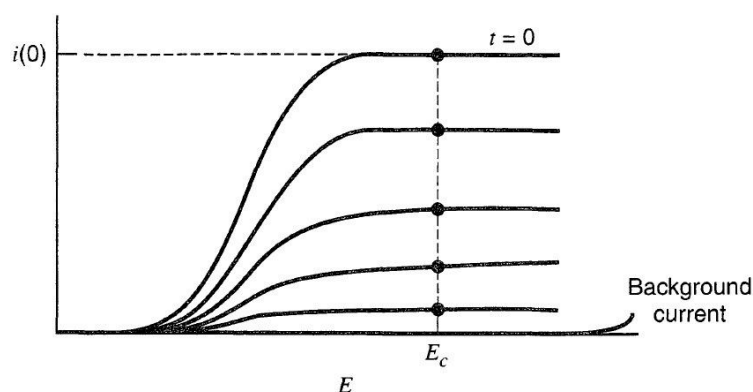


Figure 15. Steady-state current-potential curves obtained at different times during the course of a controlled-potential bulk electrolysis experiment undertaken at a controlled $E = E_c$ for an irreversible process. [98]

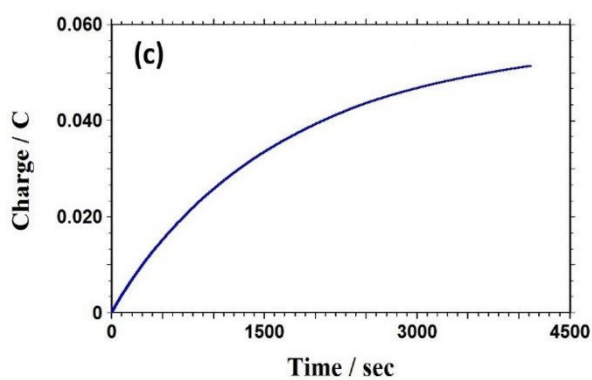


Figure 16. Total coulombs (Q) passed (total electric charge) plotted versus time

The Q - t curve (Figure 16) displays the outcome of bulk electrolysis. One can calculate the total charge (Q) passed during the electrolysis from Equation 12.

$$Q^0 = nFN_0 = nFVC_0^*(0) \quad (12)$$

where, Q^0 is the value of Q at the time of completion of electrolysis ($t \rightarrow \infty$), N_0 is the total number of moles of O initially present and V is the volume of the solution. The value of n can be calculated by coulometry.

1.3 Spectroelectrochemistry:

Spectroelectrochemistry is a coupled characterisation method in which nonelectrochemical techniques (e.g. spectroscopy) are coupled with an electrochemical system. In-situ and ex-situ are the two general types of spectroelectrochemical techniques. In-situ methods involve inspection of the response at the electrode surface during the course of an electrochemical experiment, usually under controlled potential conditions and during the passage of current. Only in-situ techniques will be discussed as this is the only spectroelectrochemical approach used in this thesis.

Basic Principles of Ultra-violet and Visible Spectroscopy:

In UV-Vis spectrometry, a UV-Vis light beam passes through the cell and the absorbance change resulting from transmittance is measured. Transmittance (T) is the ratio of the intensity of the light (I_t) after the light beam passes through the sample cell (see Figure 17) and the intensity of the light (I_o) before the light beam passes through the sample cell expressed by the following equation.

$$T = \frac{I_t}{I_o} \quad (13)$$

Transmittance is related to absorbance (A) by the following expression:

$$A = -\text{Log}(T) = -\text{Log}\left(\frac{I_t}{I_o}\right) = \text{Log}\left(\frac{I_o}{I_t}\right) \quad (14)$$

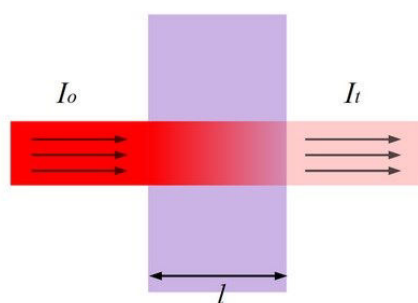


Figure 17. Illustration of Transmittance [122]

Spectroscopy combined with electrochemistry allows spectra (absorbance vs. wavelength (λ)) to be obtained during an electrochemical experiment. Figure 18 shows the spectral changes that accompany the reductive electrolysis of 3,4,7,8-tetramethyl- 1,10-phenanthroline in DMF [123].

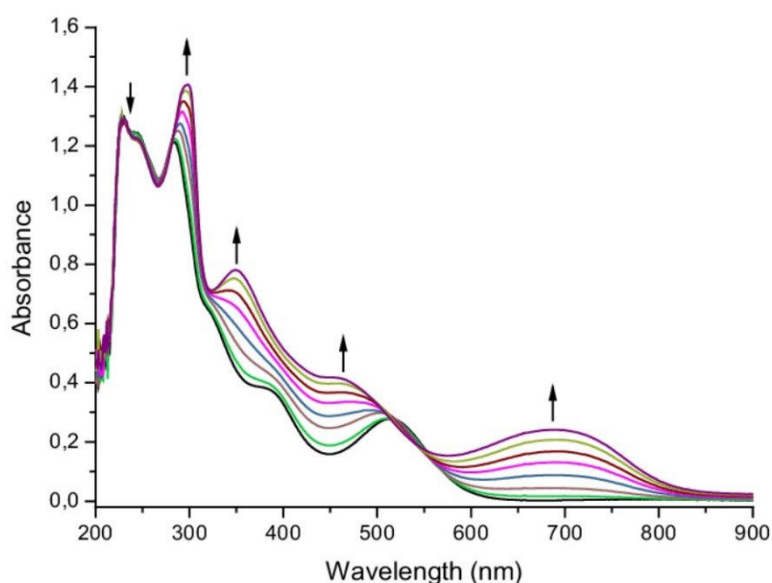


Figure 18. Reduction spectroelectrochemistry of 3,4,7,8-tetramethyl- 1,10-phenanthroline in DMF [123]

1.4 Alternating Current Voltammetry:

After the invention of alternating current (AC) voltammetry in 1950 [124], a significant series of advancements were made by Smith and co-workers [125-129]. In the original form of AC

voltammetry, a sinusoidal oscillating voltage superimposed onto the DC waveform is applied to an electrochemical cell to provide an output that corresponds to the magnitude of AC current versus dc potential (E_{dc}). This AC current or the phase angle (Φ) between the AC current and AC voltage (E_{ac}) can be used to extract the electrode kinetics. In the early days of AC voltammetry, amplitudes of less than 10 mV were used so the theory was relatively simple. In the late 70s, AC voltammetric works with larger amplitudes began to appear [130, 131]. Advanced computer simulation techniques [132] were still not available to fully exploit the method.

This century saw the advancements in the field of large amplitude Fourier transformed alternating current voltammetry (FTACV) by Bond and co-workers [133-135] along with the development of advanced numerical simulation software that gives access to sophisticated data analysis. Higher kinetic sensitivity is accessible by large amplitude Fourier transformed alternating current voltammetry as the higher order AC harmonics is kinetically sensitive. Quantitative measurement of electron transfer kinetics can be attained by comparing experimental and simulated data.

FTACV can partially minimise many of the shortcomings of DC cyclic voltammetry. In this method, a large amplitude sine wave (Figure 19b) is superimposed onto the DC ramp (Figure 19a) to originate the waveform (Figure 19c) and provides the total current versus time (or potential) (Figure 20a). An inverse Fourier transformation (IFT) procedure is used to resolve DC and fundamental and higher order AC harmonic components by selecting the region of interest in the frequency domain or power spectrum (Figure 20b) after conversion from total current–time data (Figure 20a) by Fourier transformation.

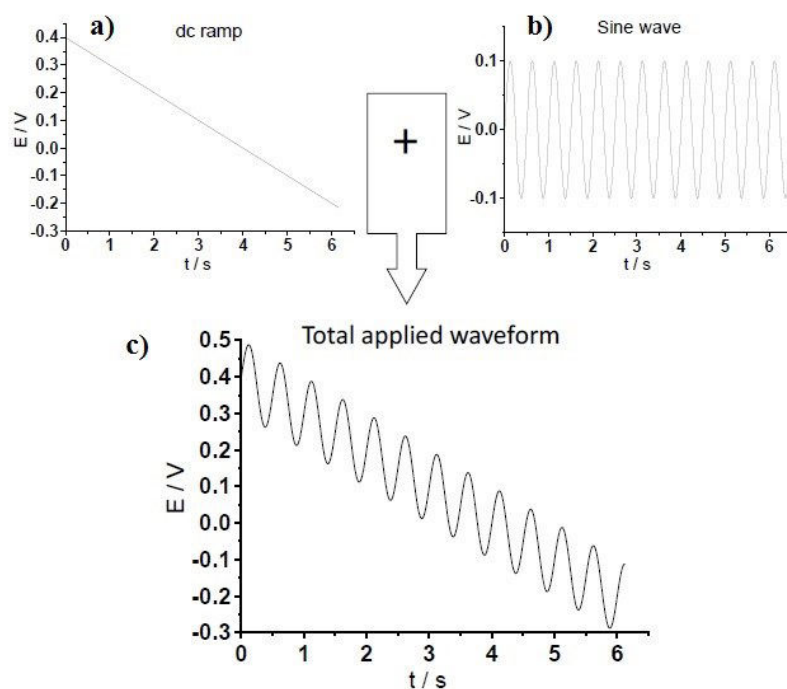


Figure 19. A schematic representation of the FTACV waveform

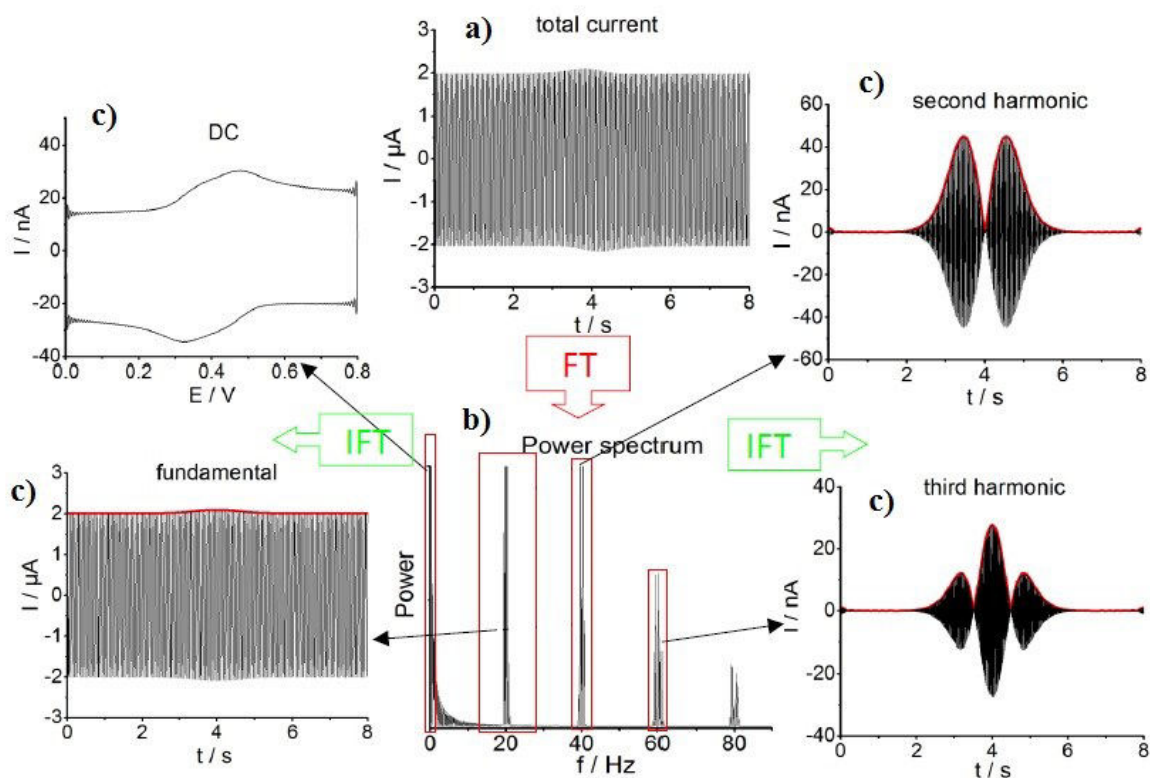


Figure 20: A schematic representation of the data analysis protocols employed in FTACV

FTACV offers some advantages over DC voltammetry during the quantitative analysis of electron transfer kinetics including the followings: i) a non-faradaic current is essentially absent in the higher order harmonic components [136, 137]; ii) higher harmonics can differentiate between the effect of uncompensated resistance and slow electrode kinetics [138]; iii) the current magnitude of higher harmonics are extremely sensitive to the kinetics parameters [139, 140]. These advantages allow large amplitude FTACV to be advantageous for enumerating electrode kinetics relative to DC voltammetry.

In this research, after obtaining experimental data from a home built AC instrument [141], Fourier transformation, band filtering and inverse Fourier transformation were applied to obtain aperiodic DC and fundamental and higher order AC harmonic components. The treated experimental data are then compared with simulated data (obtained using Monash electrochemistry simulator software package, MECSim [142]) to quantify the kinetic parameters.

It is necessary to input an extensive number of parameters [143] such as $E^{0'}$ (reversible potential), k^0 (heterogeneous electron transfer kinetics), α (charge transfer co-efficient), R_u (uncompensated resistance), C_{dl} (double layer capacitance), A (active area of the electrode), D (diffusion coefficient) and concentration (c) into the MECSim software. The RC time constant using data obtained prior to the faradaic process by the CHI 700 E electrochemical workstation was used to determine R_u . The average of the oxidation (E_p^{ox}) and reduction (E_p^{red}) peak potentials in DC cyclic voltammetric experiments can be used to provide an estimate of E^0 . The diffusion coefficient (D) can be calculated from the Randles-Sevcik relationship [98]. C_{dl} was evaluated from the background current in the potential region of the fundamental harmonic of the FTACV response, where the faradaic current is absent [144]. Finally, k^0 (heterogeneous electron transfer kinetics) and α (charge transfer co-efficient) can be estimated by comparison

of experimental and simulated data [145-149]. Figure 21 shows the excellent agreement between experimental and simulated data where all known parameters were used in the MECSim software, k_1^0, α_1 and k_2^0, α_2 were found as $0.054 \text{ cm s}^{-1}, 0.70$ and $0.038 \text{ cm s}^{-1}, 0.68$, respectively.

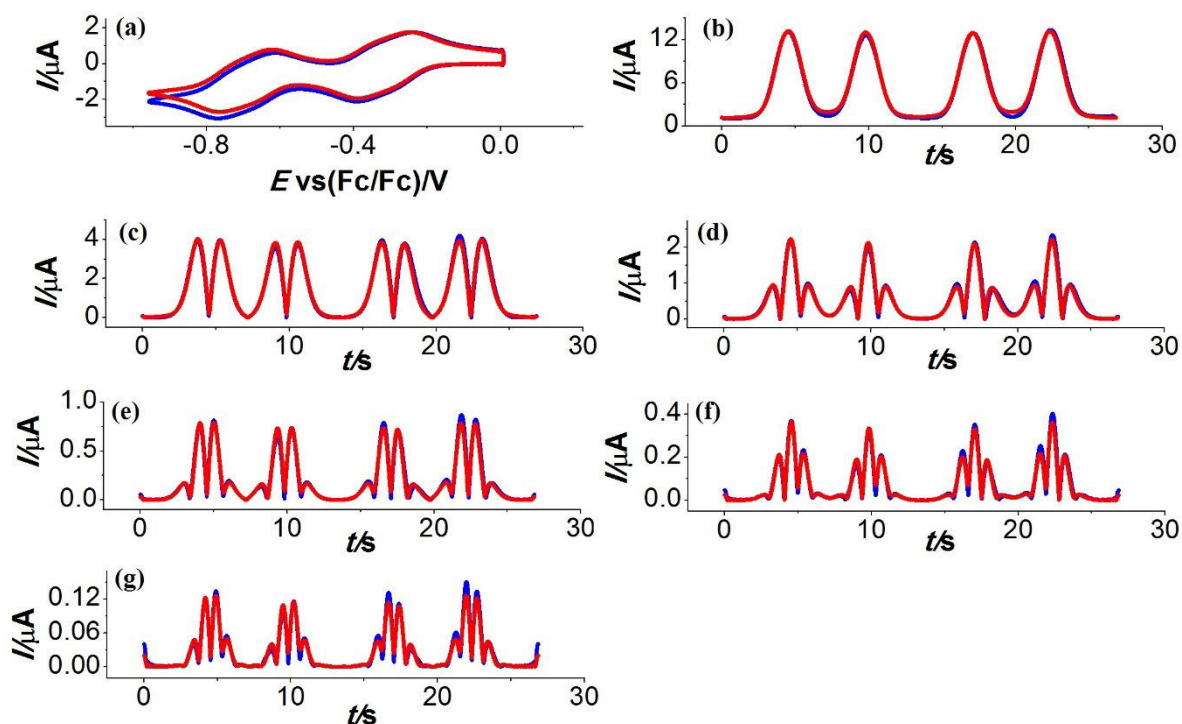


Figure 21. Heuristic comparison of simulated (red line) and experimental (blue line) AC voltammetric data for the α -[S₂W₁₈O₆₂]^{4-/5-/6-} processes, obtained with 2.5 mM α -[S₂W₁₈O₆₂]⁴⁻ in CH₃CN (0.5 M [*n*-Bu₄N][PF₆]) at an Au electrode. Amplitude, $\Delta E = 80 \text{ mV}$, frequency, $f = 27.01 \text{ Hz}$ and scan rate, $\nu = 0.067 \text{ Vs}^{-1}$. (a) DC component, (b-g) 1st to 6th harmonic components. $R_u = 195 \text{ } \Omega$, $D = 2.9 \times 10^{-6} \text{ cm}^2 \text{ s}^{-1}$, $C_{dl}(c_0, c_1, c_2, c_3, c_4) = 34.9, -25.6, 20.5, 97.8, 58.5 \text{ } \mu\text{F cm}^{-2}$. Further details can be found in Chapter 2 [97].

The advanced computer-assisted data analysis method is also used in the analysis of AC data to obtain the kinetic parameters (E^0, k^0 and α) that are free of experimenter bias. In the data

optimisation method, combinations of unknown parameters are achieved by coding the MECSim software script [150]. Therefore, simulated data derived from these combinations are computationally compared with experimental data to attain the best fit. However, in this automation method, the experimenter needs to be conscious of the physically insensitive data derived from the kinetically fast electron transfer process that lies at or near the reversible limit.

In this study, both heuristic and computer-assisted data analysis approaches have been used to parameterise the electrode kinetics associated with several POM (e.g. α -[S₂W₁₈O₆₂]⁴⁻, K^W_{Sn}[N₃C₄H₁₀]⁴⁻) reduction processes in CH₃CN (0.50 or 0.10 M [*n*-Bu₄N][PF₆]) to characterise the electrolyte concentration and electrode material dependent electrode kinetic parameters.

This study also examines non-idealities in the Butler-Volmer model of electron transfer that usually encountered in both solution-phase and surface-confined FTAC voltammetry. Ion-pairing that occurs between electrolyte cation and highly negative POM species or reduced POM species can interact with the simple electron transfer process and hence bring complexity in the AC components, which appear as a difference in the current magnitude of reduction and oxidation components. In this case, only the reduction component (see Figure 22a) of the AC data is considered in the heuristic analysis to derive the electrode kinetic parameters by neglecting ion-pairing. However, incorporating this effect in the model in the future will help to simulate the asymmetric reduction-oxidation component and achieve the more appropriate electrode kinetic parameters. Nevertheless, without the specific instruction, both reduction-oxidation components (see Figure 22b) are considered in the computer-assisted data analysis method regardless of the asymmetry in AC components resulting in an average kinetic value for both components. Adsorption of POMs or reduced POMs provides the modified electrode

surface, which could change the shape and other features of the voltammetry in a potential or time-dependent appearance not accommodated by the theory.

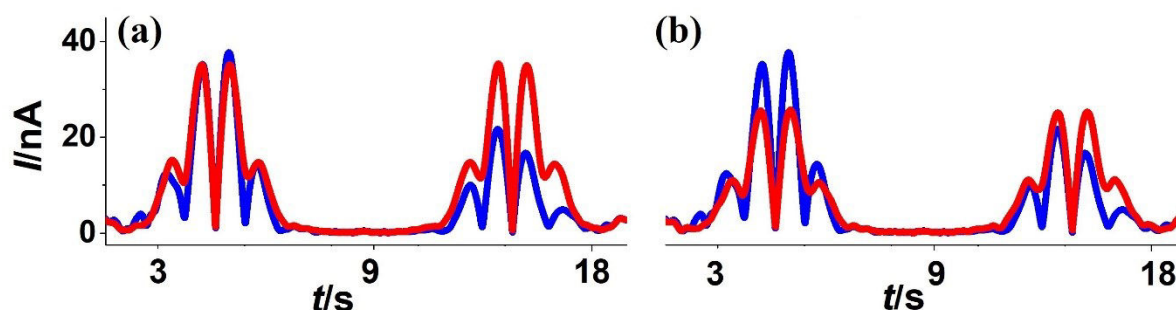


Figure 22. (a) Heuristic and (b) computer-assisted comparison of simulated (red) and experimental (blue) AC voltammetric data [97].

1.5 Electron Paramagnetic Resonance Spectroscopy:

Electron paramagnetic resonance (EPR), also known as electron spin resonance (ESR), is a spectroscopic method used for investigating the paramagnetic properties of chemical species such as free radicals (organic or inorganic) or transition metal complexes with unpaired electrons. The technique used in EPR spectroscopy is similar to nuclear magnetic resonance (NMR) since in both techniques magnetic moments arise from the absorption of electromagnetic radiation. However, in the former spectroscopic technique, paramagnetism is induced by the electrons rather than nuclei. A vital breakthrough occurred in the field of EPR in 1945, when the Soviet physicist Yevgeny Zavoisky [151] observed the paramagnetic resonance spectra of $\text{CuCl}_2 \cdot 2\text{H}_2\text{O}$, which were interpreted by Frankel [152].

Basic Principles of Electron Paramagnetic Resonance:

Spectroscopy represents the assessment and analysis of energy variations between different atomic states. With a knowledge of the energy difference between different alignments of

electron magnetic moments in EPR spectroscopy, one can gain information [153] about the character, structure and dynamic properties of the sample.

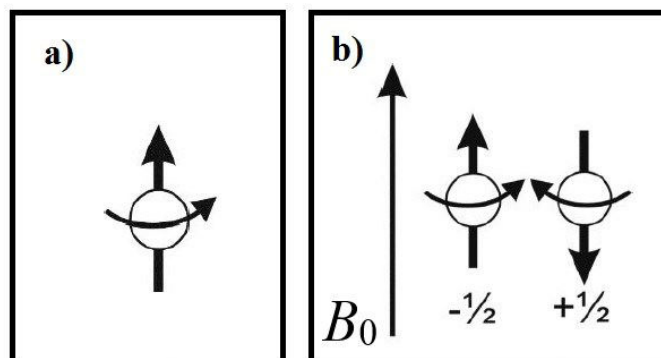


Figure 23. a) Angular momentum of unpaired electron and b) energy orientations of magnetic moment $\bar{\mu}$ with respect to the magnetic field B_0 . [154]

In the presence of external energy, the inherent angular momentum (or spin quantum number, $\bar{S} = \frac{1}{2}$) of an electron can generate a magnetic field around it and hence behave like a tiny bar magnet having a magnetic moment ' $\bar{\mu}$ '. When external a magnetic field B_0 interacts with an unpaired electron, minimum and maximum energy levels are produced for the magnetic moment ' $\bar{\mu}$ ' by either parallel ($m_s = -\frac{1}{2}$) or antiparallel ($m_s = +\frac{1}{2}$) field (see Figure 23) alignment, respectively. This energy is called the Zeeman Effect and is given by Equation 15.

$$E = m_s g \beta B_0 \quad (15)$$

where, m_s = magnetic component, g = g factor and β = Bohr magneton.

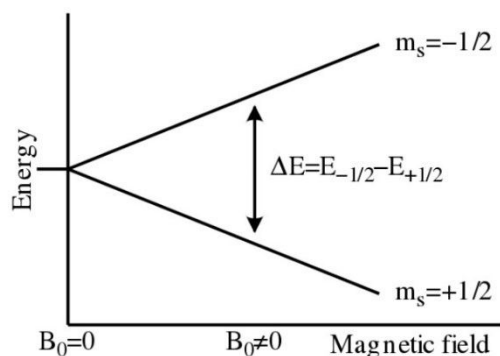


Figure 24. Induction of the spin state energies as a function of the magnetic field B_0 [98]

Based on Figure 24, $\Delta E = E_{-1/2} - E_{+1/2} = g\beta B_0$ is the energy difference between the lower and the upper state of unpaired free electrons. According to Planck, movement of an unpaired electron between the two energy levels can be driven by either absorbing or emitting a photon of energy ' $h\nu$ ' where h = Planck constant and ν = frequency of photon (Eqn. 16).

$$\Delta E = h\nu \quad (16)$$

Equation 16 leads to the fundamental Equation 17 of the EPR spectroscopy:

$$h\nu = g\beta B_0 \quad (17)$$

As μ_B is a constant and B_0 is known from the Equation 17, the value of the 'g' factor calculated as described below can be considered a fingerprint of the molecule of interest. g is calculated from the value of ΔE and measures the magnitude of B_0 from the experiment, as in Equations 16 and 17

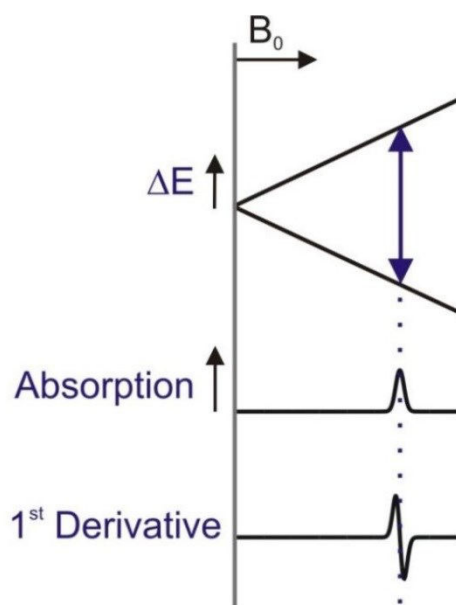


Figure 25. EPR spectrum [98]

The unpaired electron will absorb energy if the condition in Equation 17 is fulfilled. Thus, g factor also can be estimated from ν and B_0 in Equations 18 and 19

$$g = \frac{h\nu}{\beta} \quad (18)$$

$$\text{or } g = 0.7145 \frac{\nu(\text{MHz})}{B_0(\text{Gauss})} \quad (19)$$

$$(h = 6.626 \times 10^{-34} \text{ J.s; } \beta = 9.274 \times 10^{-28} \text{ J G}^{-1})$$

1.6 Research Objectives

The main aim of this research is to develop the strategies described below:

- Parameterise the electrode kinetics associated with POMs by the sensitive FTACV technique to assess whether the Butler-Volmer model of electron transfer is applicable.
- Identify the origin of non-idealities and examine if there is any associated with POM electrode kinetics to have better insight knowledge of their electrochemistry.
- Use a heuristic data analysis approach in conjunction with a computer-assisted automated data optimisation approach in all electrode kinetic studies of this thesis to get the global best fit value by eliminating the shortcomings of both methods.
- Identify the source of reduction process in one electron reduced Zn(II), Cu(II) and Co(II) and two electron reduced Fe(III) functionalized vanadium POMs by electron paramagnetic resonance (EPR) spectroscopy.

References:

- [1] U. Kortz, A. Mueller, J. van Slageren, J. Schnack, N.S. Dalal, M. Dressel, Polyoxometalates: Fascinating structures, unique magnetic properties, *Coord. Chem. Rev.* 253(19-20) (2009) 2315-2327.
- [2] A. Alhanash, E.F. Kozhevnikova, I.V. Kozhevnikov, Hydrogenolysis of glycerol to propanediol over Ru: polyoxometalate bifunctional catalyst, *Catal. Lett.* 120(3-4) (2008) 307-311.

-
- [3] J. Kaur, I.V. Kozhevnikov, Efficient acylation of toluene and anisole with aliphatic carboxylic acids catalysed by heteropoly salt Cs 2.5 H_{0.5}PW₁₂O₄₀, *Chem. Commun.* (21) (2002) 2508-2509.
- [4] M. Musawir, E.F. Kozhevnikova, I.V. Kozhevnikov, Fries rearrangement of phenyl acetate catalysed by platinum-doped heteropoly salt: Catalyst regeneration and reuse, *J. Mol. Catal. A: Chem.* 262(1-2) (2007) 93-97.
- [5] J.S. Santos, J.A. Dias, S.C. Dias, F.A. Garcia, J.L. Macedo, F.S. Sousa, L.S. Almeida, Mixed salts of cesium and ammonium derivatives of 12-tungstophosphoric acid: Synthesis and structural characterization, *Appl. Catal. A-Gen.* 394(1-2) (2011) 138-148.
- [6] L. Fan, L. Xu, G. Gao, F. Li, Z. Li, Y. Qiu, A novel polyoxometalate chain constructed from sandwich lanthanide-containing polyanion [Ce(PW₁₁O₃₉)₂]¹⁰⁻ and sodium ion linker, *Inorg. Chem. Commun.* 9(12) (2006) 1308-1311.
- [7] K. Inumaru, T. Ishihara, Y. Kamiya, T. Okuhara, S. Yamanaka, Water - Tolerant, Highly Active Solid Acid Catalysts Composed of the Keggin - Type Polyoxometalate H₃PW₁₂O₄₀ Immobilized in Hydrophobic Nanospaces of Organomodified Mesoporous Silica, *Angew. Chem. Int. Ed.* 46(40) (2007) 7625-7628.
- [8] J. Lehmann, A. Gaita-Arino, E. Coronado, D. Loss, Spin qubits with electrically gated polyoxometalate molecules, *Nat. Nanotechnol.* 2(5) (2007) 312.
- [9] C. Ritchie, A. Ferguson, H. Nojiri, H.N. Miras, Y.F. Song, D.L. Long, E. Burkholder, M. Murrie, P. Kogerler, E.K. Brechin, L. Cronin, Polyoxometalate-mediated self-assembly of single-molecule magnets: {[XW₉O₃₄]₂[Mn(III)₄Mn(II)₂O₄(H₂O)₄]}¹²⁻, *Angew. Chem. Int. Ed. Engl.* 47(30) (2008) 5609-12.
- [10] D.L. Long, R. Tsunashima, L. Cronin, Polyoxometalates: building blocks for functional nanoscale systems, *Angew. Chem. Int. Ed.* 49(10) (2010) 1736-1758.
- [11] M.T. Pope, Structural chemistry of actinide polyoxometalates, *Structural Chemistry of Inorganic Actinide Compounds*, Elsevier 2007, pp. 341-361.
- [12] J.J. Berzelius, Beitrag zur näheren Kenntniss des Molybdäns, *Annalen der Physik* 82(4) (1826) 369-392.
- [13] J.F. Keggin, Structure of the Crystals of 12-Phosphotungstic Acid, *Nature* 132 (1933) 351.
- [14] C. Chen, W. Zhao, P. Lei, J. Zhao, N. Serpone, Photosensitized degradation of dyes in polyoxometalate solutions versus TiO₂ dispersions under visible-light irradiation: mechanistic implications, *Chemistry (Weinheim an der Bergstrasse, Germany)* 10(8) (2004) 1956-65.
- [15] N. Kawasaki, H. Wang, R. Nakanishi, S. Hamanaka, R. Kitaura, H. Shinohara, T. Yokoyama, H. Yoshikawa, K. Awaga, Nanohybridization of polyoxometalate clusters and single-wall carbon nanotubes: applications in molecular cluster batteries, *Angew. Chem. Int. Ed. Engl.* 50(15) (2011) 3471-4.
- [16] A. Sartorel, M. Carraro, G. Scorrano, R. De Zorzi, S. Geremia, N.D. McDaniel, S. Bernhard, M. Bonchio, Polyoxometalate embedding of a tetraruthenium(IV)-oxo-core by template-directed metalation of [γ-SiW₁₀O₃₆]⁸⁻: a totally inorganic oxygen-evolving catalyst, *J. Am. Chem. Soc.* 130(15) (2008) 5006-7.
- [17] M.H. Seo, S.M. Choi, H.J. Kim, J.H. Kim, B.K. Cho, W.B. Kim, A polyoxometalate-deposited Pt/CNT electrocatalyst via chemical synthesis for methanol electrooxidation, *J. Power Sources* 179(1) (2008) 81-86.
- [18] J. Song, Z. Luo, D.K. Britt, H. Furukawa, O.M. Yaghi, K.I. Hardcastle, C.L. Hill, A multiunit catalyst with synergistic stability and reactivity: a polyoxometalate-metal organic framework for aerobic decontamination, *J. Am. Chem. Soc.* 133(42) (2011) 16839-46.
-

-
- [19] A. Troupis, A. Hiskia, E. Papaconstantinou, Synthesis of metal nanoparticles by using polyoxometalates as photocatalysts and stabilizers, *Angew. Chem. Int. Ed. Engl.* 41(11) (2002) 1911-4.
- [20] I.A. Weinstock, R.H. Atalla, R.S. Reiner, M.A. Moen, K.E. Hammel, C.J. Houtman, C.L. Hill, M.K. Harrup, A new environmentally benign technology for transforming wood pulp into paper. Engineering polyoxometalates as catalysts for multiple processes, *J. Mol. Catal. A: Chem.* 116(1) (1997) 59-84.
- [21] H. Yang, T. Liu, M. Cao, H. Li, S. Gao, R. Cao, A water-insoluble and visible light induced polyoxometalate-based photocatalyst, *Chem Commun (Camb)* 46(14) (2010) 2429-31.
- [22] C. Zou, Z. Zhang, X. Xu, Q. Gong, J. Li, C.D. Wu, A multifunctional organic-inorganic hybrid structure based on Mn(III)-porphyrin and polyoxometalate as a highly effective dye scavenger and heterogenous catalyst, *J. Am. Chem. Soc.* 134(1) (2012) 87-90.
- [23] D.M. Boudreau, Lubricant compositions containing Lindqvist metalates, Google Patents, 2015.
- [24] I.V. Kozhevnikov, G.P. Mulder, M.C. Steverink-de Zoete, M.G. Oostwal, Epoxidation of oleic acid catalyzed by peroxo phosphotungstate in a two-phase system, *J. Mol. Catal. A: Chem.* 134(1) (1998) 223-228.
- [25] D.L. Barnard, C.L. Hill, T. Gage, J.E. Matheson, J.H. Huffman, R.W. Sidwell, M.I. Otto, R.F. Schinazi, Potent inhibition of respiratory syncytial virus by polyoxometalates of several structural classes, *Antivir. Res.* 34(1) (1997) 27-37.
- [26] F. Bussereau, M. Picard, C. Malick, A. Tézé, J. Blancou, Efficacy of heteropolyanions against rabies virus infection in mice, *Annales de l'Institut Pasteur / Virologie* 137 (1986) 391-400.
- [27] J. Huffman, R. Sidwell, D. Barnard, A. Morrison, M. Otto, C. Hill, R. Schinazi, Influenza Virus-Inhibitory Effects of a Series of Germanium- and Silicon-Centred Polyoxometalates, *Antiviral Chem. Chemother.* 8(2) (1997) 75-83.
- [28] Y. Inouye, Y. Tokutake, T. Yoshida, Y. Seto, H. Hujita, K. Dan, A. Yamamoto, S. Nishiya, T. Yamase, S. Nakamura, In vitro antiviral activity of polyoxomolybdates. Mechanism of inhibitory effect of PM-104 $(\text{NH}_4)_{12}\text{H}_2(\text{Eu}_4(\text{MoO}_4)(\text{H}_2\text{O})_{16}(\text{Mo}_7\text{O}_{24})_4)\cdot 13\text{H}_2\text{O}$ on human immunodeficiency virus type 1, *Antivir. Res.* 20(4) (1993) 317-31.
- [29] C. Jasmin, J.C. Chermann, G. Herve, A. Teze, P. Souchay, C. Boy-Loustau, N. Raybaud, F. Sinoussi, M. Raynaud, In vivo inhibition of murine leukemia and sarcoma viruses by the heteropolyanion 5-tungsto-2-antimoniate, *J Natl Cancer Inst* 53(2) (1974) 469-74.
- [30] R.H. Kimberlin, C.A. Walker, Suppression of scrapie infection in mice by heteropolyanion 23, dextran sulfate, and some other polyanions, *Antimicrob. Agents Chemother.* 30(3) (1986) 409-13.
- [31] S.G. Sarafianos, U. Kortz, M.T. Pope, M.J. Modak, Mechanism of polyoxometalate-mediated inactivation of DNA polymerases: an analysis with HIV-1 reverse transcriptase indicates specificity for the DNA-binding cleft, *Biochem. J.* 319 (Pt 2) (1996) 619-26.
- [32] X. Fang, P. Kogerler, Y. Furukawa, M. Speldrich, M. Luban, Molecular growth of a core-shell polyoxometalate, *Angew. Chem. Int. Ed. Engl.* 50(22) (2011) 5212-6.
- [33] Z. Kang, C.H. Tsang, Z. Zhang, M. Zhang, N.B. Wong, J.A. Zapien, Y. Shan, S.T. Lee, A polyoxometalate-assisted electrochemical method for silicon nanostructures preparation: from quantum dots to nanowires, *J. Am. Chem. Soc.* 129(17) (2007) 5326-7.
-

- [34] Z. Kang, Y. Wang, E. Wang, S. Lian, L. Gao, W. You, C. Hu, L. Xu, Polyoxometalates nanoparticles: synthesis, characterization and carbon nanotube modification, *Solid State Commun.* 129(9) (2004) 559-564.
- [35] F.J. Ma, S.X. Liu, C.Y. Sun, D.D. Liang, G.J. Ren, F. Wei, Y.G. Chen, Z.M. Su, A sodalite-type porous metal-organic framework with polyoxometalate templates: adsorption and decomposition of dimethyl methylphosphonate, *J. Am. Chem. Soc.* 133(12) (2011) 4178-81.
- [36] H.J. Pang, J. Peng, C.J. Zhang, Y.G. Li, P.P. Zhang, H.Y. Ma, Z.M. Su, A polyoxometalate-encapsulated 3D porous metal-organic pseudo-rotaxane framework, *Chem Commun (Camb)* 46(28) (2010) 5097-9.
- [37] C.P. Pradeep, M.F. Misrahi, F.Y. Li, J. Zhang, L. Xu, D.L. Long, T. Liu, L. Cronin, Synthesis of modular "inorganic-organic-inorganic" polyoxometalates and their assembly into vesicles, *Angew. Chem. Int. Ed. Engl.* 48(44) (2009) 8309-13.
- [38] C.Y. Sun, S.X. Liu, D.D. Liang, K.Z. Shao, Y.H. Ren, Z.M. Su, Highly stable crystalline catalysts based on a microporous metal-organic framework and polyoxometalates, *J. Am. Chem. Soc.* 131(5) (2009) 1883-8.
- [39] L. Xu, H. Zhang, E. Wang, A. Wu, Z. Li, Preparation and characterization of photoluminescent ultrathin films based on polyoxometalates, *Mater. Chem. Phys.* 77(2) (2003) 484-488.
- [40] Y. Yan, H. Wang, B. Li, G. Hou, Z. Yin, L. Wu, V.W. Yam, Smart self-assemblies based on a surfactant-encapsulated photoresponsive polyoxometalate complex, *Angew. Chem. Int. Ed. Engl.* 49(48) (2010) 9233-6.
- [41] A. Bijelic, A. Rompel, The use of polyoxometalates in protein crystallography - An attempt to widen a well-known bottleneck, *Coord. Chem. Rev.* 299 (2015) 22-38.
- [42] M.T. Pope, *Heteropoly and isopoly oxometalates*, Springer-Verlag (1983).
- [43] A.J. Bridgeman, G. Cavigliasso, Structure and bonding in $[M(6)O(19)]^{(n-)}$ isopolyanions, *Inorg. Chem.* 41(7) (2002) 1761-70.
- [44] I. LINDQVIST, The Structure of the Hexaniobate Ion in $7Na_2O \cdot 6Nb_2O_5 \cdot 32H_2O$, *Arkiv for Kemi* 5(3) (1953) 247-250.
- [45] J. Sloan, G. Matthewman, C. Dyer-Smith, A.Y. Sung, Z. Liu, K. Suenaga, A.I. Kirkland, E. Flahaut, Direct imaging of the structure, relaxation, and sterically constrained motion of encapsulated tungsten polyoxometalate lindqvist ions within carbon nanotubes, *ACS nano* 2(5) (2008) 966-76.
- [46] Y. Xia, Y. Wei, Y. Wang, H. Guo, A kinetically controlled trans bifunctionalized organoimido derivative of the Lindqvist-type hexamolybdate: synthesis, spectroscopic characterization, and crystal structure of $(n-Bu_4N)_2\{trans-[Mo_6O_{17}(NAr)_2]\}$ (Ar = 2,6-dimethylphenyl), *Inorg. Chem.* 44(26) (2005) 9823-8.
- [47] X. Yang, T. Waters, X.-B. Wang, R.A.J. O'Hair, A.G. Wedd, J. Li, D.A. Dixon, L.-S. Wang, Photoelectron Spectroscopy of Free Polyoxoanions $Mo_6O_{19}^{2-}$ and $W_6O_{19}^{2-}$ in the Gas Phase, *J. Phys. Chem. A* 108(46) (2004) 10089-10093.
- [48] J.B. Strong, G.P.A. Yap, R. Ostrander, L.M. Liable-Sands, A.L. Rheingold, R. Thouvenot, P. Gouzerh, E.A. Maatta, A New Class of Functionalized Polyoxometalates: Synthetic, Structural, Spectroscopic, and Electrochemical Studies of Organoimido Derivatives of $[Mo_6O_{19}]^{2-}$, *J. Am. Chem. Soc.* 122(4) (2000) 639-649.
- [49] Y.P. Jeannin, The Nomenclature of Polyoxometalates: How To Connect a Name and a Structure, *Chem. Rev.* 98(1) (1998) 51-76.

-
- [50] G. Li, Y. Ding, J. Wang, X. Wang, J. Suo, New progress of Keggin and Wells–Dawson type polyoxometalates catalyze acid and oxidative reactions, *J. Mol. Catal. A: Chem.* 262(1) (2007) 67-76.
- [51] L.E. Briand, G.T. Baronetti, H.J. Thomas, The state of the art on Wells–Dawson heteropoly-compounds: A review of their properties and applications, *Appl. Catal. A-Gen.* 256(1) (2003) 37-50.
- [52] H. D'Amour, Vergleich der heteropolyanionen $[\text{PMo}_9\text{O}_{31}(\text{H}_2\text{O})_3]^{3-}$, $[\text{P}_2\text{Mo}_{18}\text{O}_{62}]^{6-}$ und $[\text{P}_2\text{W}_{18}\text{O}_{62}]^{6-}$, *Acta Crystallogr. B* 32(3) (1976) 729-740.
- [53] B. Hasenknopf, R. Delmont, P. Herson, P. Gouzerh, Anderson-Type Heteropolymolybdates Containing Tris(alkoxo) Ligands: Synthesis and Structural Characterization, *Eur. J. Inorg. Chem.* 2002(5) (2002) 1081-1087.
- [54] Y.-F. Song, D.-L. Long, L. Cronin, Noncovalently Connected Frameworks with Nanoscale Channels Assembled from a Tethered Polyoxometalate–Pyrene Hybrid, *Angew. Chem. Int. Ed.* 46(21) (2007) 3900-3904.
- [55] Y.-F. Song, D.-L. Long, L. Cronin, Hybrid polyoxometalate clusters with appended aromatic platforms, *CrystEngComm* 12(1) (2010) 109-115.
- [56] Y.-F. Song, D.-L. Long, S.E. Kelly, L. Cronin, Sorting the Assemblies of Unsymmetrically Covalently Functionalized Mn-Anderson Polyoxometalate Clusters with Mass Spectrometry, *Inorg. Chem.* 47(20) (2008) 9137-9139.
- [57] Y.-F. Song, N. McMillan, D.-L. Long, S. Kane, J. Malm, M.O. Riehle, C.P. Pradeep, N. Gadegaard, L. Cronin, Micropatterned Surfaces with Covalently Grafted Unsymmetrical Polyoxometalate-Hybrid Clusters Lead to Selective Cell Adhesion, *J. Am. Chem. Soc.* 131(4) (2009) 1340-1341.
- [58] C. Yvon, A. Macdonell, S. Buchwald, A.J. Surman, N. Follet, J. Alex, D.-L. Long, L. Cronin, A collection of robust methodologies for the preparation of asymmetric hybrid Mn–Anderson polyoxometalates for multifunctional materials, *Chem. Sci.* 4(10) (2013) 3810-3817.
- [59] C.a.C. Moiras, L., Polyoxometalate Nanocapsules: From Structure to Function, *Chem Inform* 41(23) (2010) i.
- [60] A. Müller, E. Krickemeyer, J. Meyer, H. Bögge, F. Peters, W. Plass, E. Diemann, S. Dillinger, F. Nonnenbruch, M. Randerath, C. Menke, $[\text{Mo}_{154}(\text{NO})_{14}\text{O}_{420}(\text{OH})_{28}(\text{H}_2\text{O})_{70}]^{(25 \pm 5)-}$: A Water-Soluble Big Wheel with More than 700 Atoms and a Relative Molecular Mass of About 24000, *Angew. Chem. Int. Ed. Engl.* 34(19) (1995) 2122-2124.
- [61] A. Müller, E. Krickemeyer, H. Bögge, M. Schmidtman, F. Peters, Organizational forms of matter: an inorganic super fullerene and keplerate based on molybdenum oxide, *Angew. Chem. Int. Ed.* 37(24) (1998) 3359-3363.
- [62] Polyoxometalate Chemistry for Nano-Composite Design, KLUWER ACADEMIC PUBLISHERS, NEW YORK.
- [63] F.A. Couto, A.M. Cavaleiro, J.D.P. de Jesus, J.E. Simão, Study of polyoxotungstates with the Keggin structure by cyclic voltammetry, *Inorg. Chim. Acta* 281(2) (1998) 225-228.
- [64] M. Sadakane, E. Steckhan, Electrochemical Properties of Polyoxometalates as Electrocatalysts, *Chem. Rev.* 98(1) (1998) 219-238.
- [65] K. Essaadi, B. Keita, L. Nadjo, R. Contant, Oxidation of NADH by oxometalates, *J. Electroanal. Chem.* 367(1) (1994) 275-278.
- [66] B. Keita, K. Essaadi, L. Nadjo, M. Desmadril, Rate-limiting one-electron transfer in the oxidation of NADH by polyoxometalates, *Chem. Phys. Lett.* 237(5) (1995) 411-418.
-

-
- [67] J. Han, D. Wang, Y. Du, S. Xi, Z. Chen, S. Yin, T. Zhou, R. Xu, Polyoxometalate immobilized in MIL-101(Cr) as an efficient catalyst for water oxidation, *Appl. Catal. A- Gen.* 521 (2016) 83-89.
- [68] Z. Han, A.M. Bond, C. Zhao, Recent trends in the use of polyoxometalate-based material for efficient water oxidation, *Sci. China Chem.* 54(12) (2011) 1877-1887.
- [69] Y.V. Geletii, Z. Huang, Y. Hou, D.G. Musaev, T. Lian, C.L. Hill, Homogeneous Light-Driven Water Oxidation Catalyzed by a Tetra-ruthenium Complex with All Inorganic Ligands, *J. Am. Chem. Soc.* 131(22) (2009) 7522-7523.
- [70] Z. Huang, Z. Luo, Y.V. Geletii, J.W. Vickers, Q. Yin, D. Wu, Y. Hou, Y. Ding, J. Song, D.G. Musaev, C.L. Hill, T. Lian, Efficient Light-Driven Carbon-Free Cobalt-Based Molecular Catalyst for Water Oxidation, *J. Am. Chem. Soc.* 133(7) (2011) 2068-2071.
- [71] B. Keita, L. Nadjo, New aspects of the electrochemistry of heteropolyacids: Part II. Coupled electron and proton transfers in the reduction of silicotungstic species, *J. Electroanal. Chem. Interf. Electrochem.* 217(2) (1987) 287-304.
- [72] B. Keita, L. Nadjo, New aspects of the electrochemistry of heteropolyacids: Part IV. Acidity dependent cyclic voltammetric behaviour of phosphotungstic and silicotungstic heteropolyanions in water and N,N-dimethylformamide, *J. Electroanal. Chem. Interf. Electrochem.* 227(1) (1987) 77-98.
- [73] B. Keita, L. Nadjo, J.P. Haeussler, Distribution of oxometalates on polymer-covered electrodes: Compared catalytic activity of these new polymers and the corresponding oxometalates in solution, *J. Electroanal. Chem. Interf. Electrochem.* 243(2) (1988) 481-491.
- [74] S. Dong, X. Xi, M. Tian, Study of the electrocatalytic reduction of nitrite with silicotungstic heteropolyanion, *J. Electroanal. Chem.* 385(2) (1995) 227-233.
- [75] X. Xi, S. Dong, Electrocatalytic reduction of nitrite using Dawson-type tungstodiphosphate anions in aqueous solutions, adsorbed on a glassy carbon electrode and doped in polypyrrole film, *J. Mol. Catal. A: Chem.* 114(1) (1996) 257-265.
- [76] M.T. Pope, Molybdenum Oxygen Chemistry: Oxides, Oxo Complexes, and Polyoxoanions, *Prog. Inorg. Chem.* 1991, pp. 181-257.
- [77] W.A. Neiwert, J.J. Cowan, K.I. Hardcastle, C.L. Hill, I.A. Weinstock, Stability and Structure in α - and β -Keggin Heteropolytungstates, $[X^{n+}W_{12}O_{40}](8-n)^-$, X = p-Block Cation, *Inorg. Chem.* 41(26) (2002) 6950-6952.
- [78] R. Neumann, M. Dahan, A ruthenium-substituted polyoxometalate as an inorganic dioxygenase for activation of molecular oxygen, *Nature* 388 (1997) 353.
- [79] I.A. Weinstock, E.M.G. Barbuzzi, M.W. Wemple, J.J. Cowan, R.S. Reiner, D.M. Sonnen, R.A. Heintz, J.S. Bond, C.L. Hill, Equilibrating metal-oxide cluster ensembles for oxidation reactions using oxygen in water, *Nature* 414 (2001) 191.
- [80] S. Liu, D.G. Kurth, D. Volkmer, Polyoxometalates as pH-sensitive probes in self-assembled multilayers, *Chem Commun (Camb)* (9) (2002) 976-7.
- [81] J.T. Rhule, C.L. Hill, D.A. Judd, R.F. Schinazi, Polyoxometalates in Medicine, *Chem. Rev.* 98(1) (1998) 327-358.
- [82] C. Cibert, C. Jasmin, Determination of the intracellular localization of a polyoxotungstate (HPA-23) by raman laser and X fluorescence spectroscopies, *Biochem. Biophys. Res. Commun.* 108(4) (1982) 1424-1433.
- [83] M. Cholewa, G.J.F. Legge, H. Weigold, G. Holan, C.J. Birch, The use of a scanning proton microprobe to observe anti-HIV drugs within cells, *Life Sci.* 54(21) (1994) 1607-1612.
-

-
- [84] M. Raynaud, J.C. Chermann, F. Plata, C. Jasmin, G. Mathe, [Inhibitors of the murine leukemia sarcoma group viruses. Silicotungstates], *C R Acad Sci Hebd Seances Acad Sci D* 272(2) (1971) 347-8.
- [85] F. Bussereau, J.C. Chermann, D. De Clercq, C. Hannoun, Search for compounds which have an inhibitory effect on rhabdovirus multiplication In Vitro, *Annales de l'Institut Pasteur / Virologie* 134(1) (1983) 127-134.
- [86] F. Bussereau, A. Ermine, Effects of heteropolyanions and nucleoside analogues on rabies virus: In vitro study of syntheses and viral production, *Annales de l'Institut Pasteur / Virologie* 134(4) (1983) 487-506.
- [87] J.-C. Chermann, F.C. Sinoussi, C. Jasmin, Inhibition of RNA-dependent DNA polymerase of murine oncornaviruses by ammonium-5-tungsto-2-antimoniate, *Biochem. Biophys. Res. Commun.* 65(4) (1975) 1229-1236.
- [88] H. Tsiang, P. Atanasiu, J.C. Chermann, C. Jasmin, Inhibition of Rabies Virus in vitro by the Ammonium-5-Tungsto-2-Antimoniate, *J. Gen. Virol.* 40(3) (1978) 665-668.
- [89] H. Fujita, T. Fujita, T. Sakurai, T. Yamase, Y. Seto, Antitumor Activity of New Antitumor Substance, Polyoxomolybdate, against Several Human Cancers in Athymic Nude Mice, *The Tohoku J. Exp. Med.* 168(2) (1992) 421-426.
- [90] H.N. Mukherjee, Treatment of Cancer of the Intestinal tract with a Complex Compound of Phosphotungstic Phosphomolybdic Acids and Caffeine, *J Indian Med Assoc* 44 (1965) 477-479.
- [91] T. Yamase, N. Fukuda, Y. Tajima, Synergistic Effect of Polyoxotungstates in Combination with β -Lactam Antibiotics on Antibacterial Activity against Methicillin-Resistant *Staphylococcus aureus*, *Biol. Pharm. Bull.* 19(3) (1996) 459-465.
- [92] K. Kastner, J.T. Margraf, T. Clark, C. Streb, A Molecular Placeholder Strategy To Access a Family of Transition - Metal - Functionalized Vanadium Oxide Clusters, *Chem. A Europ.* 20(38) (2014) 12269-12273.
- [93] J. Li, C.L. Bentley, A.M. Bond, J. Zhang, T. Ueda, Influence of 1-butyl-3-methylimidazolium on the electron transfer kinetics associated with the $[\text{SVW}_{11}\text{O}_{40}]^{3-/4-}(\text{V}^{\text{V/IV}})$ and $[\text{SVW}_{11}\text{O}_{40}]^{4-/5-}(\text{W}^{\text{VI/V}})$ processes in dimethylformamide, *J. Electroanal. Chem.* 779 (2016) 67-74.
- [94] J. Li, A.M. Bond, J. Zhang, Probing electrolyte cation effects on the electron transfer kinetics of the $[\alpha\text{-SiW}_{12}\text{O}_{40}]^{4-/5-}$ and $[\alpha\text{-SiW}_{12}\text{O}_{40}]^{5-/6-}$ processes using a boron-doped diamond electrode, *Electrochim. Acta* 178 (2015) 631-637.
- [95] J. Li, S.-X. Guo, C.L. Bentley, K. Bano, A.M. Bond, J. Zhang, T. Ueda, Electrode material dependence of the electron transfer kinetics associated with the $[\text{SVW}_{11}\text{O}_{40}]^{3-/4-}(\text{V}^{\text{V/IV}})$ and $[\text{SVW}_{11}\text{O}_{40}]^{4-/5-}(\text{W}^{\text{VI/V}})$ processes in dimethylformamide, *Electrochim. Acta* 201 (2016) 45-56.
- [96] J. Zhang, A.M. Bond, P.J. Richardt, A.G. Wedd, Voltammetric Reduction of α - and γ - $[\text{S}_2\text{W}_{18}\text{O}_{62}]^{4-}$ and α -, β -, and γ - $[\text{SiW}_{12}\text{O}_{40}]^{4-}$: isomeric dependence of reversible potentials of polyoxometalate anions using data obtained by novel dissolution and conventional solution-phase processes, *Inorg. Chem.* 43(26) (2004) 8263-71.
- [97] M.A. Rahman, J. Li, S.-X. Guo, G. Kennedy, T. Ueda, A.M. Bond, J. Zhang, Modelling limitations encountered in the thermodynamic and electrode kinetic parameterization of the α - $[\text{S}_2\text{W}_{18}\text{O}_{62}]^{4-/5-/6-}$ processes at glassy carbon and metal electrodes, *J. Electroanal. Chem.* (2019) 113786.
- [98] A.a.F. Bard, Larry R, *Electrochemical Methods: Fundamentals and applications*, 2nd ed., Wiley, New York, 2001.
- [99] A. Demortier, A.J. Bard, Electrochemical reactions of organic compounds in liquid ammonia. I. Reduction of benzophenone, *J. Am. Chem. Soc.* 95(11) (1973) 3495-3500.
-

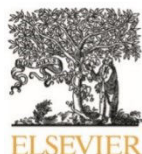
-
- [100] L. Meites, *Polarographic Techniques*, 2nd ed. ed., Wiley-Interscience, New York, 1965.
- [101] P.E. Kissinger, Heineman, W. (Ed.), *Laboratory Techniques in Electroanalytical Chemistry, Revised and Expanded.*, Boca Raton: CRC Press 1996.
- [102] C.G. Zoski, *Handbook of Electrochemistry*, Elsevier, Amsterdam, 2007.
- [103] A.S. Blyr, C., Amatucci, G., Guyomard, D., Chabre, Y. and Tarascon, J.M., Self -Discharge of LiMn₂O₄/C Li - Ion Cells in Their Discharged State Understanding by Means of Three - Electrode Measurements, *J. Electrochem. Soc.* 145(1) (1998) 194-209.
- [104] M. Dollé, Orsini, F., Gozdz, A.S. and Tarascon, J.-M., Development of reliable three-electrode impedance measurements in plastic Li-ion batteries, *J. Electrochem. Soc.* 148(8) (2001) A851-A857.
- [105] T. Hoshikawa, M. Yamada, R. Kikuchi, K. Eguchi, Impedance analysis for dye-sensitized solar cells with a three-electrode system, *J. Electroanal. Chem.* 577(2) (2005) 339-348.
- [106] M.D. Stoller, R.S. Ruoff, Best practice methods for determining an electrode material's performance for ultracapacitors, *Energy Environ. Sci.* 3(9) (2010) 1294-1301.
- [107] C. Amatore, B. Fosset, J. Bartelt, M. Deakin, R. Wightman, Electrochemical kinetics at microelectrodes: Part V. Migrational effects on steady or quasi-steady-state voltammograms, *J. Electroanal. Chem. Interf. Electrochem.* 256(2) (1988) 255-268.
- [108] S. Daniele, I. Lavagnini, M.A. Baldo, F. Magno, Steady state voltammetry at microelectrodes for the hydrogen evolution from strong and weak acids under pseudo-first and second order kinetic conditions, *J. Electroanal. Chem.* 404(1) (1996) 105-111.
- [109] K.B. Oldham, Steady-state microelectrode voltammetry as a route to homogeneous kinetics, *J. Electroanal. Chem. Interf. Electrochem.* 313(1-2) (1991) 3-16.
- [110] C.G. Zoski, A.M. Bond, E.T. Allinson, K.B. Oldham, How long does it take a microelectrode to reach a voltammetric steady state?, *Anal. Chem.* 62(1) (1990) 37-45.
- [111] J. Butler, Studies in heterogeneous equilibria. Part II.—The kinetic interpretation of the nernst theory of electromotive force, *Trans. Faraday Soc.* 19(March) (1924) 729-733.
- [112] T. Erdey-Grúz, M. Volmer, Zur theorie der wasserstoff überspannung, *Zeitschrift für physikalische Chemie* 150(1) (1930) 203-213.
- [113] S.-X. Guo, A.M. Bond, J. Zhang, Fourier transformed large amplitude alternating current voltammetry: principles and applications, *Rev. Polarogr.* 61(1) (2015) 21-32.
- [114] R.S. Nicholson, Theory and application of cyclic voltammetry for measurement of electrode reaction kinetics, *Anal. Chem.* 37(11) (1965) 1351-1355.
- [115] H.S. Barcena, B. Liu, M.V. Mirkin, J.W. Canary, An electrochiroptical molecular switch: Mechanistic and kinetic studies, *Inorg. Chem.* 44(21) (2005) 7652-7660.
- [116] M. Rudolph, D.P. Reddy, S.W. Feldberg, A simulator for cyclic voltammetric responses, *Anal. Chem.* 66(10) (1994) 589A-600A.
- [117] D.A.H. Skoog, F. James; Nieman, Timothy A., *Principles of Instrumental Analysis*, 5 ed., Brooks Cole 1997.
- [118] D.A.W. Skoog, Donald M.; Holler, F. James, *Fundamentals of Analytical Chemistry*, 7 ed., Harcourt Brace College Publishers 1995.
- [119] J.J. Lingane, Controlled potential electroanalysis, *Anal. Chim. Acta* 2 (1948) 584-601.
- [120] J.J. Lingane, Coulometric analysis, *J. Am. Chem. Soc.* 67(11) (1945) 1916-1922.
- [121] W.H. Smith, A.J. Bard, Electrochemical reactions of organic compounds in liquid ammonia. II. Nitrobenzene and nitrosobenzene, *J. Am. Chem. Soc.* 97(18) (1975) 5203-5210.
- [122] <https://chem.libretexts.org/>.
-

-
- [123] M. Al-Noaimi, Keto–enol tautomers of mixed-ligand ruthenium(II) complexes containing α -diamine and azoimine bearing alkyne group ligands, 2017.
- [124] D.C. Grahame, Mathematical theory of the faradaic admittance, *J. electrochem. Soc* 99(12) (1952) 370-385.
- [125] E.R. Brown, E. Smith, D.D. DeFORD, Instrumentation for Digital Data Acquisition in Voltammetric Techniques. DC And AC Polarography, *Anal. Chem.* 38(9) (1966) 1130-1136.
- [126] J.W. Hayes, I. Ruić, D.E. Smith, G.L. Booman, J.R. Delmastro, Fundamental harmonic ac polarography with irreversible dimerization following the charge transfer step: Theory and experimental results with the benzaldehyd system, *J. Electroanal. Chem. Interf. Electrochem.* 51(2) (1974) 269-285.
- [127] T. McCord, E. Brown, D. Smith, Influence of Spherical Diffusion in Second Harmonic AC Polarography and Related Techniques, *Anal. Chem.* 38(11) (1966) 1615-1620.
- [128] T.G. McCord, D.E. Smith, Second harmonic alternating current polarography. Some experimental observations with zinc ion-zinc amalgam system in chloride media, *Anal. Chem.* 42(1) (1970) 126-127.
- [129] D. Smith, W. Reinmuth, Second Harmonic Alternating Current Polarography with a Reversible Electrode Process, *Anal. Chem.* 33(4) (1961) 482-485.
- [130] C. Mooring, H. Kies, AC Voltammetry at large amplitudes: A simplified theoretical approach, *J. Electroanal. Chem. Interf. Electrochem.* 78(2) (1977) 219-227.
- [131] D. Saur, R. Neeb, Grundlagen der nichtlinearen wechselstrompolarographischen Analysenverfahren, *Fresenius' Zeitschrift für analytische Chemie* 290(5) (1978) 374-381.
- [132] A.M. Bond, R.J. O'Halloran, I. Ruzic, D.E. Smith, AC Cyclic voltammetry: A digital simulation study of the slow scan limit condition for a reversible electrode process, *J. Electroanal. Chem. Interf. Electrochem.* 90(3) (1978) 381-388.
- [133] S.O. Engblom, J.C. Myland, K.B. Oldham, Must ac voltammetry employ small signals?, *J. Electroanal. Chem.* 480(1-2) (2000) 120-132.
- [134] S.O. Engblom, J.C. Myland, K.B. Oldham, A.L. Taylor, Large amplitude AC voltammetry– A comparison between theory and experiment, *Electroanalysis: An International Journal Devoted to Fundamental and Practical Aspects of Electroanalysis* 13(8 - 9) (2001) 626-630.
- [135] D. Gavaghan, A. Bond, A complete numerical simulation of the techniques of alternating current linear sweep and cyclic voltammetry: analysis of a reversible process by conventional and fast Fourier transform methods, *J. Electroanal. Chem.* 480(1-2) (2000) 133-149.
- [136] A.P. O'Mullane, J. Zhang, A. Brajter-Toth, A.M. Bond, Higher harmonic large-amplitude fourier transformed alternating current voltammetry: analytical attributes derived from studies of the oxidation of ferrocenemethanol and uric acid at a glassy carbon electrode, *Anal. Chem.* 80(12) (2008) 4614-4626.
- [137] J. Zhang, S.-X. Guo, A.M. Bond, F. Marken, Large-amplitude Fourier transformed high-harmonic alternating current cyclic voltammetry: kinetic discrimination of interfering faradaic processes at glassy carbon and at boron-doped diamond electrodes, *Anal. Chem.* 76(13) (2004) 3619-3629.
- [138] J. Zhang, S.-X. Guo, A.M. Bond, Discrimination and evaluation of the effects of uncompensated resistance and slow electrode kinetics from the higher harmonic components of a fourier transformed large-amplitude alternating current voltammogram, *Anal. Chem.* 79(6) (2007) 2276-2288.
-

-
- [139] B.D. Fleming, J. Zhang, A.M. Bond, S.G. Bell, L.-L. Wong, Separation of electron-transfer and coupled chemical reaction components of biocatalytic processes using Fourier transform ac voltammetry, *Anal. Chem.* 77(11) (2005) 3502-3510.
- [140] J. Zhang, S.-X. Guo, A.M. Bond, M.J. Honeychurch, K.B. Oldham, Novel kinetic and background current selectivity in the even harmonic components of Fourier transformed square-wave voltammograms of surface-confined azurin, *J. Phys. Chem. B* 109(18) (2005) 8935-8947.
- [141] A.M. Bond, N.W. Duffy, S.-X. Guo, J. Zhang, D. Elton, *Changing the look of voltammetry*, ACS Publications, 2005.
- [142] G.F. Kennedy, MECSim software package, 2018.
- [143] A.M. Bond, D. Elton, S.-X. Guo, G.F. Kennedy, E. Mashkina, A.N. Simonov, J. Zhang, An integrated instrumental and theoretical approach to quantitative electrode kinetic studies based on large amplitude Fourier transformed ac voltammetry: A mini review, *Electrochem. Commun.* 57 (2015) 78-83.
- [144] A.M. Bond, N.W. Duffy, D.M. Elton, B.D. Fleming, Characterization of nonlinear background components in voltammetry by use of large amplitude periodic perturbations and Fourier transform analysis, *Anal. Chem.* 81(21) (2009) 8801-8808.
- [145] K. Bano, A.M. Bond, J. Zhang, Determination of Fast Electrode Kinetics Facilitated by Use of an Internal Reference, *Anal. Chem.* 87(16) (2015) 8387-8393.
- [146] K. Bano, G.F. Kennedy, J. Zhang, A.M. Bond, Large amplitude Fourier transformed ac voltammetry at a rotating disc electrode: a versatile technique for covering Levich and flow rate insensitive regimes in a single experiment, *Phys. Chem. Chem. Phys.* 14(14) (2012) 4742-4752.
- [147] K. Bano, J. Zhang, A.M. Bond, P.R. Unwin, J.V. Macpherson, Diminished Electron Transfer Kinetics for $[\text{Ru}(\text{NH}_3)_6]^{3+/2+}$, $[\alpha\text{-SiW}_{12}\text{O}_{40}]^{4-/5-}$, and $[\alpha\text{-SiW}_{12}\text{O}_{40}]^{5-/6-}$ Processes at Boron-Doped Diamond Electrodes, *J. Phys. Chem. C* 119(22) (2015) 12464-12472.
- [148] C.L. Bentley, J. Li, A.M. Bond, J. Zhang, Mass-transport and heterogeneous electron-transfer kinetics associated with the ferrocene/ferrocenium process in ionic liquids, *J. Phys. Chem. C* 120(30) (2016) 16516-16525.
- [149] A.M. Bond, K. Bano, S. Adeel, L.L. Martin, J. Zhang, Fourier - Transformed Large - Amplitude AC Voltammetric Study of Tetrathiafulvalene (TTF): Electrode Kinetics of the $\text{TTF}^0/\text{TTF}^{+\cdot}$ and $\text{TTF}^{+\cdot}/\text{TTF}^{2+}$ Processes, *ChemElectroChem* 1(1) (2014) 99-107.
- [150] G.F. Kennedy, A.M. Bond, A.N. Simonov, Modelling ac voltammetry with MECSim: facilitating simulation-experiment comparisons, *Curr. Opin. Electrochem.* 1(1) (2017) 140-147.
- [151] E. Zavoisky, Spin-magnetic resonance in paramagnetics, *J Phys USSR* 9 (1945) 211-245.
- [152] J. Frenkel, *J. Phys. U.S.S.R.* 9 (1945) 299.
- [153] M.H. Anjass, K. Kastner, F. Nägele, M. Ringenberg, J.F. Boas, J. Zhang, A.M. Bond, T. Jacob, C. Streb, Stabilization of Low - Valent Iron (I) in a High - Valent Vanadium (V) Oxide Cluster, *Angew. Chem. Int. Ed.* 56(46) (2017) 14749-14752.
- [154] E. Duin, Electron Paramagnetic Resonance Theory. https://www.auburn.edu/~duinedu/epr/1_theory.
-

Chapter 2:

Modelling Limitations Encountered in the Thermodynamic and Electrode Kinetic Parameterization of the α -[S₂W₁₈O₆₂]^{4-/5-/6-} Processes at Glassy Carbon and Metal Electrodes



Contents lists available at ScienceDirect

Journal of Electroanalytical Chemistry

journal homepage: www.elsevier.com/locate/jelechem

Modelling limitations encountered in the thermodynamic and electrode kinetic parameterization of the α -[S₂W₁₈O₆₂]^{4-/-5-/-6-} processes at glassy carbon and metal electrodes

Md Anisur Rahman^a, Jiezheng Li^a, Si-Xuan Guo^{a,b}, Gareth Kennedy^a, Tadaharu Ueda^c, Alan M. Bond^{a,b,*}, Jie Zhang^{a,b,*}

^a School of Chemistry, Monash University, Clayton, Victoria 3800, Australia

^b ARC Centre of Excellence for Electrochemical Science, Monash University, Clayton, Victoria 3800, Australia

^c Department of Marine Resource Science, Faculty of Agriculture and Marine Science, Kochi University, Kochi 780-8520, Japan

ARTICLE INFO

Article history:

Received 8 November 2019

Received in revised form 18 December 2019

Accepted 18 December 2019

Available online xxxxx

Keywords:

Polyoxometalates

Fourier transformed alternating current voltammetry

Electrode kinetics

Electrode material dependence

Electrolyte dependence

ABSTRACT

Fourier transformed large amplitude alternating current voltammetry has been used to examine the electrode material and electrolyte dependence of the thermodynamics (E^0 value) and heterogeneous electron-transfer kinetics (k^0 and α values) for the α -[S₂W₁₈O₆₂]^{4-/-5-/-6-} polyoxometalate reduction processes in acetonitrile (0.50 or 0.10 M [n-Bu₄N][PF₆]). Initial estimates of the E^0 , k^0 and α values were made heuristically, and used to allow a computationally based data optimization method of data analysis to be performed more efficiently and to ensure the computer derived parameters are physically significant. At glassy carbon (GC), gold (Au) and platinum (Pt) electrodes, the first α -[S₂W₁₈O₆₂]^{4-/-5-} electron transfer process is always significantly faster than the second α -[S₂W₁₈O₆₂]^{5-/-6-} process, with k^0 values following the order Pt < Au < GC, using the Butler-Volmer model for electron transfer. However, at the Pt electrode, agreement between simulation and experiment for the α -[S₂W₁₈O₆₂]^{5-/-6-} process was poor. Since E^0 significantly depends on the electrolyte concentration, implying the presence of ion-pairing reactions, the implication of neglecting ion-pairing in data analysis was investigated.

© 2020 Elsevier B.V. All rights reserved.

1. Introduction

Polyoxometalates (POMs) represent an extensive series of anionic, inorganic metal oxide compounds which have attracted attention for many years due to their high degree of electronic adaptability [1–3]. Isopolyoxoanions (M_mO_y)ⁿ⁻ and heteropolyoxoanions (X_xM_mO_y)ⁿ⁻ represent the major classes of POMs, where M and X are the addenda atom and heteroatom [4], respectively. POMs are structurally formed via the association of polyhedra, MO_n (most notably octahedral) by one, two or three oxygen atoms in corner, edge and face sharing configurations [5], respectively. The so called Keggin, Wells–Dawson, Anderson, Lindqvist and Preyssler archetypes are the best known structural forms and are usually made from high oxidation state earth-abundant group VI (Mo, W) or V (V, Nb, Ta) transition metals. This combination of redox active elements and structural features allow POMs to undergo fast multi-electron transfer redox reaction which facilitates applications in diverse fields [6] such as

photochemistry [7], oxidative catalysis [8,9], sensing [10], materials science [11] and medicine [12,13].

Thermodynamic effects of the POM structure, counter cations and solvent systems on the redox chemistry have been widely examined [14–16]. In contrast, quantitative electrode kinetics studies [17,18] associated with electron transfer rates are relatively rare. Typically, DC voltammetry [19] has been used to reveal an extensive series of redox processes [17,18,20]. For example, α -[S₂W₁₈O₆₂]⁴⁻ (see Fig. 1) which is the POM of interest in this study, at a glassy carbon (GC) electrode in acetonitrile displays at least six one-electron transfer processes (Eqs. (1)–(6)) [21]. In principle, these processes are defined thermodynamically by the formal reversible potential (E^0) and kinetically according to Butler-Volmer theory by the heterogeneous charge transfer rate constant (k^0) value at E^0 and the charge transfer coefficient (α).



* Corresponding authors at: School of Chemistry, Monash University, Clayton, Victoria 3800, Australia.

E-mail addresses: alan.bond@monash.edu, (A.M. Bond), jie.zhang@monash.edu (J. Zhang).

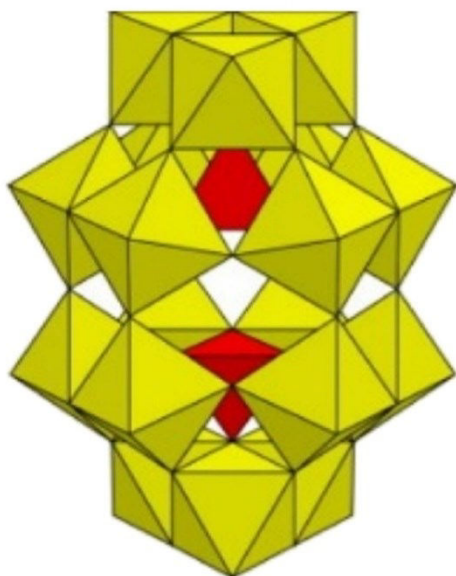


Fig. 1. The structure of α -[S₂W₁₈O₆₂]⁴⁻. Red represents the sulphur heteroatom and yellow the tungsten addenda atom.



In practice, it has been commonly difficult to quantitatively determine the k^0 and α values associated with POM electron transfer processes by transient DC cyclic voltammetry at macrodisk electrodes [22–24], because the electrode kinetics lie very close to the reversible limit [17]. As a consequence, most DC voltammetric studies obscure possible electrode material dependence on the electrode kinetics due to the insensitivity of the DC technique to changes in k^0 and α unless a micro- or even a nano-electrode is used [25–27]. In this situation, higher order harmonic AC components obtained from Fourier transformed large amplitude alternating current voltammetry (FTACV) [28] have been introduced because they are free of background charging current and significantly more sensitive to fast electrode kinetics than DC methods [29]. Furthermore, the impacts of electrode kinetics and uncompensated resistance (R_u) can be resolved by the systematic analysis of the AC harmonic components [30].

In a study based on parameter estimation by analysis of data obtained by DC and FTAC voltammetry [18,20], the [SVW₁₁O₄₀]^{3-/4-/5-} reduction processes showed remarkably more facile electrode kinetics at glassy carbon (GC) than at metal electrodes, such as gold (Au) and platinum (Pt). Intriguingly, the shape of the second tungsten-based reduction process with apparently very slow kinetics at a platinum electrode, does not fully comply with predictions based on the Butler-Volmer relationship. In this study, the FTACV technique is now used to estimate the E^0 , k^0 and α values associated with α -[S₂W₁₈O₆₂]^{4-/5-/6-} processes at GC, Au and Pt electrodes in acetonitrile containing tetrabutylammonium hexafluorophosphate ([n-Bu₄N]

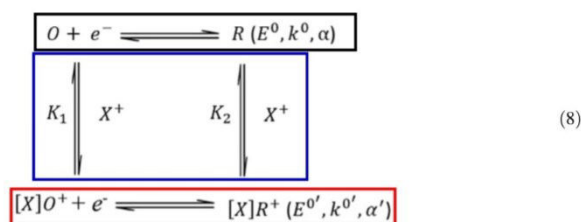
[PF₆]) as the supporting electrolyte. The aim was to investigate if the GC, Au, Pt electrode dependence established with the [SVW₁₁O₄₀]^{3-/4-/5-} system also applies to the α -[S₂W₁₈O₆₂]^{4-/5-} or α -[S₂W₁₈O₆₂]^{5-/6-} processes and if so to establish if non-conformance to Butler-Volmer model observed in the earlier study, again accompanied slow electron transfer at Pt.

According to Butler-Volmer theory [31,32],

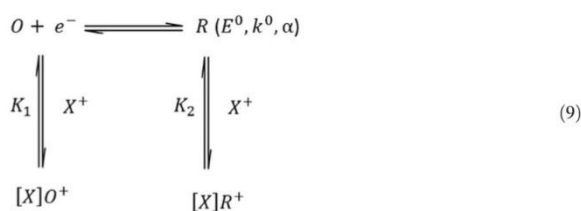
$$I = FAK^0 \left[C_O(0,t)e^{-\alpha f(E-E^0)} - C_R(0,t)e^{(1-\alpha)f(E-E^0)} \right] \quad (7)$$

In this equation, I is current, E is potential, F is the Faraday constant, A is the electrode area and $f = F/RT$, $R =$ universal gas constant, $T =$ temperature in Kelvin, and the concentrations of the oxidized (O) and reduced (R) forms at time t are expressed as $C_O(x,t)$ and $C_R(x,t)$ for O and R, respectively where, x represents the distance from the electrode surface. Hence the surface concentrations of O and R used in Eq. (7) are $C_O(0,t)$ and $C_R(0,t)$, respectively. However, it needs to be recognised that the Butler-Volmer formalism converges to that predicted by Nernst equation when k^0 is sufficiently large. In this circumstance, Butler-Volmer kinetic parameters k^0 and α are irrelevant and only a knowledge of E^0 is needed to define the voltammetry. This situation is encountered in some of the present studies with a GC electrode.

In the case of POM electrochemistry, the reactions are invariably coupled with ion-pairing [33] which in its simplest form with only 1:1 ion pairs present can be described by a square reaction scheme (Eq. (8)).



In this scenario, reaction (i) describes electron transfer involving non ion-paired POMs; reaction (ii) describes ion-pairing of O or R with the supporting electrolyte cation ($X^+ = [n\text{-Bu}_4\text{N}]^+$ in the present study). K_1 and K_2 are ion-pairing equilibrium constants while reaction (iii) is the electron transfer reaction involving the ion-paired species. $E^{0'}$, $k^{0'}$ and α' represent the formal potential, rate constant and charge transfer coefficient, respectively for reaction (iii). However, of course the use of two equilibrium constants for ion pairing and two reversible potentials to define this system represents a thermodynamically superfluous scenario since once E^0 , K_1 and K_2 are known, $E^{0'}$ is defined. Thus, the abbreviated version presented in Eq. (9) below, which is a CEC mechanism (C = Chemical step, E = electron transfer step) is adequate to define thermodynamic properties of the system. In this context, the ion pairs need not be electroactive and electron transfer can take place solely via non-ion paired POMs, but can be limited by rate of conversion of ion-paired to non-ion-paired forms.



The square scheme (Eq. (8)), has been analysed as an apparent one-electron process (Eq. 10), with an apparent reversible formal potential E_{app}^0 , an apparent electron transfer rate constant (k_{app}^0) and an apparent charge transfer coefficient (α_{app}) [34,35].



When the concentration of X^+ ($[n\text{-Bu}_4\text{N}]^+$) is in a large excess and the ion-pairing reactions are reversible,

$$k_{app}^0 = \frac{k^0(K_2/K_1)^{\alpha_{app}} + k^0([X^+]/K_1)}{[1 + ([X^+]/K_1)^{1-\alpha_{app}}][(K_2/K_1) + ([X^+]/K_1)^{\alpha_{app}}]} \quad (11)$$

Bond and Oldham [36,37] have also shown that square schemes that mimic ion-pairing as described above, can have subtle effects on the shapes of voltammograms relative to those predicted on the basis of Nernstian or Butler-Volmer theory. All these considerations imply that imperfections in the model (Eq. (10)) used to describe the voltammetry of highly charged species could unknowingly have been present since ion-pairing reactions may not be reversible.

In this study, simulations derived from MECSim [38] software are compared with experimental data obtained with 0.50 M and 0.10 M $[n\text{-Bu}_4\text{N}][\text{PF}_6]$ supporting electrolyte and the apparent electrode kinetic parameters estimated as a function of electrode material and electrolyte concentration. Both heuristic and computer assisted data optimization methods of data analysis are employed. In the heuristic method, variables are changed manually and the investigator decides on the basis of their experience when acceptable theory-experiment agreement has been achieved. This approach is very tedious, but ensures that chemically sensible values of parameters are generated. A disadvantage is that almost inevitably, experimenter dependent parameters will be reported. However, knowledge of the heuristically estimated parameter values provides a valuable guide to achieving computationally efficient automated data optimisation [39,40]. In the automated method, the best fit data sets are deduced from the range of variables used in the simulations. This method, produces parameters representing the global best fit and are independent of experimenter bias, but does not necessarily provide an intelligent interrogation of discrepancies between experimental and simulated data sets that for example could be a possible outcome of neglect of ion-pairing.

2. Experimental

2.1. Reagents and solvents

$[n\text{-Bu}_4\text{N}]_4(\alpha\text{-}[\text{S}_2\text{W}_{18}\text{O}_{62}])$ was prepared according to a literature method [41]. Ferrocene (Fc, 98%, Sigma-Aldrich), Al_2O_3 (Buehler), acetonitrile (CH_3CN , 99.9%, Sigma-Aldrich) and ethanol (96%, Merck) were used as received from the manufacturer. Tetrabutylammonium hexafluorophosphate ($[n\text{-Bu}_4\text{N}][\text{PF}_6]$, 98%) was obtained from Sigma-Aldrich and recrystallized from hot ethanol [42].

2.2. Instrumentation

DC cyclic voltammetric measurements were undertaken with a BAS Epsilon (Bioanalytical Systems) electrochemical workstation. FTACV experiments employed home-built [43] instrumentation using a sinusoidal perturbation having an amplitude of 80 mV and a frequency of 9.02 or 27.01 Hz superimposed upon the DC ramp. Fourier transformation (FT) was initially used to convert the total current-time data into a power spectrum (frequency domain). Then the aperiodic DC, fundamental and higher harmonic components were obtained by selecting the frequency region of interest in the power spectrum followed by use of the inverse Fourier transform (IFT) procedure [43]. All experiments were executed at $22 \pm 2^\circ\text{C}$ in a 3-electrode electrochemical cell. Oxygen was removed by purging with N_2 for at least 10 min before each measurement. Glassy carbon, gold, platinum

(nominal diameter = 1.0 mm, eDAQ) were employed as the working electrodes. Prior to each experiment, they were polished with an aqueous Al_2O_3 slurry (0.3 μm for GC and 0.05 μm for Au and Pt), rinsed consecutively with water and acetone, and then dried under N_2 . Pt wires were used as both the quasi-reference and auxiliary electrodes. The IUPAC suggested $\text{Fe}^{0/+}$ process [44] was used to calibrate the potential of the Pt quasi-reference electrode.

Surface immobilization of $\alpha\text{-}[\text{S}_2\text{W}_{18}\text{O}_{62}]^{4-}$ on a freshly polished GC electrode was achieved by dipping the electrode into CH_3CN (0.50 M $[n\text{-Bu}_4\text{N}][\text{PF}_6]$) solution containing 2.5 mM of $\alpha\text{-}[\text{S}_2\text{W}_{18}\text{O}_{62}]^{4-}$. After 5 min, the electrode was removed from the solution, rinsed thoroughly with acetone and dried under nitrogen. This electrode was then used as the working electrode in electrochemical experiments in CH_3CN containing only 0.50 M $[n\text{-Bu}_4\text{N}][\text{PF}_6]$.

Effective electroactive areas (A) of all macrodisk working electrodes were determined from the peak current for oxidation of 1.0 mM Fc to Fc^+ in CH_3CN (0.10 M $[n\text{-Bu}_4\text{N}][\text{PF}_6]$) and use of Randles-Sevcik relationship [19] (see Eq. (12)) with a known diffusion coefficient (D) of $2.4 \times 10^{-5} \text{ cm}^2 \text{ s}^{-1}$ for Fc under the conditions used [30].

$$I_p = 0.4463nFA \left(\frac{nFDv}{RT} \right)^{1/2} C \quad (12)$$

In this equation, I_p , n , C , and A denote the oxidation peak current, number of electrons transferred ($n = 1$), bulk solution concentration, and electrode area, respectively. The determined areas of the GC, Au and Pt macrodisk electrodes were 8.0×10^{-3} , 8.1×10^{-3} , and $8.0 \times 10^{-3} \text{ cm}^2$, respectively.

2.3. Simulations

The Monash Electro-Chemistry Simulator (MECSim) [38] software package, which is based on Rudolph computational approach [45] and spatial grid formulation [46] was used to simulate the FTACV data. To model a simple one-electron transfer process (Eq. (8)(i)), Butler-Volmer theory with mass transfer by planar diffusion was adopted. Even for these simulations that neglect ion-pairing, a significant number of parameters such as E^0 , k^0 , α , R_u (uncompensated resistance), C_{dl} (double layer capacitance), A and D are required as inputs for the MECSim software. However, some of these parameters can be independently determined experimentally. The average of the oxidation (E_p^{ox}) and reduction (E_p^{red}) peak potentials in DC cyclic voltammetric experiments provided an estimate of E^0 or more strictly speaking E_{app}^0 , which was used in the heuristic form of data analysis. The diffusion coefficient of $\alpha\text{-}[\text{S}_2\text{W}_{18}\text{O}_{62}]^{4-}$ (D) was calculated to be $2.9 \times 10^{-6} \text{ cm}^2 \text{ s}^{-1}$ from the DC voltammetric peak current [47] associated with the $\alpha\text{-}[\text{S}_2\text{W}_{18}\text{O}_{62}]^{4-/-5-}$ reversible process at a GC electrode in CH_3CN and use of the Randles-Sevcik relationship (see Eq. (12)). R_u was estimated by analysis of the $R_u C_{dl}$ time constant using data obtained prior to reduction of the polyoxometalate and hence where neither DC or AC faradaic current is present. C_{dl} was evaluated from the background current in the potential region of the fundamental harmonic of the FTACV response where AC faradaic current is absent. A non-linear model (Eq. (13)) was used to mimic the potential dependence of C_{dl} [48].

$$C_{dl}(t) = c_0 + c_1 E(t) + c_2 E(t)^2 + c_3 E(t)^3 + c_4 E(t)^4 \quad (13)$$

In this equation, the nonlinearity of the capacitor is defined by the coefficients c_0 , c_1 , c_2 , c_3 , and c_4 and the time dependent potential is designated by $E(t)$. The coefficients were obtained at both frequencies used (9.02 and 27.01 Hz). Finally, a comparison of AC harmonic components derived from experimental and simulated data were used to obtain the k^0 and α values (heuristic method) and E^0 , k^0 and α (automated data optimization method) for the initial two one-electron transfer processes (see Eqs. (1) and (2)) by simulating the reaction as an EE mechanism. A small number of simulations based on a partial square scheme (Eq. (9)) also were derived from use of MECSim. In this case, chemical

steps that represented ion-pairing were coupled with electron transfer with details provided below in the Results and Discussion Section.

When data optimization analysis was used to compute E^0 , k^0 and α , variation in the parameters was achieved by coding the MECSSim script [39] so that simulated data obtained from many combinations of these parameters within specified ranges could be calculated and computationally compared with experimental data to obtain the best fit. Simulations using MECSSim with 2^{16} points took <20 s on a 1.6 GHz computer. Fourier transformation followed by inverse FT was performed in the automated method as in the heuristic method to obtain the AC harmonics. Data optimisation was undertaken on the envelope versus time form of data representation for the AC harmonics (see Fig. S1 in Supporting Information). A python code which stores the maximum current each ac cycle was used to generate the envelop data (Fig. S1(c)) for simulated or experimental data. Each of the smoothed harmonics for simulated and experimental data are then compared using python codes freely available online and a comparison metric based on a relative sum of squares combining selected harmonics is made. Agreement between experimental and simulated data are reported by use of a least squares function (LS) (see Eq. (14)).

$$LS = \left[1 - \frac{1}{H-m+1} \left(\frac{\sum_{h=m}^H \sqrt{\sum_{i=1}^N \left(f_h^{\text{exp}}(t_i) - f_h^{\text{sim}}(t_i) \right)^2}}{\sum_{i=1}^N f_h^{\text{exp}}(t_i)^2} \right) \right] \times 100\% \quad (14)$$

where $f^{\text{exp}}(t_i)$ and $f^{\text{sim}}(t_i)$ represent the experimental and simulated functions, respectively, m is an integer in the range of 0 and H , h represents the aperiodic DC component when $h = 0$ or the AC harmonic component when $h = 1$ to H , H is the total number of AC harmonic components and N is the number of data points. Here, 2nd to 6th harmonics were employed where unlike the DC and fundamental harmonic components, contribution of background current is negligible. Repetition of this approach was applied for every simulated combination of the E^0 , k^0 and α parameters selected; 2000 parameter sets in total. Full details of the automated data optimisation protocol and the code used for each process of the analysis are available online (<http://www.garethkennedy.net/MECsim.html>).

Visualization of the quality of agreement is done by a color contour plot as a function of unknown parameters, such as k^0 , α and E^0 , using the sum of squared residuals of the 6th harmonic normalized by the sum of squares of the experimental function calculated by Eq. (15).

$$S = \frac{\sum_{i=1}^N \left[\left(f_6^{\text{exp}}(t_i) - f_6^{\text{sim}}(t_i) \right)^2 \right]}{\sum_{i=1}^N f_6^{\text{exp}}(t_i)^2} \quad (15)$$

3. Results and discussion

3.1. DC cyclic voltammetry of α -[S₂W₁₈O₆₂]^{4-/-5-}: E^0 and ΔE_p characterization

Fig. 2 displays DC cyclic voltammograms at GC, Au and Pt electrodes for the reduction of α -[S₂W₁₈O₆₂]⁴⁻ to α -[S₂W₁₈O₆₂]⁵⁻ and then to α -

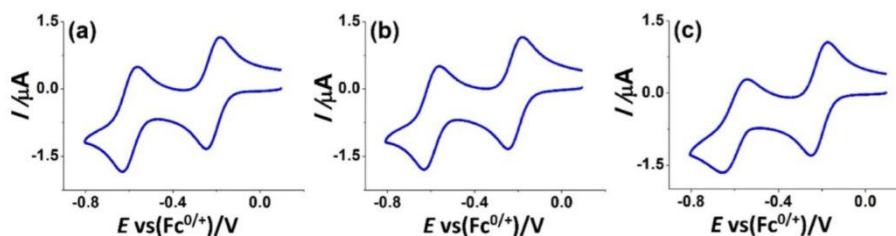


Fig. 2. DC cyclic voltammograms obtained at a scan rate (ν) of 0.100 V s⁻¹ for the α -[S₂W₁₈O₆₂]^{4-/-5-/6-} processes obtained from reduction of 1.0 mM α -[S₂W₁₈O₆₂]⁴⁻ in CH₃CN (0.50 M of [n-Bu₄N][PF₆]) with (a) GC; (b) Au and (c) Pt electrodes.

Table 1
DC cyclic voltammetric data derived from the reduction of 2.5 mM α -[S₂W₁₈O₆₂]⁴⁻ in CH₃CN (0.50 M [n-Bu₄N][PF₆]) at a scan rate of 0.100 V s⁻¹.

Electrode	E_{app1}^0	E_{app2}^0	ΔE_{p1}	ΔE_{p2}
	V ⁰ vs Fc ^{0/+}		V	
GC	-0.215	-0.593	0.060	0.063
Au	-0.215	-0.593	0.063	0.065
Pt	-0.218	-0.593	0.064	0.078

^a Uncertainty is ± 5 mV.

Table 2
Dependence of E_{app}^0 for the reduction of α -[S₂W₁₈O₆₂]⁴⁻ in CH₃CN at a GC electrode on the concentration of [n-Bu₄N][PF₆].

[n-Bu ₄ N][PF ₆]/conc. (M)	E_{app1}^0	E_{app2}^0
	V vs Fc ^{0/+}	
0.50	-0.215	-0.593
0.10	-0.232	-0.610

[S₂W₁₈O₆₂]⁶⁻ in CH₃CN (0.50 M [n-Bu₄N][PF₆]) at a scan rate of 0.100 V s⁻¹. These two initial well defined one-electron reduction processes are of interest in this paper, although at least six one-electron reduction processes have been reported at a GC electrode [21]. The reversible potentials (E_{app}^0), assumed to be equal to the mid-point potentials (E_m) which is the average of the reduction (E_p^{red}) and oxidation (E_p^{ox}) peak potentials, are about -0.22 and -0.59 V vs Fc^{0/+} for the α -[S₂W₁₈O₆₂]^{4-/-5-} and α -[S₂W₁₈O₆₂]^{5-/6-} processes respectively at all electrode materials. The approximation $E_{app}^0 = E_m$ assumes that the oxidized and reduced forms of the polyoxometalate have equal diffusion coefficients.

Table 1 summarizes the E_{app}^0 values along with the peak-to-peak separation ΔE_p ($E_p^{\text{ox}} - E_p^{\text{red}}$) values for the α -[S₂W₁₈O₆₂]^{4-/-5-} and α -[S₂W₁₈O₆₂]^{5-/6-} processes in CH₃CN (0.50 M [n-Bu₄N][PF₆]) with GC, Au and Pt electrodes. The symbols E_{app1}^0 , E_{app2}^0 , ΔE_{p1} and ΔE_{p2} are used to designate the α -[S₂W₁₈O₆₂]^{4-/-5-} and α -[S₂W₁₈O₆₂]^{5-/6-} processes respectively in subsequent discussion. Both processes occur at a more negative potential when a lower concentration of supporting electrolyte (0.10 M [n-Bu₄N][PF₆]) is present (see Table 2 for E_{app}^0 data at GC), which is in agreement with a literature report [21]. The positive E_{app}^0 shift in potential with 0.50 M supporting electrolyte in comparison with 0.10 M confirms that these thermodynamic parameters are dependent on the supporting cation concentration in a manner predicted by the presence of ion-pairing. The extent of interaction of the polyoxometalates with the supporting electrolyte cation is in the order α -[S₂W₁₈O₆₂]^{6-} > \alpha-[S₂W₁₈O₆₂]^{5-} > \alpha-[S₂W₁₈O₆₂]^{4-}.}}}

The experimentally determined ΔE_{p1} value of 60 mV obtained at a scan rate of 0.100 V s⁻¹ for the first process at the GC electrode (Table 1) is close to the value of 56.4 mV theoretically predicted [19] for a reversible one-electron process at 22 °C. Thus, on the DC voltammetric time scale ($\nu = 0.100$ V s⁻¹) this process is essentially reversible. In general, ΔE_p values associated with the first process (0.060, 0.063 and 0.064 V) are smaller than

ARTICLE IN PRESS

M.A. Rahman et al.

Journal of Electroanalytical Chemistry xxx (xxxx) xxx

for the second one (0.063, 0.065 and 0.078 V) at each of the GC, Au and Pt electrodes respectively, implying that k_{app2}^0 is smaller than k_{app1}^0 . ΔE_p values are also smaller at the GC electrode ($\Delta E_{p1} = 0.060$ V and $\Delta E_{p2} = 0.063$ V) than at the two metal electrodes ($\Delta E_{p1} = 0.063$ V and $\Delta E_{p2} = 0.065$ V at Au and $\Delta E_{p1} = 0.064$ V and $\Delta E_{p2} = 0.078$ V at Pt) which implies faster kinetics at the carbon based electrode relative to the metal electrodes given the fact that IR_u effect in all cases are comparable. Significantly, the ΔE_p value at Pt for the second process is indicative of a kinetically quite slow quasi-reversible electron transfer process.

3.2. Theoretical analysis of kinetic sensitivity

The upper limit of measurement of electron transfer kinetics (k^0) at a macrodisk electrode ($d = 1.0$ mm) by FTACV experiments accessible in this study was estimated by theoretical analysis using values of parameters that closely mimic those in experimental studies. Thus, in this exercise, R_u was assumed to be 200Ω , $D = 2.9 \times 10^{-6} \text{ cm}^2 \text{ s}^{-1}$, $T = 295 \text{ K}$, $A = 7.85 \times 10^{-3} \text{ cm}^2$ and $C_{dl} = 10 \mu\text{F cm}^{-2}$. The k^0 value affiliated with an electron transfer process that generates a peak current (I_p) of 90% of a reversible limit was conservatively considered to represent the upper limit of detection (ULD). This ULD concept is readily implemented in the heuristic method of data analysis by an experienced experimentalist, but often overlooked in the automated data optimisation method where unrealistically large k^0 values may easily be inadvertently reported unless the outcome of the data optimisation exercises is carefully scrutinised by appropriate statistical methods [49].

Quantification of the ULD for the determination of k^0 values by FTACV voltammetric experiments relevant to this study was undertaken by examination of a graphical plots of I_p (peak current of the central lobes for the 6th harmonic component) versus $\log_{10}(k^0)$ as provided in Fig. S2 at frequencies of 9.02 and 27.01 Hz. From inspection of the data where I_p has a value corresponding to 90% of the reversible limit, ULD = 0.35 cm s^{-1} at the higher frequency of 27.01 Hz as compared to 0.10 cm s^{-1} at the lower frequency of 9.02 Hz, because a higher kinetic sensitivity is achieved at a shorter time scale of the measurement by using a higher frequency [50].

The sensitivity of the α was assessed by an analogous form of theoretical analysis. In this case, α was varied from 0.30 to 0.70 with k^0 values of 0.10, 0.05, 0.01 and 0.005 cm s^{-1} in simulations where $R_u = 200 \Omega$, $D = 2.9 \times 10^{-6} \text{ cm}^2 \text{ s}^{-1}$, $T = 295 \text{ K}$, $A = 7.85 \times 10^{-3} \text{ cm}^2$

and $C_{dl} = 10 \mu\text{F cm}^{-2}$. Results for the 6th harmonic component of FTAC voltammetry are shown in Fig. S3. The 6th harmonic AC response is now insensitive to the α value for fast kinetics (0.10 cm s^{-1} , Fig. S3(a)) at the lower frequency (9.02 Hz). At the higher frequency (27.01 Hz, Fig. S3(b)) α sensitivity is available because the kinetic sensitivity (see Fig. S2) is enhanced at this shorter time scale. Higher α sensitivity also is available with slower electron transfer rate constants with the sensitivity order being k^0 of $0.05 \text{ cm s}^{-1} < 0.01 \text{ cm s}^{-1} < 0.005 \text{ cm s}^{-1}$. With $k^0 = 0.005 \text{ cm s}^{-1}$ (Fig. S3(e)), substantial asymmetry is obtained when α departs from 0.50.

3.3. Heuristic form of FTAC voltammetric parametrisation of the α -[S₂W₁₈O₆₂]^{4-/-5-/-6-} reduction processes in CH₃CN neglecting ion pairing

The k_{app}^0 and α_{app} values associated with the first two processes obtained for reduction of $2.5 \text{ mM } \alpha$ -[S₂W₁₈O₆₂]⁴⁻ at GC, Au and Pt in acetonitrile containing $0.50 \text{ M } [n\text{-Bu}_4\text{N}][\text{PF}_6]$ supporting electrolyte were initially determined by FTACV using the heuristic form of data analysis. Electrode kinetic parameters obtained in this manner with a sinusoidal perturbation having an amplitude of 80 mV and a frequency of 9.02 or 27.01 Hz are summarized in Table 3. All electrodes gave frequency independent heuristically determined k_{app}^0 and α_{app} values.

The FTACV of the $2.5 \text{ mM } \alpha$ -[S₂W₁₈O₆₂]^{4-/-5-/-6-} processes in CH₃CN ($0.50 \text{ M } [n\text{-Bu}_4\text{N}][\text{PF}_6]$) at GC, Au and Pt electrodes over the potential range of 0.15 V to $-0.825 \text{ V Fc}^{0/+}$ and a comparison with simulated data using parameters given in Table 3 are displayed in Figs. 3 and S4 for GC, S5 for Au and Fig. 4 for the Pt electrode. In the heuristic method of data evaluation, the simulated responses presented in these figures were selected by the experimentalist to represent the "best fit" found by trial and error. In general, the simulated voltammograms with respect to the DC component and all AC harmonics are considered to be in excellent agreement with those derived experimentally, particularly when the limitations of what can be achieved when using the highly tedious heuristic method, are taken into account.

Despite the limitations, use of the heuristic method by an experienced experimentalist does enable important modelling limitations to be detected which may be missed by the sole use of automated data optimisation approaches. For example, and as noted above, only lower limits of k^0 values can really be determined by FTACV or any other voltammetric method when the response lies at or very close to the reversible limit. At a GC

Table 3

Electrode kinetic parameters^a derived from a heuristic comparison of simulated and experimental FTACV data for the α -[S₂W₁₈O₆₂]^{4-/-5-/-6-} processes in CH₃CN ($0.50 \text{ M } [n\text{-Bu}_4\text{N}][\text{PF}_6]$).

Electrode	Conc. (mM)	f (Hz)	$R_u(\Omega)^b$	$C_{dl}(c_0, c_1, c_2, c_3, c_4)$ ($\mu\text{F cm}^{-2}$)	k_{app}^0		α_{app1}	α_{app2}
					cm s^{-1}			
GC	2.5	9.02	205	39, -14.7, -24.8, 1.8, 9.22	$\geq 0.10^c$	$\geq 0.10^c$	- ^c	- ^c
		27.01	195	30.2, -3.96, 14.9, 43.4, 25.4	0.1	0.1	0.57	0.60
	1.0	9.02	195	33.6, -1.01, -18.4, -21, -6.29	$\geq 0.10^c$	$\geq 0.10^c$	- ^c	- ^c
		27.01	205	24.5, -1.43, -18.4, -28.1, -13.9	0.10	0.095	0.51	0.55
Au	2.5	9.02	195	34.9, -25.6, 20.5, 97.8, 58.5	0.050	0.039	0.60	0.62
		27.01	165	26.9, -2.72, 31.1, 63.9, 31.4	0.054	0.038	0.70	0.68
	1.0	9.02	195	40.5, -23, 18.7, 110, 72.6	0.050	0.040	0.62	0.68
		27.01	175	32.4, -7.45, 19.1, 65.8, 38.5	0.052	0.042	0.68	0.68
Pt	2.5	9.02	201	19.1, -16.7, -20, 2.46, 6.46	0.037	0.012 ^d	0.60	0.50 ^d
		27.01	201	16.4, -8.52, -16.2, -9.92, -1.72	0.040	0.012 ^d	0.60	0.53 ^d
	1.0	9.02	215	15, -5.88, -8.46, 2.3, 4.23	0.038	0.010 ^d	0.63	0.50 ^d
		27.01	220	13.1, -3.17, -5.28, -0.84, 0.81	0.040	0.009 ^d	0.60	0.50 ^d

^a Other parameters used in the simulations are: $E_{app1}^0 = -0.215 \text{ V vs Fc}^{0/+}$, $E_{app2}^0 = -0.593 \text{ V vs Fc}^{0/+}$, $A_{GC} = 8.0 \times 10^{-3} \text{ cm}^2$, $A_{Au} = 8.1 \times 10^{-3} \text{ cm}^2$, $A_{Pt} = 8.0 \times 10^{-3} \text{ cm}^2$, $\Delta E = 80 \text{ mV}$, $D = 2.9 \times 10^{-6} \text{ cm}^2 \text{ s}^{-1}$, $T = 295 \text{ K}$, $v_{GC} = 0.067 \text{ V s}^{-1}$, $v_{Au \text{ and Pt}} = 0.072 \text{ V s}^{-1}$ and $f_{GC, Au \text{ and Pt}} = 9.02, 27.01 \text{ Hz}$.

^b Minor variations in R_u are attributed to small differences in electrode arrangement in each experiment

^c Considerable uncertainty as response lies near to reversible limit

^d Determined from forward component only, see text for further details.

ARTICLE IN PRESS

M.A. Rahman et al.

Journal of Electroanalytical Chemistry xxx (xxxx) xxx

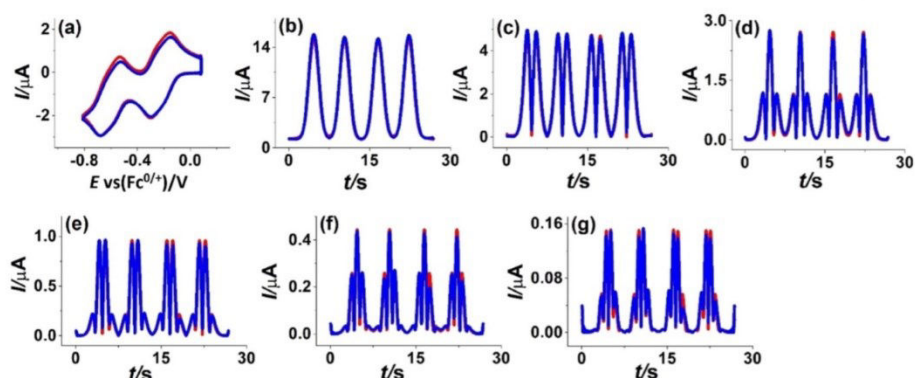


Fig. 3. Heuristic comparison of simulated (red line) and experimental (blue line) AC voltammetric data for the α -[S₂W₁₈O₆₂]^{4-/-5-/-6-} processes obtained from reduction of 2.5 mM α -[S₂W₁₈O₆₂]⁴⁻ in CH₃CN (0.50 M [n-Bu₄N][PF₆]) at a GC electrode. $\Delta E = 80$ mV, $f = 9.02$ Hz and $\nu = 0.067$ V s⁻¹. (a) DC component, (b–g) 1st to 6th harmonic components. Simulation data are based on the assumption of a reversible process.

electrode, with a frequency of 9.02 Hz, this limitation is encountered according to considerations provided in Section 3.2 with data obtained at GC electrode. Thus, the k_{app1}^0 and k_{app2}^0 values at the GC electrode (Table 3,

also see Fig. 3) determined with the frequency of 9.02 Hz of 0.10 cm s⁻¹ are described as lower limits. Fig. 3 clearly shows that experimental data also match closely with those predicted on the basis of reversible theory for

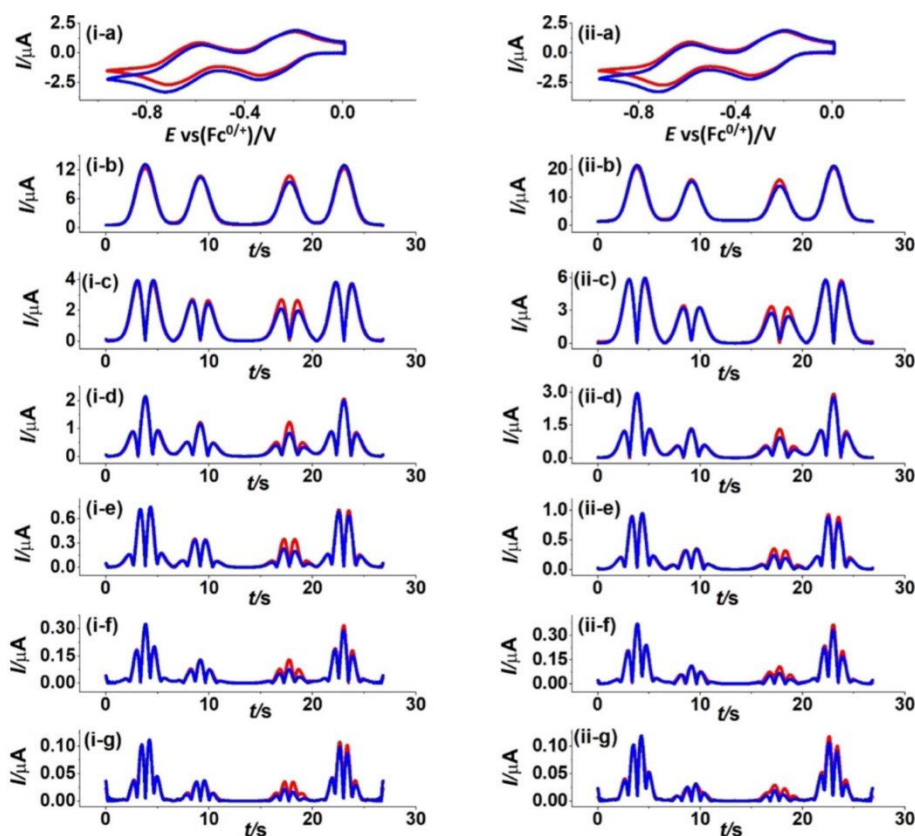


Fig. 4. Heuristic comparison of simulated (red line) and experimental (blue line) AC voltammetric data for the α -[S₂W₁₈O₆₂]^{4-/-5-/-6-} processes obtained for the reduction of 2.5 mM α -[S₂W₁₈O₆₂]⁴⁻ in CH₃CN (0.50 M [n-Bu₄N][PF₆]) at a Pt electrode with $\Delta E = 80$ mV, $f =$ (i) 9.02 Hz and (ii) 27.01 Hz and $\nu = 0.072$ V s⁻¹. (a) DC component, (b–g) 1st to 6th harmonic components. Other parameters given in Table 3 and text.

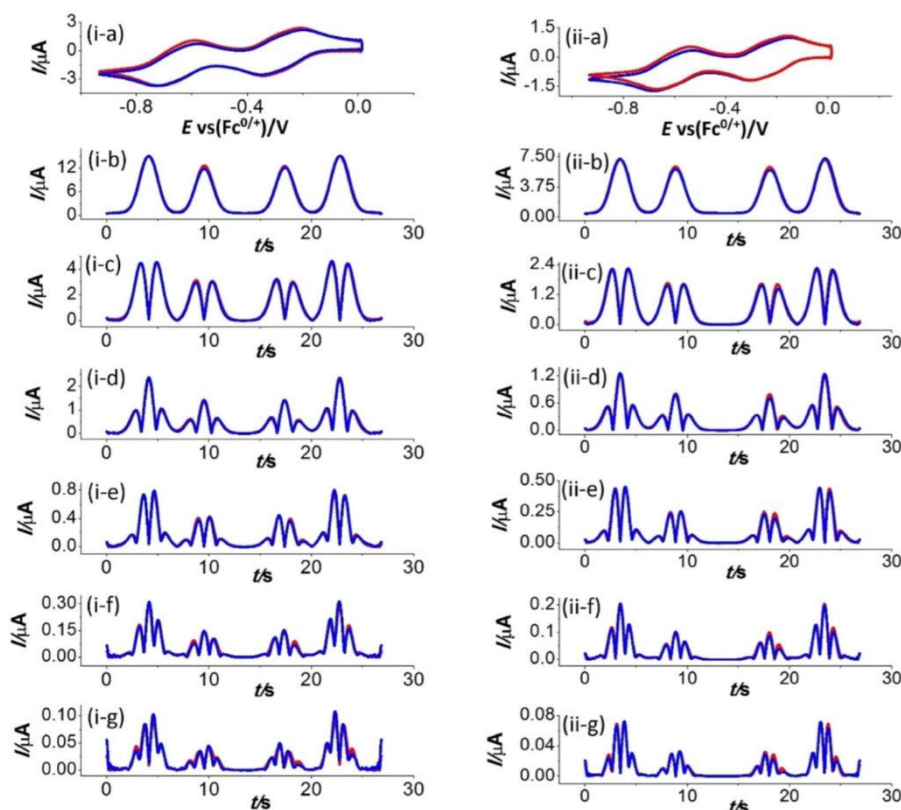


Fig. 5. A comparison of simulated (red line) and experimental (blue line) AC voltammetric data for the α -[S₂W₁₈O₆₂]^{4-/-5-/-6-} processes derived heuristically for the reduction of i) 2.5 mM and ii) 1.0 mM α -[S₂W₁₈O₆₂]⁴⁻ in CH₃CN (0.10 M [n-Bu₄N][PF₆]) at a Pt electrode with $\Delta E = 80$ mV, $f = 9.02$ Hz and $\nu = 0.072$ V s⁻¹. (a) DC component, (b-g) 1st to 6th harmonic components. Other parameters used in simulations are $E_{app1}^0 = -0.232$ V, $E_{app2}^0 = -0.610$ V, $k_{app1}^0 = 0.075$ cm s⁻¹, $\alpha_{app1} = 0.57$, $k_{app2}^0 = 0.024$ cm s⁻¹, $\alpha_{app2} = 0.55$ with 2.5 mM and $k_{app1}^0 = 0.072$ cm s⁻¹, $\alpha_{app1} = 0.57$, $k_{app2}^0 = 0.024$ cm s⁻¹, $\alpha_{app2} = 0.55$ with 1.0 mM α -[S₂W₁₈O₆₂]⁴⁻.

all AC harmonics. As shown in Fig. S3, simulated responses are also insensitive to α_1 and α_2 values when undertaken at or close to the reversible limit. Consequently, this parameter is considered not to be determinable at low frequency with a GC electrode by an experienced experimentalist using the heuristic approach. At the higher frequency ($f = 27.01$ Hz), use of this AC perturbation is assessed in the heuristic context as being suitable for the determination of k_{app}^0 and α_{app} at GC since the shorter time scale of the measurement provides sufficient departure from the reversible limit. That is, the estimated k_{app1}^0 and k_{app2}^0 values of 0.10 cm s⁻¹ reported at higher frequency are now adequately below the anticipated reversible detection limit of 0.35 cm s⁻¹ at 27.01 Hz (Fig. S4). On the basis of the heuristic form of data analysis, an interesting concern now arises with respect to automated data optimisation as to what parameters will be reported on the basis of use of a quasi-reversible model near the reversible limit. Effectively the heuristic analysis implies that there is a risk of overparameterisation (only the single E^0 parameter rather than 3 parameters (E^0 , k^0 , α) actually needed to model the voltammetry at a GC electrode).

In contrast to close to reversible behaviour at the GC electrode, the electron transfer kinetics are considered in terms of heuristic evaluation to lie well below the reversible limit even at the low frequency of 9.02 Hz, at Au and Pt electrodes implying significantly slower electrode kinetics at these metal electrodes. However, it will emerge that close inspection of the data derived from heuristic analysis reveals a subtle, but systematic levels of discrepancy between experimental and simulated data based solely on use of a quasi-reversible process and the Butler-

Volmer model at a Pt electrode. Furthermore, this discrepancy again may be difficult to discern using standard automated data optimisation methods.

For simulations relevant to the Au and Pt electrode data, the same E_{app}^0 values as used in heuristic data analysis at the GC electrode were used as fundamentally this parameter cannot depend on electrode material. Values of all parameters derived for the Au electrode using the heuristic method of data analysis are provided in Table 3. For this electrode, and with 2.5 mM α -[S₂W₁₈O₆₂]⁴⁻, values for k_{app1}^0 and k_{app2}^0 were concluded to be 0.050 and 0.039 cm s⁻¹ respectively at 9.02 Hz and 0.054 and 0.038 cm s⁻¹ respectively at 27.01 Hz. These values are again frequency independent as expected on the basis of Butler-Volmer theory, with $k_{app1}^0 > k_{app2}^0$ as at GC. Again, agreement between simulated and experimental data is considered excellent (see Fig. S5) as was the case at the GC electrode.

In the case of heuristic analysis of the Pt electrode (Fig. 4) data with 2.5 mM α -[S₂W₁₈O₆₂]⁴⁻, current magnitudes in all AC harmonics are much smaller than at GC or Au. This implies a much slower electrode kinetics. k_{app1}^0 values of 0.037 and 0.040 cm s⁻¹, were obtained, respectively at 9.02 and 27.01 Hz. However, there is a dilemma for the experimentalist to address in this data analysis as significant asymmetry appears in the 2nd α -[S₂W₁₈O₆₂]^{5-/-6-} process in the high frequency case where AC currents for the higher order harmonics now differ in magnitude in reduction and oxidation components. The authors of this paper, somewhat arbitrarily, chose to use only the reduction component of the data in the simulation-experimental comparisons to heuristically estimate the kinetic parameters.

ARTICLE IN PRESS

M.A. Rahman et al.

Journal of Electroanalytical Chemistry xxx (xxxx) xxx

Table 4

Ranges of parameters used as an input in the 'GenerateScript.py' file in the automatic simulations using MECSSim. The resolution used was 1.0 mV for the E_{app}^0 range, 0.01 for the α_{app} range with the k_{app}^0 range consisting of at least 20 equally spaced values.

Electrode	Conc. (mM)	f (Hz)	Reduction process	k_{app}^0 (cm s ⁻¹)	α_{app}	E_{app}^0 (V vs Fc ^{0/+})			
GC	2.5	9.02	1st	Range	0.070 to 0.135	0.40 to 0.70	-0.216 to -0.211		
			Estimated	0.101	0.58	-0.214			
		27.01	2nd	Range	0.070 to 0.135	0.40 to 0.70	-0.596 to -0.591		
			Estimated	0.099	0.61	-0.592			
		1.0	9.02	1st	Range	0.070 to 0.135	0.40 to 0.70	-0.216 to -0.212	
				Estimated	0.099	0.60	-0.214		
	27.01		2nd	Range	0.070 to 0.135	0.40 to 0.70	-0.595 to -0.593		
			Estimated	0.099	0.58	-0.592			
	2.5		9.02	1st	Range	0.070 to 0.135	0.40 to 0.70	-0.216 to -0.213	
				Estimated	0.103	0.59	-0.214		
		27.01	2nd	Range	0.070 to 0.135	0.40 to 0.70	-0.594 to -0.591		
			Estimated	0.096	0.60	-0.592			
		1.0	9.02	1st	Range	0.070 to 0.120	0.40 to 0.70	-0.217 to -0.212	
				Estimated	0.103	0.63	-0.214		
	27.01		2nd	Range	0.070 to 0.120	0.40 to 0.70	-0.595 to -0.591		
			Estimated	0.099	0.60	-0.594			
	Au		2.5	9.02	1st	Range	0.035 to 0.070	0.40 to 0.70	-0.218 to -0.212
					Estimated	0.059	0.63	-0.213	
		27.01		2nd	Range	0.031 to 0.043	0.40 to 0.70	-0.599 to -0.592	
				Estimated	0.037	0.056	-0.595		
		1.0		9.02	1st	Range	0.046 to 0.061	0.40 to 0.70	-0.217 to -0.207
					Estimated	0.054	0.67	-0.211	
			27.01	2nd	Range	0.033 to 0.043	0.40 to 0.70	-0.596 to -0.588	
				Estimated	0.041	0.56	-0.594		
2.5			9.02	1st	Range	0.040 to 0.070	0.40 to 0.70	-0.217 to -0.214	
				Estimated	0.058	0.60	-0.216		
		27.01	2nd	Range	0.025 to 0.055	0.40 to 0.70	-0.595 to -0.591		
			Estimated	0.039	0.64	-0.593			
		1.0	9.02	1st	Range	0.040 to 0.070	0.40 to 0.70	-0.218 to -0.214	
				Estimated	0.062	0.65	-0.216		
27.01			2nd	Range	0.030 to 0.060	0.40 to 0.70	-0.596 to -0.592		
			Estimated	0.040	0.62	-0.594			
Pt			2.5	9.02	1st	Range	0.025 to 0.045	0.40 to 0.70	-0.220 to -0.214
					Estimated	0.036	0.57	-0.218	
		27.01		2nd	Range	0.004 to 0.013	0.44 to 0.60	-0.596 to -0.589	
				Estimated	0.009	0.53	-0.591		
		1.0		9.02	1st	Range	0.033 to 0.042	0.50 to 0.67	-0.220 to -0.214
					Estimated	0.038	0.56	-0.219	
			27.01	2nd	Range	0.004 to 0.014	0.44 to 0.65	-0.599 to -0.592	
				Estimated	0.010	0.52	-0.592		
	2.5		9.02	1st	Range	0.025 to 0.045	0.40 to 0.70	-0.220 to -0.214	
				Estimated	0.035	0.60	-0.218		
		27.01	2nd	Range	0.003 to 0.011	0.47 to 0.60	-0.596 to -0.590		
			Estimated	0.007	0.54	-0.591			
		1.0	9.02	1st	Range	0.033 to 0.042	0.52 to 0.65	-0.220 to -0.214	
				Estimated	0.036	0.56	-0.219		
	27.01		2nd	Range	0.003 to 0.011	0.47 to 0.60	-0.597 to -0.589		
			Estimated	0.007	0.51	-0.592			

ARTICLE IN PRESS

M.A. Rahman et al.

Journal of Electroanalytical Chemistry xxx (xxxx) xxx

Table 5
Comparison of E_{app}^0 , k_{app}^0 and α_{app} values^a derived for the α -[S₂W₁₈O₆₂]^{4-/-5-/-6-} processes in CH₃CN (0.50 M [n-Bu₄N][PF₆]) by the automated computational and heuristic methods of data analysis.

Electrode	Conc. (mM)	f (Hz)	Simulation method	E_{app1}^0	E_{app2}^0	k_{app1}^0	k_{app2}^0	α_{app1}	α_{app2}	LS (%)	
				V vs Fc ^{0/+}		cm s ⁻¹					
GC	2.5	9.02	Heuristic	-0.215	-0.593	≥ 0.10	≥ 0.10	- ^b	- ^b		
			Automated	-0.214	-0.592	0.101 ^c	0.099 ^c	0.58 ^c	0.61 ^c	92	
		27.01	Heuristic	-0.215	-0.593	0.10	0.10	0.57	0.60		
			Automated	-0.214	-0.592	0.099	0.099	0.60	0.58	92	
		1.0	9.02	Heuristic	-0.215	-0.593	≥ 0.10	≥ 0.10	- ^b	- ^b	
				Automated	-0.214	-0.592	0.103 ^c	0.096 ^c	0.59 ^c	0.60 ^c	90
	27.01		Heuristic	-0.215	-0.593	0.10	0.095	0.51	0.55		
			Automated	-0.214	-0.594	0.103	0.099	0.63	0.60	85	
	2.5		9.02	Heuristic	-0.215	-0.593	0.050	0.039	0.60	0.62	
				Automated	-0.213	-0.595	0.059	0.037	0.63	0.56	94
		27.01	Heuristic	-0.215	-0.593	0.054	0.038	0.70	0.68		
			Automated	-0.211	-0.594	0.054	0.041	0.67	0.56	92	
Au		1.0	9.02	Heuristic	-0.215	-0.593	0.050	0.040	0.62	0.68	
				Automated	-0.216	-0.593	0.058	0.039	0.60	0.64	91
	27.01		Heuristic	-0.215	-0.593	0.052	0.042	0.68	0.68		
			Automated	-0.216	-0.594	0.062 ^d	0.040	0.65	0.62	88	
	2.5		9.02	Heuristic	-0.218	-0.593	0.037	0.012 ^c	0.60	0.50	
				Automated	-0.218	-0.591	0.036	0.009 ^d	0.57	0.53	78
		27.01	Heuristic	-0.218	-0.593	0.040	0.012 ^c	0.60	0.53		
			Automated	-0.219	-0.592	0.038	0.010 ^d	0.56	0.52	78	
		1.0	9.02	Heuristic	-0.218	-0.593	0.038	0.010 ^c	0.63	0.50	
				Automated	-0.218	-0.591	0.035	0.007 ^d	0.60	0.54	79
	27.01		Heuristic	-0.218	-0.593	0.040	0.009 ^c	0.60	0.50		
			Automated	-0.219	-0.592	0.036	0.007 ^d	0.56	0.51	77	

^a Other parameters used in the simulations are: $A_{GC} = 8.0 \times 10^{-3} \text{ cm}^2$, $A_{Au} = 8.1 \times 10^{-3} \text{ cm}^2$, $A_{Pt} = 8.0 \times 10^{-3} \text{ cm}^2$, $\Delta E = 80 \text{ mV}$, $D = 2.9 \times 10^{-6} \text{ cm}^2 \text{ s}^{-1}$, $T = 295 \text{ K}$, $v_{GC} = 0.067 \text{ V s}^{-1}$, v_{Au} and $v_{Pt} = 0.072 \text{ V s}^{-1}$, $f_{GC, Au}$ and $f_{Pt} = 9.02, 27.01 \text{ Hz}$.

^b Too close to reversible limit to be determined.

^c Near reversible limit so uncertainty substantial (see text for further details).

^d Derived from use of all data even though asymmetry is present in reduction and oxidation components.

^e Determined from reduction component of data only.

Using this procedure, k_{app2}^0 and α_{app2} values of 0.012 cm s^{-1} and 0.50 were obtained at 9.02 Hz and 0.012 cm s^{-1} and 0.53 at 27.01 Hz , respectively. Again, the automated method, without instructions to the contrary, will use all data and inevitably simply find the best fit based on the maximum LS value. In all likelihood this approach will generate a different set of electrode kinetic parameters to those obtained heuristically.

Heuristic parameter estimation with a lower concentration (1.0 mM) of α -[S₂W₁₈O₆₂]⁴⁻ also was investigated by the FTACV technique, again with 0.50 M [n-Bu₄N][PF₆] as the supporting electrolyte. Results obtained are presented in Table 3, while Figs. S6 to S8 in Supporting Information provide the comparison of experimental and theoretical data under these conditions. Electrode kinetic parameters are concentration independent which suggests that IR_u has been correctly modelled.

3.4. AC voltammetry of the α -[S₂W₁₈O₆₂]^{4-/-5-/-6-} processes at a Pt electrode in CH₃CN (0.10 M [n-Bu₄N][PF₆])

Heuristic estimation of the apparent electrode kinetics with a lower concentration (0.10 M) of supporting electrolyte also was used to probe the possible impact of neglect of ion-pairing on data obtained at the Pt electrode. The hypothesis is that ion pairing should be less significant with 0.10 M than with 0.50 M [n-Bu₄N][PF₆] as the supporting electrolyte. The E^0 values of -0.232 and $-0.610 \text{ V vs Fc}^{0/+}$ relevant to the lower

electrolyte concentration obtained a GC electrode (Table 2) was assumed to be appropriate for the data analysis as was the Butler-Volmer model as traditionally used in studies of this kind. A comparison of simulated and experimental data for the lower electrolyte concentration situation at the Pt electrode (see Fig. 5) with either 2.5 or 1.0 mM α -[S₂W₁₈O₆₂]⁴⁻ now are devoid of any anomalies with almost perfect simulation-experiment agreement obtained with all harmonics for both reduction and oxidation components using k_{app1}^0 and α_{app1} values of 0.075 cm s^{-1} and 0.57 and k_{app2}^0 and α_{app2} values of 0.024 cm s^{-1} and 0.55 with 2.5 mM and k_{app1}^0 and α_{app1} values of 0.072 cm s^{-1} and 0.57 and k_{app2}^0 and α_{app2} values of 0.024 cm s^{-1} and 0.55 with 1.0 mM , respectively. Clearly the apparent rate of electron transfer increases with the use of a more dilute electrolyte concentration and the match with the Butler-Volmer model is improved.

3.5. Automated data optimization

In computationally supported automated method of data analysis, selected ranges of the three parameters E_{app}^0 , k_{app}^0 and α_{app} were introduced in the MECSim script as variables. In the Linux operating system employed for the simulation, (\$) symbol was used to mark the parameters as set variables in the 'Master.sk' file. The ranges of parameters were then input in the 'GenerateScript.py' file as was the resolution associated with each parameter. The ranges chosen were limited to minimize the computation time required

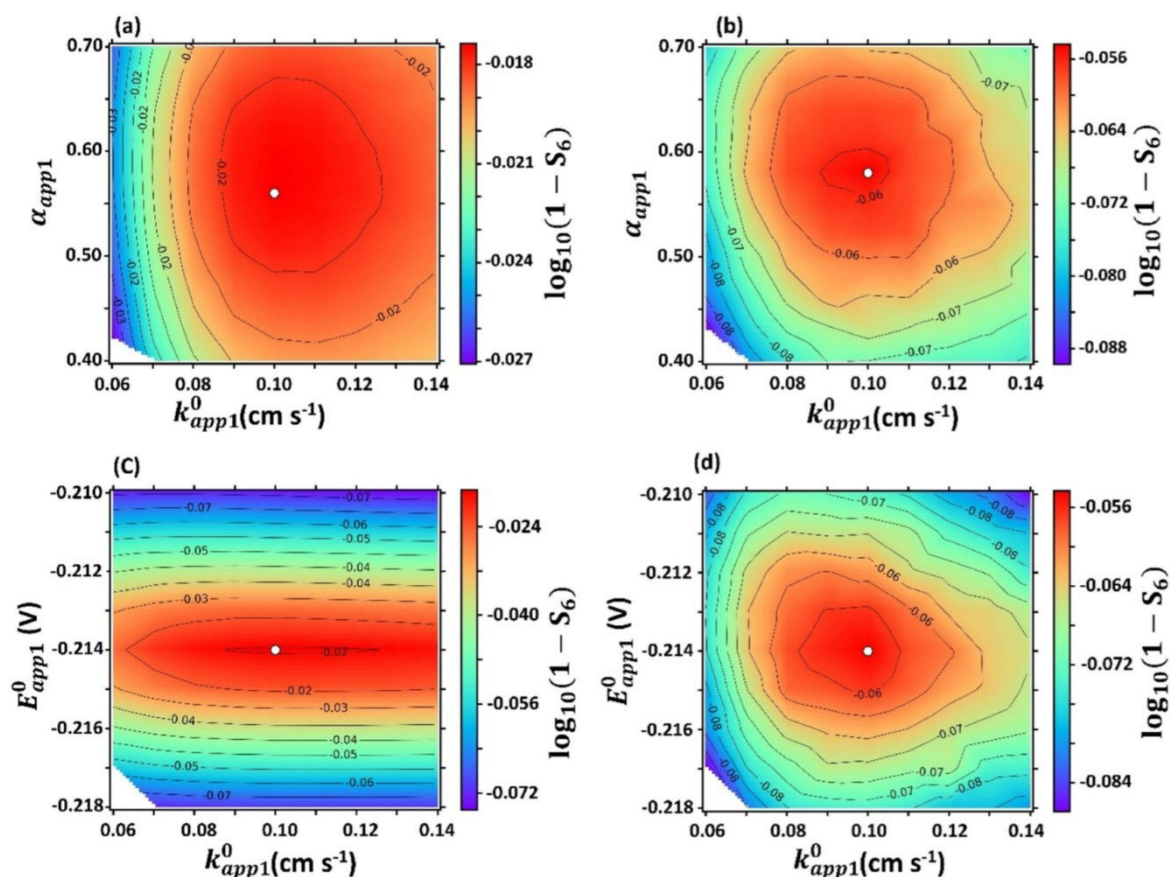


Fig. 6. Contour plots. Comparison of the sum of squares between simulated and experimental data for the α -[S₂W₁₈O₆₂]^{4-/-5-} process in CH₃CN (0.50 M [n-Bu₄N][PF₆]) as a function of α_{app1} and k_{app1}^0 ((a) and (b)) and E_{app1}^0 and k_{app1}^0 ((c) and (d)) when other parameters assumed to be known. Best fit parameters are shown as white circle (a) and (c) for 9.02 Hz, (b) and (d) for 27.01 Hz. Here, only the sum of the squares (S_6) of the 6th harmonic is used since this harmonic is highly sensitive to kinetic parameters.

in the data optimisation method by implementing knowledge gained from the heuristic form of analysis. Thus, for example at the Pt electrode, $k_{app1}^0 = 0.025$ to 0.045 cm s⁻¹, $k_{app2}^0 = 0.004$ to 0.013 cm s⁻¹, $\alpha_{app1} = 0.40$ to

0.70 , $\alpha_{app2} = 0.44$ to 0.60 , $E_{app1}^0 = -0.220$ to -0.214 V and $E_{app2}^0 = -0.596$ to -0.589 V were the ranges selected for E_{app1}^0 , k_{app1}^0 and α_{app1} respectively in the 'GenerateScript.py' file for reduction of 2.5 mM α -[S₂W₁₈O₆₂]⁴⁻

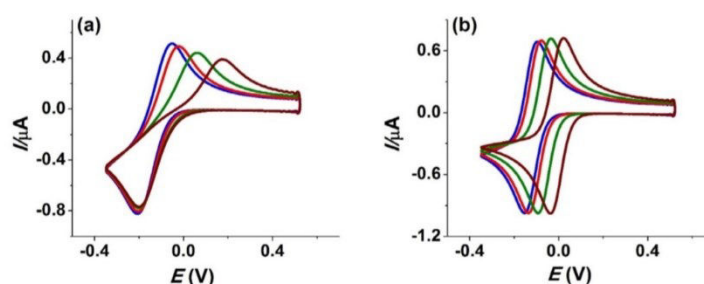


Fig. 7. Simulated data obtained for a one-electron reduction processes (see Eq. (8)(i)) followed by an ion-pairing reaction involving product R, where (a) and (b) represent examples of slow (0.001 cm s⁻¹) and reversible (100 cm s⁻¹) electron transfer process when a chemical reaction such as ion-pairing occurs after electron transfer (blue). Other parameters used in the simulations are: $C = 1.0$ mM, $A = 7.85 \times 10^{-3}$ cm², $R_u = 175$ Ω , $C_{dl} = 10$ μ F cm⁻², $D = 2.9 \times 10^{-6}$ cm² s⁻¹, $T = 295$ K, $\nu = 0.072$ V s⁻¹, $\alpha = 0.50$, the forward reaction rate constant, $k_f = 10^9$ s⁻¹, the backward reaction rate constants (k_b): red = 10^6 , green = 10^5 , maroon = 10^4 s⁻¹ and hence the equilibrium constants (K): red = 1.00, green = 10.0, maroon = 100. In this example the chemical reaction, $R + X^+ \leftrightarrow [X]R^+$ (Eq. (8)(ii) following electron transfer) is treated as a pseudo 1st order reaction (concentration of X^+ is in a large excess).

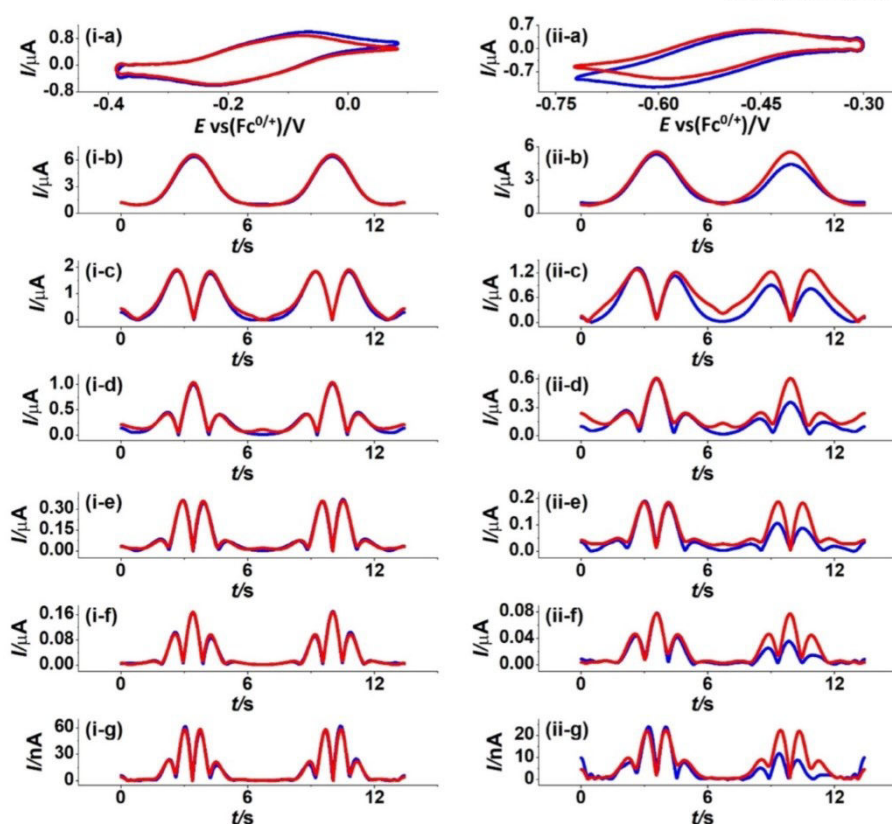


Fig. 8. A comparison of experimental (blue line) and simulated (red line) AC voltammetry for the i) oxidation and ii) reduction of 1.2 mM α -[S₂W₁₈O₆₂]⁵⁻ in CH₃CN (0.50 M [n-Bu₄N][PF₆]), at a Pt electrode with $\Delta E = 80$ mV, $f = 9.02$ Hz and $\nu = 0.072$ V s⁻¹. (a) DC component, (b-g) 1st to 6th harmonic components. Simulated data obtained with $k_{app1}^0 = 0.037$ cm s⁻¹ and $k_{app2}^0 = 0.012$ cm s⁻¹ and $\alpha_{app1} = 0.50$ and $\alpha_{app2} = 0.51$.

at 9.02 Hz in order to obtain best fit values. The range of parameters used in the automated data optimisation approach are summarized in Table 4.

For both the α -[S₂W₁₈O₆₂]^{4-/5-} and α -[S₂W₁₈O₆₂]^{5-/6-} processes, the best-fit values using the simple electron transfer mechanism were found to be consistent with those obtained by the heuristic method except for the Pt data (Table 5). Thus for example, at the Au electrode with 2.5 mM α -[S₂W₁₈O₆₂]⁴⁻ and a frequency of 9.02 Hz, $E_{app1}^0 = -0.213$ V, $E_{app2}^0 = -0.595$ V, $k_{app1}^0 = 0.059$ cm s⁻¹, $k_{app2}^0 = 0.037$ cm s⁻¹, $\alpha_{app1} = 0.63$, $\alpha_{app2} = 0.56$ which are very similar to parameters estimated heuristically of $E_{app1}^0 = -0.215$ V, $E_{app2}^0 = -0.593$ V, $k_{app1}^0 = 0.050$ cm s⁻¹, $k_{app2}^0 = 0.039$ cm s⁻¹, $\alpha_{app1} = 0.60$, $\alpha_{app2} = 0.62$. On the other hand, at a Pt electrode, the 2nd process gave slower kinetics in the automated ($k_{app2}^0 = 0.009$ cm s⁻¹, $\alpha_{app2} = 0.53$ at 9.02 Hz with 2.5 mM concentration) than with the heuristic ($k_{app2}^0 = 0.012$ cm s⁻¹, $\alpha_{app2} = 0.50$) simulation approach. This difference arises because the automatic method for the Pt data estimates the kinetics essentially using the average of the reduction and oxidation components (see Fig. S9) whereas in the heuristic method, data were derived solely from the reduction component. The heuristic treatment of the GC electrode case led to the conclusion that only a lower limit of 0.10 cm s⁻¹ should be reported and that α_{app1} and α_{app2} values could not be estimated from the experimental data obtained at 9.02 Hz. The outcome for the data optimisation method is that the best fit values are close to 0.10 cm s⁻¹ for both k_{app1}^0 and k_{app2}^0 and that α_{app1} and α_{app2} are both approximately 0.60. An issue is that data optimisation, as applied in this study, will in all likelihood always find a set of parameters that provide

a best fit for the model whereas an experienced experimentalist is aware of uncertainties close to the reversible limit. Bayesian inference or other methods need to be used to statistically address the issue of over parameterisation [49]. In the present case, the GC data obtained at 9.02 Hz according to heuristic form of data analysis can indeed just as well be described by use of the model derived from the Nernst equation with only E_{app1}^0 and E_{app2}^0 regarded as parameters that need to be evaluated. The contour plots shown in Fig. 6(a) derived from automated data optimisation analysis at 9.02 Hz for the α -[S₂W₁₈O₆₂]^{4-/5-} process in CH₃CN (0.50 M [n-Bu₄N][PF₆]) provide a clear indication that k_{app1}^0 value should be regarded as a lower limit and that α_{app1} cannot be estimated. In contrast, at 27.01 Hz, the α_{app} value can be determined because the kinetic sensitivity (see Fig. 6(b)) is enhanced with use of this shorter time scale. On the other hand, the E_{app1}^0 value is very precise at both applied frequencies. Thus, integration of heuristic and automated approaches does represent a valuable approach to data reporting in voltammetry. In the present case this strategy assists in identifying issues with fast (reversible) electron transfer at GC and slow electron transfer (asymmetry) at Pt electrodes.

In terms of modelling, it is in principle possible to include ion-pairing, and try to establish qualitatively if this could be the origin of the anomalous Pt data obtained with 0.50 M [n-Bu₄N][PF₆] as the supporting electrolyte. Chemical reactions such as ion-pairing can alter the shape of a process when coupled with slow electrode kinetics. Thus, the cyclic voltammetry of an EC process (Fig. 7(a)) with slow electron transfer kinetics is predicted

ARTICLE IN PRESS

M.A. Rahman et al.

Journal of Electroanalytical Chemistry xxx (xxxx) xxx

to be dependent on the rate of ion-pairing when the rate constant (k_f) for formation is greater than for dissociation (k_b). On the other hand, for a reversible process (Fig. 7(b)), the voltammetry is simply shifted to more positive values to an extent that is dependent on k_f and k_b , but with the reversible shape always being maintained. The full ion-pairing simulation represented by an ECE reaction has far too many unknown parameters to be realistically applied to the present Pt electrode data. The problem is that while the data may well be mimicked, the so called “best fit” solution will almost certainly be non-unique because of mathematical coupling of chemical and electrochemical parameters [51]. At this time, all we can state is that ion-pairing may account for asymmetry in the Pt data. However, it should be noted that other phenomena, such as electrode fouling due to product adsorption, could also account for the non-ideality.

Despite uncertainty as to how to accommodate the impact of ion-pairing, it is clear that $k_{appGC}^0 > k_{appAu}^0 > k_{appPt}^0$ for the reduction of α -[S₂W₁₈O₆₂]⁴⁻ in CH₃CN as is the case with other polyoxometalates [18,20]. According to the theory for adiabatic electron transfer, k^0 values are predicted to be independent of the electrode material when electroactive species undergo strong electronic interaction with a metal electrode. On the other hand, k^0 values are predicted to be dependent on the electronic properties of the electrode material in nonadiabatic pathways where the electronic interaction with the electrode is weak. Some literature reports [18,50] support the Marcus theory [52] predictions where properties of the electrode material govern the heterogeneous rate constant for a non-adiabatic electron transfer process.

Glassy carbon displays some electronically similar properties to metals (e.g. highly conducting), but varies significantly with respect to surface chemistry. The electrochemistry can be strongly influenced by the surface functional groups on a GC electrode that may play a critical role in electron transfer processes [53]. In the case of highly charged polyoxometalates such as [PMO₁₂O₄₀]³⁻, [P₂Mo₁₈O₆₂]⁶⁻ and [P₂W₁₈O₆₂]⁶⁻ strong spontaneous adsorption has been reported by Rong and Anson [54] with GC and other forms of carbon and metal electrodes from aqueous solutions. However, adsorption is much less extensive from non-aqueous solvents. With α -[S₂W₁₈O₆₂]⁴⁻, as shown in Fig. S10, surface confined voltammetry displaying the characteristic diffusionless shape is observed after leaving the GC electrode in contact with a solution of α -[S₂W₁₈O₆₂]⁴⁻ for 5 min, removing the electrode from the solution, washing with acetone, drying and replacing the α -[S₂W₁₈O₆₂]⁴⁻ modified electrode in a fresh electrolyte solution. Surface confined voltammetry is not detected at Au and Pt electrodes so that interaction with the surface may follow the order GC > Au > Pt as is the case with the rate of electron transfer. There are other variables that may affect the k^0 value for an inner sphere electron transfer reaction at a GC electrode. The microstructure can affect k^0 [55] since the GC surface represents a mixture of basal and edge plane. The polishing procedure also may contribute [53]. For example, abrasive material like alumina can fracture the GC surface giving rise to enhanced electrochemical reactivity [56,57]. Further details on factors that impact the electrochemistry at GC electrodes are available in references [58–63]. Thus, the rate order $k_{appGC}^0 > k_{appAu}^0 > k_{appPt}^0$ for the reduction of α -[S₂W₁₈O₆₂]⁴⁻ appears to follow that for the extent of interaction with the electrode surface rather than density of states [64,65] which lie in the reverse order. Therefore, the trend observed implies inner rather than outer sphere electron transfer processes are associated with the polyoxometalate voltammetry.

Homogeneous chemical cross redox reactions between say an ion-paired two electron reduced α -[S₂W₁₈O₆₂]⁶⁻ product and non-ion paired α -[S₂W₁₈O₆₂]⁴⁻ reactant (see details in Introduction) could accompany electron transfer as the reaction is thermodynamically favoured. To avoid the possibility of their occurrence and rule out this being the source of asymmetry of the second process at the Pt electrode, bulk one-electron reduction of α -[S₂W₁₈O₆₂]⁴⁻ to α -[S₂W₁₈O₆₂]⁵⁻ was undertaken. The FTACV and the electrode kinetics derived from experiments starting with α -[S₂W₁₈O₆₂]⁵⁻ instead of α -[S₂W₁₈O₆₂]⁴⁻ in bulk CH₃CN (0.50 M [n-Bu₄N][PF₆]) solution were indistinguishable at GC, Au or Pt electrodes (see Fig. 8 for Pt electrode case). Significantly, the poor fit is retained for the α -[S₂W₁₈O₆₂]^{5-/6-} process at the Pt electrode as shown in Fig. 8. Furthermore, at Pt $k_{app1}^0 =$

0.037 cm s⁻¹ and $k_{app2}^0 = 0.012$ cm s⁻¹ were obtained with α -[S₂W₁₈O₆₂]⁵⁻ in bulk solution as is the case with α -[S₂W₁₈O₆₂]⁴⁻ when data analysis is implemented heuristically using the same protocol for both situations.

4. Conclusions

The thermodynamics and electron transfer kinetics associated with the α -[S₂W₁₈O₆₂]^{4-/5-} and α -[S₂W₁₈O₆₂]^{5-/6-} processes at GC, Au and Pt electrodes in CH₃CN containing [n-Bu₄N][PF₆] as the supporting electrolyte have been determined by FTACV using integration of experimenter-based heuristic and computationally supported data optimisation approaches for comparison of simulated and experimental data. Use of a 0.50 M concentration of [n-Bu₄N][PF₆] caused a positive shift of reversible potential relative to use of 0.10 M [n-Bu₄N][PF₆] and also led to slower apparent rates of electron transfer. Additionally, departure from behaviour theoretically predicted via use of the Butler-Volmer model was found at the Pt electrode with 0.50 M supporting electrolyte. The electrolyte concentration dependence implies that ion-pairing plays a significant role in the mechanism for voltammetric reduction of α -[S₂W₁₈O₆₂]⁴⁻. In general, the electron transfer kinetics for the α -[S₂W₁₈O₆₂]^{4-/5-} process are greater than for α -[S₂W₁₈O₆₂]^{5-/6-} and the metal electrodes exhibited slower electron transfer kinetics than GC. Excellent simulation-experiment data fits were found when modelling was based on a simple one electron transfer process and Butler-Volmer electron transfer kinetics, except for the second α -[S₂W₁₈O₆₂]^{5-/6-} process on Pt electrode which showed asymmetry in oxidation and reduction components of the reaction. This outcome indicates complications from ion-pairing may be detected when present in combination with slow electron transfer. The order $k_{appGC}^0 > k_{appAu}^0 > k_{appPt}^0$ for the reduction of α -[S₂W₁₈O₆₂]⁴⁻ follows that for the extent of polyoxometalate interaction with the electrode surface rather than density of states [64,65] which lie in the reverse order. Thus, the trend in k_{app} values observed implies inner rather than outer sphere electron transfer processes are associated with the polyoxometalate voltammetry.

The advantages of undertaking heuristic data analysis by an experienced electrochemist in conjunction with automated data optimisation methods is demonstrated in this paper as a means of ensuring the fidelity of parameter estimates. Clearly, the heuristic method is tedious, but minimize prospects for the computer assisted automated method unknowingly and rapidly arriving at an incorrect outcome.

Acknowledgements

The authors would like to thank the Australian Research Council for financial assistance through a Discovery Project grant. This paper is dedicated to our friend Professor Richard Compton on the occasion of his 65th birthday.

Author contributions

Md Anisur Rahman: experiment design, electrochemical measurements, data analysis and manuscript preparation.

Jiezhen Li, Si-Xuan Guo and Gareth Kennedy: data analysis and manuscript preparation.

Tadaharu Ueda: polyoxometalate synthesis.

Alan M. Bond and Jie Zhang: development of concepts, result interpretation and manuscript preparation.

Appendix A. Supplementary data

Supplementary data to this article can be found online at <https://doi.org/10.1016/j.jelechem.2019.113786>.

References

- [1] C.L. Hill, Introduction: polyoxometalates-multicomponent molecular vehicles to probe fundamental issues and practical problems, Chem. Rev. 98 (1) (1998) 1–2, <https://doi.org/10.1021/cr960395y>.

- [2] D.L. Long, R. Tsunashima, I. Cronin, Polyoxometalates: building blocks for functional nanoscale systems, *Angew. Chem. Int. Ed. Engl.* 49 (10) (2010) 1736–1758, <https://doi.org/10.1002/anie.200902483>.
- [3] A. Proust, R. Thouvenot, P. Gouzerh, Functionalization of polyoxometalates: towards advanced applications in catalysis and materials science, *Chem. Comm.* (16) (2008) 1837–1852, <https://doi.org/10.1039/b715502f>.
- [4] M.T. Pope, *Heteropoly and Isopoly Oxometalates*, Springer-Verlag, 1983 <https://doi.org/10.1002/ange.19840960939>.
- [5] A. Bijelic, A. Rompel, The use of polyoxometalates in protein crystallography—an attempt to widen a well-known bottleneck, *Coord. Chem. Rev.* 299 (2015) 22–38, <https://doi.org/10.1016/j.ccr.2015.03.018>.
- [6] D.E. Katsoulis, A survey of applications of Polyoxometalates, *Chem. Rev.* 98 (1) (1998) 359–388, <https://doi.org/10.1021/cr960398a>.
- [7] B. König, *Chemical Photocatalysis*, Walter de Gruyter 2013.
- [8] F.A.R.S. Couto, A.M.V. Cavaleiro, J.D. Pedrosa de Jesus, J.E.J. Simão, Study of polyoxotungstates with the Keggin structure by cyclic voltammetry, *Inorg. Chim. Acta* 281 (2) (1998) 225–228, [https://doi.org/10.1016/S0020-1693\(98\)00161-3](https://doi.org/10.1016/S0020-1693(98)00161-3).
- [9] M. Sadakane, E. Steckhan, Electrochemical properties of polyoxometalates as electrocatalysts, *Chem. Rev.* 98 (1) (1998) 219–238, <https://doi.org/10.1021/cr960403a>.
- [10] S. Liu, D.G. Kurth, D. Volkmer, Polyoxometalates as pH-sensitive probes in self-assembled multilayers, *Chem. Comm.* (9) (2002) 976–977, <https://doi.org/10.1039/B200942K>.
- [11] E. Papaconstantinou, Photochemistry of polyoxometalates of molybdenum and tungsten and/or vanadium, *Chem. Soc. Rev.* 18 (1989) 1–31, <https://doi.org/10.1039/CS9891800001>.
- [12] E. Coronado, C.J. Gomez-Garcia, Polyoxometalate-based molecular materials, *Chem. Rev.* 98 (1) (1998) 273–296, <https://doi.org/10.1021/cr970471c>.
- [13] M. Pope, A. Muller, Polyoxometalates: Form Platonic Solids to Anti-Retroviral Activity, Kluwer Academic Publishers, Dordrecht, The Netherlands, 1994.
- [14] C. Baffert, S.W. Feldberg, A.M. Bond, D.L. Long, L. Cronin, pH-dependence of the aqueous electrochemistry of the two-electron reduced α -[Mo₁₈O₅₄(SO₃)₂] sulfite Dawson-like polyoxometalate anion derived from its triethanolammonium salt, *Dalton Trans.* (40) (2007) 4599–4607, <https://doi.org/10.1039/b705991d>.
- [15] A.W. Mariotti, J. Xie, B.F. Abrahams, A.M. Bond, A.G. Wedd, Synthesis and voltammetry of [bmim]₄[α -S₂W₁₈O₆₂] and related compounds: rapid precipitation and dissolution of reduced surface films, *Inorg. Chem.* 46 (7) (2007) 2530–2540, <https://doi.org/10.1021/ic062022d>.
- [16] J. Zhang, A.M. Bond, D.R. MacFarlane, S.A. Forsyth, J.M. Pringle, A.W. Mariotti, A.F. Glowinski, A.G. Wedd, Voltammetric studies on the reduction of polyoxometalate anions in ionic liquids, *Inorg. Chem.* 44 (14) (2005) 5123–5132, <https://doi.org/10.1021/ic050032t>.
- [17] J. Li, A.M. Bond, J. Zhang, Probing electrolyte cation effects on the electron transfer kinetics of the $[\alpha$ -SiW₁₂O₄₀]^{4-/-5-} and $[\alpha$ -SiW₁₂O₄₀]^{5-/-6-} processes using a boron-doped diamond electrode, *Electrochim. Acta* 178 (2015) 631–637, <https://doi.org/10.1016/j.electacta.2015.08.049>.
- [18] J. Li, S.-X. Guo, C.L. Bentley, K. Bano, A.M. Bond, J. Zhang, T. Ueda, Electrode material dependence of the electron transfer kinetics associated with the [SW₁₁O₄₀]^{3-/-4-} (V^{IV/V}) and [SW₁₁O₄₀]^{4-/-5-} (W^{VI/V}) processes in dimethylformamide, *Electrochim. Acta* 201 (2016) 45–56, <https://doi.org/10.1016/j.electacta.2016.03.107>.
- [19] A.J. Bard, L.R. Faulkner, *Electrochemical Methods: Fundamentals and Applications*, 2nd ed. Wiley, New York, 2001.
- [20] J. Li, C.L. Bentley, A.M. Bond, J. Zhang, T. Ueda, Influence of 1-butyl-3-methylimidazolium on the electron transfer kinetics associated with the [SW₁₁O₄₀]^{3-/-4-} (V^{IV/V}) and [SW₁₁O₄₀]^{4-/-5-} (W^{VI/V}) processes in dimethylformamide, *J. Electroanal. Chem.* 779 (2016) 67–74, <https://doi.org/10.1016/j.jelechem.2016.04.050>.
- [21] J. Zhang, A.M. Bond, P.J. Richardt, A.G. Wedd, Voltammetric reduction of alpha- and gamma-[S₂W₁₈O₆₂]⁴⁻ and α -, β -, and γ -[SiW₁₂O₄₀]⁴⁻: isomeric dependence of reversible potentials of polyoxometalate anions using data obtained by novel dissolution and conventional solution-phase processes, *Inorg. Chem.* 43 (26) (2004) 8263–8271, <https://doi.org/10.1021/ic049043x>.
- [22] K. Oldham, J. Myland, *Fundamentals of Electrochemical Science*, Elsevier, Amsterdam, 1993.
- [23] D.K. Gosser, *Cyclic Voltammetry: Simulation and Analysis of Reaction Mechanisms*, VCH New York 1993.
- [24] R.S. Nicholson, I. Shain, Theory of stationary electrode polarography. Single scan and cyclic methods applied to reversible, irreversible, and kinetic systems, *Anal. Chem.* 36 (4) (1964) 706–723, <https://doi.org/10.1021/ac60210a007>.
- [25] M.V. Mirkin, T.C. Richards, A.J. Bard, Scanning electrochemical microscopy. 20. Steady-state measurements of the fast heterogeneous kinetics in the ferrocene/acetonitrile system, *J. Phys. Chem.* 97 (29) (1993) 7672–7677, <https://doi.org/10.1021/j100131a042>.
- [26] P. Sun, M.V. Mirkin, Kinetics of electron-transfer reactions at nanoelectrodes, *Anal. Chem.* 78 (18) (2006) 6526–6534, <https://doi.org/10.1021/ac060924q>.
- [27] C.G. Zoski, *Handbook of electrochemistry*, Elsevier 2006.
- [28] J. Zhang, S.-X. Guo, A.M. Bond, F. Marken, Large-amplitude Fourier transformed high-harmonic alternating current cyclic voltammetry: kinetic discrimination of interfering faradaic processes at glassy carbon and at boron-doped diamond electrodes, *Anal. Chem.* 76 (13) (2004) 3619–3629, <https://doi.org/10.1021/ac049744b>.
- [29] S.-X. Guo, A.M. Bond, J. Zhang, Fourier transformed large amplitude alternating current voltammetry: principles and applications, *Rev. Polarogr.* 61 (1) (2015) 21–32, <https://doi.org/10.5189/revpolarography.61.21>.
- [30] J. Zhang, S.-X. Guo, A.M. Bond, Discrimination and evaluation of the effects of uncompensated resistance and slow electrode kinetics from the higher harmonic components of a fourier transformed large-amplitude alternating current voltammogram, *Anal. Chem.* 79 (6) (2007) 2276–2288, <https://doi.org/10.1021/ac061859n>.
- [31] J. Butler, Studies in heterogeneous equilibria. Part II.—The kinetic interpretation of the nemst theory of electromotive force, *Trans. Faraday Soc.* 19 (1924) 729–733, <https://doi.org/10.1039/TF9241900729>.
- [32] T. Erdey-Grúz, M. Volmer, Zur theorie der wasserstoff überspannung, *Z. Phys. Chem.* 150 (1) (1930) 203–213, <https://doi.org/10.1515/zpch-1930-15020>.
- [33] J.M. Gomez-Gil, E. Laborda, J. Gonzalez, A. Molina, R.G. Compton, Electrochemical and computational study of ion association in the electroreduction of PW₁₂O₄₀³⁻, *J. Phys. Chem. C* 121 (48) (2017) 26751–26763, <https://doi.org/10.1021/acs.jpcc.7b07073>.
- [34] S.-X. Guo, S.W. Feldberg, A.M. Bond, D.L. Callahan, P.J. Richardt, A.G. Wedd, Systematic approach to the quantitative voltammetric analysis of the FeII/FeIII component of the $[\alpha$ -Fe(OH₂)P₂W₁₇O₆₁]^{7-/-8-} reduction process in buffered and unbuffered aqueous media, *J. Phys. Chem. B* 109 (43) (2005) 20641–20651, <https://doi.org/10.1021/jp0528459>.
- [35] Y. Liu, S.-X. Guo, A.M. Bond, J. Zhang, Y.V. Geletii, C.L. Hill, Voltammetric determination of the reversible potentials for [(Ru₄O₄(OH)₂(H₂O)₄](γ -SiW₁₀O₃₆)₂]¹⁰⁻ over the pH range of 2–12: electrolyte dependence and implications for water oxidation catalysis, *Inorg. Chem.* 52 (20) (2013) 11986–11996, <https://doi.org/10.1021/ic401748y>.
- [36] A.M. Bond, K.B. Oldham, Electrochemical reduction of an isomeric pair when the products interconvert, *J. Phys. Chem.* 87 (14) (1983) 2492–2502, <https://doi.org/10.1021/j100237a012>.
- [37] A.M. Bond, K.B. Oldham, Electrochemical mechanisms involving isomeric species, *J. Phys. Chem.* 89 (17) (1985) 3739–3747, <https://doi.org/10.1021/j100263a031>.
- [38] G.F. Kennedy, MECSim software package. <http://www.garethkennedy.net/MECSim.html>, 2019 (accessed 10 December 2019).
- [39] G.F. Kennedy, A.M. Bond, A.N. Simonov, Modelling ac voltammetry with MECSim: facilitating simulation–experiment comparisons, *Curr. Opin. Electrochem.* 1 (1) (2017) 140–147, <https://doi.org/10.1016/j.coelec.2016.12.001>.
- [40] G.P. Morris, A.N. Simonov, E.A. Mashkina, R. Bordes, K. Gillow, R.E. Baker, D.J. Gavaghan, A.M. Bond, A comparison of fully automated methods of data analysis and computer assisted heuristic methods in an electrode kinetic study of the pathologically variable [Fe(CN)₆]^{3-/-4-} process by AC voltammetry, *Anal. Chem.* 85 (24) (2013) 11780–11787, <https://doi.org/10.1021/ac4022105>.
- [41] S. Himeno, H. Tatewaki, M. Hashimoto, Synthesis, structure, and characterization of an α -Dawson-type [S₂W₁₈O₆₂]⁴⁻ complex, *Bull. Chem. Soc. Japan* 74 (9) (2001) 1623–1628, <https://doi.org/10.1246/bcsj.74.1623>.
- [42] D. Sawyer, A. Sobkowiak, J. Roberts Jr., *Electrochemistry for Chemists*, John Wiley & Sons, 1995.
- [43] A.M. Bond, N.W. Duffy, S.-X. Guo, J. Zhang, D. Elton, Changing the look of voltammetry, *Anal. Chem.* (2005) <https://doi.org/10.1021/ac053370k>.
- [44] G. Gritzner, J. Kuta, Recommendations on reporting electrode potentials in nonaqueous solvents (recommendations 1983), *Pure Appl. Chem.* 56 (4) (1984) 461–466, <https://doi.org/10.1351/pac198456040461>.
- [45] S.W. Feldberg, C.I. Goldstein, M. Rudolph, A stability criterion for accurate simulation of electrochemical diffusion-kinetic phenomena at the rotating disk electrode and implications for simulation of diffusion-migration and other problems, *J. Electroanal. Chem.* 413 (1–2) (1996) 25–36, [https://doi.org/10.1016/0022-0728\(96\)04625-6](https://doi.org/10.1016/0022-0728(96)04625-6).
- [46] S.W. Feldberg, Optimization of explicit finite-difference simulation of electrochemical phenomena utilizing an exponentially expanded space grid: refinement of the Joslin-Pletcher algorithm, *J. Electroanal. Chem. Interf. Electrochem.* 127 (1–3) (1981) 1–10, [https://doi.org/10.1016/S0022-0728\(81\)80462-7](https://doi.org/10.1016/S0022-0728(81)80462-7).
- [47] A.M. Bond, K. Bano, S. Adeel, L.L. Martin, J. Zhang, Fourier-transformed large-amplitude AC voltammetric study of tetrathiafulvalene (TTF): electrode kinetics of the TTF⁰/TTF⁺ and TTF⁺/TTF²⁺ processes, *ChemElectroChem* 1 (1) (2014) 99–107, <https://doi.org/10.1002/celc.201300129>.
- [48] A.M. Bond, N.W. Duffy, D.M. Elton, B.D. Fleming, Characterization of nonlinear background components in voltammetry by use of large amplitude periodic perturbations and Fourier transform analysis, *Anal. Chem.* 81 (21) (2009) 8801–8808, <https://doi.org/10.1021/ac901318r>.
- [49] G.E. Box, G.C. Tiao, *Bayesian Inference in Statistical Analysis*, John Wiley & Sons, 2011.
- [50] K. Bano, J. Zhang, A.M. Bond, P.R. Unwin, J.V. Macpherson, Diminished electron transfer kinetics for [Ru(NH₃)₆]^{3+/-2+}, $[\alpha$ -SiW₁₂O₄₀]^{4-/-5-}, and $[\alpha$ -SiW₁₂O₄₀]^{5-/-6-} processes at boron-doped diamond electrodes, *J. Phys. Chem. C* 119 (22) (2015) 12464–12472, <https://doi.org/10.1021/acs.jpcc.5b02642>.
- [51] S.W. Feldberg, Digital simulation: a general method for solving electrochemical diffusion-kinetic problems, *Electroanal. Chem.* 3 (1969) 199–296.
- [52] R.A. Marcus, On the theory of oxidation-reduction reactions involving electron transfer. I, *The J. Chem. Phys.* 24 (5) (1956) 966–978, <https://doi.org/10.1063/1.1742723>.
- [53] R.J. Rice, N.M. Pontikos, R.L. McCreery, Quantitative correlations of heterogeneous electron-transfer kinetics with surface properties of glassy carbon electrodes, *J. Am. Chem. Soc.* 112 (12) (1990) 4617–4622, <https://doi.org/10.1021/ja00168a001>.
- [54] C. Rong, F.C. Anson, Spontaneous adsorption of heteropolytungstates and heteropolymolybdates on the surfaces of solid electrodes and the electrocatalytic activity of the adsorbed anions, *Inorg. Chim. Acta* 242 (1–2) (1996) 11–16, [https://doi.org/10.1016/0020-1693\(95\)04843-X](https://doi.org/10.1016/0020-1693(95)04843-X).
- [55] R.J. Bowling, R.T. Packard, R.L. McCreery, Activation of highly ordered pyrolytic graphite for heterogeneous electron transfer: relationship between electrochemical performance and carbon microstructure, *J. Am. Chem. Soc.* 111 (4) (1989) 1217–1223, <https://doi.org/10.1021/ja00186a008>.
- [56] C.D. Allred, R.L. McCreery, Adsorption of catechols on fractured glassy carbon electrode surfaces, *Anal. Chem.* 64 (4) (1992) 444–448, <https://doi.org/10.1021/ac00028a020>.
- [57] R. Rice, C. Allred, R. McCreery, Fast heterogeneous electron transfer rates for glassy carbon electrodes without polishing or activation procedures, *J. Electroanal. Chem. Interf. Electrochem.* 263 (1) (1989) 163–169, [https://doi.org/10.1016/0022-0728\(89\)80133-0](https://doi.org/10.1016/0022-0728(89)80133-0).

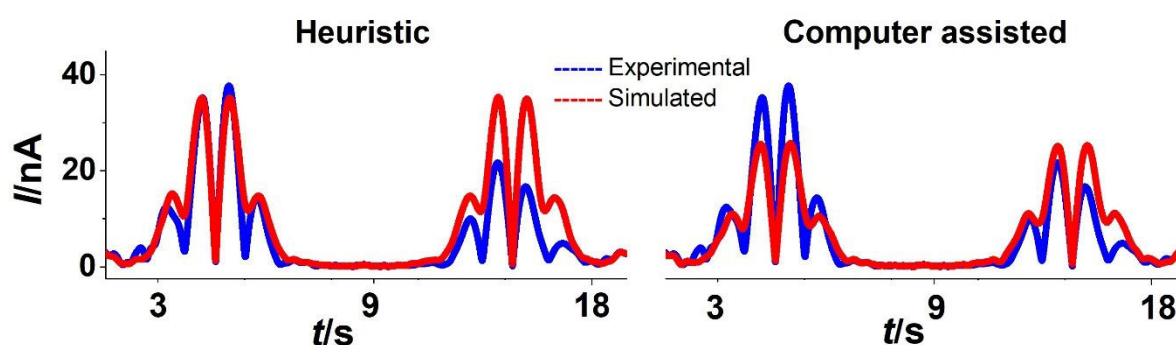
ARTICLE IN PRESS

M.A. Rahman et al.

Journal of Electroanalytical Chemistry xxx (xxxx) xxx

- [58] M.R. Deakin, P.M. Kovach, K. Stutts, R.M. Wightman, Heterogeneous mechanisms of the oxidation of catechols and ascorbic acid at carbon electrodes, *Anal. Chem.* 58 (7) (1986) 1474–1480, <https://doi.org/10.1021/ac00298a046>.
- [59] R.C. Engstrom, V.A. Strasser, Characterization of electrochemically pretreated glassy carbon electrodes, *Anal. Chem.* 56 (2) (1984) 136–141, <https://doi.org/10.1021/ac00266a005>.
- [60] F. Hu, D.H. Karweik, T. Kuwana, Activation and deactivation of glassy carbon electrodes, *J. Electroanal. Chem. Interf. Electrochem.* 188 (1–2) (1985) 59–72, [https://doi.org/10.1016/S0022-0728\(85\)80050-4](https://doi.org/10.1016/S0022-0728(85)80050-4).
- [61] G.K. Kiema, M. Aktay, M.T. McDermott, Preparation of reproducible glassy carbon electrodes by removal of polishing impurities, *J. Electroanal. Chem.* 540 (2003) 7–15, [https://doi.org/10.1016/S0022-0728\(02\)01264-0](https://doi.org/10.1016/S0022-0728(02)01264-0).
- [62] T.-C. Kuo, R.L. McCreery, Surface chemistry and electron-transfer kinetics of hydrogen-modified glassy carbon electrodes, *Anal. Chem.* 71 (8) (1999) 1553–1560, <https://doi.org/10.1021/ac9807666>.
- [63] R.M. Wightman, M.R. Deakin, P.M. Kovach, W.G. Kuhr, K.J. Stutts, Methods to improve electrochemical reversibility at carbon electrodes, *J. Electrochem. Soc.* 131 (7) (1984) 1578–1583, <https://doi.org/10.1149/1.2115913>.
- [64] S. Gosavi, R. Marcus, Nonadiabatic electron transfer at metal surfaces, *J. Phys. Chem. B* 104 (9) (2000) 2067–2072, <https://doi.org/10.1021/jp9933673>.
- [65] J. Velmurugan, P. Sun, M.V. Mirkin, Scanning electrochemical microscopy with gold nanotips: the effect of electrode material on electron transfer rates, *J. Phys. Chem. C* 113 (1) (2008) 459–464, <https://doi.org/10.1021/jp808632w>.

TOC



Supporting Information

Modelling Limitations Encountered in the Thermodynamic and Electrode Kinetic Parameterization of the α -[S₂W₁₈O₆₂]^{4-/5-/6-} Processes at Glassy Carbon and Metal Electrodes

Md Anisur Rahman^a, Jiezhen Li^a, Si-Xuan Guo^{a, b}, Gareth Kennedy^a, Tadaharu Ueda^c, Alan M. Bond^{a, b, *} and Jie Zhang^{a, b, *}

^a School of Chemistry, Monash University, Clayton, Victoria 3800, Australia

^b ARC Centre of Excellence for Electrochemical Science, Monash University, Clayton, Victoria 3800, Australia

^c Department of Marine Resource Science, Faculty of Agriculture and Marine Science, Kochi University, Kochi 780-8520, Japan

*Corresponding authors: jie.zhang@monash.edu, alan.bond@monash.edu

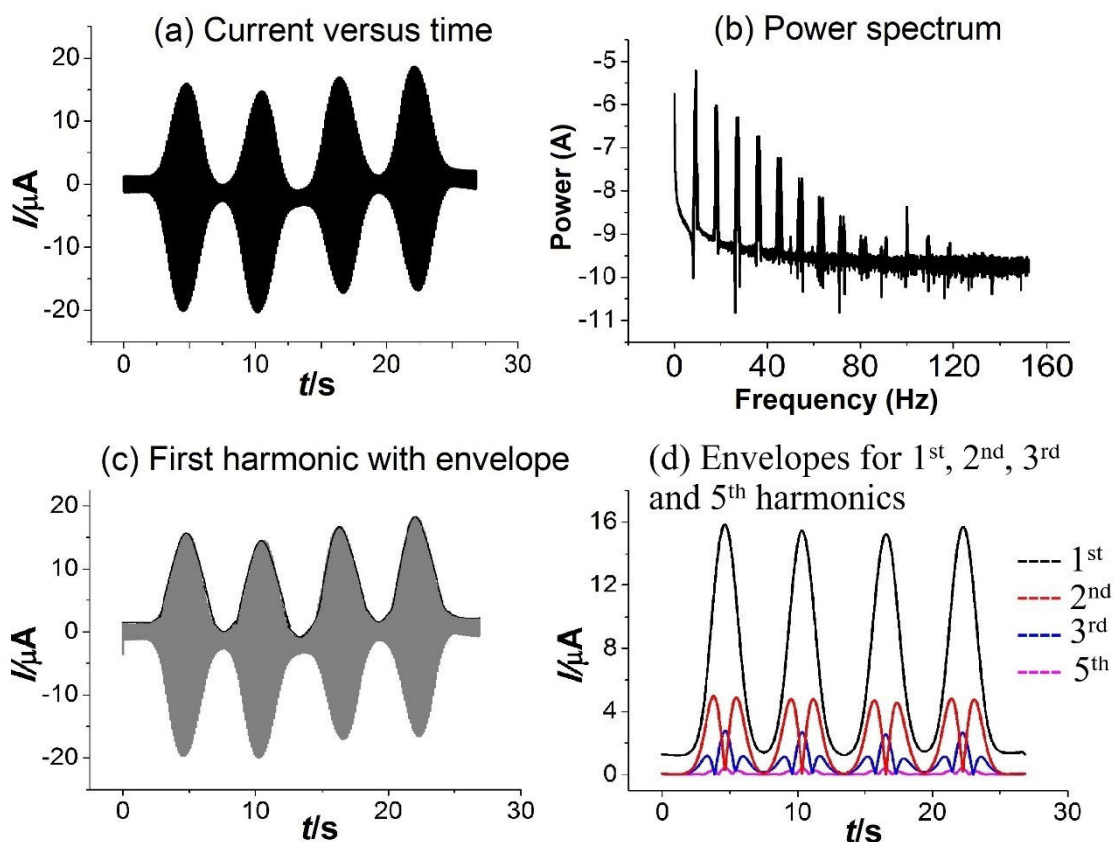


Fig. S1. Conversion of AC voltammetric data into aperiodic DC and AC harmonic components using a Fourier transformation (FT), band filtering and inverse Fourier transformation (IFT) sequence of processes [1]. First, the time data (a) are converted to the frequency domain by FT. Next, the DC aperiodic harmonic or AC harmonic of interest is selected in the frequency domain (b). Finally, the IFT procedure is used to obtain the resolved aperiodic DC and AC harmonic component of interest (c and d). The envelope form of presentation is shown in (c) and (d) for the 1st (black), 2nd (red), 3rd (blue) and 5th (magenta) AC harmonics. The example displayed here is based on the simulation of two reversible one-electron transfer processes with $\Delta E = 80$ mV, $f = 9.02$ Hz and $\nu = 0.067$ V s⁻¹.

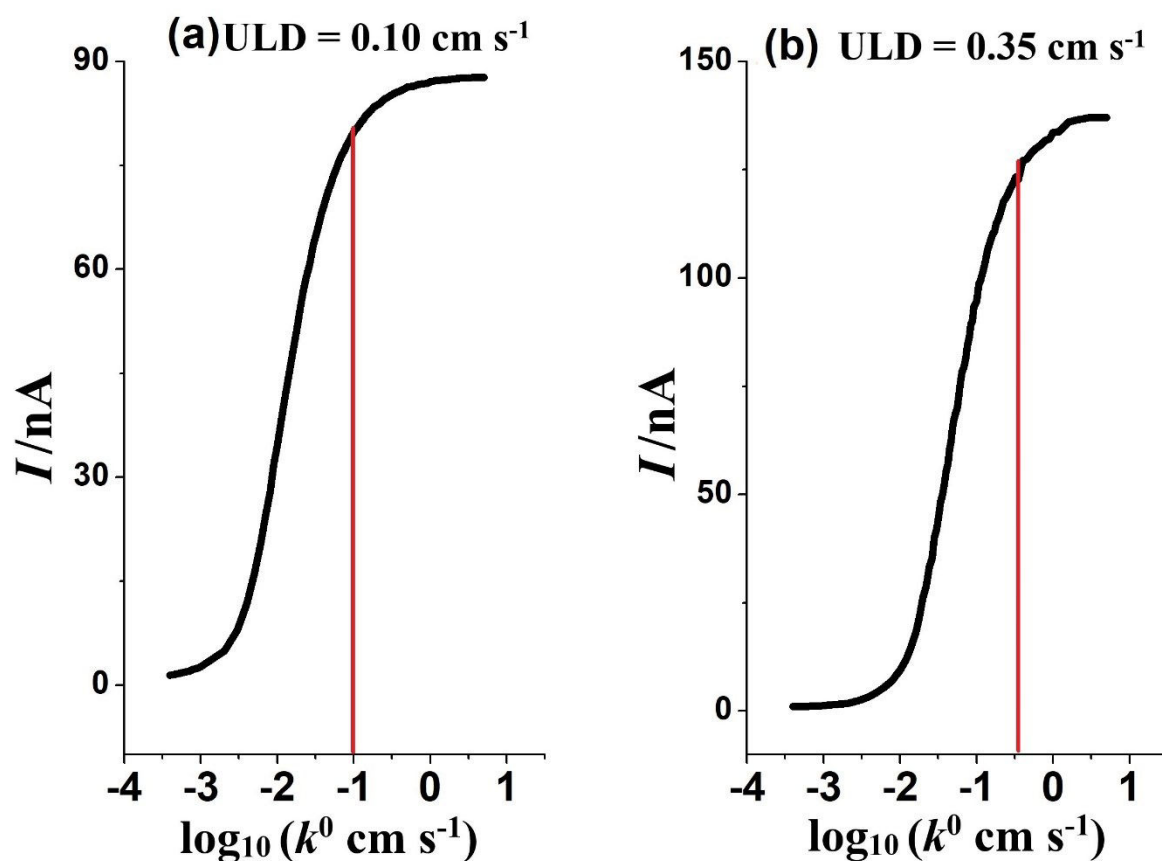


Fig. S2. Maximum value of the peak current estimated by simulation for the 6th harmonic vs $\log_{10}(k^0)$. Data obtained using frequencies of (a) 9.02 Hz and (b) 27.01 Hz with $\Delta E = 80 \text{ mV}$, $C = 1.0 \text{ mM}$, $v = 0.100 \text{ V s}^{-1}$, $R_u = 200 \Omega$, $T = 295 \text{ K}$, $D = 2.90 \times 10^{-6} \text{ cm}^2 \text{ s}^{-1}$, $C_{dl} = 10 \mu\text{F cm}^{-2}$, $\alpha = 0.50$, and $A = 7.85 \times 10^{-3} \text{ cm}^2$.

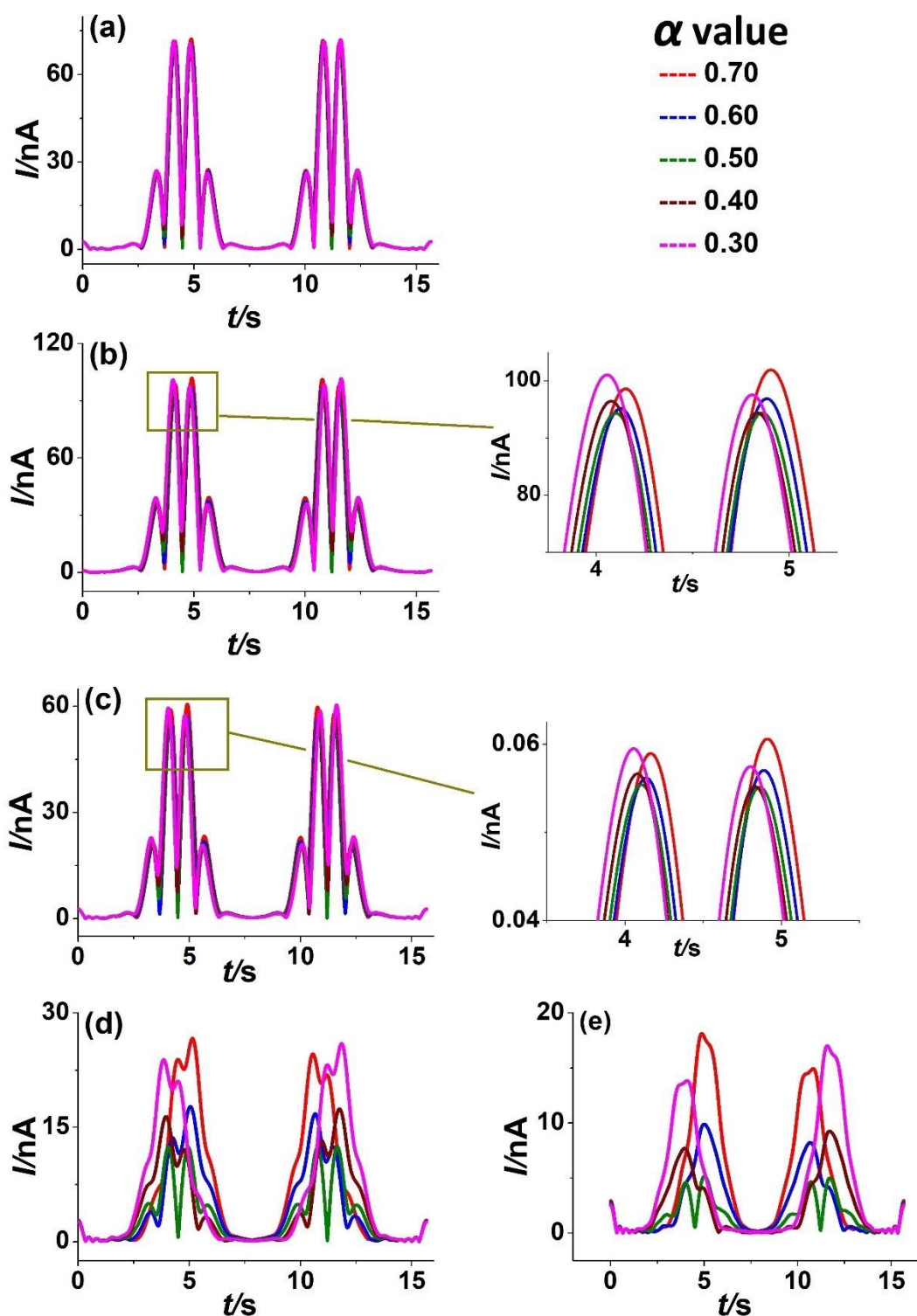


Fig. S3. Sensitivity test of the 6th AC harmonic in FTAC voltammetry to α as a function of k^0 based on analysis of simulated data. (a) $k^0 = 0.1 \text{ cm s}^{-1}$ and $f = 9.02 \text{ Hz}$, (b) $k^0 = 0.1 \text{ cm s}^{-1}$ and $f = 27.01 \text{ Hz}$, (c) $k^0 = 0.05 \text{ cm s}^{-1}$ and $f = 9.02 \text{ Hz}$, (d) $k^0 = 0.01 \text{ cm s}^{-1}$ and $f = 9.02 \text{ Hz}$ and (e) $k^0 = 0.001 \text{ cm s}^{-1}$ and $f = 9.02 \text{ Hz}$. $\Delta E = 80 \text{ mV}$, $C = 1.0 \text{ mM}$, $v = 0.067 \text{ V s}^{-1}$, $R_u = 200 \text{ } \Omega$, $T = 295 \text{ K}$, $A = 7.85 \times 10^{-3} \text{ cm}^2$, $D = 2.90 \times 10^{-6} \text{ cm}^2 \text{ s}^{-1}$, $C_{dl} = 10 \text{ } \mu\text{F cm}^{-2}$.

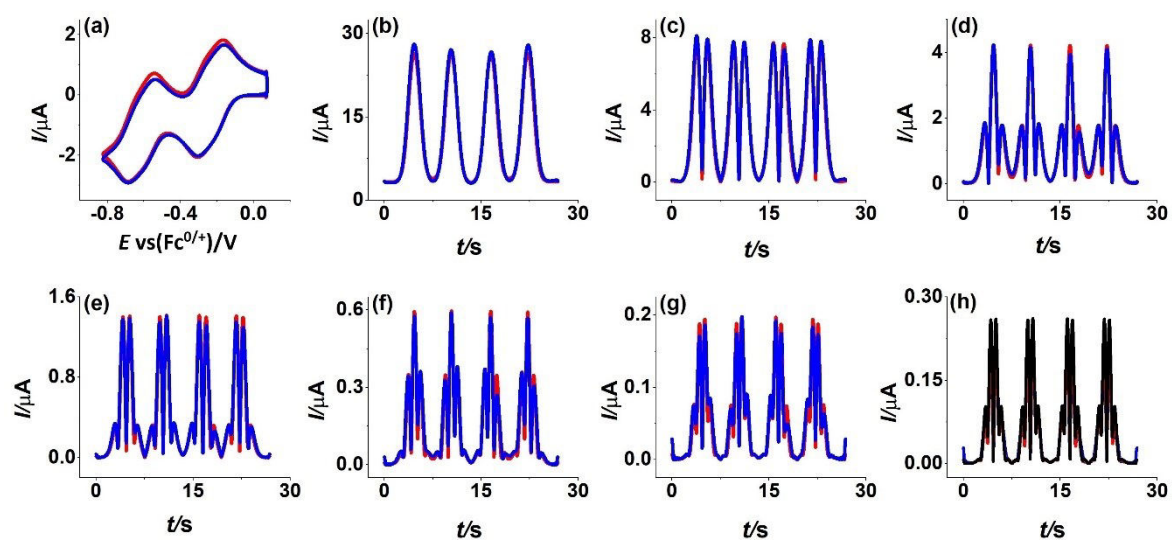


Fig. S4. Heuristic comparison of simulated (red line) and experimental (blue line) AC voltammetric data for the $\alpha\text{-}[\text{S}_2\text{W}_{18}\text{O}_{62}]^{4-/-5-/-6-}$ processes obtained with 2.5 mM $\alpha\text{-}[\text{S}_2\text{W}_{18}\text{O}_{62}]^{4-}$ in CH_3CN (0.50 M $[\text{n-Bu}_4\text{N}][\text{PF}_6]$) at a GC electrode. $\Delta E = 80 \text{ mV}$, $f = 27.01 \text{ Hz}$ and $v = 0.067 \text{ V s}^{-1}$. (a) DC component, (b-g) 1st to 6th harmonic components. Parameters used to simulate the quasi-reversible model are provided in Table 3. (h) Comparison of experimental data with simulations for the 6th harmonic AC component that are based on a reversible process (black line).

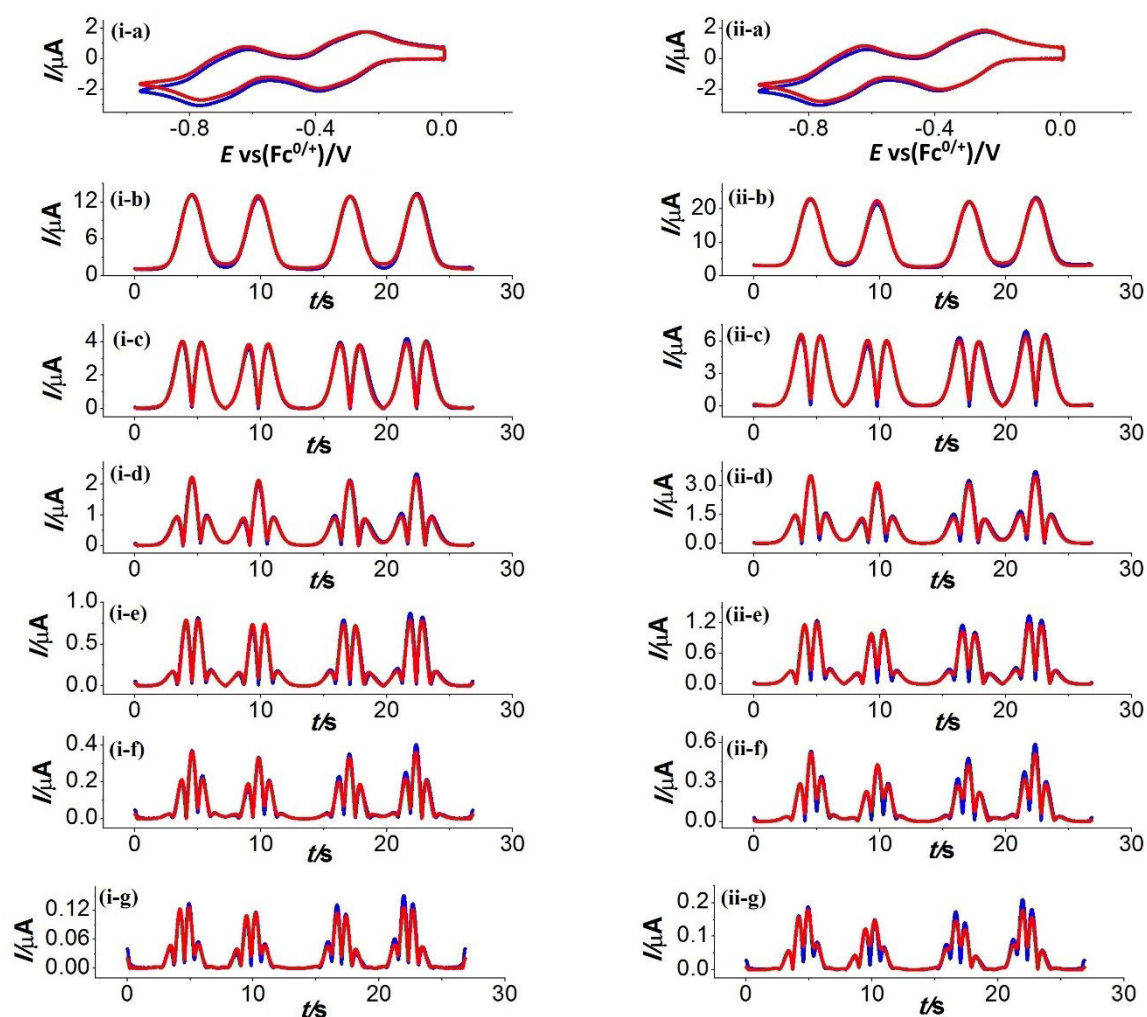


Fig. S5. Heuristic comparison of simulated (red line) and experimental (blue line) AC voltammetric data for the α -[S₂W₁₈O₆₂]^{4-/5-/6-} processes obtained for the reduction of 2.5 mM α -[S₂W₁₈O₆₂]⁴⁻ in CH₃CN (0.50 M [*n*-Bu₄N][PF₆]) at an Au electrode with $\Delta E = 80$ mV, $f =$ (i) 9.02 Hz and (ii) 27.01 Hz and $v = 0.072$ V s⁻¹. (a) DC component, (b-g) 1st to 6th harmonic components. Other parameters used to simulate the quasi-reversible response are provided in Table 3.

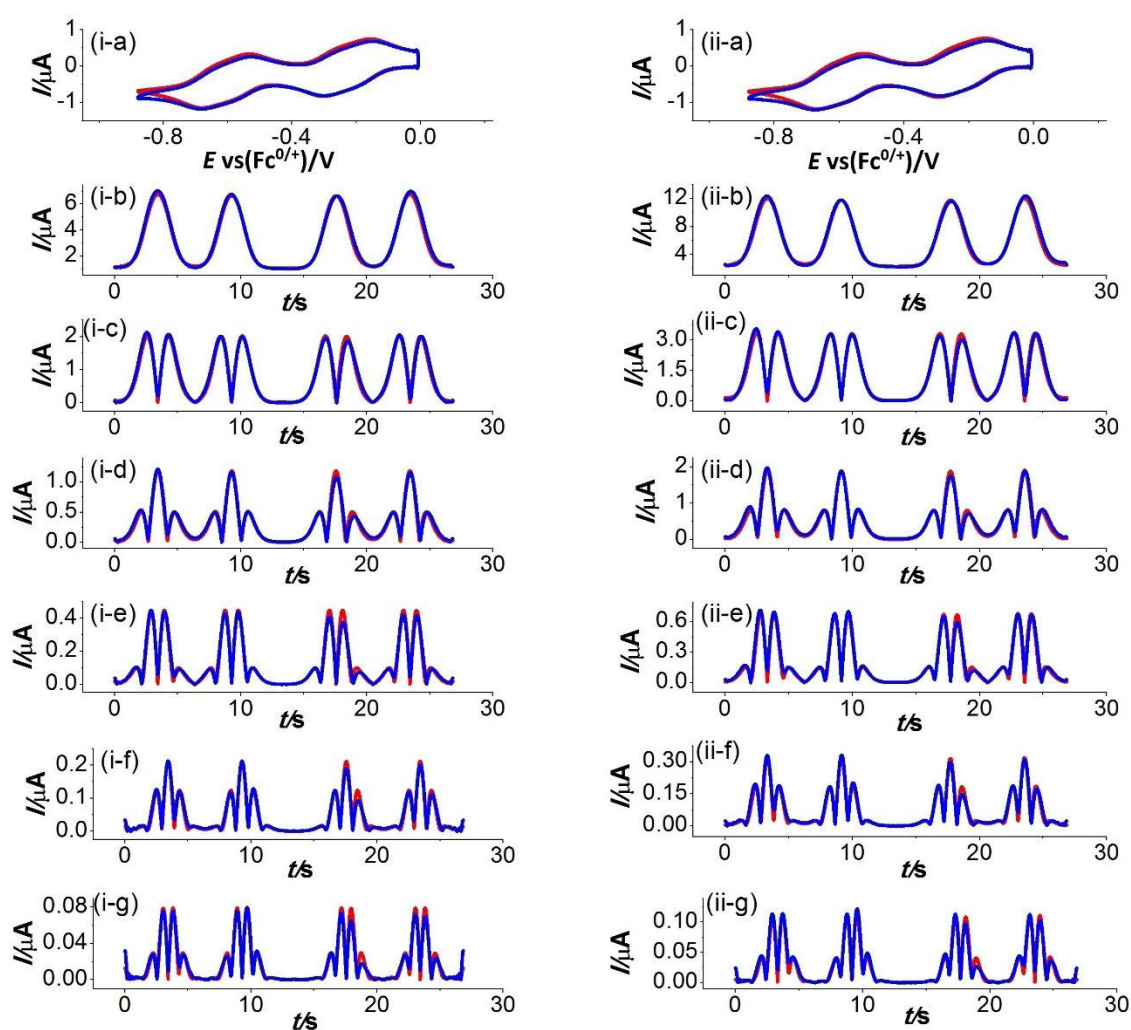


Fig. S6. Heuristic comparison of simulated (red line) and experimental (blue line) AC voltammetric data for the α -[S₂W₁₈O₆₂]^{4-/5-/6-} processes obtained for the reduction of 1.0 mM α -[S₂W₁₈O₆₂]⁴⁻ in CH₃CN (0.50 M [*n*-Bu₄N][PF₆]) at a GC electrode with $\Delta E = 80$ mV, $f =$ (i) 9.02 Hz and (ii) 27.01 Hz and $v = 0.067$ V s⁻¹. (a) DC component, (b-g) 1st to 6th harmonic components. Other parameters used in simulation are given in Tables 1, 3 and text.

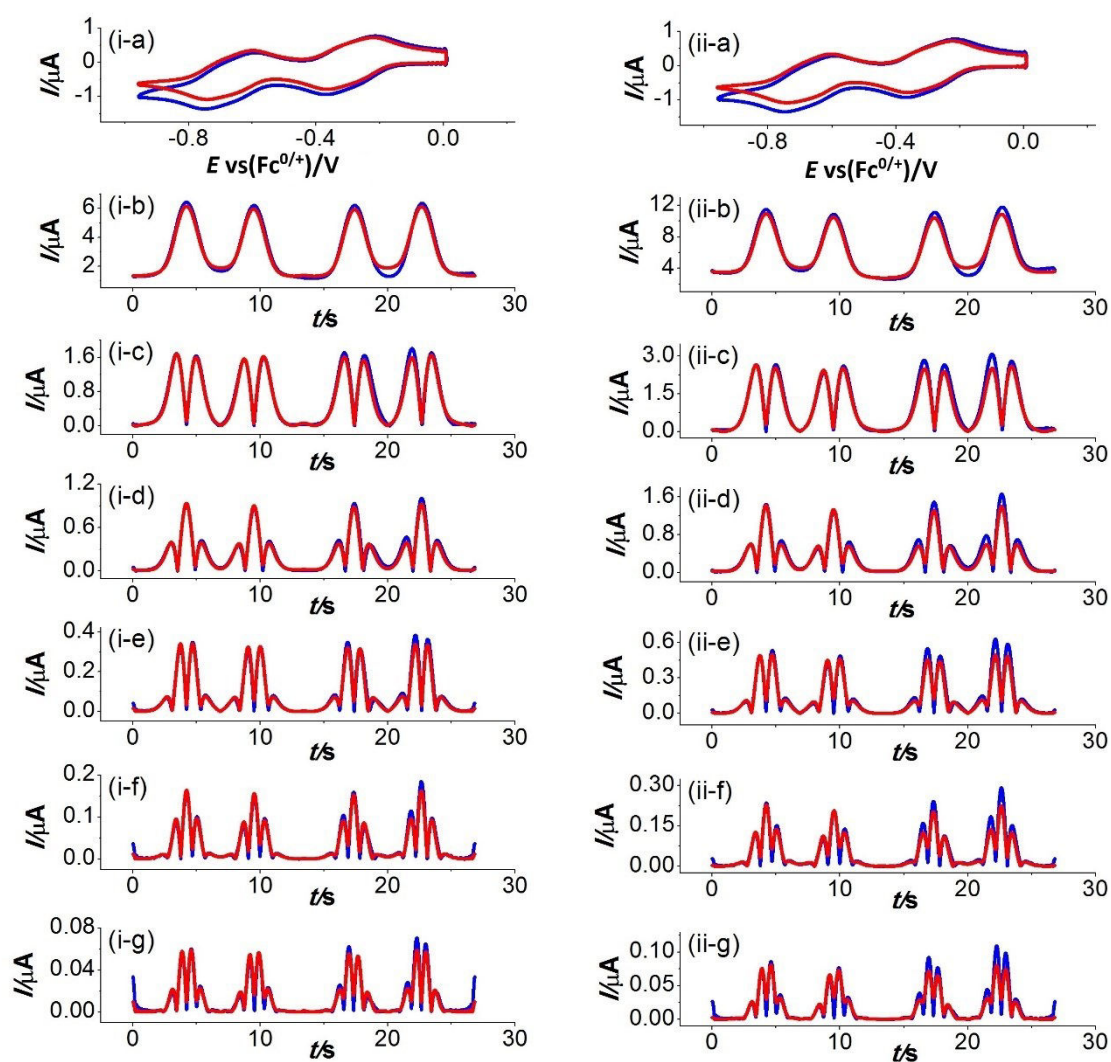


Fig. S7. Heuristic comparison of simulated (red line) and experimental (blue line) AC voltammetric data for the α -[S₂W₁₈O₆₂]^{4-/5-/6-} processes obtained for the reduction of 1.0 mM α -[S₂W₁₈O₆₂]⁴⁻ in CH₃CN (0.50 M [*n*-Bu₄N][PF₆]) at an Au electrode with $\Delta E = 80$ mV, $f =$ (i) 9.02 Hz and (ii) 27.01 Hz and $v = 0.072$ V s⁻¹. (a) DC component, (b-g) 1st to 6th harmonic components. Other parameters used in simulation are given in Tables 1, 3 and text.

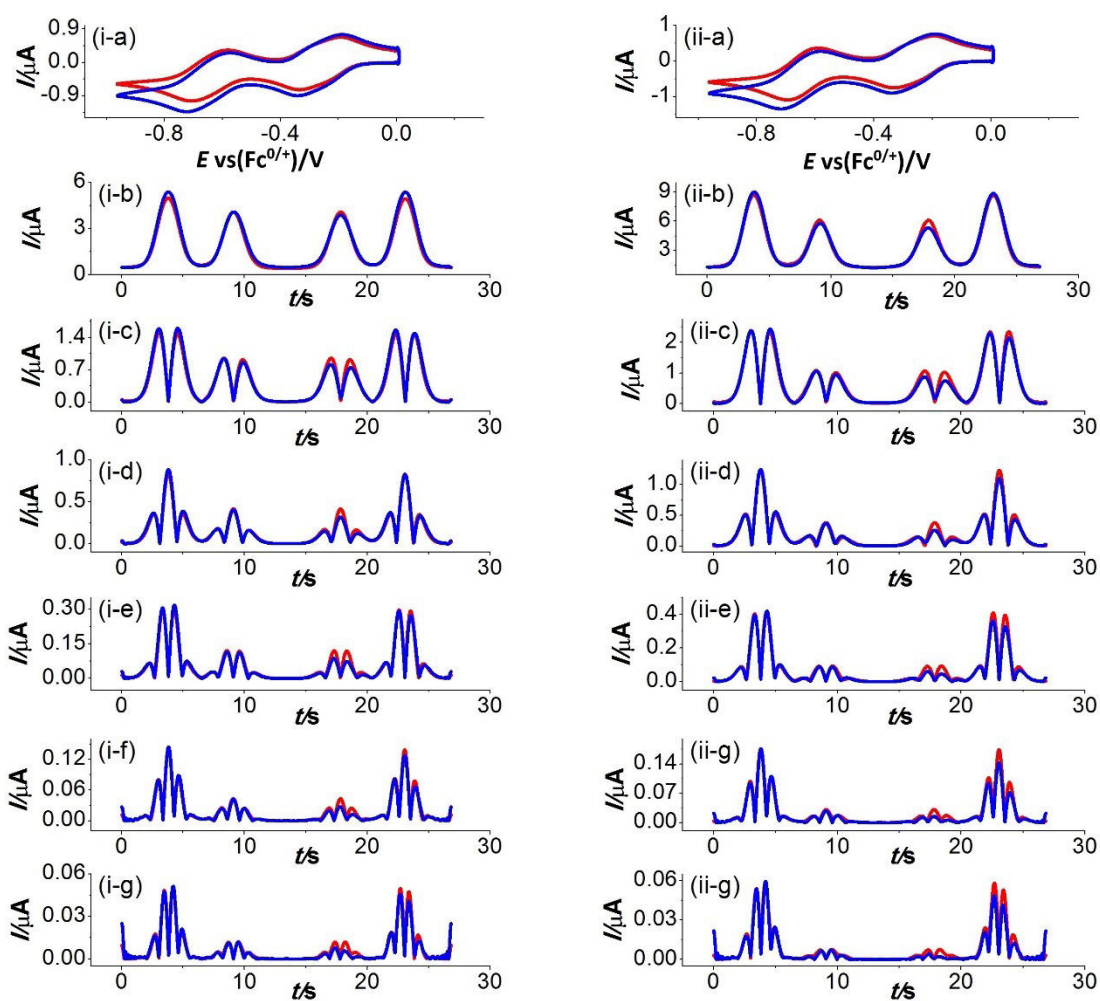


Fig. S8. Heuristic comparison of simulated (red line) and experimental (blue line) AC voltammetric data for the α -[S₂W₁₈O₆₂]^{4-/5-/6-} processes obtained for the reduction of 1.0 mM α -[S₂W₁₈O₆₂]⁴⁻ in CH₃CN (0.50 M [*n*-Bu₄N][PF₆]) at a Pt electrode with $\Delta E = 80$ mV, $f =$ (i) 9.02 Hz and (ii) 27.01 Hz and $v = 0.072$ V s⁻¹. (a) DC component, (b-g) 1st to 6th harmonic components. Other parameters used in simulation are given in Tables 1, 3 and text.

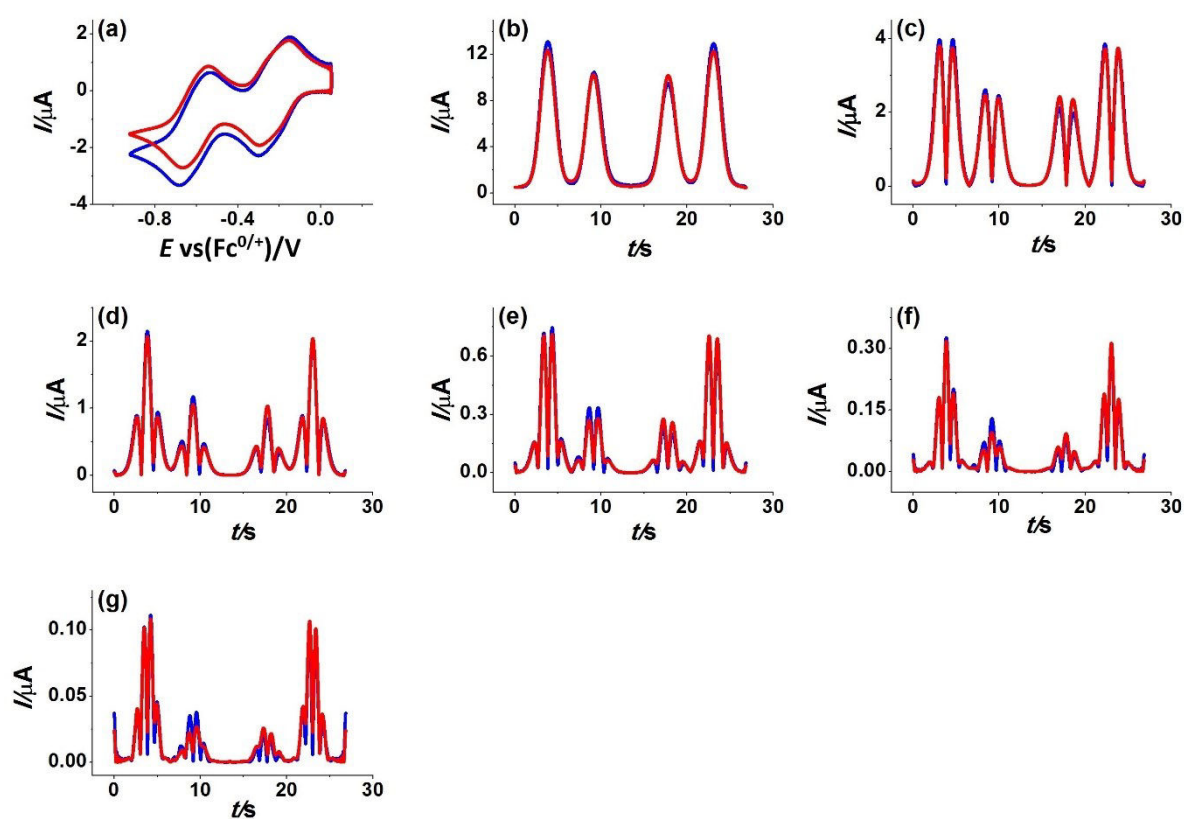


Fig. S9. Comparison of simulated (red line) data obtained by automated data optimisation and experimental (blue line) AC voltammetric data for the α - $[\text{S}_2\text{W}_{18}\text{O}_{62}]^{4-}/5-/6-$ processes obtained for the reduction of 2.5 mM α - $[\text{S}_2\text{W}_{18}\text{O}_{62}]^{4-}$ in CH_3CN (0.50 M $[\text{n-Bu}_4\text{N}][\text{PF}_6]$) at a Pt electrode with $\Delta E = 80$ mV, $f = 9.02$ Hz and $v = 0.072$ V s^{-1} . (a) DC component, (b-g) 1st to 6th harmonic components. Other parameters used in simulation are given in Table 4 and text.

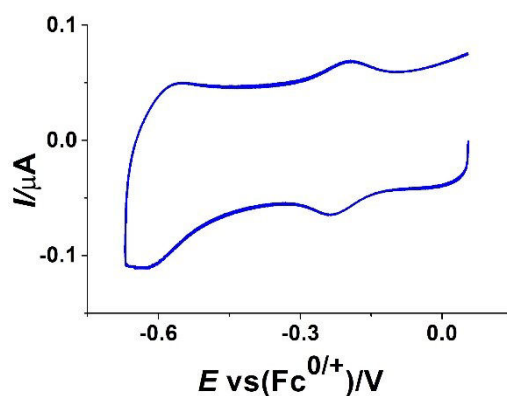


Fig. S10. Cyclic voltammetry obtained at a scan rate of 0.100 V s^{-1} when $\alpha\text{-[S}_2\text{W}_{18}\text{O}_{62}]^{4-}$ is surface confined to a GC electrode in CH_3CN ($0.50 \text{ M } [n\text{-Bu}_4\text{N}][\text{PF}_6]$).

Reference:

1. S.-X. Guo, A.M. Bond and J. Zhang, Fourier transformed large amplitude alternating current voltammetry: principles and applications, *Rev. Polarogr.* 61(1) (2015) 21-32. <https://doi.org/10.5189/revpolarography.61.21>.

Chapter 3

Identification of Mechanistic Subtleties that Apply to Voltammetric Studies at Boron Doped Diamond Electrodes: The α -[S₂W₁₈O₆₂]^{4-/5-/6-} Processes

Md Anisur Rahman^a, Julie V. Macpherson^b, Alan M. Bond^{a, c *} and Jie Zhang^{a, c *}

^a School of Chemistry, Monash University, Clayton, Victoria 3800, Australia

^b Department of Chemistry, University of Warwick, Coventry, CV4 7AL, UK.

^c ARC Centre of Excellence for Electrochemical Science, Monash University, Clayton,
Victoria 3800, Australia

*Corresponding authors: jie.zhang@monash.edu, alan.bond@monash.edu

ABSTRACT

The α -[S₂W₁₈O₆₂]^{4-/5-} and α -[S₂W₁₈O₆₂]^{5-/6-} polyoxometalate (POM) reduction processes at boron doped diamond (BDD) disk electrodes in acetonitrile (0.50 M [*n*-Bu₄N][PF₆]) have been investigated using large amplitude Fourier transformed alternating current (FTAC) voltammetry. The origins of subtle differences in experimental data and simulated data based on a simplified model involving an overall one-electron transfer reaction using Butler-Volmer electrode kinetics and assuming a uniform non-fouling electrode surface and planar diffusion, are considered. A substantial contribution from ion pairing is implicitly incorporated into this model. Parameters estimated are the apparent heterogeneous electron-transfer kinetics ($k_{app}^{0'}$), apparent formal reversible potential ($E_{app}^{0'}$) and apparent charge transfer coefficient (α'_{app}). The electrode kinetic parameters, in contrast to theoretical predictions of the model employed, are dependent on frequency, POM concentration and data analysis method. Reasons for non-conformance to the model include the adsorption of POM on the graphite-like sp² bonded carbon impurity, as well as limitations in the availability of charge carriers in BDD and the method of incorporating ion pairing into the model when slow electrode kinetics apply. This form of heterogeneity gives rise to the AC harmonic and frequency dependent electrode kinetics for both the α -[S₂W₁₈O₆₂]^{4-/5-} and α -[S₂W₁₈O₆₂]^{5-/6-} processes and explains the electrode origin and data optimisation dependent variations in $k_{app}^{0'}$. Masking of the sp² carbon rich (edge) region of the BDD disk provided FTAC voltammetric data that complied much more closely with the simulated data. Nevertheless, data analysis still shows a small concentration dependence in estimated $k_{app}^{0'}$ values, which is considered in terms of the assumption of an infinite number of charge carriers. Conclusions derived from this study are likely to be generally applicable to electrode kinetic investigations at BDD electrodes.

Keywords: boron doped diamond, polyoxometalates, Fourier transformed alternating current voltammetry, non-ideality, sp² impurity, electrode heterogeneity

INTRODUCTION

The use of conducting forms of carbon as an electrode material has a long history in electrochemistry due to advantageous features such as the ability to be chemically functionalized and large potential windows¹⁻⁵. For example, glassy carbon (GC), carbon nanotube and pyrolytic graphite² electrodes have been employed extensively for over 50 years^{2-4,6}. More recently, boron doped diamond (BDD) has been introduced as an electrode material⁷⁻⁹. Although the pure sp^3 diamond form of carbon is an electrical insulator and cannot be used as an electrode material, doping with sufficient boron (p-type dopant) enables metal-like conductivity to be achieved⁸. Properties of BDD electrodes that are attractive for use in electroanalytical include large potential windows (e.g. -1.25 to +2.3 V vs. standard hydrogen electrode (SHE) in 0.5 M H_2SO_4)¹⁰, low capacitance, corrosion resistance in high temperature and pressure environments and biocompatibility⁷⁻⁹. Apart from the boron dopant concentration, the behaviour of polycrystalline BDD electrodes is governed by factors such as the presence of sp^2 bonded carbon impurities, surface functionalization with H, O, F and non-uniform dopant levels across the surface caused by variation in boron uptake by the different crystal facets^{11,12}.

Electron transfer between an electrode and an electroactive species is a fundamental phenomenon in electrochemistry. A number of investigations have been undertaken to understand the factors that govern the electron transfer rate at BDD electrodes. In initial reports¹³⁻¹⁹, the electrode kinetics were found to be significantly slower than at metal or GC electrodes. However, the heterogeneous nature, of the electrode surface in terms of variable boron doping levels and the presence of sp^2 bonded carbon content, provides significant complexity in interpreting the data. The extent of sp^2 bonded carbon content, which is thought to reside predominantly in grain boundaries, depends on the diamond growth conditions²⁰. Obtaining minimal sp^2 bonded carbon content is challenging with high levels of boron doping. However,

this has been achieved with micro-crystalline microwave chemical vapour deposited (MW-CVD) BDD²¹. Other sources of sp² bonded carbon incorporation are also possible as a result of the BDD electrode processing technique²². For example, it is common to use ns-laser micromachining to cut cylinders of BDD from the BDD growth wafer in order to produce conventional disk-shaped electrodes. This process leaves behind a very thin layer of sp² bonded carbon on the laser cut surface *i.e.* the sidewalls of the cylinder²³. If unremoved, when the cylinder is embedded in glass or another insulating material, then preferential polishing of the inherently softer insulator can lead to a small amount of sidewall exposure and hence a sp² bonded carbon rich edge (incorporating sidewall) region. Under these conditions, the rate of electron transfer at the exposed sp² bonded carbon surface can be significantly different to the rest of the sp³ bonded carbon surface. In a viscous ionic liquid medium, abnormal apparently harmonic dependent electron transfer kinetics were found as a consequence of incomplete diffusion layer overlap between these sp² and sp³ bonded carbon regions²². The equivalent of this dual electron transfer rate scenario has been examined theoretically by Tan et. al.²⁴.

In this present study, large amplitude Fourier transformed alternating current (FTAC) voltammetry has been employed to probe the impact of sp² bonded carbon and other features of heterogeneous BDD electrodes on the parameterisation of the electrode kinetics of the α -[S₂W₁₈O₆₂]^{4- /5- /6-} single electron transfer processes. Voltammetry of polyoxometalate (POM) α -[S₂W₁₈O₆₂]⁴⁻ has been described quantitatively in detail at metal and GC disks, but not at BDD electrodes²⁵. In conventional aprotic organic solvents^{21,26,27} and ionic liquids²⁸, at least six one-electron reduction processes have been observed under DC voltammetric conditions at GC electrodes, with only the initial two being of interest in this study as those involving further reduction contain considerable additional complexity²⁷. FTAC voltammetry was chosen for electrode kinetic measurements rather than conventional DC voltammetry since

it offers higher kinetic sensitivity and has the ability to discriminate between the effects of slow electron transfer kinetics and uncompensated resistance (R_u)²⁹.

Electrode kinetic studies of quasi-reversible processes requires comparison of experimental results with theoretical data derived from simulation of a model that is selected to mimic the experimental data. To date, modelling with BDD disk electrodes has been undertaken using the Butler-Volmer relationship and Fick's Laws for planar diffusion to describe the electron transfer and mass transport processes respectively. This model also assumes a homogeneous and non-fouling electrode surface. When applied with FTAC voltammetry, it predicts that the calculated heterogeneous electron-transfer kinetics (k^0) and charge transfer coefficient (α') parameters are independent of AC harmonic, frequency, concentration of analyte and method of data optimisation. Significantly, in this POM electrochemistry study using BDD electrodes, dependencies on all these factors are found under certain experimental regimes. These discrepancies require that limitations in the model used to parameterise the electrode kinetics should be interrogated in detail in terms of BDD electrode heterogeneity, POM surface interactions, POM ion pairing and other features of BDD electrodes, such as heterogeneity and low density of states, not accounted for in the modelling.

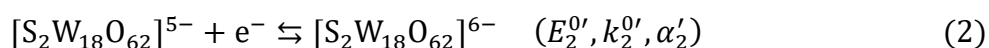
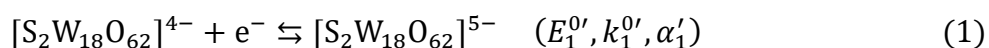
EXPERIMENTAL

Full details of instrumentation, BDD electrodes and other experimental details are available in the Supporting Information

SIMULATIONS AND DATA ANALYSIS

MECSim software³⁰ was used to simulate the FTAC voltammetric data assuming that the Butler-Volmer model for a simple one-electron quasi-reversible electron transfer processes applies to both α -[S₂W₁₈O₆₂]^{4-/5-/6-} processes which are described and parameterised in

Equations 1 and 2. The BDD disk electrodes employed were assumed to be fully homogeneous on the FTAC voltammetric timescale which allows mass transport to be modelled according to Fick's Laws for planar diffusion. The model used also assumes no interaction of oxidised or reduced POMs with the BDD surface, and that there is an infinite number of charge carriers within the BDD electrode.



As noted in reference ²⁵, $k^{0'}$ and α' parameters (equation 1) which are relevant to the formal reversible potential ($E^{0'}$) in the Butler-Volmer model are better described as $k_{app}^{0'}$ and α'_{app} at $E_{app}^{0'}$ because POM ion-pairing is incorporated into these parameters in the modelling used in this and other studies of electrode kinetics ^{25,31,32}. Coupling of electron transfer and ion-pairing is satisfactory if ion pairing is reversible and electron transfer is fast, but if the electrode kinetics are slow as often is the case with BDD electrodes, it may be problematic²⁵. It will also emerge from this study that there are several other reasons why the apparent (*app*) electrode kinetic notation is more appropriate at BDD electrodes.

In the simulation of electron transfer process described by Equations 1 and 2, parameters such as electroactive area (A), diffusion coefficient (D), R_u , double layer capacitance (C_{dl}), temperature (T), scan rate (ν), bulk concentration (C), AC amplitude (ΔE) and frequency (f) are either known or determined separately. A was estimated using the method described in the Experimental Section (see Supporting Information). R_u was calculated from the $R_u C_{dl}$ time constant method by applying software provided with the CHI 760 E instrument to data obtained from the potential region just prior to the onset of the α - $[\text{S}_2\text{W}_{18}\text{O}_{62}]^{4-/5-}$ reduction process, which is devoid of Faradaic current. In the heuristic form of data analysis, $E_{app}^{0'}$ was estimated

from the average of the reduction and oxidation peak potentials ($\frac{E_p^{\text{red}} + E_p^{\text{ox}}}{2}$) derived from DC cyclic voltammetry. The potential dependence of C_{dl} ³³ was determined from the potential regions in the fundamental ac harmonic data that are devoid of Faradaic alternating current via [Equation 3](#) where c_0 , c_1 , c_2 , c_3 , and c_4 are coefficients associated with the polynomial.

$$C_{dl}(t) = c_0 + c_1E(t) + c_2E(t)^2 + c_3E(t)^3 + c_4E(t)^4 \quad (3)$$

The frequency dependent polynomial coefficients were measured individually at each applied frequency (9.02 or 27.01 Hz)³⁴.

In the heuristic form of data analysis, $k_{app}^{0'}$ and α'_{app} values were varied manually until an acceptable agreement between the simulated and experimental data was attained based on the judgement of the experimenter^{16,17,19}. Although this data analysis method is exceptionally tedious and prone to experimenter bias, an experienced electrochemist can ensure that physically sensible parameter estimates are achieved and also detect systematic deviations in comparisons of experimental and simulated data²⁵. Furthermore, these estimates allow the parameter space search range to be significantly restricted so that the computationally supported data optimisation method can be used in an efficient manner^{25,35}.

In the computationally supported data optimisation method, comparison of simulated and experimental data was achieved using the least squares (LS) function given in [Equation 4](#), where $f^{\text{exp}}(t_i)$ and $f^{\text{sim}}(t_i)$ are the experimental and simulated data, respectively and h and N denote the individual (from 2nd to 6th) AC harmonic component and number of data points, respectively. Data optimisation was only applied to the 2nd to 6th AC harmonic components where the contribution from background current is minimal.

$$LS = \left[1 - \left(\sum_{h=2}^6 \sqrt{\frac{\sum_{i=1}^N [(f_h^{\text{exp}}(t_i) - f_h^{\text{sim}}(t_i))^2]}{\sum_{i=1}^N f_h^{\text{exp}}(t_i)^2}} \right) / 5 \right] \times 100\% \quad (4)$$

RESULTS

DC cyclic voltammetry for reduction of α -[S₂W₁₈O₆₂]⁴⁻ at BDD electrodes.

The BDD wafers used to prepare disc electrodes in this study (see Supporting Information) were grown using the MW-CVD method, aimed to minimise sp² bonded carbon formation²¹. Laser cutting was then used to prepare cylinders of BDD, which were then sealed in either Teflon or glass. As shown in Figure 1a, the DC cyclic voltammetry (CV) of α -[S₂W₁₈O₆₂]⁴⁻ in CH₃CN (0.50 M tetrabutylammonium hexafluorophosphate ([*n*-Bu₄N][PF₆])) using the glass-sealed BDD electrode is similar to that obtained at a GC electrode²⁶ with six well-resolved one electron transfer processes evident prior to the solvent limit. In this study only the α -[S₂W₁₈O₆₂]^{4-/5-/6-} processes are subjected to parameterisation. A comparison of the DC cyclic voltammetry for both the glass-sealed BDD and Teflon-sealed BDD electrodes is presented in Figure 1b and is based on the current density (*i*) to normalize the electrode area differences.

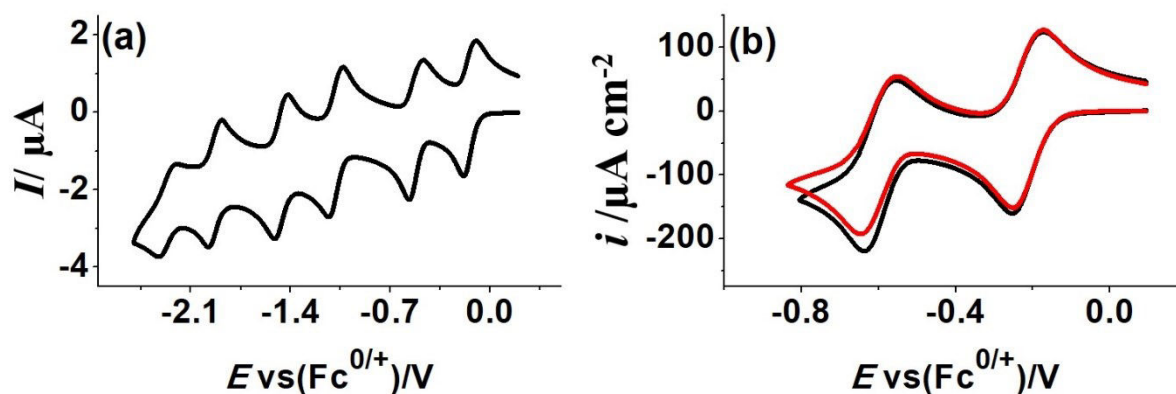


Figure 1. DC cyclic voltammetry for reduction of 1.0 mM α -[S₂W₁₈O₆₂]⁴⁻ at a BDD electrode in CH₃CN (0.50 M [*n*-Bu₄N][PF₆])) at a scan rate of 0.100 V s⁻¹. (a) Glass-sealed BDD over a wide potential range. (b) Glass-sealed BDD (—) and Teflon-sealed BDD (—) electrodes over a potential range encompassing the α -[S₂W₁₈O₆₂]^{4-/5-/6-} processes only.

$E_{app}^{0'}$ values calculated from DC CV are summarized in Table 1. $E_{app1}^{0'}$ and $E_{app2}^{0'}$ values are similar at both BDD electrodes to those reported at GC, Au and Pt electrodes²⁵. This independence of electrode material is in accordance with theoretical predictions since $E_{app}^{0'}$ is a thermodynamic parameter.

Table 1. Data derived from the reduction of 1.0 mM α -[S₂W₁₈O₆₂]⁴⁻ in CH₃CN (0.50 M [n-Bu₄N][PF₆]) using DC cyclic voltammetry with a scan rate of 0.100 V s⁻¹.

Electrode	$E_{app1}^{0'}$	$E_{app2}^{0'}$	ΔE_{p1}	ΔE_{p2}
	V vs Fc ^{0/+} a (Fc = Ferrocene)		V ^b	
Glass-sealed BDD	-0.211	-0.595	0.080	0.084
Teflon-sealed BDD	-0.214	-0.601	0.085	0.097
Wax treated glass-sealed BDD	-0.215	0.599	0.096	0.101
Wax treated Teflon-sealed BDD	-0.216	-0.600	0.095	0.106

^a Uncertainty in $E_{app}^{0'}$ is ± 5 mV

^b Uncertainty in ΔE_p is ± 2 mV

Peak-to-peak separations ($\Delta E_p = (E_p^{\text{red}} - E_p^{\text{ox}})$) are also included in Table 1. Values of $\Delta E_{p1} = 0.080$ V and $\Delta E_{p2} = 0.084$ V for the glass-sealed BDD are slightly smaller than those of $\Delta E_{p1} = 0.085$ V and $\Delta E_{p2} = 0.097$ V found with the Teflon-sealed electrode. Larger ΔE values (Table 1) are found after the BDD electrodes were treated with wax, as described in the Supporting Information, to remove contributions to the voltammetry from sp² bonded carbon edge effects introduced from the laser micromachining process²². Assuming IR_u drop is unimportant, the ΔE_p data, with application of the widely used Nicholson method³⁶ of electrode kinetic data analysis, imply that $k_{app}^{0'}$ values at the glass-sealed BDD electrode are greater than at the Teflon-sealed BDD one, which in turn are greater than the $k_{app}^{0'}$ values at both wax treated electrodes. Furthermore, all ΔE_p values are significantly larger than those of

$\Delta E_{p1} = 0.060$ V and $\Delta E_{p2} = 0.063$ V found at a GC electrode²⁵, implying that $k_{app}^{0'}$ at BDD is significantly smaller than at GC. However, use of this two-point method of data analysis is very simplistic. It does not lead to an in depth understanding provided by detailed comparisons of the full experimental data set with predictions based on simulated data, as undertaken in the FTAC voltammetric studies described below.

FTAC voltammetry for reduction of α -[S₂W₁₈O₆₂]⁴⁻ at BDD electrodes

Parameterisation of FTAC voltammetric data obtained at glass and Teflon-sealed BDD electrodes. FTAC voltammetric data were obtained for the reduction of 2.5 mM α -[S₂W₁₈O₆₂]⁴⁻ in CH₃CN (0.50 M [*n*-Bu₄N][PF₆]) at glass and Teflon-sealed BDD electrodes using a sinusoidal perturbation with $f = 9.02$ or 27.01 Hz and $\Delta E = 80$ mV. Table 2 summarises the values of the $E_{app}^{0'}$, $k_{app}^{0'}$ and α'_{app} for both electron transfer processes derived from the heuristic form of data analysis as well as by automated data optimisation.

Table 2. Parameters^a derived by heuristic and automated data optimisation methods of analysis of FTAC voltammetric data obtained at BDD electrodes for the reduction of 2.5 mM α -[S₂W₁₈O₆₂]⁴⁻ in CH₃CN (0.50 M [*n*-Bu₄N][PF₆]).

Electrode	<i>f</i> (Hz)	Parameterisation method	$E_{app1}^{0'}$	$E_{app2}^{0'}$	$k_{app1}^{0'}$	$k_{app2}^{0'}$	α'_{app1}	α'_{app2}	LS %	
			V vs Fc ^{0/+}		cm s ⁻¹					
Glass-sealed	9.02	Heuristic	-0.211	-0.595	0.010 ^b	0.029 ^b	0.52	0.52	73	
		Automated	Range Searched	-0.216 to -0.206	-0.602 to -0.592	0.001 to 0.025	0.005 to 0.050	0.40 to 0.70		0.40 to 0.70
			Estd.	-0.208	-0.595	0.009 ^c	0.016 ^c	0.56		0.50
	27.01	Heuristic	-0.211	-0.595	0.010 ^b	0.033 ^b	0.50	0.53		
		Automated	Range Searched	-0.215 to -0.206	-0.602 to -0.592	0.001 to 0.025	0.001 to 0.050	0.40 to 0.70		0.40 to 0.70
			Estd.	-0.208	-0.593	0.009 ^c	0.016 ^c	0.52		0.64
Teflon-sealed	9.02	Heuristic	-0.214	-0.601	0.007 ^b	0.004 ^b	0.52	0.50	51	
		Automated	Range Searched	-0.216 to -0.208	-0.603 to -0.594	0.001 to 0.012	0.001 to 0.010	0.40 to 0.70		0.40 to 0.70
			Estd.	-0.210	-0.598	0.005 ^c	0.003 ^c	0.57		0.52
	27.01	Heuristic	-0.214	-0.601	0.008 ^b	0.004 ^b	0.51	0.47		
		Automated	Range Searched	-0.216 to -0.204	-0.603 to -0.594	0.001 to 0.012	0.001 to 0.010	0.40 to 0.70		0.40 to 0.70
			Estd.	-0.211	-0.595	0.005 ^c	0.003 ^c	0.55		0.51

^a Other parameters used in the simulations were: $A_{\text{Glass-sealed BDD}} = 8.9 \times 10^{-3} \text{ cm}^2$, $A_{\text{Teflon-sealed BDD}} = 7.1 \times 10^{-2} \text{ cm}^2$, diffusion coefficient (D) = $2.9 \times 10^{-6} \text{ cm}^2 \text{ s}^{-1}$, $T = 295 \text{ K}$, $\nu_{\text{Glass-sealed BDD}} = 0.072 \text{ V s}^{-1}$, $\nu_{\text{Teflon-sealed BDD}} = 0.076 \text{ V s}^{-1}$, $\Delta E = 80 \text{ mV}$, $f = 9.02, 27.01 \text{ Hz}$. $R_{u-\text{Glass-sealed BDD}} = 155$ and 120Ω and $R_{u-\text{Teflon-sealed BDD}} = 101$ and 80Ω for 9.02 and 27.01 Hz, respectively. Estd. = estimated.

^b obtained from sixth AC harmonic (see text for details) ^c derived from analysis of the second to sixth AC harmonics (see text for details).

There are many ways of implementing the heuristic form of data analysis, with the approach being at the experimenter's discretion. For the glass and Teflon-sealed BDD electrodes, the experimental and simulated sixth harmonics were initially compared because

they are expected to be the most sensitive to variations in the electrode kinetics^{37,38} and also fully devoid of background current^{39,40}. Subsequently, simulations of the lower order (1st to 5th) AC harmonics, and aperiodic DC component were undertaken, using the values of $k_{app}^{0'}$ and α'_{app} derived heuristically from the sixth harmonic and the predicted results compared with experimental data. Figures 2 and 3 provide the outcomes of heuristic comparison of the experimental data for the α -[S₂W₁₈O₆₂]^{4-/5-/6-} processes undertaken in this manner for both the glass and Teflon-sealed electrodes.

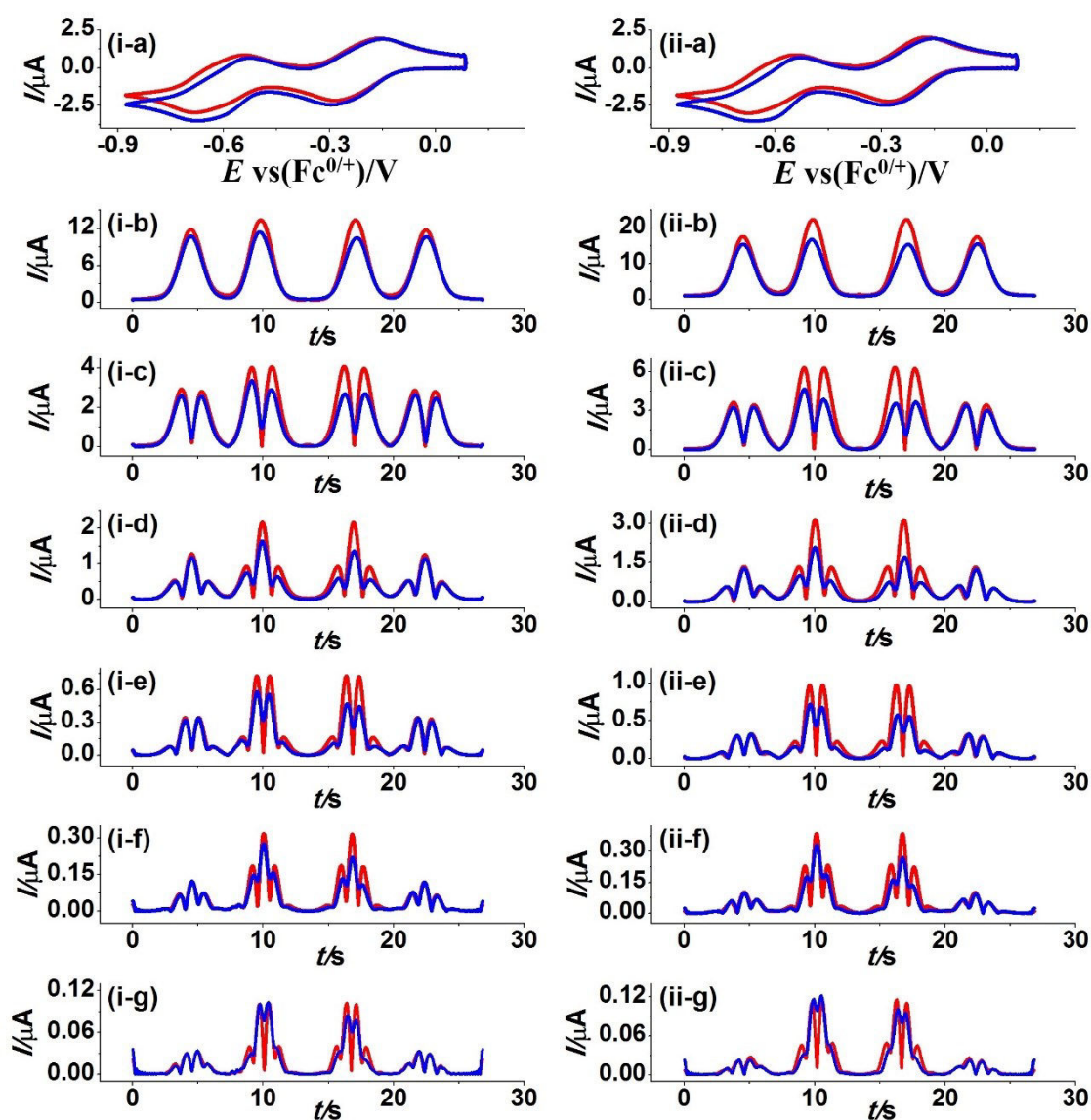


Figure 2. Heuristically based comparison of simulated (red) and experimental (blue) AC voltammetric data obtained with $\Delta E = 80$ mV, $f =$ (i) 9.02 and (ii) 27.01 Hz, electroactive area (A) = 8.9×10^{-3} cm² and $v = 0.072$ V s⁻¹ for the α -[S₂W₁₈O₆₂]^{4- /5- /6-} processes derived from reduction of 2.5 mM α -[S₂W₁₈O₆₂]⁴⁻ in CH₃CN (0.50 M [*n*-Bu₄N][PF₆]) at a glass-sealed BDD electrode. (a) DC component, (b-g) 1st to 6th harmonic components. Values of electrode kinetic and other parameters used in the simulations are provided in Table 2. Details of the heuristic approach used to obtain the electrode kinetic parameters are available in the text.

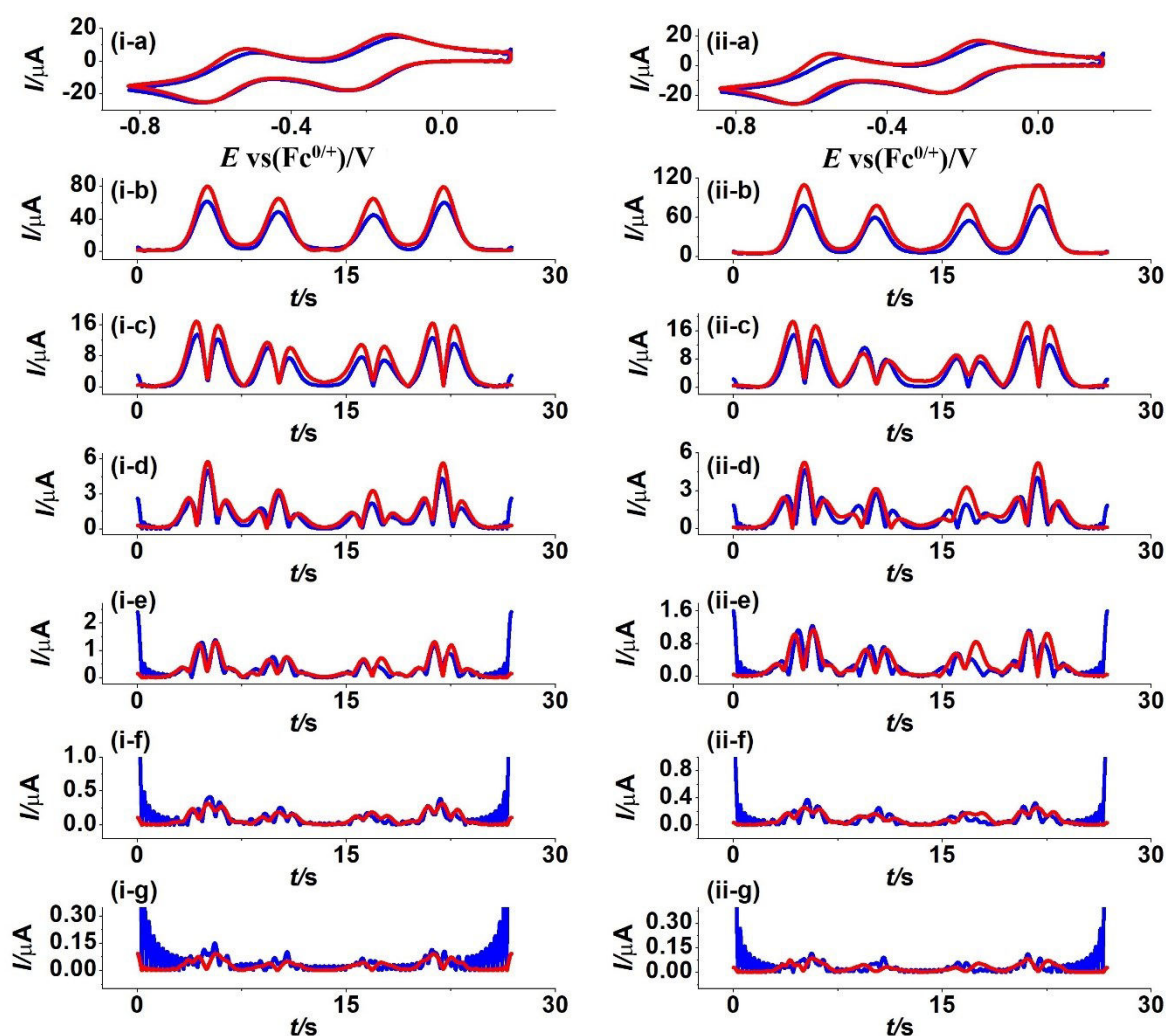


Figure 3. Heuristically based comparison of simulated (red) and experimental (blue) AC voltammetric data obtained with $\Delta E = 80$ mV, $f =$ (i) 9.02 and (ii) 27.01 Hz, $A = 7.1 \times 10^{-2}$

cm² and $v = 0.076 \text{ V s}^{-1}$ for the $\alpha\text{-[S}_2\text{W}_{18}\text{O}_{62}]^{4-}$ processes derived from reduction of 2.5 mM $\alpha\text{-[S}_2\text{W}_{18}\text{O}_{62}]^{4-}$ in CH₃CN (0.50 M [*n*-Bu₄N][PF₆]) at a Teflon-sealed BDD electrode. (a) DC component, (b-g) 1st to 6th harmonic components. Values of electrode kinetic and other parameters used in the simulations are provided in Table 2. Details of the heuristic approach used to obtain the electrode kinetic parameters are available in the text.

For a homogeneous electrode surface, use of the Butler-Volmer model with mass transport by planar diffusion requires that $k_{app}^{0'}$ and α'_{app} values derived from analysis of the sixth harmonic should also be valid equally for all the other AC harmonics. However, this was not the case. Agreement of simulated and experimental data, which by definition was excellent for the sixth harmonic using the parameters mentioned above, deteriorated significantly and systematically when applied to the lower order harmonics, as shown in Figures 2 and 3. That is, at both the glass- and Teflon-sealed BDD electrodes, if the heuristic form of parameter estimation had been applied individually to each harmonic, apparently harmonic and frequency dependant $k_{app}^{0'}$ values would be estimated for data obtained at either 9.02 or 27.01 Hz. Clearly, use of the Butler-Volmer model with mass transport by planar diffusion is not satisfactory for these BDD electrodes. Interestingly, whilst $k_{app1}^{0'} > k_{app2}^{0'}$ for GC and metal electrodes²¹ as is the case with Teflon-sealed BDD electrodes as evaluated heuristically from the sixth harmonic data set, somewhat unexpectedly, for the glass-sealed BDD electrode, $k_{app2}^{0'} > k_{app1}^{0'}$.

The $k_{app}^{0'}$ and α'_{app} values obtained by the automated data optimisation approach differ from the heuristically estimated ones. In the automated approach the software was programmed to find the best fit values of $E_{app}^{0'}$, $k_{app}^{0'}$, α'_{app} from second to sixth harmonics based on the minimization of the LS function using all data; lower percentages in LS signify poorer agreement between theoretical and experimental data. Since there is no experimenter based

intelligence involved with the version of the automated method, unlike the experimenter controlled heuristic method, $E_{app}^{0'}$, $k_{app}^{0'}$, α_{app}' values reported in Table 1 simply represent a statistically based estimate of the best fit to the data and not just from the sixth harmonic. However, the fact that the LS values given in Table 1 are always significantly below 100% confirms the presence of a pronounced discrepancy between theory and experiment, which is consistent with the finding of the heuristic analysis. As seen from LS values in Table 2, the fit of the modelled and experimental data is poorer at the Teflon-sealed BDD electrodes and at the higher frequency where the process is less reversible. In all cases, $k_{app}^{0'}$ estimated by the automated data optimisation method is smaller.

FTAC voltammetric data analysis with a wax-treated, glass-sealed BDD electrode. A major origin of the considerable departure of the experimental data from that predicted theoretically was hypothesised to be a consequence of electrode heterogeneity resulting from the sp^2 bonded carbon present at the BDD electrode edge due to laser cutting as described in the Introduction²². To mask this imperfection, the edge regions of both electrodes were wax treated as described in the Experimental Section so that only the centre of the electrode was exposed to the electrolyte solution. Since the BDD used in the fabrication of both electrodes was grown under conditions where sp^2 bonded carbon is negligible²¹, the wax-treated forms of the electrode were assumed to contain purely sp^3 bonded carbon. Even though uneven boron doping will still be present given the material is polycrystalline⁸, overlap of diffusion layers should allow data to be modelled with the Butler-Volmer and planar diffusion relationships and provide $E_{app}^{0'}$, $k_{app}^{0'}$, α_{app}' values that are independent of AC harmonic and frequency.

A heuristic comparison of simulated and experimental AC voltammetric data at the wax-treated glass-sealed BDD electrode is shown in Figure 4 for all harmonics, based on

parameters estimated from analysis of the fourth harmonic. As in all heuristically based data analysis exercises, the investigators in this study again used their experience to decide how to compare this experimental and simulated data. Since the electroactive area ($A = 3.4 \times 10^{-3} \text{ cm}^2$) of the masked electrode is now much smaller than that of the untreated electrode ($A = 8.9 \times 10^{-3} \text{ cm}^2$) so are the current magnitudes of all AC harmonics. Thus, the starting point for the heuristic data analysis in this case was not the now noisy sixth harmonic response (see Figure 4) as before, but the fourth where excellent signal to noise is available. Furthermore, since $k_{app}^{0'}$ values at this masked electrode are now significantly smaller, considerable kinetic selectivity is still available in the fourth harmonic. Nevertheless, the difference in current magnitudes in reduction (negative scan direction) and oxidation data sets (asymmetry) could not be accommodated in the simulations.

The choice, based on experience with data analysis involving equivalently slow electron transfer at Pt electrodes ²¹, was to estimate electrode kinetic parameters based on achievement of an almost perfect fit to the reduction component of the data set. The observed asymmetry has been tentatively attributed to either ion-pairing coupled with slow electron transfer or surface interaction, neither of which are included the simulated data ²⁵. Parameters obtained heuristically using the protocol chosen are summarised in Table 3. Notably, while perfect agreement of experimental and simulated data is still not achieved with respect to the oxidation component data set (see Figure 4), estimates of $k_{app}^{0'}$ and α'_{app} for both of the α - $[\text{S}_2\text{W}_{18}\text{O}_{62}]^{4-/5-}$ and α - $[\text{S}_2\text{W}_{18}\text{O}_{62}]^{5-/6-}$ reduction processes at the wax-treated BDD electrode are now harmonic and frequency independent, as predicted theoretically. This outcome is consistent with negligible levels of sp^2 bonded carbon (within the limits of experimental discrimination) in the central area of the BDD electrodes, as expected given the MW-CVD growth conditions employed ²¹.

Table 3. Parameters^a obtained by heuristic and computational methods of data analysis for the α -[S₂W₁₈O₆₂]^{4-/5-/6-} processes from analysis of data derived from reduction of 2.5 mM α -[S₂W₁₈O₆₂]⁴⁻ in CH₃CN (0.50 M [*n*-Bu₄N][PF₆]) at the wax-treated glass-sealed BDD electrode.

f (Hz)	Simulation method	Ru (Ω) ^b	$E_{app1}^{0'}$ V vs Fc ^{0/+}	$E_{app2}^{0'}$	$k_{app1}^{0'}$ cm s ⁻¹	$k_{app2}^{0'}$	α'_{app1}	α'_{app2}	LS %	
9.02	Heuristic	983	-0.211	-0.595	0.007 ^c	0.005 ^c	0.52	0.50	74	
	Automated		Range searched	-0.214 to -0.205	-0.600 to -0.590	0.001 to 0.015	0.001 to 0.015	0.40 to 0.70		0.40 to 0.70
			Estimated	-0.209	-0.593	0.007 ^d	0.003 ^d	0.54		0.54
			Heuristic	-0.211	-0.595	0.008 ^c	0.005 ^c	0.52		0.48
27.01	Automated	1183	Range searched	-0.214 to -0.205	-0.603 to -0.590	0.001 to 0.015	0.001 to 0.015	0.40 to 0.70	0.40 to 0.70	73
			Estimated	-0.210	-0.592	0.008 ^d	0.003 ^d	0.53	0.53	
			Heuristic	-0.211	-0.595	0.008 ^c	0.005 ^c	0.52	0.48	
	Automated		Range searched	-0.214 to -0.205	-0.603 to -0.590	0.001 to 0.015	0.001 to 0.015	0.40 to 0.70	0.40 to 0.70	

^a Other parameters used in the simulations are: Electroactive area of wax-treated glass-sealed BDD electrode, $A = 3.4 \times 10^{-3} \text{ cm}^2$, $D = 2.9 \times 10^{-6} \text{ cm}^2 \text{ s}^{-1}$, $T = 295 \text{ K}$, $\nu = 0.076 \text{ V s}^{-1}$, $\Delta E = 80 \text{ mV}$, $f = 9.02$ or 27.01 Hz .

^b values vary due to slight difference in electrode arrangement in cell.

^c estimated using reduction component of data only (see text for details).

^d determined from analysis of the second to sixth AC harmonics (see text for details).

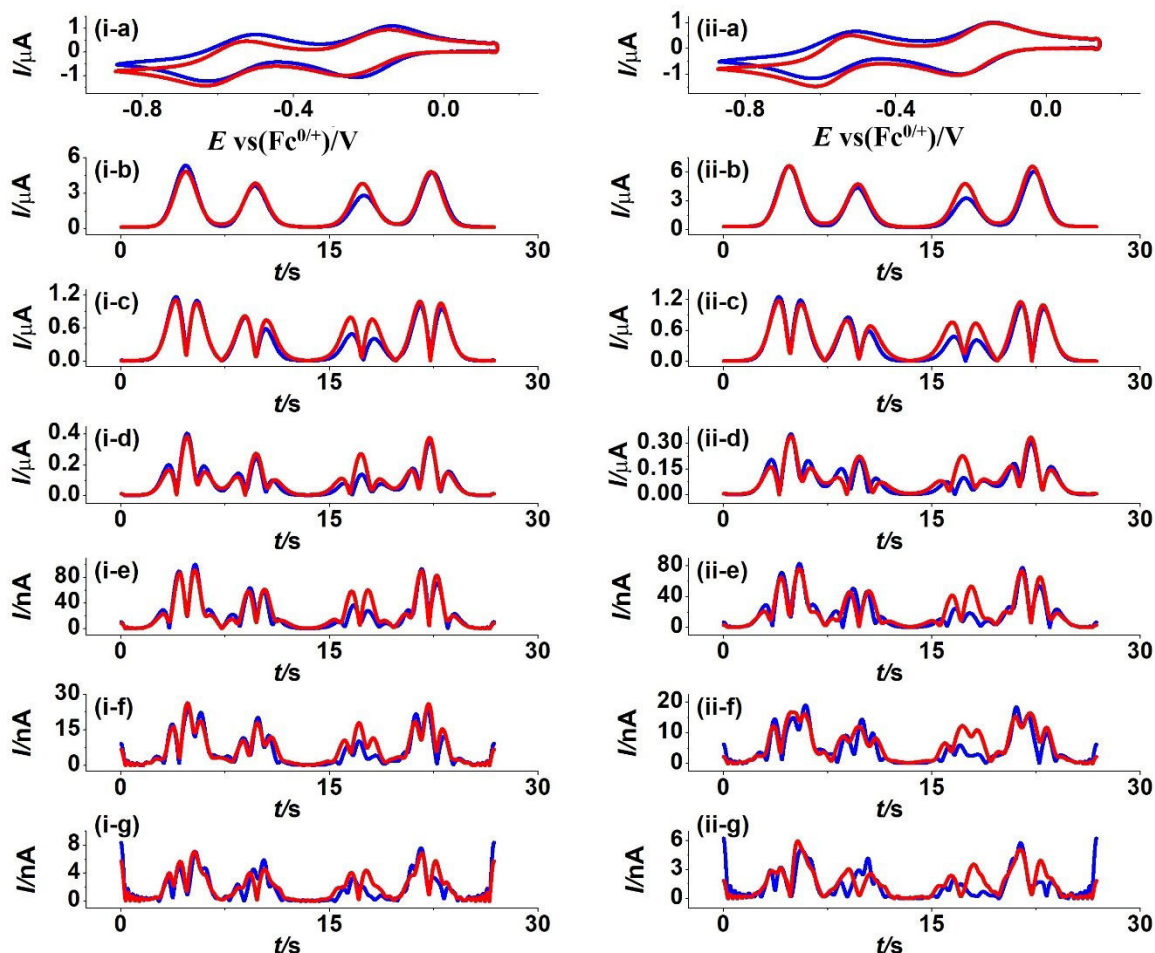


Figure 4. Heuristically based comparison of simulated (red) and experimental (blue) AC voltammetric data obtained with $\Delta E = 80$ mV, $f =$ (i) 9.02 and (ii) 27.01 Hz, $A = 3.4 \times 10^{-3}$ cm² and $\nu = 0.076$ V s⁻¹ for the α -[S₂W₁₈O₆₂]^{4-/-5-/-6-} processes derived from reduction of 2.5 mM α -[S₂W₁₈O₆₂]⁴⁻ in CH₃CN (0.50 M [*n*-Bu₄N][PF₆]) at a wax-treated glass-sealed BDD electrode. (a) DC component, (b-g) 1st to 6th harmonic components. Note that only the reduction component of data was used in this analysis (see text for details). Other parameters used in simulation are provide in Table 3.

The method of accommodating modelling imperfections in the heuristic form of data analysis was not use in automated data optimisation. In the latter method, data obtained for both oxidation and reduction components were used and treated equally. Therefore, even with

the wax treatment of the glass-sealed BDD electrode, data analysis dependent parameter values are anticipated. Heuristically, $k_{app1}^{0'} = 0.007 > k_{app2}^{0'} = 0.005 \text{ cm s}^{-1}$ and $k_{app1}^{0'} = 0.008 > k_{app2}^{0'} = 0.005 \text{ cm s}^{-1}$ at 9.02 and 27.01 Hz, respectively. In particular, lower $k_{app}^{0'}$ values are estimated at both frequencies for the α -[S₂W₁₈O₆₂]^{5-/6-} process ($k_{app2}^{0'} = 0.003 \text{ cm s}^{-1}$) using automated data optimisation. These decreased $k_{app}^{0'}$ values as well as the still relatively low LS values of ~73% are a consequence of inclusion of the oxidation component data set, which has a lower current than the reduction one. Nevertheless, the difference between the α'_{app} values obtained by the heuristic and automated methods are now small ($\alpha'_{app1} = 0.52$ and $\alpha'_{app2} = 0.50$ at 9.02 Hz versus $\alpha'_{app1} = 0.54$ and $\alpha'_{app2} = 0.54$ for heuristic and automated method, respectively) and the $E_{app}^{0'}$ values remain robustly independent of data analysis or electrode format.

FTAC voltammetric data analysis with a wax-treated Teflon-sealed BDD electrode. The $k_{app}^{0'}$ and α'_{app} values for the α -[S₂W₁₈O₆₂]^{4-/5-/6-} processes in CH₃CN (0.50 M [*n*-Bu₄N][PF₆]) at the wax-treated Teflon-sealed BDD electrode also were obtained heuristically and computationally by FTAC voltammetry using the same protocols as with the wax-treated glass sealed BDD electrode. However, in this study, α -[S₂W₁₈O₆₂]⁴⁻ concentrations of 2.5, 1.0, 0.50 and 0.25 mM were used to see if $k_{app}^{0'}$ is independent of concentration, as predicted theoretically. Electrode kinetics as well as $E_{app}^{0'}$ values obtained are summarized in Table 4.

Table 4. Parameters^a obtained by heuristic and computational methods of data analysis for the α -[S₂W₁₈O₆₂]^{4-/-5-/-6-} processes in CH₃CN (0.50 M [*n*-Bu₄N][PF₆]) at the wax-treated Teflon-sealed BDD electrode.

Conc. (mM)	<i>f</i> (Hz)	Simulation method	Ru (Ω) ^b	E_{app1}^0		E_{app2}^0		k_{app1}^0		k_{app2}^0		α_{app1}	α_{app2}	LS %
				V vs Fc ^{0/+}				cm s ⁻¹						
2.5	9.02	Heuristic	125		-0.216	-0.600	0.0050	0.0040	0.54	0.51				
		Automated		Range	-0.225	-0.608	0.001	0.001	0.40	0.40			82	
					to	to	to	to	to	to				
					-0.208	-0.592	0.015	0.015	0.70	0.70				
					Estd.	-0.211	-0.596	0.0053	0.0043	0.53	0.53			
					Heuristic		-0.216	-0.600	0.0052	0.0045	0.54	0.53		
	27.01	Automated	Range	-0.223	-0.605	0.001	0.001	0.40	0.40					
			to	to	to	to	to	to						
			-0.207	-0.590	0.015	0.015	0.70	0.70						
			Estd.	-0.213	-0.597	0.0057	0.0045	0.52	0.52					
	1.0	9.02	Heuristic	110		-0.216	-0.600	0.0072	0.0050	0.54	0.51			
			Automated		Range	-0.223	-0.603	0.001	0.001	0.40	0.40			85
					to	to	to	to	to	to				
					-0.213	-0.591	0.025	0.015	0.70	0.70				
					Estd.	-0.218	-0.600	0.0074	0.0045	0.55	0.53			
					Heuristic		-0.216	-0.600	0.0075	0.0055	0.52	0.51		
27.01		Automated	Range	-0.222	-0.605	0.001	0.001	0.40	0.40					
			to	to	to	to	to	to						
			-0.208	-0.590	0.025	0.015	0.70	0.70						
			Estd.	-0.213	-0.595	0.0071	0.0044	0.53	0.53					
0.50		9.02	Heuristic	50		-0.216	-0.600	0.013	0.010	0.52	0.53			
			Automated		Range	-0.219	-0.610	0.005	0.005	0.40	0.40			90
					to	to	to	to	to	to				
					-0.210	-0.593	0.025	0.025	0.70	0.70				
					Estd.	-0.214	-0.597	0.012	0.009	0.57	0.59			
					Heuristic		-0.216	-0.600	0.0135	0.011	0.52	0.52		
	27.01	Automated	Range	-0.220	-0.607	0.005	0.005	0.40	0.40					
			to	to	to	to	to	to						
			-0.211	-0.595	0.025	0.025	0.70	0.70						
			Estd.	-0.214	-0.598	0.0125	0.010	0.56	0.58					
	0.25	9.02	Heuristic	123		-0.216	-0.600	0.019	0.012	0.52	0.52			
			Auto- mated		Range	-0.220	-0.603	0.005	0.005	0.40	0.40			92
					to	to	to	to	to	to				
					-0.212	-0.594	0.030	0.025	0.70	0.70				
					Estd.	-0.215	-0.599	0.018	0.010	0.58	0.56			
					Heuristic		-0.216	-0.600	0.020	0.012	0.53	0.53		
27.01		Automated	Range	-0.219	-0.604	0.005	0.005	0.40	0.40					
			to	to	to	to	to	to						
			-0.212	-0.595	0.030	0.025	0.70	0.70						
			Estd.	-0.216	-0.602	0.018	0.011	0.54	0.53					

^aOther parameters used in the simulations are: Electroactive area of wax-treated Teflon-sealed BDD electrode, $A_{2.5 \text{ mM}} = 1.5 \times 10^{-2}$, $A_{1.0 \text{ mM}} = 3.3 \times 10^{-2}$, $A_{0.5 \text{ mM}} = 4.7 \times 10^{-2}$, $A_{0.25 \text{ mM}} =$

$4.3 \times 10^{-2} \text{ cm}^2$, $D = 2.9 \times 10^{-6} \text{ cm}^2 \text{ s}^{-1}$, $T = 295 \text{ K}$, $v_{2.5 \text{ mM}} = 0.077 \text{ V s}^{-1}$, $v_{1.0 \text{ mM}} = 0.073 \text{ V s}^{-1}$, $v_{0.5 \text{ mM}} = 0.073 \text{ V s}^{-1}$, $v_{0.25 \text{ mM}} = 0.073 \text{ V s}^{-1}$, $\Delta E = 80 \text{ mV}$, $f = 9.02 \text{ or } 27.01 \text{ Hz}$. Estd. = estimated

^b values vary due to slight difference in electrode arrangement in cell and electrode area.

In the case of the Teflon-sealed electrode, the electroactive area ($A = 3.3 \times 10^{-2} \text{ cm}^2$) after wax treatment was approximately half that of the untreated electrode ($A = 7.1 \times 10^{-2} \text{ cm}^2$). Both $\alpha\text{-[S}_2\text{W}_{18}\text{O}_{62}]^{4-/5-}$ and $\alpha\text{-[S}_2\text{W}_{18}\text{O}_{62}]^{5-/6-}$ still provided access to the aperiodic DC and first to sixth AC harmonics for simulation-experiment comparisons. As expected, $E_{\text{app1}}^{0'} = -0.216 \text{ V}$ and $E_{\text{app2}}^{0'} = -0.600 \text{ V}$ again are close to the values estimated at GC, Au and Pt electrodes ²⁵. With this masked electrode configuration, excellent simulated versus experimental data agreement was achieved heuristically at both 9.02 and 27.01 Hz as shown in Figure 5 for reduction of 1.0 mM $\alpha\text{-[S}_2\text{W}_{18}\text{O}_{62}]^{4-}$. Heuristically estimated $k_{\text{app}}^{0'}$ values are now $k_{\text{app1}}^{0'} = 0.0072$, $k_{\text{app2}}^{0'} = 0.0050$ and $k_{\text{app1}}^{0'} = 0.0075$, $k_{\text{app2}}^{0'} = 0.0055 \text{ cm s}^{-1}$ at 9.02 Hz and 27.01 Hz, respectively. α'_{app1} and α'_{app2} were 0.54 and 0.51, and 0.52 and 0.51 at 9.02 and 27.01 Hz, respectively. These values of $k_{\text{app}}^{0'}$ and α'_{app} , as with the wax treated glass-sealed BDD electrode provide equally acceptable fits to all harmonics and are independent of frequency. However, a small, but reduced level of asymmetry not accommodated by Butler-Volmer theory again is found in the reduction and oxidation components for the second process. For this reason, with the wax-treated Teflon-sealed BDD electrode, parameters derived from the automated data optimisation method still differ slightly from those obtained by the heuristic method (see Table 4). In a statistical sense, a substantial increase in the LS percentages to values approaching 90%, when the sp^2 bonded carbon rich edge is removed, reflects the significantly improved agreement between theoretical and experimental data achieved at the wax masked electrode. Importantly, the $k_{\text{app}}^{0'}$ values at both the wax-treated Teflon-sealed and

glass-sealed BDD electrodes also are now similar. The only detail now not in agreement with simulations of the model based on Butler-Volmer theory is the dependence of $k_{app}^{0'}$ on concentration. $k_{app}^{0'}$ increases as the concentration of $\alpha\text{-[S}_2\text{W}_{18}\text{O}_{62}]^{4-}$ decreases, as shown by the data summarized in Table 4 and SI 2 and by results displayed in Figures S2, S3 and S4. For example, for the wax-treated Teflon-sealed BDD (heuristic analysis) frequency = 9.02 Hz, the $k_{app1}^{0'}$ and $k_{app2}^{0'}$ values increase from 0.0072 cm s⁻¹ and 0.0050 cm s⁻¹ to 0.013 cm s⁻¹ and 0.010 cm s⁻¹ on decreasing the concentration from 1.0 to 0.50 mM.

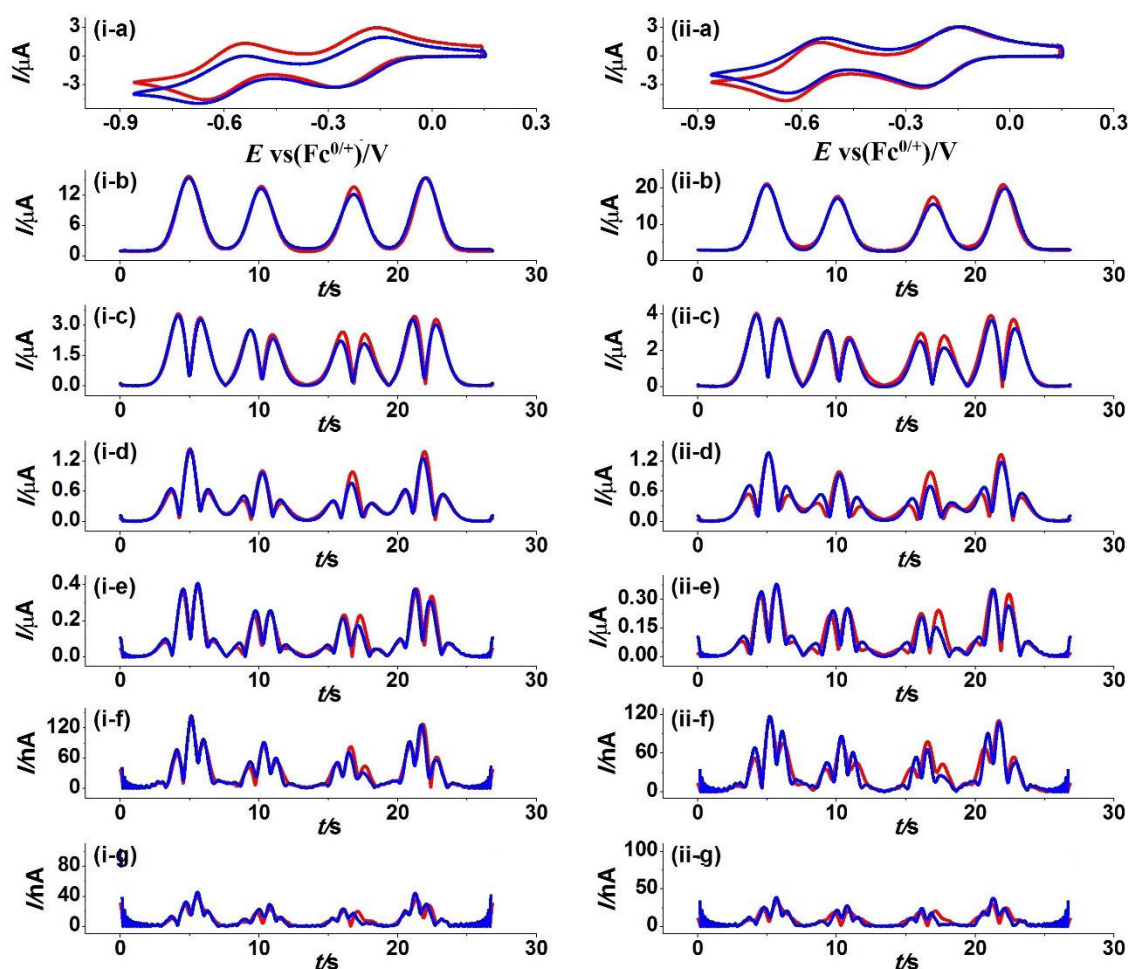


Figure 5. Heuristically based comparison of simulated (red) and experimental (blue) AC voltammetric data obtained with $\Delta E = 80$ mV, $f =$ (i) 9.02 and (ii) 27.01 Hz, $A = 3.3 \times 10^{-2}$ cm² and $v = 0.073$ V s⁻¹ for the $\alpha\text{-[S}_2\text{W}_{18}\text{O}_{62}]^{4-/-5-/-6-}$ processes derived from reduction of

1.0 mM α -[S₂W₁₈O₆₂]⁴⁻ in CH₃CN (0.50 M [*n*-Bu₄N][PF₆]) at a wax-treated Teflon-sealed BDD electrode. (a) DC component, (b-g) 1st to 6th harmonic components. Other parameters used in simulation are provide in Table 4.

FTAC voltammetric data analysis at an edge plane graphite electrode. The presence of sp² bonded carbon at the edge of what should be a purely sp³ - based BDD electrode has been hypothesised to be the reason why analysis of the electron transfer kinetics is compromised. High resolution transmission electron microscopy has revealed that the sp² bonded carbon, which originates from the laser cutting procedure, consists of highly ordered graphite layers and amorphous carbon ²³. To establish the electrode kinetics that apply at sp² bonded carbon only, FTAC voltammetric measurements of the α -[S₂W₁₈O₆₂]^{4-/5-/6-} processes in CH₃CN (0.50 M [*n*-Bu₄N][PF₆]) at an edge plane graphite (EPG) electrode were undertaken. As shown in Figure 6, excellent agreement between the simulated and experimental data for the DC and first to sixth harmonic components was obtained at frequencies of 9.02 and 27.01 Hz with $E_{app}^{0'}$ and the kinetic parameters summarized in Table 5. Significantly, the peak currents in the higher order harmonics for the second reduction process are now slightly larger than the first, a feature also found with glass-sealed BDD electrode (Figure 2), prior to masking of the edge region with wax. This translates into $k_{app2}^{0'}$ being greater than $k_{app1}^{0'}$, again a feature of the outcome of data analysis with the glass-sealed BDD electrode.

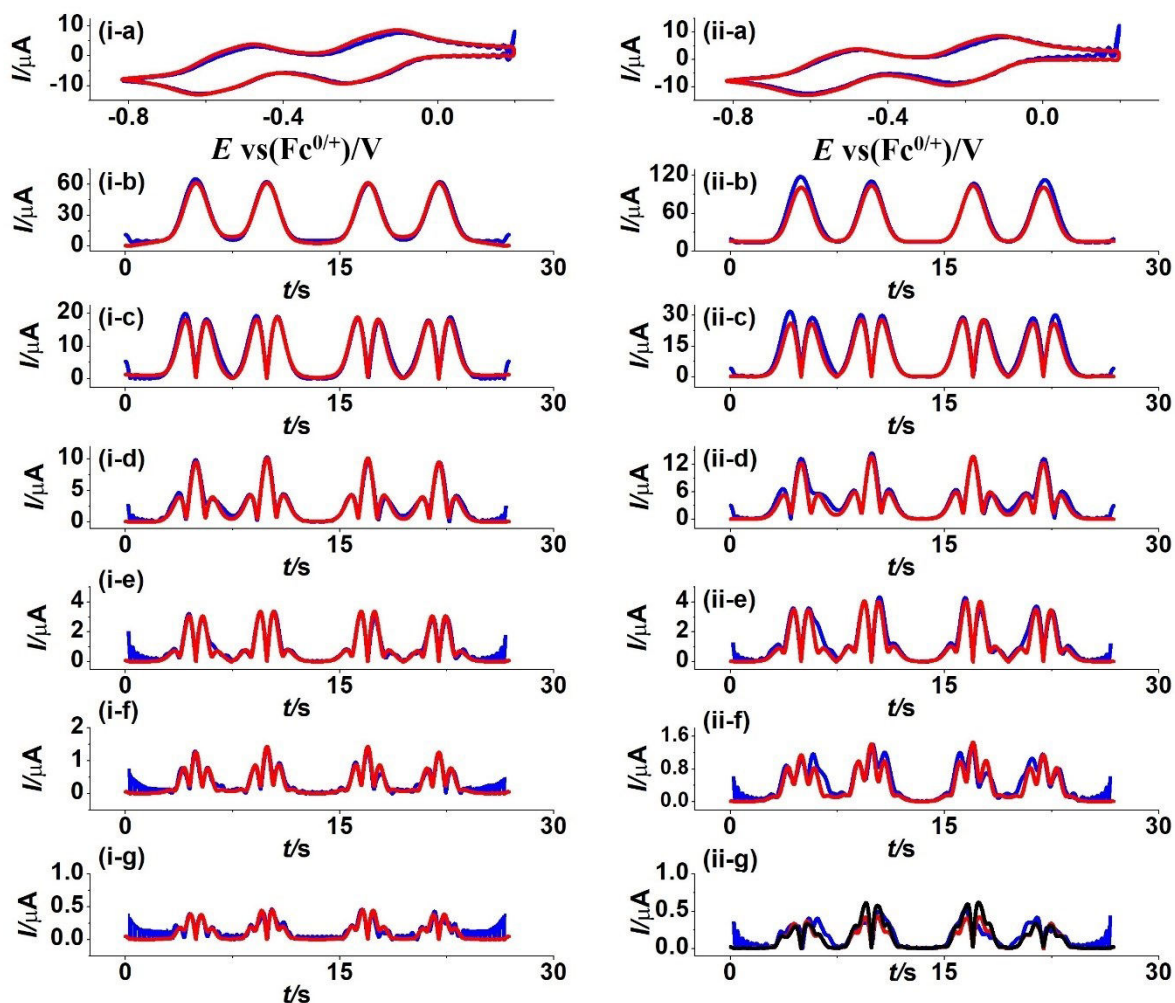


Figure 6. Heuristically based comparison of simulated (red) and experimental (blue) AC voltammetric data obtained with $\Delta E = 80$ mV, $f =$ (i) 9.02 and (ii) 27.01 Hz, $A = 3.8 \times 10^{-2}$ cm² and $\nu = 0.076$ V s⁻¹ for the α -[S₂W₁₈O₆₂]^{4-/-5-/6-} processes derived from reduction of 2.5 mM α -[S₂W₁₈O₆₂]⁴⁻ in CH₃CN (0.50 M [*n*-Bu₄N][PF₆]) at an EPG electrode. (a) DC component, (b-g) 1st to 6th harmonic components and (ii-g) comparison with simulated 6th harmonic component based on a reversible process (black line) where $k_{app2}^{0'} = 1000$ cm s⁻¹ was used to obtain simulated data. Other parameters used in simulation are provided in Table 5.

Table 5. Parameters^a derived from heuristic and computational data analysis for the reduction of 2.5 mM α -[S₂W₁₈O₆₂]⁴⁻ in CH₃CN (0.50 M [*n*-Bu₄N][PF₆]) at an EPG electrode.

<i>f</i> (Hz)	Simulation method	<i>Ru</i> (Ω)		E_{app1}^0	E_{app2}^0	k_{app1}^0	k_{app2}^0	α_{app1}	α_{app2}	LS %	
				V vs Fe ^{0/+}		cm s ⁻¹					
9	Heuristic	115		-0.215	-0.593	0.06	≥0.10 ^b	0.55	0.56 ^b		
	Automated		Range searched	-0.218	-0.596	0.045	0.075	0.40	0.40		
				-0.212	-0.589	0.090	0.125	0.70	0.70		
				Estd.	-0.213	-0.593	0.065	0.107 ^c	0.59	0.58 ^c	84
Heuristic		-0.215	-0.593	0.06	0.10	0.53	0.58				
27	Automated	115	Range	-0.216	-0.596	0.045	0.075	0.40	0.40		
				-0.210	-0.590	0.090	0.135	0.70	0.70		
				Estd.	-0.213	-0.592	0.064	0.097	0.60	0.63	84

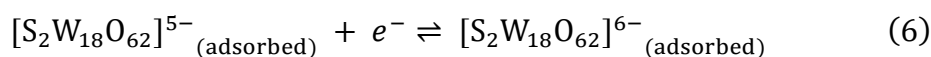
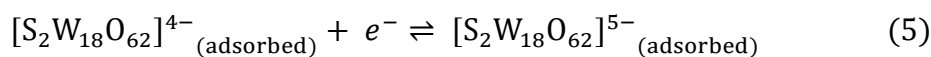
^a Other parameters used in the simulations were: $A = 3.8 \times 10^{-2}$ cm², $D = 2.9 \times 10^{-6}$ cm² s⁻¹, $T = 295$ K, $\nu = 0.076$ V s⁻¹, $\Delta E = 80$ mV, $f = 9.02, 27.01$ Hz. Estd. = estimated.

^b to close to reversible limit to be estimated

^c too close to reversible limit to be reliably estimated (see text for details)

At the EPG electrode, $k_{app1}^{0'}$ and $k_{app2}^{0'}$ were found to be 0.06 and ≥ 0.10 cm s⁻¹, respectively at 9.02 Hz, with the kinetics for the second process being too close to the reversible limit to allow quantification. However, $k_{app2}^{0'}$ could be determined as 0.10 cm s⁻¹ at the higher frequency of 27.01 Hz, which is comparable to the value obtained at GC.²⁵ On this shorter measurement timescale, $k_{app2}^{0'}$ is now significantly below the reversible limit, as indicated in Figure 6ii-g. The fact that $k_{app2}^{0'} > k_{app1}^{0'}$ at the EPG electrode, as found with the glass-sealed BDD electrode, implies that graphite-like sp² bonded carbon present at the edge of this electrode contributes to the non-ideal behaviour. An explanation for why this outcome is not detected with the Teflon-sealed electrode is provided below.

DC Cyclic voltammetry of surface confined α -[S₂W₁₈O₆₂]⁴⁻ at EPG, wax treated and untreated glass- and Teflon-sealed BDD electrodes. POMs are known to adsorb irreversibly on GC and metal surfaces^{25,41-43}. Due the BDD oxygen-terminated surface chemistry, low levels of surface adsorption are observed (albeit species dependant)⁹, relative to sp² bonded forms of carbon. To test the extent to which the POM, α -[S₂W₁₈O₆₂]⁴⁻, is adsorbed onto BDD and EPG, dipping experiments were undertaken following the procedure described in the Experimental Section in the Supporting Information. Figure S5 shows DC CVs obtained from surface-confined α -[S₂W₁₈O₆₂]⁴⁻ with EPG, glass-sealed BDD and Teflon-sealed BDD electrodes with and without the wax treatment. Prior to measurement these electrodes had been dipped into a CH₃CN (0.50 M [*n*-Bu₄N][PF₆]) solution containing 2.5 mM α -[S₂W₁₈O₆₂]⁴⁻, removed and voltammetrically scanned in background electrolyte containing MeCN only. Two well-defined surface confined processes are present for each electrode configuration as describe by Equations 5 and 6.



The dipping experiments confirm that α -[S₂W₁₈O₆₂]⁴⁻ spontaneously and irreversibly adsorbs onto the BDD electrode surfaces as shown previously with GC electrodes²⁵. However, the current density (*i* / μ A cm⁻²) at the BDD electrodes is much smaller than at the sp² bonded carbon rich EPG electrode. The surface concentrations calculated for α -[S₂W₁₈O₆₂]⁴⁻ are 2.3 $\times 10^{-10}$, 3.3 $\times 10^{-11}$ and 1.1 $\times 10^{-12}$ mol cm², respectively at the EPG, glass-sealed BDD and Teflon-sealed BDD electrodes. The surface concentration for α -[S₂W₁₈O₆₂]⁴⁻ at GC is 1.2 $\times 10^{-11}$ mol cm² estimated from the CV data published previously²⁵. The adsorption of α -[S₂W₁₈O₆₂]⁴⁻ on BDD, especially the glass-sealed one, was significantly suppressed after wax treatment (Figure S5c). The double layer capacitance value determined at -0.10 V is ~ 10 μ F

cm⁻² on the masked BDD electrodes, which is close to that found on high quality BDD²¹. These results demonstrate that the sp² bonded carbon rich edge of the BDD electrodes used in these studies is more prone to α -[S₂W₁₈O₆₂]⁴⁻ adsorption than the central region, which consists of sp³-based BDD. Irreversible adsorption of α -[S₂W₁₈O₆₂]⁴⁻ could be one possible origin of the concentration dependence of $k_{app}^{0'}$ at BDD. However, the fact GC, which displays much greater level of adsorption, does not display concentration dependence²¹, means other factors must be considered, and are discussed below.

DISCUSSION

The thermodynamics and electrode kinetics associated with the α -[S₂W₁₈O₆₂]^{4-/5-/6-} processes have been investigated by FTAC voltammetry at BDD electrodes. With use of the Butler-Volmer model of electron transfer, slower electron transfer kinetics are found for both electron transfer processes at BDD compared to EPG and GC. Slower electron transfer kinetics at BDD compared to GC were also found for the reduction of other POMs^{17,19}. Smaller $k_{app}^{0'}$ values at BDD electrodes, compared to other electrode materials, have also been found for the [Ru(NH₃)₆]^{3+/2+} and FcTMA⁺²⁺ electron transfer processes and were attributed to the potential-dependant low density of states (DOS) of BDD¹⁹. However, for reduction of α -[S₂W₁₈O₆₂]⁴⁻, this correlation does not follow as although Pt has a DOS at least three orders of magnitude higher than BDD^{18,19}, the $k_{app}^{0'}$ values at Pt and BDD are similar.²⁵ This suggests that the POM processes are inner- rather than outer- sphere and the POM-electrode interaction is likely to be a significant factor contributing to the electrode material dependent $k_{app}^{0'}$. Double layer effects, which are also predicted to be electrode material dependent, are probably less important.

Clearly, an important feature of BDD electrodes complicating data analysis is the sp³/sp² carbon ratio. For this POM, the sp³-bonded carbon in BDD gives rise to sluggish kinetics while the sp² bonded carbon impurity provides much more facile kinetics⁴⁴. Faster

kinetics (Figure 6 and Table 5) at the sp^2 bonded carbon based EPG, and GC, electrodes²⁵ support this hypothesis. The unexpected order $k_{app1}^{0'} < k_{app2}^{0'}$ found at the glass-sealed BDD electrode (Figure 2) is also a consequence of an appreciable level of graphite-like sp^2 carbon present at the exposed edge of this electrode, of the same order as also observed at the EPG electrode.

Although the BDD growth conditions such as time, pressure, temperature, gas composition (hydrogen to boron and carbon ratios) and addition of noble gas (argon)⁴⁵ have been controlled to minimise sp^2 bonded carbon impurity levels,^{8,46} they are introduced at the sidewalls and edge of the BDD electrode during the laser cutting process⁴⁷. All, or at least the vast majority of sp^2 bonded carbon content is masked when freshly sealed in the borosilicate glass capillary or Teflon sleeve. However, the sp^2 bonded carbon rich edges/sidewalls are prone to exposure by polishing with abrasive material e.g. alumina powder in order to clean the electrode. This is as a result of the softer Teflon and glass sleeves being mechanically removed at the expense of the extremely hard BDD. Hence, the sp^2 bonded carbon content on the exposed edge will vary from electrode to electrode dependant on e.g. fabrication procedure, number of times alumina polished etc. This is unless the edges are masked, as in this study, or thermal oxidation procedures have been employed, prior to sealing, to remove any sp^2 bonded carbon²³.

Variable sp^2 bonded carbon levels lead to non-conformance to the Butler-Volmer model of electron transfer for the α -[S₂W₁₈O₆₂]^{4-/5-/6-} processes, as only a single $k_{app}^{0'}$ value is included in the model to describe each electron transfer step, rather than two $k_{app}^{0'}$ values as required to treat electron transfer at both the sp^3 and sp^2 bonded carbon²⁴. In the present study, the Teflon-sealed BDD is larger in diameter than the glass-sealed one, so the edge to non-edge

ratio is smaller and hence the impact of sp^2 -bonded carbon is less. The $k_{app2}^{0'} > k_{app1}^{0'}$ outcome can also be seen as a fingerprint for appreciable levels of sp^2 bonded carbon contributing to the BDD electrochemistry. $k_{app1}^{0'} = 0.06 < k_{app2}^{0'} = \geq 0.10 \text{ cm s}^{-1}$ values determined at the pure graphite (sp^2 carbon) EPG electrode (Figure 6) are consistent with the hypothesis that sp^2 bonded carbon induced the $k_{app1}^{0'} < k_{app2}^{0'}$ pattern at the glass-sealed BDD.

Upon masking the edge of the BDD electrodes with wax, significantly improved simulation-experiment agreement with FTAC voltametric data modelled using the Butler-Volmer relationship is achieved for the α -[S₂W₁₈O₆₂]^{4- /5- /6-} processes in CH₃CN (0.50 M [n-Bu₄N][PF₆]). $k_{app}^{0'}$ values are now essentially frequency independent and close to being independent of the BDD electrode sealing and data analysis methods employed. Nevertheless, a non-predicted feature of the model remains in that estimated $k_{app}^{0'}$ values decrease with increasing concentration. A similar observation has been reported for other studies using BDD electrodes^{48,49}. Such effects have been attributed to Ohmic drop,⁴⁸ or a (potential-dependant) reduced DOS for BDD compared to sp^2 bonded carbon and metal electrodes.⁴⁹ The latter will manifest as an Ohmic drop-like effect, as the more the electrode is challenged to turn over electroactive species i.e. the higher the analyte concentration, the harder this process becomes due to the limited charge carrier availability. Pt electrodes which have a higher electrical conductivity and DOS, do not exhibit this concentration effect²⁵.

To investigate the plausibility of charge carrier limitations being the origin of the concentration dependence, FTAC voltammetric measurements of the oxidation of Fc to Fc⁺ (Fc = ferrocene), which is considered an outer sphere electron transfer process⁵⁰, with a wax-sealed Teflon-coated BDD electrode in CH₃CN (0.50 M [n-Bu₄N][PF₆]). Fc concentrations of 0.10 and 1.0 mM were chosen to mimic the current densities produced with α -[S₂W₁₈O₆₂]⁴⁻ processes over the concentration range used in the POM study (see Table 4). Excellent FTAC

voltametric theory-experiment agreement was observed for both Fc concentrations (Figure S6 and Table S1) using a frequency of 27.05 Hz, but as for the POM electrochemistry, concentration dependant $k_{app}^{0'}$ values of 0.042 and 0.030 cm s⁻¹ for 0.10 and 1.0 mM Fc were obtained, respectively. In this Fc^{0/+} electrode kinetic study, the process at BDD is again significantly slower than at GC and indeed also at Pt for this outer sphere reaction⁵⁰. Nevertheless, the Fc^{0/+} process was still sufficiently fast. Consequently, values of $k_{app}^{0'}$ for this process were quantified using a frequency of 27.05 Hz instead of 9.02 Hz.

The role of irreversible adsorption of POM and strong redox level ion pairing are also factors that may need to be considered, particularly when coupled with slow electron transfer at BDD electrodes. Such phenomena could contribute to unequal conformance of the modelled and experimental reductive and oxidative data components for the BDD electrodes.

CONCLUSION

Experimental data associated with the α -[S₂W₁₈O₆₂]^{4-/5-} and α -[S₂W₁₈O₆₂]^{5-/6-} electron transfer processes at both glass-sealed BDD and Teflon-sealed BDD electrodes in CH₃CN containing 0.50 M [*n*-Bu₄N][PF₆] as the supporting electrolyte was obtained using FTAC voltammetry. Neither processes fully conformed with simulated data based on the Butler-Volmer relationship and planar diffusion using both heuristic or automated data optimisation methods of data analysis. Furthermore, AC harmonic and frequency dependent $k_{app}^{0'}$ and α'_{app} values were obtained in disagreement with the theoretical model. Discrepancies were hypothesised to be the result of a sp² bonded carbon edge/sidewall rich region which has faster electrode kinetics than in the central purely sp³ bonded carbon area of the electrode.

By simply masking the edge of the BDD electrodes with wax, the harmonic and frequency dependence was removed, and concomitantly a significant improvement in

agreement of simulated and experiment data was achieved. $k_{app}^{0'}$ values at the sp^3 bonded carbon BDD electrode surface, after removal of the sp^2 bonded carbon electrode region, became almost equal for both the glass and Teflon sealed BDD electrodes and significantly decreased in magnitude. The electrode kinetics at BDD were much slower than obtained with sp^2 bonded carbon electrodes such as GC and EPG, but were of a similar magnitude compared to Pt²⁵. For the wax treated glass-sealed and Teflon-sealed BDD electrodes, and as for GC and metal electrodes²¹, $k_{app2}^{0'} < k_{app1}^{0'}$. In contrast parameterisation of data obtained with the untreated glass-sealed BDD electrode produced the inverse order $k_{app2}^{0'} > k_{app1}^{0'}$, which also was found at EPG. This apparently anomalous feature at the glass not Teflon sealed electrode is attributed to a higher ratio of graphite-like sp^2/sp^3 bonded carbon for the smaller area glass-sealed BDD electrode. Importantly, parameterisation of the thermodynamic parameter $E_{app}^{0'}$ was robustly independent of the nuances in the electrode kinetic evaluations.

Despite the improved conformance to the Butler-Volmer model of electron transfer with mass transport by planar diffusion, the wax-sealed BDD electrodes provided concentration dependent $k_{app}^{0'}$ values for the α -[S₂W₁₈O₆₂]^{4-/-5-/-6-} processes. Since the outer-sphere Fc^{0/+} electron transfer processes also displays a concentration dependent $k_{app}^{0'}$ value, a component of the residual non-conformance to the theory was attributed to the limited charge carrier density associated with BDD, which became progressively challenged as the concentration of electroactive species increased. Other plausible reasons for a concentration dependence may be adsorption and non-separation of ion pairing and electron transfer. The voltammetry of α -[S₂W₁₈O₆₂]⁴⁻ and other POMs were found to be consistent with an inner-sphere process involving POM interactions with the electrode surface. Weaker irreversible adsorption of POMs occurs at BDD, compared to sp^2 bonded carbon with the extent of surface confinement in dipping experiments being EPG > BDD.

To advance this work considerably more sophisticated data analysis methods would be needed. A major issue is that additional unknown variables would need to be parameterised, meaning that decisions on whether a better fit to data is achieved cannot be solely based on LS values. Limitations and future prospects for modelling complex voltammetric mechanisms in machine learning and Bayesian frameworks have been considered in a recent opinion article by one of the authors⁵¹ However, the conclusions derived from this study are likely to be generally applicable to electrode kinetic investigations at BDD electrodes. Finally, it should be noted that subtle departures of experimental data from that predicated by the model used herein would not be as readily detected if DC cyclic voltammetry had been used instead of the kinetically far more sensitive FTAC voltammetric method.

ASSOCIATED CONTENT

Supporting Information

Experimental details: Description of the fabrication of the wax-treated BDD electrodes (**Figure S1**); Comparison of simulated and experimental FTAC voltammetric data for the α -[S₂W₁₈O₆₂]^{4- /5- /6-} processes derived from reduction of 0.50, 0.25 and 2.5 mM α -[S₂W₁₈O₆₂]⁴⁻ at wax treated Teflon-sealed BDD electrodes (**Figures S2-4**); DC cyclic voltammogram for the surface-confined α -[S₂W₁₈O₆₂]^{4- /5- /6-} reduction processes at EPG, glass-sealed and Teflon-sealed BDD electrodes with or without the wax treatment (**Figure S5**); Comparison of simulated and experimental FTAC voltammetric data for the Fc^{0/+} processes at wax treated Teflon-sealed BDD electrodes (**Figure S6**) and parameters derived from the FTAC voltammetric data for the Fc^{0/+} process (**Table S1**).

AUTHOR INFORMATION

Corresponding Authors

Alan M. Bond - School of Chemistry and ARC Centre of Excellence for Electrochemical Science, Monash University, Clayton, Victoria 3800, Australia; ORCID: orcid.org/0000-0002-1113-5205; Email: alan.bond@monash.edu

Jie Zhang - School of Chemistry and ARC Centre of Excellence for Electrochemical Science, Monash University, Clayton, Victoria 3800, Australia; ORCID: orcid.org/0000-0003-2493-5209; Email: jie.zhang@monash.edu

Authors

Md Anisur Rahman - School of Chemistry, Monash University, Clayton, Victoria 3800, Australia.

Julie V. Macpherson - Department of Chemistry, University of Warwick, Coventry, CV4 7AL, UK. ORCID: orcid.org/0000-0002-4249-8383.

ACKNOWLEDGEMENTS

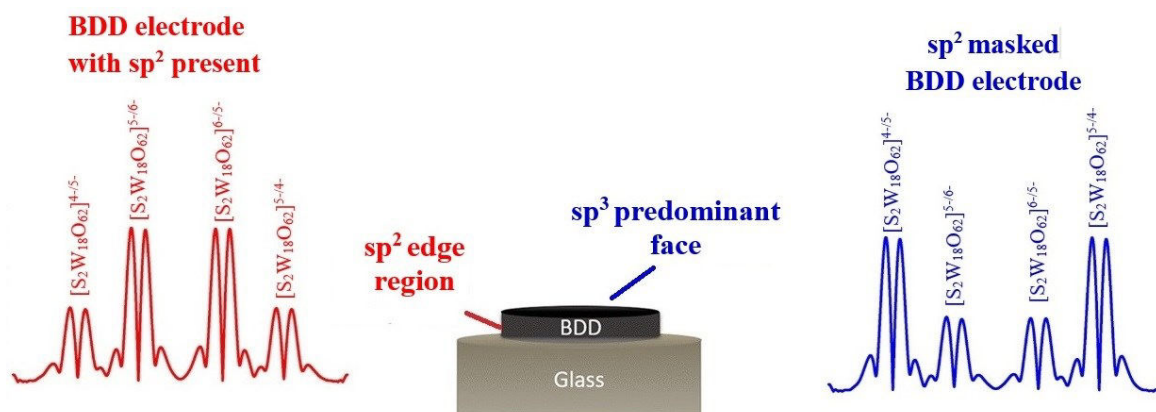
The authors would like to thank the Australian Research Council for financial assistance through a Discovery Program grant. The assistance of Dr Jiezhen Li in the fabrication of the BDD-wax electrodes also is gratefully acknowledged.

REFERENCES

- (1) Chen, R.; Nioradze, N.; Santhosh, P.; Li, Z.; Surwade, S. P.; Shenoy, G. J.; Parobek, D. G.; Kim, M. A.; Liu, H.; Amemiya, S. *Angew. Chem. Int. Ed.* **2015**, *54*, 15134-15137.
- (2) McCreery, R. L. *Chem. Rev.* **2008**, *108*, 2646-2687.
- (3) Ratinac, K. R.; Yang, W.; Gooding, J. J.; Thordarson, P.; Braet, F. *Electroanalysis* **2011**, *23*, 803-826.
- (4) Zhang, W.; Zhu, S.; Luque, R.; Han, S.; Hu, L.; Xu, G. *Chem. Soc. Rev.* **2016**, *45*, 715-752.
- (5) Zhou, M.; Guo, L.-p.; Lin, F.-y.; Liu, H.-x. *Anal. Chim. Acta* **2007**, *587*, 124-131.
- (6) Ambrosi, A.; Chua, C. K.; Bonanni, A.; Pumera, M. *Chem. Rev.* **2014**, *114*, 7150-7188.
- (7) Cobb, S. J.; Ayres, Z. J.; Macpherson, J. V. *Annu. Rev. Anal. Chem.* **2018**.
- (8) Macpherson, J. V. *Phys. Chem. Chem. Phys.* **2015**, *17*, 2935-2949.
- (9) Yang, N.; Yu, S.; Macpherson, J. V.; Einaga, Y.; Zhao, H.; Zhao, G.; Swain, G. M.; Jiang, X. *Chem. Soc. Rev.* **2019**, *48*, 157-204.
- (10) Martin, H. B.; Argoitia, A.; Landau, U.; Anderson, A. B.; Angus, J. C. *J. Electrochem. Soc.* **1996**, *143*, L133-L136.
- (11) Morooka, S.; Fukui, T.; Semoto, K.; Tsubota, T.; Saito, T.; Kusakabe, K.; Maeda, H.; Hayashi, Y.; Asano, T. *Diamond Relat. Mater.* **1999**, *8*, 42-47.
- (12) Sato, Y.; Kamo, M. *Synthesis of diamond from the vapour phase*; Academic Press: London, UK, 1992.
- (13) Alehashem, S.; Chambers, F.; Strojek, J. W.; Swain, G. M.; Ramesham, R. *Anal. Chem.* **1995**, *67*, 2812-2821.
- (14) Swain, G. M.; Ramesham, R. *Anal. Chem.* **1993**, *65*, 345-351.
- (15) Li, J.; Bentley, C. L.; Bond, A. M.; Zhang, J.; Ueda, T. *J. Electroanal. Chem.* **2016**, *779*, 67-74.
- (16) Li, J.; Bond, A. M.; Zhang, J. *Electrochim. Acta* **2015**, *178*, 631-637.
- (17) Li, J.; Guo, S.-X.; Bentley, C. L.; Bano, K.; Bond, A. M.; Zhang, J.; Ueda, T. *Electrochim. Acta* **2016**, *201*, 45-56.
- (18) Patten, H. V.; Meadows, K. E.; Hutton, L. A.; Iacobini, J. G.; Battistel, D.; McKelvey, K.; Colburn, A. W.; Newton, M. E.; Macpherson, J. V.; Unwin, P. R. *Angewandte Chemie-International Edition* **2012**, *51*, 7002-7006.
- (19) Bano, K.; Zhang, J.; Bond, A. M.; Unwin, P. R.; Macpherson, J. V. *J. Phys. Chem. C* **2015**, *119*, 12464-12472.
- (20) Williams, O. *Diamond Relat. Mater.* **2011**, *20*, 621-640.
- (21) Hutton, L. A.; Iacobini, J. G.; Bitziou, E.; Channon, R. B.; Newton, M. E.; Macpherson, J. V. *Anal. Chem.* **2013**, *85*, 7230-7240.
- (22) Li, J.; Bentley, C. L.; Tan, S. Y.; Mosali, V. S.; Rahman, M. A.; Cobb, S. J.; Guo, S.-X.; Macpherson, J. V.; Unwin, P. R.; Bond, A. M. *J. Phys. Chem. C* **2019**.
- (23) Cobb, S. J.; Laidlaw, F. H. J.; West, G.; Wood, G.; Newton, M. E.; Beanland, R.; Macpherson, J. V. *Carbon* **2020**.
- (24) Tan, S.-y.; Unwin, P. R.; Macpherson, J. V.; Zhang, J.; Bond, A. M. *Electrochim. Acta* **2017**, *240*, 514-521.
- (25) Rahman, M. A.; Li, J.; Guo, S.-X.; Kennedy, G.; Ueda, T.; Bond, A. M.; Zhang, J. *J. Electroanal. Chem.* **2019**, 113786.
- (26) Zhang, J.; Bond, A. M.; Richardt, P. J.; Wedd, A. G. *Inorg. Chem.* **2004**, *43*, 8263-8271.
- (27) Rahman, M. A. G., Luke; Ueda, Tadaharu; Bond, Alan M.; Zhang, Jie. *J. Phys. Chem. C* **2020**, submitted.
- (28) Zhang, J.; Bond, A. M.; MacFarlane, D. R.; Forsyth, S. A.; Pringle, J. M.; Mariotti, A. W.; Glowinski, A. F.; Wedd, A. G. *Inorg. Chem.* **2005**, *44*, 5123-5132.
- (29) Zhang, J.; Guo, S.-X.; Bond, A. M. *Anal. Chem.* **2007**, *79*, 2276-2288.
- (30) Kennedy, G. F., 2018.
- (31) Gomez-Gil, J. M.; Laborda, E.; Gonzalez, J.; Molina, A.; Compton, R. G. *J. Phys. Chem. C* **2017**, *121*, 26751-26763.

-
- (32) Liu, Y. P.; Guo, S. X.; Bond, A. M.; Zhang, J.; Geletii, Y. V.; Hill, C. L. *Inorg. Chem.* **2013**, *52*, 11986-11996.
- (33) Bond, A. M.; Duffy, N. W.; Elton, D. M.; Fleming, B. D. *Anal. Chem.* **2009**, *81*, 8801-8808.
- (34) Aoki, K.; Hayashi, K. *J. Electroanal. Chem.* **1995**, *384*, 31-37.
- (35) Kennedy, G. F.; Bond, A. M.; Simonov, A. N. *Curr. Opin. Electrochem.* **2017**, *1*, 140-147.
- (36) Nicholson, R. S. *Anal. Chem.* **1965**, *37*, 1351-1355.
- (37) Fleming, B. D.; Zhang, J.; Bond, A. M.; Bell, S. G.; Wong, L.-L. *Anal. Chem.* **2005**, *77*, 3502-3510.
- (38) Zhang, J.; Guo, S.-X.; Bond, A. M.; Honeychurch, M. J.; Oldham, K. B. *J. Phys. Chem. B* **2005**, *109*, 8935-8947.
- (39) O'Mullane, A. P.; Zhang, J.; Brajter-Toth, A.; Bond, A. M. *Anal. Chem.* **2008**, *80*, 4614-4626.
- (40) Zhang, J.; Guo, S.-X.; Bond, A. M.; Marken, F. *Anal. Chem.* **2004**, *76*, 3619-3629.
- (41) Kuhn, A.; Mano, N.; Vidal, C. *J. Electroanal. Chem.* **1999**, *462*, 187-194.
- (42) Rong, C.; Anson, F. C. *Inorg. Chim. Acta* **1996**, *242*, 11-16.
- (43) Zhang, J.; Ting, B. P.; Koh, Y. T.; Ying, J. Y. *Chem. Mater.* **2011**, *23*, 4688-4693.
- (44) Garcia-Segura, S.; Dos Santos, E. V.; Martínez-Huitle, C. A. *Electrochem. Commun.* **2015**, *59*, 52-55.
- (45) May, P. W.; Mankelevich, Y. A. *J. Phys. Chem. C* **2008**, *112*, 12432-12441.
- (46) Hutton, L. A.; Iacobini, J. G.; Bitziou, E.; Channon, R. B.; Newton, M. E.; Macpherson, J. V. *J. A. c.* **2013**, *85*, 7230-7240.
- (47) Newland, J. C. *The Fabrication and application of diamond sensors for electrochemical analysis in single and multiple phase systems*. University of Warwick 2014.
- (48) Cinková, K.; Batchelor-McAuley, C.; Marton, M.; Vojs, M.; Švorc, L.; Compton, R. G. *Carbon* **2016**, *110*, 148-154.
- (49) Tan, S.-y.; Lazenby, R. A.; Bano, K.; Zhang, J.; Bond, A. M.; Macpherson, J. V.; Unwin, P. R. *Phys. Chem. Chem. Phys.* **2017**, *19*, 8726-8734.
- (50) Sun, P.; Mirkin, M. V. *Anal. Chem.* **2006**, *78*, 6526-6534.
- (51) Bond, A. M. *J. Solid State Electrochem.* **2020**.

TOC:



Supporting Information

Identification of Mechanistic Subtleties that Apply to Voltammetric Studies at Boron Doped Diamond Electrodes: The α -[S₂W₁₈O₆₂]^{4-/5-/6-} Processes

Md Anisur Rahman^a, Julie V. Macpherson^b, Alan M. Bond^{a,c *} and Jie Zhang^{a,c *}

^a School of Chemistry, Monash University, Clayton, Victoria 3800, Australia

^b Department of Chemistry, University of Warwick, Coventry, CV4 7AL, UK.

^c ARC Centre of Excellence for Electrochemical Science, Monash University, Clayton,
Victoria 3800, Australia

* Corresponding Author

TABLE OF CONTENTS

S1: Experimental

S2: Effect of Concentration

S1: Experimental

Reagents and solvents. The α isomer of $[n\text{-Bu}_4\text{N}]_4(\alpha\text{-[S}_2\text{W}_{18}\text{O}_{62}])$ was synthesized as reported by Himeno *et al*^{S1} and kindly supplied by Professor Tadaharu Ueda (Kochi University, Japan). Al_2O_3 (0.3 μm , Buehler), ethanol (99.5%, Ajax Finechem) and acetonitrile (CH_3CN , 99.9%, Sigma-Aldrich) were used as supplied. Ferrocene (Fc, 98%, Sigma-Aldrich), was recrystallized from n-pentane (Merck, EMSURE). Recrystallized^{S2} tetrabutylammonium hexafluorophosphate ($n\text{-[Bu}_4\text{N][PF}_6]$, 98% Sigma-Aldrich) was used as the supporting electrolyte.

Electrochemical instrumentation and procedures. Conventional DC cyclic voltammetric experiments were undertaken with a CHI 760E electrochemical workstation. AC voltammetry employed home built instrumentation^{S3}. In FTAC voltammetric experiments, sinewave perturbations having a frequency of 9.02 or 27.01 Hz and an amplitude of 80 mV were superimposed on to the DC ramp to generate the AC waveform. Fourier transformation of the total current-time data gave the power spectrum. Band filtering followed by inverse Fourier transformation led to resolution of the fundamental, and higher order AC harmonics and aperiodic DC component^{S3}.

All voltammetric experiments were undertaken at 22 ± 2 °C in a small volume electrochemical cell (1.5 ml) using a three-electrode arrangement. Two BDD macrodisk working electrodes were used. The BDD used in the fabrication of both electrodes was grown in the form of a wafer using microwave chemical vapour deposition. The front (growth) face of the BDD wafer, used for electrochemical studies, was mechanically polished, and the required geometry cut using laser micromachining. Working electrode one consisted of a (i) 1.0 mm diameter disk of BDD (Electroanalysis Grade minimal sp^2 bonded carbon content BDD, $\sim 3 \times 10^{20}$ atoms cm^{-3} ^{S4,5}, Element Six, Harwell, UK⁵) laser cut (355 nm Nd:YAG 34 ns

laser micromachinery; E-355H-ATHI-O system, Oxford Lasers) from a 500 μm thick BDD wafer and sealed in glass. Working electrode two comprised a 3.0 mm diameter disk of BDD sealed in Teflon (Windsor Scientific, UK). No information is available on the boron dopant density of this material, although as it is electrochemical grade it will have a boron content above the metallic dopant threshold ($> 10^{20}$ B atoms cm^{-3})^{S6}. For convenience, these electrodes will be described as glass-sealed BDD and Teflon-sealed BDD. A 2.0 mm \times 1.9 mm edge plane graphite macro-electrode (EPG; RS Components, Australia) sealed in Teflon and a 1.0 mm diameter macrodisk GC electrode sealed in Teflon were also used as working electrodes. Prior to each experiment, all electrodes were polished with 0.3 μm Al_2O_3 aqueous slurry, rinsed successively with water and acetone, and then dried under nitrogen flow. Sonication was applied after polishing for several seconds with the Teflon sealed electrodes. Sonication was avoided with the glass sealed electrode due to concerns about glass fragility. Pt wire and Pt wire inside a plastic capillary tube were used as auxiliary and quasi-reference electrodes, respectively. Oxygen was removed by purging with nitrogen for at least five minutes before each experiment.

The electroactive area (A) of the working electrodes was estimated using the peak current (I_p^{ox}) for oxidation of 1.0 mM ferrocene (Fc) to ferrocenium (Fc^+) in acetonitrile (0.10 M [$n\text{-Bu}_4\text{N}$][PF_6]) and use of the Randles-Sevcik equation ^{S7} and the known diffusion coefficient (D) value of 2.4×10^{-5} $\text{cm}^2 \text{s}^{-1}$ for Fc ^{S8} in this electrolyte medium. This equation also was used to calculate D for $\alpha\text{-[S}_2\text{W}_{18}\text{O}_{62}]^{4-}$ ^{S7}, using the reduction peak current (I_p^{red}) at the GC electrode for the initial one electron ($n = 1$) transfer ($\alpha\text{-[S}_2\text{W}_{18}\text{O}_{62}]^{4-/5-}$) process, assuming this process is reversible on the DC voltammetric time scale ^{S9}. Accordingly, the electroactive area of the glass-sealed BDD, Teflon-sealed BDD, GC and edge plane graphite (EPG) electrodes were 8.9×10^{-3} , 7.1×10^{-2} , 8.0×10^{-3} and 3.8×10^{-2} cm^2 respectively and

$D_{\alpha[\text{S}_2\text{W}_{18}\text{O}_{62}]^{4-}} = 2.9 \times 10^{-6} \text{ cm}^2 \text{ s}^{-1}$. The electroactive areas of the wax-treated BDD electrodes also were calculated using the Randles-Sevcik equation and the D value for $\alpha\text{-}[\text{S}_2\text{W}_{18}\text{O}_{62}]^{4-}$. The potential of the quasi-reference electrode was calibrated against the IUPAC recommended $\text{Fc}^{0/+}$ process ^{S10}.

Preparation of wax insulated BDD electrodes. The method of preparing the wax insulated BDD electrodes was based on that published by Li et. al ¹¹. A cap (Figure S1a) with a small hole in the centre was made from melted wax and mounted on the top of a polished BDD electrode (Figure S1b) to ensure the edge of the original surface was not exposed to the solution in electrochemical experiments. Fabrication of the BDD-wax electrode was completed by wrapping with parafilm (Figure S1c and S1d) but leaving the hole uncovered so the BDD in the centre of the electrode can be exposed to solution. Both the wax and parafilm used are insoluble in CH_3CN .

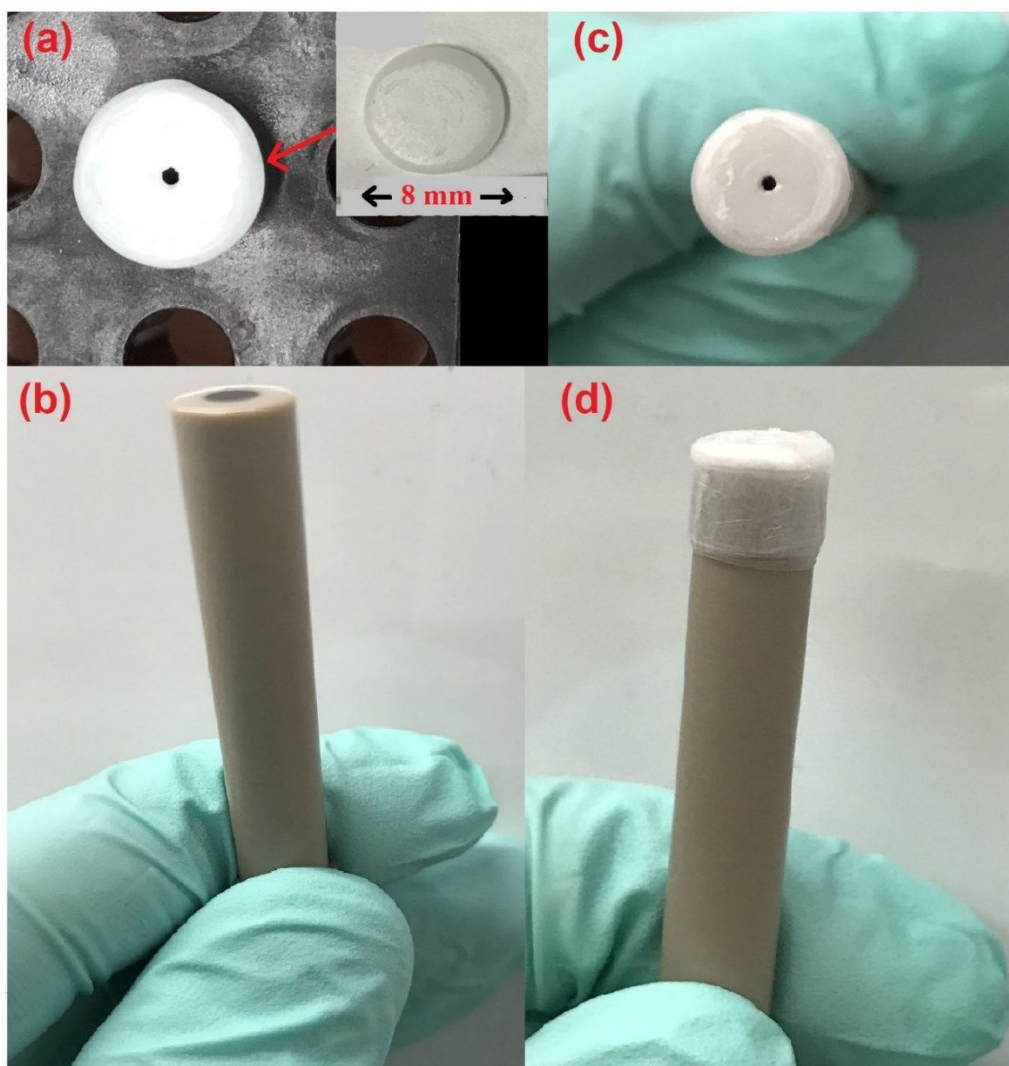


Figure S1. Fabrication of a BDD-wax electrode. (a) Disk shaped wax cap, (b) BDD electrode, (c) and (d) parafilm wrapped BDD-wax electrode.

Surface attachment of α -[S₂W₁₈O₆₂]⁴⁻ on EPG, wax treated and untreated glass- and Teflon-sealed BDD electrodes. Accumulation of α -[S₂W₁₈O₆₂]⁴⁻ onto the EPG, glass- and Teflon-sealed BDD electrodes was achieved by dipping the freshly polished electrodes into a CH₃CN solution containing 2.5 mM α -[S₂W₁₈O₆₂]⁴⁻ and 0.50 M [n-Bu₄N][PF₆]. After five minutes, the electrodes were removed from the solution, washed thoroughly with acetone and dried under nitrogen flow. These surface modified electrodes were then used as working electrodes in electrochemical experiments in CH₃CN (0.50 M [n-Bu₄N][PF₆]).

S2: Effect of Concentration

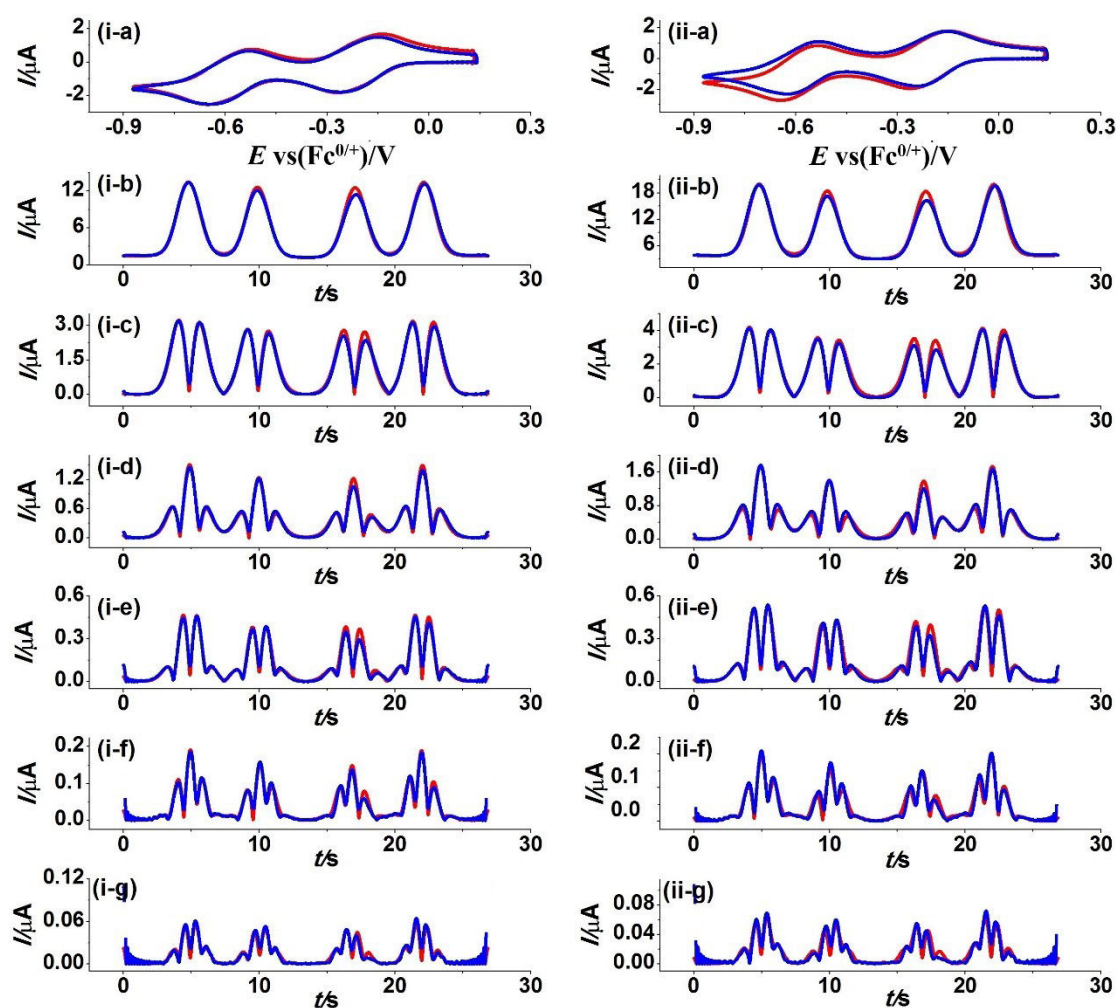


Figure S2. Heuristically based comparison of simulated (red) and experimental (blue) AC voltammetric data obtained with $\Delta E = 80$ mV, $f =$ (i) 9.02 and (ii) 27.01 Hz, $A = 4.7 \times 10^{-2}$ cm² and $\nu = 0.073$ V s⁻¹ for the α -[S₂W₁₈O₆₂]^{4-/-5-/-6-} processes derived from reduction of 0.50 mM α -[S₂W₁₈O₆₂]⁴⁻ in CH₃CN (0.50 M *n*-[Bu₄N][PF₆]) at a wax-treated Teflon-sealed BDD electrode. (a) DC component, (b-g) 1st to 6th harmonic components. Other parameters used in simulation are provide in Table 4.

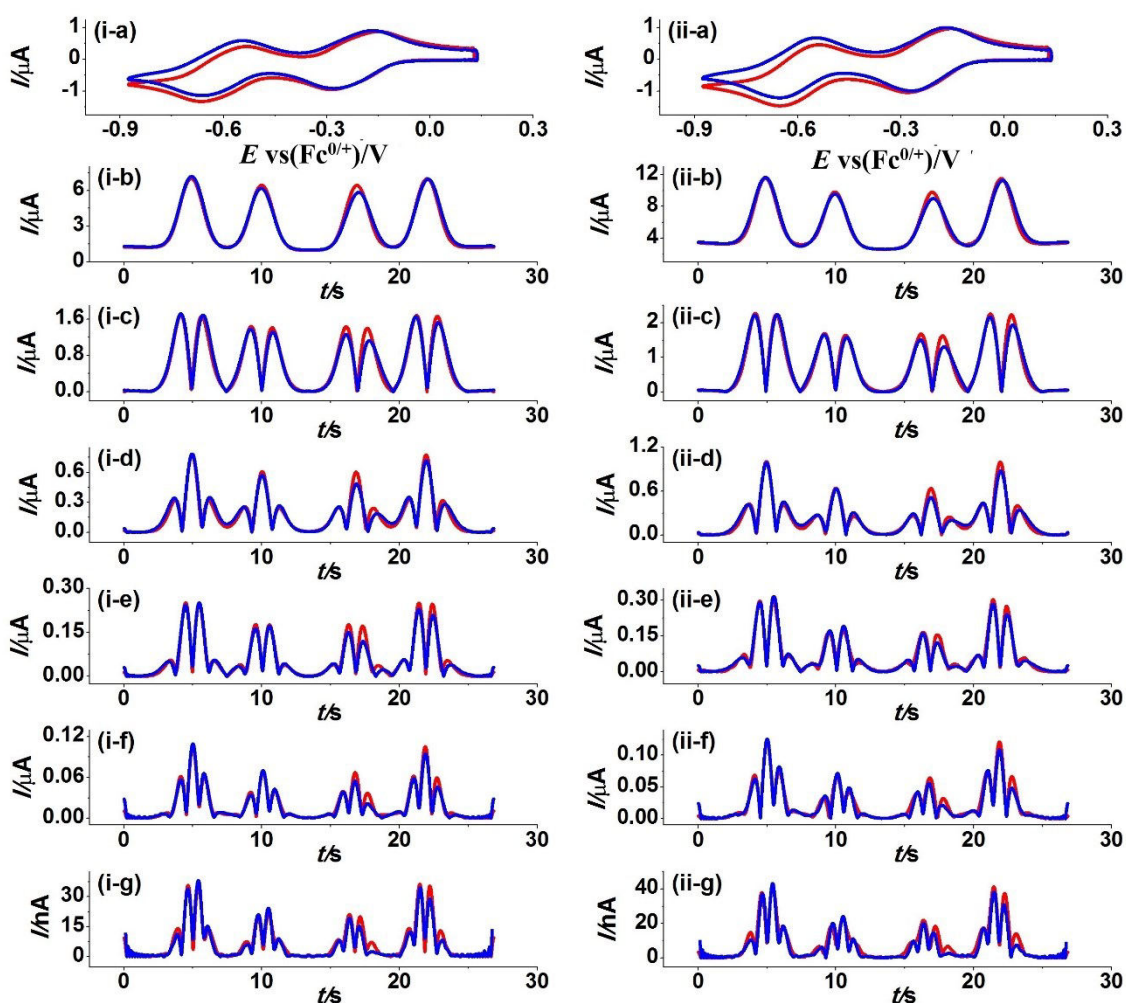


Figure S3. Heuristically based comparison of simulated (red) and experimental (blue) AC voltammetric data obtained with $\Delta E = 80$ mV, $f =$ (i) 9.02 and (ii) 27.01 Hz, $A = 4.3 \times 10^{-2}$ cm² and $\nu = 0.073$ V s⁻¹ for the α -[S₂W₁₈O₆₂]^{4-/-5-/-6-} processes derived from reduction of 0.25 mM α -[S₂W₁₈O₆₂]⁴⁻ in CH₃CN (0.50 M *n*-[Bu₄N][PF₆]) at a wax-treated Teflon-sealed BDD electrode. (a) DC component, (b-g) 1st to 6th harmonic components. Other parameters used in simulation are provide in Table 4.

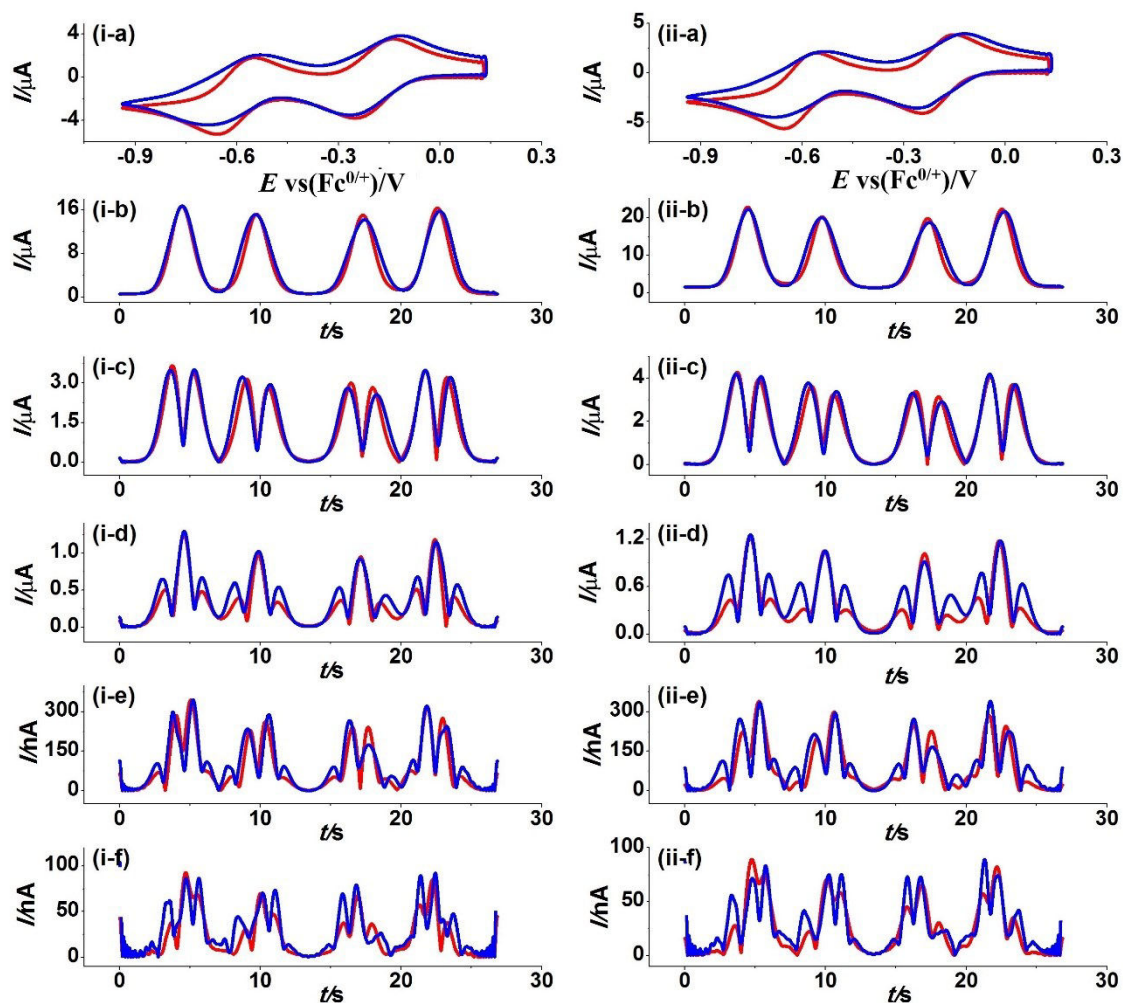


Figure S4. Heuristically based comparison of simulated (red) and experimental (blue) AC voltammetric data obtained with $\Delta E = 80$ mV, $f =$ (i) 9.02 and (ii) 27.01 Hz, $A = 1.50 \times 10^{-2}$ cm² and $v = 0.077$ V s⁻¹ for the α -[S₂W₁₈O₆₂]^{4-/-5-/-6-} processes derived from reduction of 2.5 mM α -[S₂W₁₈O₆₂]⁴⁻ in CH₃CN (0.50 M *n*-[Bu₄N][PF₆]) at a wax-treated Teflon-sealed BDD electrode. (a) DC component, (b-g) 1st to 6th harmonic components. Other parameters used in simulation are provide in Table 4.

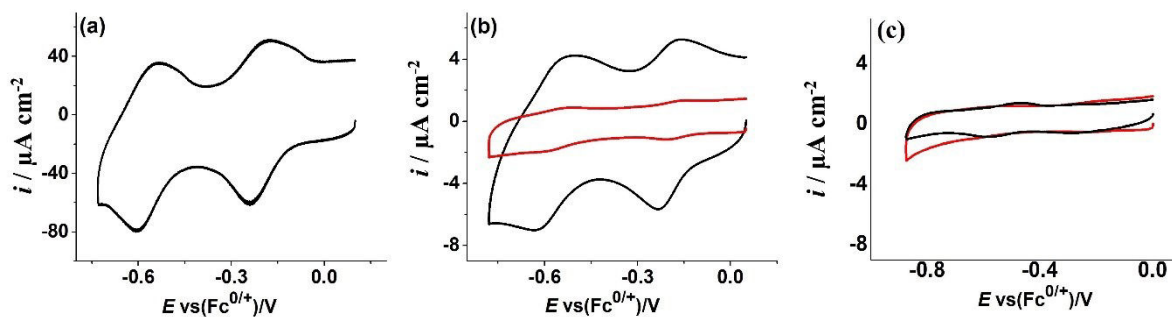


Figure S5. DC cyclic voltammogram obtained at a scan rate of 0.100 V s^{-1} for the surface-confined $\alpha\text{-[S}_2\text{W}_{18}\text{O}_{62}]^{4-/5-/6-}$ reduction processes in CH_3CN ($0.50 \text{ M } [n\text{-Bu}_4\text{N}][\text{PF}_6]$) with (a) EPG (b) glass-sealed BDD (—) and Teflon-sealed BDD (—) and (c) wax treated glass-sealed BDD (—) and Teflon-sealed BDD (—) electrodes.

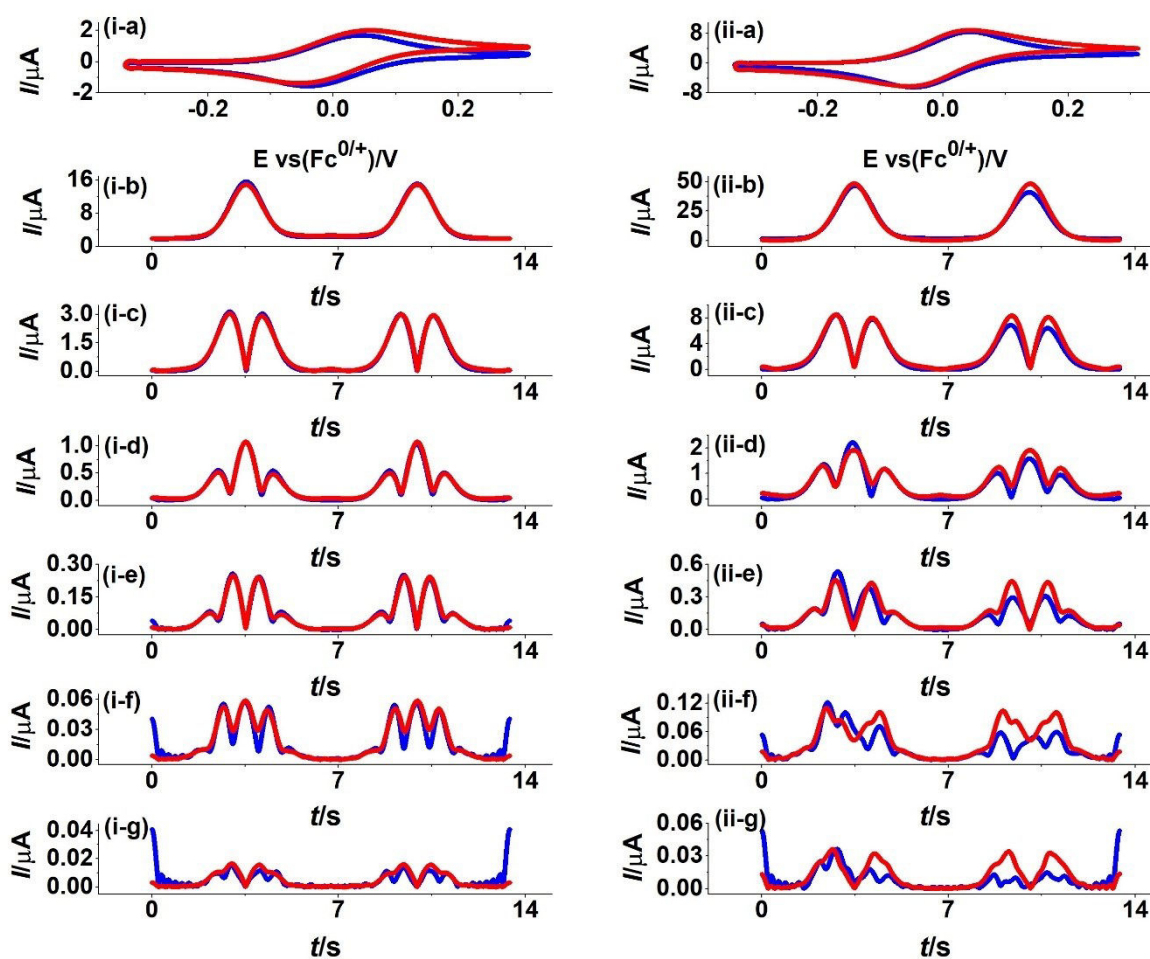


Figure S6. Heuristically based comparison of simulated (red) and experimental (blue) AC voltammetric data obtained with $\Delta E = 80 \text{ mV}$, $f = 27.05 \text{ Hz}$ and $v = 0.097 \text{ V s}^{-1}$ for the $\text{Fc}^{0/+}$ process derived from oxidation of (i) 0.1 and (ii) 1.0 mM Fc in CH_3CN (0.10 M $n\text{-}[\text{Bu}_4\text{N}][\text{PF}_6]$) at a wax-treated Teflon-sealed BDD electrode. (a) DC component, (b-g) 1st to 6th harmonic components. Other parameters used in simulation are provide in Table S1.

Table S1. Parameters^a derived from a heuristic comparison of simulated and experimental FTAC voltammetric data for the $\text{Fc}^{0/+}$ process in CH_3CN containing 0.10 M $[\text{n-Bu}_4\text{N}][\text{PF}_6]$ using a frequency of 27.05 Hz with a wax-treated Teflon-sealed BDD electrode

Conc. (mM)	R_u (Ω)	$E^{0'}$ (V vs $\text{Fc}^{0/+}$)	$k^{0'}$ (cm s^{-1})	α
0.10	603	0.000	0.042	0.50
1.0	497	0.000	0.030	0.50

^aOther parameters used in the simulations were: $A_{0.1\text{mM}} = 5.0 \times 10^{-2} \text{ cm}^2$, $A_{1.0\text{mM}} = 2.4 \times 10^{-2} \text{ cm}^2$, $D = 2.4 \times 10^{-5} \text{ cm}^2 \text{ s}^{-1}$, $T = 295 \text{ K}$, $v = 0.097 \text{ V s}^{-1}$, $\Delta E = 80 \text{ mV}$, $f = 27.05 \text{ Hz}$.

References

- (S1) Himeno, S.; Tatewaki, H.; Hashimoto, M. *Bull. Chem. Soc. Jpn.* **2001**, *74*, 1623-1628.
- (S2) Sawyer, D.; Sobkowiak, A.; Roberts Jr, J. *Electrochemistry for Chemists*, ; John Wiley&Sons, 1995.
- (S3) Bond, A. M.; Duffy, N. W.; Guo, S.-X.; Zhang, J.; Elton, D.; ACS Publications, 2005.
- (S4)
- (S5) Hutton, L. A.; Iacobini, J. G.; Bitziou, E.; Channon, R. B.; Newton, M. E.; Macpherson, J. V. *Anal. Chem.* **2013**, *85*, 7230-7240.
- (S6) Macpherson, J. V. *Phys. Chem. Chem. Phys.* **2015**, *17*, 2935-2949.
- (S7) Bard, A. a. F., Larry R. *Electrochemical Methods: Fundamentals and applications*, 2nd ed.; Wiley: New York, 2001.
- (S8) Zhang, J.; Guo, S.-X.; Bond, A. M. *Anal. Chem.* **2007**, *79*, 2276-2288.
- (S9) Rahman, M. A.; Li, J.; Guo, S.-X.; Kennedy, G.; Ueda, T.; Bond, A. M.; Zhang, J. *J. Electroanal. Chem.* **2019**, 113786.
- (S10) Gritzner, G.; Kuta, J. *Pure Appl. Chem.* **1984**, *56*, 461-466.
- (S11) Li, J.; Bentley, C. L.; Tan, S. Y.; Mosali, V. S.; Rahman, M. A.; Cobb, S. J.; Guo, S.-X.; Macpherson, J. V.; Unwin, P. R.; Bond, A. M. *J. Phys. Chem. C* **2019**.

Chapter 4:
**Electrode Material Dependence, Ion-Pairing and the Progressive
Increase in Complexity of the α -
[S₂W₁₈O₆₂]^{4-/5-/6-/7-/8-/9-/10-} Reduction Processes in
Acetonitrile Containing [*n*-Bu₄N][PF₆] as the Supporting
Electrolyte**

Md Anisur Rahman^a, Alan M. Bond^{a, b *} and Jie Zhang^{a, b *}

^a School of Chemistry, Monash University, Clayton, Victoria 3800, Australia

^b ARC Centre of Excellence for Electrochemical Science, Monash University, Clayton,
Victoria 3800, Australia

ABSTRACT

Large amplitude Fourier transform alternating current (FTAC) voltammetry has been used to parameterise the electrode kinetics associated with the reduction of α -[S₂W₁₈O₆₂]⁴⁻ in CH₃CN ([*n*-Bu₄N][PF₆]) at glassy carbon (GC), gold (Au) and platinum (Pt) electrodes by experimenter based heuristic and computer-assisted automated approaches. Electron transfer kinetics estimated at GC are faster than that at the metal electrodes. Progressively increasing departure from ideality in the experimental versus simulated data comparisons were found with reduction processes that occur at more negative potentials and with higher electrolyte concentrations. Ion-pairing between α -[S₂W₁₈O₆₂]⁴⁻ or its reduced forms and the electrolyte cation may contribute to non-conformance between theory and experiment. Electrochemical quartz crystal microbalance experiments along with other cyclic voltammetric experiments reveal that adsorption of reduced species can modify the electrode surface which also can contribute towards the asymmetry in the reduction and oxidation components of the FTAC voltammetric data. Enhanced double layer capacitance at negative potentials also could explain why the level of non-ideality increases with reduction processes at more negative potentials.

Keywords: Fourier transform alternating current voltammetry, polyoxometalate electrochemistry, non-ideality, ion-pairing, adsorption.

1 Introduction

Polyoxometalates (POMs) are negatively charged inorganic oxide clusters having framework structures. In their commonly synthesised form, they are constructed from high oxidation state tungsten (VI), molybdenum (VI), vanadium (V) and other transition metals. As a consequence, their chemical and electrochemical reductive redox chemistry, to generate for example W(VI/V), Mo(VI/V/IV), V(V/IV) containing POM clusters is usually exceptionally rich. Typically, under voltammetric conditions in aprotic solvents they undergo a series of chemically and often electrochemically reversible one electron reduction processes that represent metal based electron transfer reactions [1-3]. However, the electrons may be delocalised over all or part of POM framework rather than being localised on one metal centre [4-6].

The structure of the so-called Wells-Dawson structure of the α isomer of $[\text{S}_2\text{W}_{18}\text{O}_{62}]^{4-}$, which is of interest in this study, is provided in Figure 1. There are many possible isomers of $[\text{S}_2\text{W}_{18}\text{O}_{62}]^{4-}$ [7] but it is assumed the fully symmetrical α structure remains intact during electrochemical reduction.

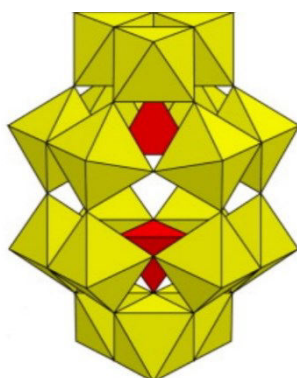


Figure 1. The structure of the α isomer of $[\text{S}_2\text{W}_{18}\text{O}_{62}]^{4-}$. Red and yellow represent the sulphur heteroatom and the tungsten addenda atom, respectively.

This POM contains 18 W(VI) metal centres, each of which in principle can be reduced to W(V) and then to W(IV) if a sufficiently strong chemical reductant is used or a sufficiently negative potential applied under electrochemical conditions. Indeed, in the presence of proton reactions coupled to electron transfer, which significantly facilitates reduction, 26 electrons have been added to the molybdenum analogue $[S_2Mo_{18}O_{62}]^{4-}$ [8]. In aprotic ionic liquids that have a wide potential range in the negative potential region, as needed for the considerably more difficult to be reduced $[S_2W_{18}O_{62}]^{4-}$, 6 well-resolved one electron reduction processes have been reported under DC voltammetric conditions at a glassy carbon (GC) electrode [9]. DC voltammetric studies in the dry organic solvent acetonitrile (CH_3CN) with different supporting electrolytes [10-12], the absence of deliberately added supporting electrolyte and in the presence of 5% water with and without acid also have been reported [9, 11]. These studies have utilised a range of electrode materials and undertaken with stationary, rotated and channel electrode configurations.

Table 1. Formal reversible potentials (E_f^0)^a and other data reported for the reduction of α - $[S_2W_{18}O_{62}]^{4-}$.

Solvent/ electrolyte	Working Electrode ^b	State	E_f^0 (I, II, III, IV, V, VI) ^c	Ref
			V vs $Fc^{0/+}$ (Fc = Ferrocene)	
$CH_3CN/[n-Bu_4N][PF_6]$ (0.10 M)	GC	Dissolved	-0.260, -0.630, -1.195, -1.580, -2.050, -2.380	[13]
Dry $CH_3CN/[n-Bu_4N][PF_6]$ (0.10 M)	GC	Dissolved	-0.245, -0.628, -1.199, -1.595, -2.094, -2.464	[9]
$CH_3CN/[n-Bu_4N][PF_6]$ (0.10 M)	GC	Dissolved	-0.240, -0.620, -1.180, -1.570, -2.020, -2.320	[12]
$CH_3CN/[Bu_4N][ClO_4]$ (0.10 M)	GC	Dissolved	-0.240, -0.620, -1.180, -1.570	[11]
$CH_3CN/H_2O(95:5)/[Bu_4N][ClO_4]$ (0.10 M)	GC	Dissolved	-0.230, -0.590, -1.120, -1.420	[11]
$CH_2Cl_2/[n-Bu_4N][PF_6]$ (0.10 M)	GC	Dissolved	-0.437, -0.802, -1.353, -1.745	[9]
$H_2O/[Et_4N]Cl$ (0.10 M) ^d	GC	Solid	0.02, -0.20, -0.64, -0.89, -1.080, -1.200	[12]
	Au	Solid	0.02, -0.19, -0.63, -0.90	
$[BMIM][PF_6]^c$	GC/Au	Dissolved	0.020, -0.257, -0.720, -1.005, -1.373, -1.628	[9]

		Solid	0.030, -0.253, -0.714, -0.986, -1.362, -1.633	
[EMIM][tfsa] ^f	GC/Au	Dissolved	-0.001, -0.249, -0.701	[9]
		Solid	0.000, -0.252, -0.700, -0.986	
[P1,4][tfsa] ^g	GC/Au	Dissolved	0.023, -0.263, -0.778, -1.120	[9]
		Solid	0.020, -0.262, -0.777, -1.130, -1.530	
[BMIM][BF ₄] ^h	GC/Au	Dissolved	-0.010, -0.287, -0.736, -1.000	[9]
		Solid	0.001, -0.280, -0.728, -0.978	

^a Estimated from the mid-point potential $[(E_p^{\text{red}} + E_p^{\text{ox}})/2]$ derived from DC cyclic voltammograms

^b GC= Glassy Carbon, BDD = boron doped diamond and Au = gold.

^c I, II, III, IV, V and VI refer to α -[S₂W₁₈O₆₂]^{4-/5-}, α -[S₂W₁₈O₆₂]^{5-/6-}, α -[S₂W₁₈O₆₂]^{6-/7-}, α -[S₂W₁₈O₆₂]^{7-/8-}, α -[S₂W₁₈O₆₂]^{8-/9-} and α -[S₂W₁₈O₆₂]^{9-/10-} processes, respectively.

^d values (vs Ag/AgCl) converted to the Fc^{0/+} scale using the Ag/AgCl and Fc^{0/+} standard potentials in aqueous media of 0.212 [14] and 0.44 [15] vs NHE, respectively at 25° C.

^e 1-Butyl-3-methylimidazolium hexafluorophosphate

^f 1-ethyl 3-methylimidazolium bis(trifluoromethane sulfonyl) amide

^g N-butyl-methylpyrrolidinium bis(trifluoromethanesulfonyl) amide

^h 1-Butyl-3-methylimidazolium tetrafluoroborate

Table 1 summarises the formal reversible potentials (E_f^0) derived from analysis of DC cyclic voltammograms for the α -[S₂W₁₈O₆₂]^{4-/5-/6-/7-/8-/9-/10-} processes (designated as I, II, III, IV, V and VI) using a range of electrodes, solvents and electrolyte. Clearly, the solvent plays a critical role and E_f^0 is strongly dependent on polarity [8]. Thus, with respect to molecular solvents, the most negative E_f^0 values (-0.437 V vs Fc/Fc⁺ for process I) were obtained in dichloromethane (least polar solvent used) whereas use of H₂O (most polar solvent used) gives a much more positive E_f^0 value (0.02 V vs Fc/Fc⁺ for process I). Accordingly, since the polarity of CH₃CN lies between that of these two solvents, so do the E_f^0 values. In general, E_f^0 values are also very positive with use of ionic liquids. Moreover, E_f^0 values become more positive with higher electrolyte concentration because of increasing ion-pairing differences

between the electrolyte cation ($[n\text{-Bu}_4\text{N}]^+$) and oxidised (e.g. $\alpha\text{-[S}_2\text{W}_{18}\text{O}_{62}]^{4-}$) and reduced (e.g. $\alpha\text{-[S}_2\text{W}_{18}\text{O}_{62}]^{5-}$) forms. Not surprisingly, the purity of solvent, particularly with respect to water content also is critical [9] with more negative E_f^0 values obtained in carefully dried CH_3CN [12].

The above survey of literature reports implies that all processes associated with DC cyclic voltammetry of $\alpha\text{-[S}_2\text{W}_{18}\text{O}_{62}]^{4-}$ at stationary macrodisc electrodes are ideal chemically and electrochemically reversible or close to reversible processes. However, close inspection of data obtained in acetonitrile containing $[n\text{-Bu}_4\text{N}][\text{PF}_6]$ as the supporting electrolyte, which is the solvent- electrolyte medium of interest in this study show significant departures from ideality under some conditions. Thus, while six well resolved $\alpha\text{-[S}_2\text{W}_{18}\text{O}_{62}]^{4-/5-/6-/7-/8-/9-/10-}$ processes have been reported at carbon based glassy carbon (GC) and boron doped diamond (BDD) electrodes under conditions of stationary electrode DC cyclic voltammetry [10, 12], it has been noted that only the first two are present at a rotated disc GC electrode [11]. Furthermore, in a quantitative electrode kinetic evaluation of the first two $\alpha\text{-[S}_2\text{W}_{18}\text{O}_{62}]^{4-/5-/6-}$ processes by large amplitude Fourier transform alternating current (FTAC) voltammetry at GC, BDD, Au and Pt disc electrodes [10] some anomalous behaviour with respect to conformance to the Butler-Volmer model of electron transfer was detected [16], particularly with respect to the $\alpha\text{-[S}_2\text{W}_{18}\text{O}_{62}]^{5-/6-}$ processes at a Pt electrode. Anomalies with respect to theoretical predictions also have been noted in other studies with this electrode material when POM reduction processes occur at fairly negative potentials [1, 17]. Processes at Pt appear to have relatively slow electrode kinetics relative to the carbon and gold electrode cases. Under these circumstances, neglect of strong ion-pairing that inevitably is a feature of POM chemistry [18-20], but rarely incorporated into parameterisation of the electrode kinetics,

was hypothesized to be a possible contributing factor to discrepancies between Pt electrode experimental and simulated data [19].

In addition to ion-pairing, another special issue that also may arise with the extensive series of α -[S₂W₁₈O₆₂]^{4-/5-/6-/7-/8-/9-/10-} processes is that they encompass a very wide potential range. This includes the very negative one near the solvent limit where the impact of the ion distribution in the electrode-solution double layer interfacial region [21, 22] could be substantial. For example, with 0.10 M [*n*-Bu₄N][PF₆] as the supporting electrolyte, the double layer region at and adjacent to a highly negatively charged electrode is expected to contain a very high concentration of the [*n*-Bu₄N]⁺ cation. Accordingly, the double layer impact on a process that occurs in this region near the negative solvent limit may be far more important than would apply at potentials near to the point of zero charge. In the present context, this means that the α -[S₂W₁₈O₆₂]^{4-/5-} process at -0.24 V vs Fc^{0/+} [12] will encounter a very different double layer environment than that of the α -[S₂W₁₈O₆₂]^{9-/10-} one at -2.32 V vs Fc^{0/+} [12]. In this context, studies by Fawcett et al [23] on the impact of tetraalkylammonium electrolytes in dynamic electrochemical studies may be relevant.

The above considerations raise issues concerning as how to model a complete thermodynamic and electrode kinetic descriptions of the very rich voltammetry of very negatively charged POMs. Historically, most voltammetric (polarographic) studies with this class of compound were undertaken at the dropping mercury electrode [24]. In recent times, use of mercury as an electrode material has been phased out due to toxicity concerns. In its place, GC has been the electrode of choice for many POM studies, because of its wide negative potential range as at mercury. With this electrode material, many more examples of well-defined, reversible processes, have been reported using DC voltammetric techniques which have allowed reversible potentials to be estimated. While many POM processes may have some of the

characteristics of close to reversible or quasi-reversible processes, parameterisation using a model based on a simple one electron for every process in the α - $[\text{S}_2\text{W}_{18}\text{O}_{62}]^{4-/-5-/-6-/-7-/-8-/-9-/-10-}$ series has to be an oversimplification. For example, the α - $[\text{S}_2\text{W}_{18}\text{O}_{62}]^{9-/-10-}$ process occurring at very negative potentials is expected to involve ion-pairing and suffer from double layer and other effects rather than being a simple outer sphere electron transfer reactions as commonly assumed. In this study, we have extended detailed studies on α - $[\text{S}_2\text{W}_{18}\text{O}_{62}]^{4-/-5-/-6-}$ process to encompass all one electron transfer processes available for reduction of $[\text{S}_2\text{W}_{18}\text{O}_{62}]^{4-}$ at GC, Au and Pt electrodes in acetonitrile containing 0.10 or 0.50 M $[n\text{-Bu}_4\text{N}][\text{PF}_6]$ by DC and FTAC voltammetry as well as by other techniques. A progressively increasing level of departure from that predicted by the Butler-Volmer model has been found in each reduction process as a consequence of enhanced ion-pairing and electrode material dependent surface interactions associated with the more highly reduced forms. Given that POMs are of widespread interest in electrocatalysis [25-29] and battery development [30-33], enhanced knowledge of subtleties that exist in the POM electrochemistry may assist both fundamental and applied aspects of the field.

2 Experimental Section

2.1 Reagents and Solvents

$[n\text{-Bu}_4\text{N}]_4(\alpha\text{-}[\text{S}_2\text{W}_{18}\text{O}_{62}])$ was synthesized according to a literature method [34] and kindly provided by Professor Tadaharu Ueda. Ferrocene (Fc, 98 %, Sigma-Aldrich), Al_2O_3 (diameter = 0.3 μm and 0.05 μm , Buehler), acetonitrile (CH_3CN , 99.9 %, Sigma-Aldrich) and ethanol (99.5 %, Ajax Finechem) were used as obtained from the manufacturers. Tetrabutylammonium hexafluorophosphate ($[n\text{-Bu}_4\text{N}][\text{PF}_6]$, 98 %, Sigma-Aldrich) was recrystallized [14] and used as the supporting electrolyte.

2.2 Electrochemical Instrumentation and techniques

Conventional DC voltammetric measurements were undertaken with an electrochemical workstation (CHI-760E). FTAC voltammetric experiments were executed with home-built [35] instrumentation using a sine wave perturbation having an amplitude (ΔE) of 80 mV and a frequency (f) of 8.98 or 26.95 Hz superimposed upon the DC ramp. Frequency domain data in the form of a power spectrum were obtained from the total current–time data by Fourier transformation. Inverse Fourier transformation applied to the power spectrum with a rectangular window used for band filtering was used to generate the resolved aperiodic DC component and the AC harmonics [35-37].

Steady state voltammetry of α -[S₂W₁₈O₆₂]⁴⁻ in CH₃CN (0.50 M Bu₄NPF₆) was achieved by the GC, Au and Pt rotating disc electrodes (RDE; 3 mm diameter) using a CHI 760E electrochemical workstation. Rotation rate of 52.4 s⁻¹ was applied by the BAS-M 1005 electrode rotator. Pt wire in a glass frit containing 0.50 M [*n*-Bu₄N][PF₆] in CH₃CN was used as reference electrode and Pt wire as the counter electrode.

A three-electrode electrochemical cell was used for all voltammetric experiments which were conducted at 22±2° C. Oxygen was removed from the test solution by purging with nitrogen for at least 10 min prior to each experiment. eDAC metal (Au and Pt) and GC (nominal diameter = 1.0 mm) disc working electrodes were polished with aqueous Al₂O₃ slurry before each voltammetric experiment. Sonication for 10 to 15 seconds was used to remove polishing residue followed by rinsing with water and acetone. Finally, the working electrodes were dried under a flow of nitrogen. Pt wires were used as both auxiliary and quasi-reference electrodes. The IUPAC recommended Fc^{0/+} oxidation process [38] was used to calibrate the potential of the Pt quasi-reference electrode.

Mass changes occurring during voltammetric experiment at gold coated quartz crystal (electrode area (A) = 0.205 cm², oscillation frequency = 8.0 MHz) were detected by the electrochemical quartz crystal microbalance (EQCM) technique using CHI 400B instrumentation.

The Randles-Sevcik equation [39] (Eqn. 1) was used to determine the effective area of the macrodisc working electrodes via the DC peak current for oxidation of 1.0 mM Fc to Fc⁺ in CH₃CN containing 0.10 M [*n*-Bu₄N][PF₆] as supporting electrolyte with a known diffusion coefficient of 2.4×10^{-5} cm² s⁻¹ for Fc [40]. In this equation, I_p , n , C , ν , T , R , F and A denote the oxidation peak current, number of electrons transferred in the Fc/Fc⁺ process ($n = 1$), bulk concentration, scan rate, absolute temperature, universal gas constant, Faraday's constant and electrode area, respectively. The estimated effective areas of the GC, Pt and Au electrodes determined by this method were 8.0×10^{-3} cm², 8.0×10^{-3} cm², and 8.1×10^{-3} cm², respectively.

$$I_p = 0.4463nFA(nFD\nu/RT)^{1/2}C \quad (1)$$

2.3 Simulations

MECSim (Monash Electro-Chemistry Simulator) software [41] was used to simulate the theoretical voltammetric data using the simple one-electron transfer process (Eqn. 2), where Ox and Red are the oxidised and reduced forms of the POM, with Butler-Volmer theory for electron transfer and mass transport by planar diffusion.



The parameters E^0 (reversible potential), k^0 (heterogeneous charge transfer rate constant) at E^0 , α (charge transfer coefficient), D (diffusion coefficient), R_u (uncompensated resistance)

and C_{dl} (double layer capacitance) have to be introduced into the simulations in order to mimic experimental data. The $R_u C_{dl}$ time constant technique available with the CHI electrochemical workstation was employed to determine R_u . In heuristic forms of data analysis E^0 was assessed from the average of the oxidation (E_p^{ox}) and reduction (E_p^{red}) peak potentials in DC cyclic voltammetric experiments. The diffusion coefficient of α -[S₂W₁₈O₆₂]⁴⁻ was estimated from the reduction peak current associated with α -[S₂W₁₈O₆₂]^{4-/5-} at a GC electrode using the Randles-Sevcik relationship [39] (Eqn. 1). Values found by this method are 2.9×10^{-6} and $6.3 \times 10^{-6} \text{ cm}^2 \text{ s}^{-1}$, with 0.50 and 0.10 M [*n*-Bu₄N][PF₆] as the supporting electrolyte, respectively. Same level of difference in diffusion coefficient was also observed with ferrocene, suggesting that the change in viscosity is the origin of this difference.

The value of C_{dl} was estimated at each potential from the fundamental harmonic AC data where faradaic current is absent and use of the potential dependent capacitor model [42].

$$C_{dl}(t) = c_0 + c_1 E(t) + c_2 E(t)^2 + c_3 E(t)^3 + c_4 E(t)^4 \quad (3)$$

In this polynomial Equation 3, the nonlinearity is defined by c_0 , c_1 , c_2 , c_3 , and c_4 and the time dependant potential is denoted by $E(t)$. These coefficients were obtained at each frequency (8.98 or 26.95 Hz).

2.4 Parameterisation

In initially used heuristic forms of parameterisation, comparisons of the AC harmonic components of experimental and simulated data were undertaken visually by the experimenter. Values of k^0 and α reported were derived from the experimentalist's assessment of the best match of experimental and simulated data. The computer assisted automated data analysis protocol used after undertaking the heuristic form of parameterisation is described in detail elsewhere [10]. This procedure was used to compare the experimental and simulated data using

the least squares (LS) based “best fit” function given in Equation 4 to estimate E^0 , k^0 and α values. The subscript *app* is now applied to the E^0 , k^0 and α parameters because a simple electron transfer scheme is used to approximate a more complete square reaction scheme where ion-pairing is involved. [43, 44] These values are a function of supporting electrolyte concentration. Minimum influence of non-faradaic current was achieved by employing 2nd to 6th harmonic components in this automated simulation.

$$LS = \left[1 - \left(\sum_{h=2}^6 \sqrt{\frac{\sum_{i=1}^N [(f_h^{\text{exp}}(t_i) - f_h^{\text{sim}}(t_i))^2]}{\sum_{i=1}^N f_h^{\text{exp}}(t_i)^2}} \right) / 5 \right] \times 100\% \quad (4)$$

where $f^{\text{exp}}(t_i)$ and $f^{\text{sim}}(t_i)$ symbolize the experimental and simulated functions, respectively and h and N represent the individual AC harmonic component and number of data points, respectively.

The tedious heuristic method is used initially to provide a good estimate of parameters. This facilitates minimisation of parameter space that needs to be searched in the data optimisation method, ensures that physically realistic parameters are reported as the outcome from the data optimisation method and enhances prospects of detection of systematic but subtle discrepancies in experimental and simulated data that are more likely to be detected by visual inspection by an experienced experimentalist than from analysis of LS values [10].

3 Results and Discussion:

3.1 DC Cyclic voltammetry of α -[S₂W₁₈O₆₂]⁴⁻ at GC, Au and Pt Electrodes:

DC cyclic voltammograms starting at potentials prior to the initial reduction of α -[S₂W₁₈O₆₂]⁴⁻ up to the solvent limit were recorded in CH₃CN at a scan rate (ν) of 0.100 V s⁻¹ at GC, Au and Pt electrodes with 0.50 M and 0.10 M [*n*-Bu₄N][PF₆] (see Figure 2) as the

supporting electrolyte. The more negative solvent reduction limit at GC allows six reduction steps to be observed, nominally (ion-pairing neglected) representing consecutive reduction of α -[S₂W₁₈O₆₂]⁴⁻ to α -[S₂W₁₈O₆₂]⁵⁻, then to α -[S₂W₁₈O₆₂]⁶⁻, α -[S₂W₁₈O₆₂]⁷⁻, α -[S₂W₁₈O₆₂]⁸⁻, α -[S₂W₁₈O₆₂]⁹⁻ and finally to α -[S₂W₁₈O₆₂]¹⁰⁻ as reported previously [11]. The lower negative potential limit at the Au electrodes restricts reduction to five steps, while the even less negative limit at Pt electrode allows only three processes to be observed. In contrast with the simpler series of processes seen at GC (six processes with equal peak heights), α -[S₂W₁₈O₆₂]⁴⁻ voltammetric reduction processes at Au show a progressive decrease in peak currents. At Pt electrodes, even the third process is barely seen and its shape is unusual relative to other processes. These observations indicate probable complexity accompanying α -[S₂W₁₈O₆₂]⁴⁻ reduction processes which means they may not be well-modelled by Butler-Volmer electron transfer theory.

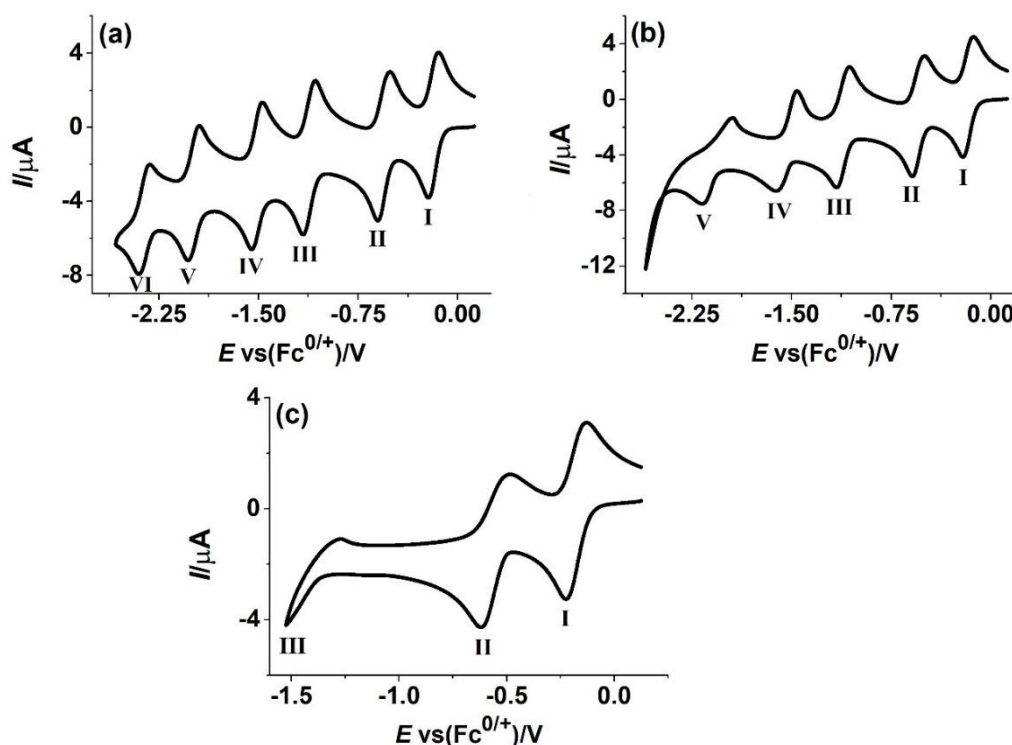


Figure 2. DC cyclic voltammograms obtained at a scan rate of 0.100 V s⁻¹ for reduction of 2.5 mM α -[S₂W₁₈O₆₂]⁴⁻ in CH₃CN (0.10 M [*n*-Bu₄N][PF₆]) at (a) GC (b) Au and (c) Pt electrodes.

Table 2 summarises the mid-point potential $E_m = (E_p^{\text{ox}} + E_p^{\text{red}})/2$, which provisionally is equated to E_{app}^0 , and peak-to-peak separation $\Delta E_p = E_p^{\text{ox}} - E_p^{\text{red}}$ values for processes in CH₃CN (0.50 and 0.10 M [*n*-Bu₄N][PF₆] at GC, Au and Pt electrodes. E_{app}^0 values at GC electrode appear at more positive potential ($E_{app1}^0 = -0.215$ V, $E_{app2}^0 = -0.592$ V, $E_{app3}^0 = -1.156$ V, $E_{app4}^0 = -1.539$ V, $E_{app5}^0 = -2.006$ V and $E_{app6}^0 = -2.344$ V) with the higher concentration (0.50 M) than with the lower concentration (0.10 M) of [*n*-Bu₄N][PF₆] ($E_{app1}^0 = -0.232$ V, $E_{app2}^0 = -0.608$ V, $E_{app3}^0 = -1.178$ V, $E_{app4}^0 = -1.563$ V, $E_{app5}^0 = -2.046$ V and $E_{app6}^0 = -2.409$ V). The same scenario also applies in most cases for the processes at Au and Pt electrodes, but E_{app}^0 values are only independent of electrode material for processes up to IV (see Table 2). E_{app}^0 is a parameter that is assumed to be thermodynamically pinned and hence should be independent of electrode material, so yet another discrepancy with theoretical predictions based on simple electron transfer reactions is evident. Nevertheless, the positive E_{app}^0 shift usually found with use of 0.50 M [*n*-Bu₄N][PF₆] instead of 0.10 M [*n*-Bu₄N][PF₆] supporting electrolyte concentration is consistent with the presence of a stronger ion-pairing impact with the higher electrolyte concentration as noted in other studies [10, 45].

Table 2. Summary of voltammetric parameters obtained from the reduction of 1.0 mM α -[S₂W₁₈O₆₂]⁴⁻ in CH₃CN (0.10 and 0.50 M [*n*-Bu₄N][PF₆]) at a scan rate of 0.100 V s⁻¹.

Electrode	[<i>n</i> -Bu ₄ N][PF ₆] C (M)	E_{app1}^0	E_{app2}^0	E_{app3}^0	E_{app4}^0	E_{app5}^0	E_{app6}^0	ΔE_{P1}	ΔE_{P2}	ΔE_{P3}	ΔE_{P4}	ΔE_{P5}	ΔE_{P6}
		V ^a vs Fc ^{0/+}						V ^b					
GC	0.50	-0.215	-0.592	-1.156	-1.539	-2.006	-2.344	0.060	0.074	0.078	0.078	0.079	0.088
	0.10	-0.232	-0.608	-1.178	-1.563	-2.046	-2.409	0.062	0.075	0.080	0.075	0.087	0.082
Au	0.50	-0.215	-0.593	-1.159	-1.540	-2.025	^d	0.063	0.077	0.086	0.094	0.150	^d
	0.10	-0.232	-0.606	-1.174	-1.566	-2.083	^d	0.068	0.083	0.090	0.100	0.240	^d
Pt	0.50	-0.218	-0.595	^c	^d	^d	^d	0.068	0.090	^c	^d	^d	^d
	0.10	-0.233	-0.606	^c	^d	^d	^d	0.070	0.100	^c	^d	^d	^d

^a Uncertainty in E_{app}^0 is ± 5 mV

^b Uncertainty in ΔE_p is ± 2 mV

^c Poorly defined

^d solvent breakdown interrupts the voltammetric response

As previously noted [10] the value $\Delta E_{p1} = 60$ mV obtained at $\nu = 0.100$ mV s⁻¹ for the α -[S₂W₁₈O₆₂]^{4-/5-} process in CH₃CN (0.50 M [*n*-Bu₄N][PF₆]) at a GC electrode is close to the theoretically predicted value of 56.4 mV [39] for a reversible one-electron process at 22 °C, signifying that on this DC voltammetric time scale process I can be regarded as being reversible. However, values of this parameter progressively increases upon more extensive reduction ($\Delta E_{p2} = 0.074$ V, $\Delta E_{p3} = 0.078$ V, $\Delta E_{p4} = 0.078$ V, $\Delta E_{p5} = 0.079$ V and $\Delta E_{p6} = 0.088$ V). In general, the scenario ($\Delta E_{p1} < \Delta E_{p2} \dots < \Delta E_{pn}$) also applies at Au and Pt electrodes, implying that $k_{app1}^0 > k_{app2}^0 \dots > k_{appn}^0$ at all electrode materials if the processes truly conform to the Butler-Vomer model and are simple quasi-reversible reactions. Also noteworthy is the fact that ΔE_p values are significantly smaller at the GC electrode than at metal ones ($\Delta E_{p1} = 0.063$ V, $\Delta E_{p2} = 0.077$ V, $\Delta E_{p3} = 0.086$ V, $\Delta E_{p4} = 0.094$ V and $\Delta E_{p5} = 0.150$ V at Au and $\Delta E_{p1} = 0.068$ V and $\Delta E_{p2} = 0.090$ V at Pt) which according to Butler-Volmer theory implies faster electrode kinetics at the carbon based electrode assuming IR_u drop at all electrode materials are comparable. Significantly, the very large ΔE_p values at Au for the α -[S₂W₁₈O₆₂]^{7-/8-} and α -[S₂W₁₈O₆₂]^{8-/9-} processes are indicative of a quite slow electrode kinetics if these are simple one-electron electron transfer reactions.

In principle, studies by DC cyclic voltammetry over a wide range of potentials could be used to assess to what extent departures from simple one-electron transfer processes occur. However, this is extremely difficult with up to six processes to evaluate with diffusion tails between processes making a major contribution and significant potential dependent charging current contributions at negative potentials. Additionally, maintaining exactly the same electrode state

for each scan rate experiment is also problematic. Thus, quantitative studies were attempted using a single FTAC voltammetric experiment and examining the extent to which the Butler-Vomer model is applicable, as was undertaken with the α -[S₂W₁₈O₆₂]^{4- /5- /6-} processes [10]. The advantages of the FTAC voltammetry in quantitative electrode kinetic studies has been described in several reviews [45-48].

3.2 FTAC voltammetric parameterization of the α - [S₂W₁₈O₆₂]^{4- /5- /6- /8- /9- /10-} reduction processes in CH₃CN (0.50 M [*n*-Bu₄N][PF₆]):

The E_{app}^0 , k_{app}^0 and α_{app} values associated with processes I and II have been established by FTAC voltammetry [10] with results and departures from ideality and virtues of using both experimenter based heuristic and computationally efficient data optimisation approaches reviewed in the introduction. In this earlier study, processes I was parameterised as a separate exercise using data obtained by collected in the potential range prior to the onset of process I and switching the potential prior to the onset of process II. Processes I and II were also parameterised using data generated in a single experiment by switching the potential prior to process III. Processes I and II along with processes III, IV, V and VI at GC, processes III, IV and V at Au and process III at Pt are now subjected to parameterisation from a single data set collected in one experiment covering the potential range encompassing all processes displayed in Figure 2. Initially, reduction of 2.5 mM α -[S₂W₁₈O₆₂]⁴⁻ in CH₃CN (0.50 M [*n*-Bu₄N][PF₆]) is studied by FTAC voltammetry using the heuristic and automated forms of data analysis. This high electrolyte concentration means that ion-pairing will be substantial.

In the heuristically based parameterisation exercise initially undertaken, E_{app}^0 values were set at the mid-point potential values derived from DC cyclic voltammetry. An extensive series of FTAC voltammetric simulations with systematically varied k_{app}^0 and α_{app} values were

generated in their resolved DC and AC harmonic components and outcomes compared visually with experimental results until the best possible agreement had been achieved in the opinion of the experimenter.

A summary of the heuristic parametrisation analysis outcome for FTAC voltammetric reduction of 2.5 mM α -[S₂W₁₈O₆₂]⁴⁻ in CH₃CN (0.50 M [*n*-Bu₄N][PF₆]) over the potential range of 0.15 V to -2.525 V for GC (six processes) and Au (five processes) and 0.15 V to -1.375 V for Pt electrodes (three processes) is provided in Table 3. A comparison of experimental and simulated FTAC voltammetric data based on parameters provided in this Table are displayed in Figures 3, and S1 for GC, and Figures S2 and S3 for Au and Figure S4 for the Pt electrode. The extensive set of thermodynamically favoured cross redox reactions and ion-pairing are neglected in this and subsequent data analysis exercises.

As noted in reference [10], only lower limits of k_{app1}^0 could be determined at GC at the low frequency of 8.98 Hz (Figure 3) by FTAC voltammetric method as this response lies at or the reversible limit within experimental error. Thus, only the thermodynamic parameter E_{app1}^0 is needed to define this FTAC voltammetry. On the other hand, subsequent processes are significantly slower than the first and can be simulated with electrode kinetic parameters that lie well below the reversible limit, even at this low frequency. In contrast, the heuristically estimated values of k_{app1}^0 and α_{app1} at the higher frequency (shorter time scale) of 26.95 Hz for the first process are considered reliable as they are parameterised from the “best fit” simulations undertaken with kinetic parameters much slower than anticipated for a reversible process (Figure S1g).

Figures 3 and S1 show the FTAC voltammetric comparison between simulated and experimental data at GC electrode as assessed heuristically. The experimenter in this exercise,

decided to achieve an almost perfect match for the AC harmonics on the reduction component for all processes, but this meant that for processes III, IV, V and VI the oxidative on reverse scan direction displayed a level of discrepancy which increased progressively towards the higher the order of the AC harmonic. Similarly, experiment- theory comparisons of the aperiodic DC component display progressively poorer agreement beyond processes I and II. Effectively, this is equivalent to the experimenter deciding to bias the parameterisation to the reduction components of the AC harmonics to give $k_{app1}^0 = \geq 0.10$, $k_{app2}^0 = 0.080$, $k_{app3}^0 = 0.053$, $k_{app4}^0 = 0.041$, $k_{app5}^0 = 0.012$ and $k_{app6}^0 = 0.002$ cm s⁻¹ at 8.98 Hz and $k_{app1}^0 = 0.10$, $k_{app2}^0 = 0.084$, $k_{app3}^0 = 0.057$, $k_{app4}^0 = 0.045$, $k_{app5}^0 = 0.014$ and $k_{app6}^0 = 0.002$ cm s⁻¹ at 26.95 Hz. A major virtue of this strategy is that the electrode kinetics for all processes are independent of frequency as required by the Butler-Volmer model. Kinetic values for 6th process were only determined from the 1st to 3rd harmonic AC components as the current magnitude in higher harmonics is very small. The experimenter could of course have chosen alternative heuristic data analysis strategies and tried to fit data to the average of the reduction and oxidation harmonic data, but this would be exceptionally tedious and experience [10] suggested the approach taken is the most reasonable one to be adopted in the present scenario. However, this highlights the subjectivity of the experimenter dependent outcome.

Commonly, voltammetric data would be analysed by switching the potential after process I to parameterise this process, then after process II to parameterises process II knowing parameters for process I , and then after process III etc., rather than by switching the potential at a sufficiently negative value to encompass all six processes in one experiment. Close inspection of Figures 3 and S1, reveals an inequality in the reduction and oxidation component peak current magnitudes for the α -[S₂W₁₈O₆₂]^{4-/5-} and α -[S₂W₁₈O₆₂]^{5-/6-} processes which is not accommodated by the model of electron transfer. Furthermore, this asymmetry does not exist

when these processes I and II were examined individually by FTAC voltammetry [10] rather than when the potential was switched after all six reduction steps had been completed. All these subtle departures from ideality for the series of quasi-reversible process detected via visual inspection of results as required in the heuristic form of data analysis, imply the presence of complexity in the voltammetry which occurs even at a GC electrode at potentials more negative than process II. Furthermore, these modelling imperfections are unlikely to be accommodated fully by inclusion of ion-pairing in combination with very sluggish electrode kinetics which was proposed as a plausible explanation for the asymmetry in reduction and oxidation components found with α -[S₂W₁₈O₆₂]^{5-/6-} process at Pt electrode [10].

Table 3. Thermodynamic and electrode kinetic parameters^a derived from heuristic and automated computer based comparison of simulated and experimental FTAC voltammetric data at GC, Au and Pt electrodes for the reduction of 2.5 mM α -[S₂W₁₈O₆₂]⁴⁻ in CH₃CN (0.50 M [*n*-Bu₄N][PF₆]).

(a) Reversible potentials:

Electrode	<i>f</i> (Hz)	<i>R_u</i> (Ω) ^b	Simulation method	<i>E</i> ⁰ _{app<i>n</i>}					
				V vs Fc ^{0/+}					
GC	8.98	225	Heuristic	-0.215	-0.592	-1.156	-1.539	-2.006	-2.344
			Automated	Range	-0.220 to -0.210	-0.596 to -0.585	-1.165 to -1.148	-1.543 to -1.531	-2.014 to -2.003
			Est.	-0.212	-0.589	-1.154	-1.537	-2.004	-2.349
	26.95	200	Heuristic	-0.215	-0.592	-1.156	-1.539	-2.006	-2.344
			Automated	Range	-0.220 to -0.210	-0.599 to -0.585	-1.163 to -1.148	-1.544 to -1.530	-2.013 to -2.003
			Est.	-0.212	-0.588	-1.153	-1.535	-2.008	-2.345
Au	8.98	180	Heuristic	-0.215	-0.593	-1.159	-1.540	-2.025	^c
			Automated	Range	-0.224 to -0.210	-0.601 to -0.587	-1.164 to -1.151	-1.548 to -1.530	-2.040 to -2.015
			Est.	-0.212	-0.589	-1.158	-1.538	-2.030	--
	26.95	180	Heuristic	-0.215	-0.593	-1.159	-1.540	-2.025	^c
			Automated	Range	-0.222 to -0.207	-0.601 to -0.585	-1.163 to -1.152	-1.550 to -1.532	-2.035 to -2.015
			Est.	-0.211	-0.588	-1.155	-1.539	-2.030	--
Pt	8.98	200	Heuristic	-0.218	-0.593	^d	^c	^c	^c
			Automated	Range	-0.220 to -0.214	-0.596 to -0.589	--	--	--
			Est.	-0.218	-0.591	--	--	--	--
	26.95	200	Heuristic	-0.218	-0.593	^d	^c	^c	^c
			Automated	Range	-0.220 to -0.214	-0.596 to -0.589	--	--	--
			Est.	-0.219	-0.592	--	--	--	--

^a Other Parameters used in the simulations are: $A_{GC} = 8.0 \times 10^{-3} \text{ cm}^2$, $A_{Au} = 8.1 \times 10^{-3} \text{ cm}^2$, $A_{Pt} = 8.0 \times 10^{-3} \text{ cm}^2$, $\Delta E = 80 \text{ mV}$, $D = 2.9 \times 10^{-6} \text{ cm}^2 \text{ s}^{-1}$, $T = 295 \text{ K}$, $v_{GC} = 0.099 \text{ V s}^{-1}$, $v_{Au} = 0.100 \text{ V s}^{-1}$ and $v_{Pt} = 0.057 \text{ V s}^{-1}$, $f_{GC,Au \text{ and } Pt} = 8.98 \text{ and } 26.95 \text{ Hz}$.

^b varies due to slight variability in electrode arrangement ^c process is not observed due to lower negative potential limit ^d poorly defined.

(b) Heterogeneous charge transfer kinetics:

Electrode	f (Hz)	Simulation method	k_{app}^0						
			k_{app1}^0	k_{app2}^0	k_{app3}^0	k_{app4}^0	k_{app5}^0	k_{app6}^0	
			cm s^{-1}						
GC	8.98	Heuristic	≥ 0.10	0.080 ^a	0.053 ^a	0.041	0.012	0.002 ^b	
		Automated	Range	0.070 to 0.140	0.045 to 0.090	0.035 to 0.065	0.030 to 0.055	0.008 to 0.014	0.0005 to 0.0050
			Est.	0.10 ^c	0.064 ^d	0.042 ^d	0.047	0.013	0.002 ^b
	26.95	Heuristic	0.10	0.084 ^a	0.057 ^a	0.045	0.014	0.002 ^b	
		Automated	Range	0.070 to 0.140	0.045 to 0.090	0.040 to 0.070	0.030 to 0.055	0.009 to 0.019	0.0005 to 0.0050
			Est.	0.099	0.060 ^d	0.045 ^d	0.045	0.014	0.0017 ^b
Au	8.98	Heuristic	0.053	0.039 ^a	0.017	0.002 ^b	0.0004 ^b	^e	
		Automated	Range	0.035 to 0.065	0.025 to 0.045	0.009 to 0.025	0.0006 to 0.005	0.0001 to 0.0008	--
			Est.	0.051	0.028 ^d	0.013	0.0042 ^b	0.0003 ^b	--
	26.95	Heuristic	0.054	0.039 ^a	0.015	0.002 ^b	0.0004 ^b	^e	
		Automated	Range	0.035 to 0.065	0.025 to 0.045	0.009 to 0.025	0.0006 to 0.005	0.0001 to 0.0008	--
			Est.	0.055	0.031 ^d	0.015	0.0044 ^b	0.0005 ^b	--
Pt	8.98	Heuristic	0.039	0.012 ^a	0.00001 ^f	^e	^e	^e	
		Automated	Range	0.025 to 0.045	0.004 to 0.014	--	--	--	--
			Est.	0.036	0.009 ^d	--	--	--	--
	26.95	Heuristic	0.037	0.011 ^a	0.00001 ^f	^e	^e	^e	
		Automated	Range	0.033 to 0.042	0.004 to 0.014	--	--	--	--
			Est.	0.038	0.008 ^d	--	--	--	--

^a determined from reduction component of data only ^b estimated from 1st to 3rd harmonic components ^c close to reversible limit so uncertainty substantial ^d derived from use of all data even though asymmetry is present in reduction and oxidation components ^e process is not observed due to lower negative potential limit ^f poorly defined.

(c) Charge transfer coefficients:

Electrode	f (Hz)	Simulation method	α_{app1}	α_{app2}	α_{app3}	α_{app4}	α_{app5}	α_{app6}	
GC	8.98	Heuristic	a	0.60	0.60	0.55	0.53	0.50 ^b	
		Automated	Range	0.40 to 0.70					
			Est.	0.58 ^c	0.48 ^d	0.54 ^d	0.41 ^d	0.51	0.48 ^b
	26.95	Heuristic	0.60	0.60	0.60	0.55	0.53	0.50 ^b	
		Automated	Range	0.40 to 0.70					
			Est.	0.49 ^d	0.59	0.57 ^d	0.51 ^d	0.51	0.51 ^b
Au	8.98	Heuristic	0.60	0.60	0.47	0.50 ^b	0.50 ^b	e	
		Automated	Range	0.40 to 0.70	--				
			Est.	0.58	0.60	0.41 ^d	0.42 ^b	0.60 ^b	e
	26.95	Heuristic	0.60	0.60	0.47	0.50 ^b	0.50 ^b	e	
		Automated	Range	0.40 to 0.70	--				
			Est.	0.64	0.64	0.47	0.41 ^b	0.47 ^b	e
Pt	8.98	Heuristic	0.57	0.50	0.50 ^f	e	e	e	
		Automated	Range	0.40 to 0.70	0.44 to 0.60	--	--	--	--
			Est.	0.57	0.53	e	e	e	e
	26.95	Heuristic	0.57	0.50	0.50 ^f	e	e	e	
		Automated	Range	0.50 to 0.67	0.44 to 0.65	--	--	--	--
			Est.	0.56	0.52	e	e	e	e

^a too close to reversible limit to be determined ^b estimated from 1st to 3rd harmonic components, ^c near reversible limit so uncertainty substantial ^d all data used ^e process is not observed due to lower negative potential limit ^f poorly defined.

Table 4. Least square (LS) values obtained from the automated computer-based comparison of simulated and experimental FTAC voltammetric data for the reduction of 2.5 mM α -[S₂W₁₈O₆₂]⁴⁻ in CH₃CN.

Electrode	f (Hz)	LS (%)						LS (%)					
		0.50 M [<i>n</i> -Bu ₄ N][PF ₆]						0.10 M [<i>n</i> -Bu ₄ N][PF ₆]					
		I	II	III	IV	V	VI	I	II	III	IV	V	VI
GC	8.98	79	63	69	87	70	53	85	68	74	90	75	82
	26.95	80	62	61	86	71	51	83	67	76	91	74	73
Au	8.98	81	62	74	43	47		85	69	90	47	53	
	26.95	80	60	68	41	46		84	67	72	48	51	
Pt	8.98	91	58					93	61				
	26.95	85	55					89	60				

All heuristically estimated k_{app}^0 and α_{app} values at Au and Pt electrode are considered as reliable in the context that their magnitudes lie significantly below the reversible limit, even with the lower frequency ($f = 8.98$ Hz) data sets. Thus, significantly slower electrode kinetics apply at these metal electrodes than at GC for all processes. Again, if the data analysis in the heuristic approach is biased to obtain an excellent fit to the reduction component of the data set, with discrepancies in the oxidation component, then parameterisation the Au electrode gives $k_{app1}^0 = 0.053$, $k_{app2}^0 = 0.039$ cm s⁻¹, $k_{app3}^0 = 0.017$, $k_{app4}^0 = 0.002$ and $k_{app5}^0 = 0.0004$ cm s⁻¹ at 8.98 Hz and $k_{app1}^0 = 0.054$, $k_{app2}^0 = 0.039$ cm s⁻¹, $k_{app3}^0 = 0.015$, $k_{app4}^0 = 0.002$ and $k_{app5}^0 = 0.0004$ cm s⁻¹ at 26.95 Hz. Thus, all rate constants determined heuristically are significantly smaller than those obtained at GC electrodes when calculated on the same basis.

Consistent with this conclusion of slower kinetics at the Au electrode, it can be noted that electrode kinetic estimations for the 4th and 5th processes were based solely on a comparison of 1st to 3rd AC harmonic components of experimental and simulated data versus 1st to 6th at GC electrode, because the current magnitudes of higher harmonics are too small and the 6th

harmonic not detectable above background noise. Significant asymmetry also appears in higher harmonic AC component data at Au electrode as at GC. Agreement between experimental and simulated data at Au electrode is displayed in Figures S2 and S3.

Electrode kinetics at the Pt electrode ($k_{app1}^0 = 0.039$, $k_{app2}^0 = 0.012$ and $k_{app2}^0 = 0.00001$ cm s⁻¹ at 8.098 Hz and $k_{app1}^0 = 0.037$, $k_{app2}^0 = 0.011$ and $k_{app2}^0 = 0.00001$ cm s⁻¹ at 26.95 Hz) (see Figure S4) are even slower than at Au electrodes. k_{app}^0 was again estimated in the heuristic approach from the reduction component of the AC harmonics due to asymmetry as noted in the earlier report [10].

With the computer assisted data optimisation approach, theory-experiment comparison was confined to the 2nd to 6th harmonics where influence of background current is negligible. Unlike the heuristic method, parameters were derived from use of all data, as in reference [10], so parameter values estimated may differ from those estimated by heuristic analysis that emphasise the oxidation component of the data set. However, to save substantial computational time in estimation of up to 18 parameters, estimates of their values obtained heuristically were still used to minimise range of the parameter space search needed in the automated data optimisation method. Significantly, implementation of this strategy meant that up to six sets of E_{app}^0 as well as six sets of k_{app}^0 and α_{app} parameter values or 18 parameter values as applies at a GC electrode can now all be conveniently and efficiently derived in one data optimisation exercise to give results summarised in Table 3.

Typically, the data optimisation methods are applied automatically and lead a best fit outcome according to the model used to mimic experimental data. The outcome of a report of LS values is not greatly informative with respect to detecting systematic errors, although strategies to detect over and under parametrisation are available, and the method could be supported by

machine learning [49, 50]. In this sense this method has significantly less “intelligence” compared to the heuristic method where an experimenter can use their discretion and judiciously modify the data analysis strategy as was done in this case.

E_{app}^0 values estimated for all processes are essentially independent of the parameterisation method. In contrast, calculated k_{app}^0 and α_{app} values differ when asymmetry is present in the reduction and oxidation data sets in the higher order AC harmonics. As expected, the data optimisation method essentially “averages” outcomes of the reduction and oxidation data sets to produce the “best fit” to the full data set whereas in the heuristic form of analysis, data analysis is deliberately biased to achieving the “best fit” to the reduction component of the data set. The outcome is that automated data optimisation method accommodates the asymmetry by fitting theory to a lower average current than for the heuristic method, and consequently produces lower estimates of k_{app}^0 and different values of α_{app} as shown in data presented in Table 3. However, the estimated k_{app}^0 values maintain close to frequency independence. For example, at the GC electrode, $k_{app2}^0 = 0.064$ and $k_{app3}^0 = 0.042$ cm s⁻¹ with a frequency of 8.98 Hz, versus $k_{app2}^0 = 0.060$ and $k_{app3}^0 = 0.045$ cm s⁻¹ at 26.95 Hz. Parallel observations are made with the modelling with Au and Pt electrodes. Attempts to mimic the asymmetry found in experimental data in the automated parametrization exercise, but not in the heuristic approach also leads to data analysis dependent α_{app} values. For example, at the GC electrode, $\alpha_{app2} = 0.48$, $\alpha_{app3} = 0.54$ at 8.98 Hz using automated data optimisation versus $\alpha_{app2} = 0.60$, $\alpha_{app3} = 0.60$ obtained heuristically.

LS values for automated computer-based comparison of simulated-experimental data (see table 4) are driven by windowing the potential (that encompasses six, five and three reduction processes at GC, Au and Pt electrode, respectively) for each reduction process. LS values for

reduction processes at more negative potential regions at GC and Au electrodes probe the departure of experimental data from the theory, where data comparisons at GC show the better agreement than Au electrode. In contrast, LS values $\sim 60\%$ for II process at Pt electrode suggest that agreement is poor in the theory-experimental comparison, which is consistent with previous findings [10].

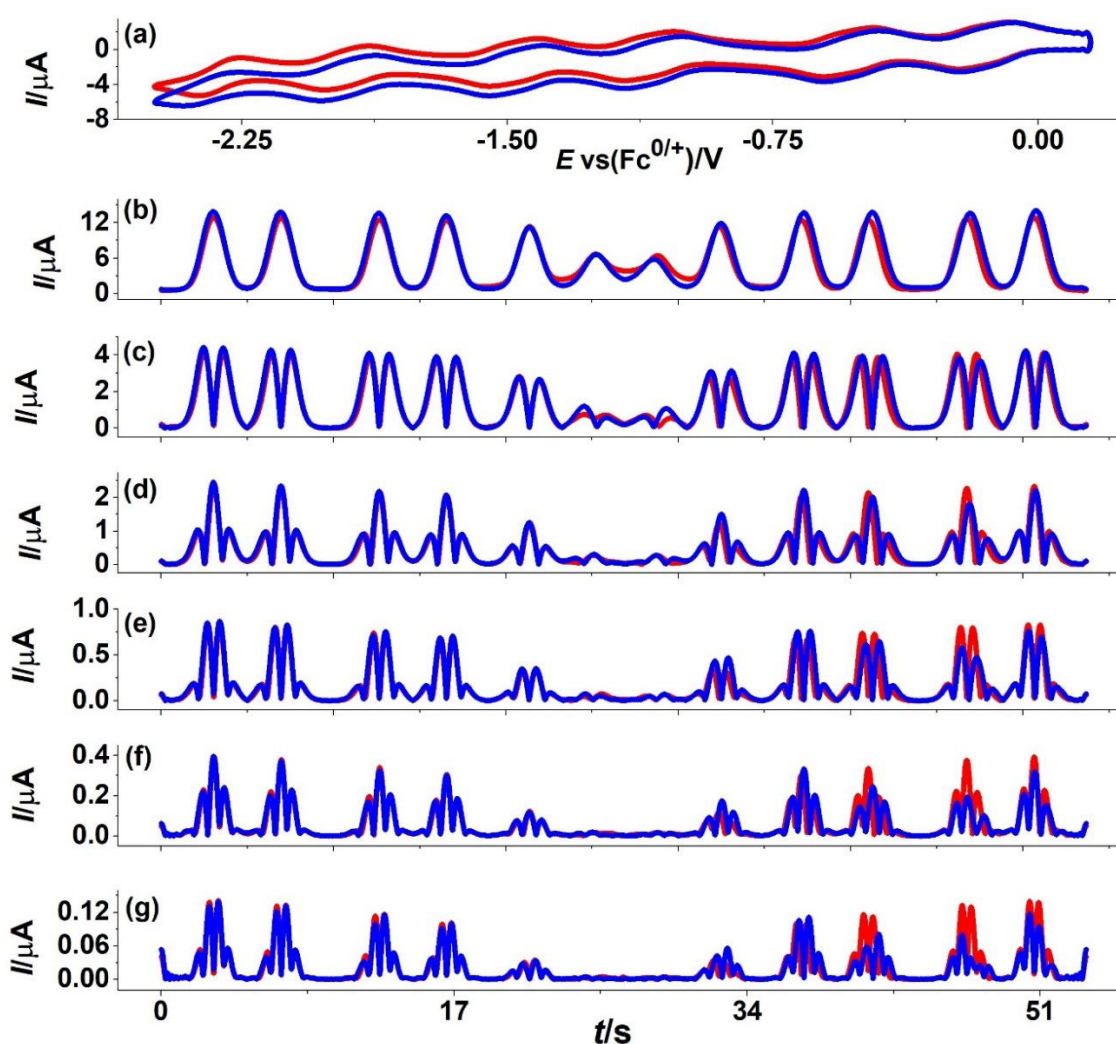


Figure 3. Heuristic comparison of simulated (red line) and experimental (blue line) AC voltammetric data for the $\alpha\text{-}[\text{S}_2\text{W}_{18}\text{O}_{62}]^{4-/-5-/-6-/-7-/-8-/-9-/-10-}$ processes obtained with $\Delta E = 80$ mV, $f = 8.98$ Hz and $\nu = 0.099$ V s^{-1} derived from reduction of 2.5 mM $\alpha\text{-}[\text{S}_2\text{W}_{18}\text{O}_{62}]^{4-}$ in CH_3CN containing 0.50 M $[n\text{-Bu}_4\text{N}][\text{PF}_6]$ at GC electrode. (a) DC component, (b-g) 1st to 6th harmonic components. Other parameters given in Table 3 and text.

3.3 FTAC voltammetric parameterization of the α -[S₂W₁₈O₆₂]^{4-/5-/6-/8-/9-/10-} reduction processes in CH₃CN (0.10 M [*n*-Bu₄N][PF₆])

A lower concentration (0.10 M) of [*n*-Bu₄N][PF₆] supporting electrolyte also was used to investigate whether the lower impact of ion-pairing predicted to present relative to the 0.50 M electrolyte studies described above had a significant impact [10].

Table 5. Electrode kinetic parameters^a derived from heuristic and computer based automated comparison of simulated and experimental FTAC voltammetric data at GC, Au and Pt electrodes for the reduction of 2.5 mM α -[S₂W₁₈O₆₂]⁴⁻ in CH₃CN containing 0.10 M [*n*-Bu₄N][PF₆].

(a) Reversible potential:

Electrode	f (Hz)	R_u^b	Simulation method	E_{app}^0						
				V vs Fc ⁰⁺						
GC	8.98	625	Heuristic	-0.232	-0.608	-1.178	-1.563	-2.046	-2.409	
			Automated	Range	-0.238 to -0.226	-0.614 to -0.600	-1.182 to -1.170	-1.567 to -1.554	-2.050 to -2.036	-2.414 to -2.399
				Est.	-0.233	-0.604	-1.172	-1.557	-2.040	-2.406
	26.95	580	Heuristic	-0.232	-0.608	-1.178	-1.563	-2.046	-2.409	
			Automated	Range	-0.236 to -0.224	-0.612 to -0.599	-1.184 to -1.172	-1.569 to -1.556	-2.052 to -2.038	-2.411 to -2.394
				Est.	-0.230	-0.606	-1.181	-1.561	-2.044	-2.401
Au	8.98	600	Heuristic	-0.232	-0.606	-1.174	-1.566	-2.083	^c	
			Automated	Range	-0.239 to -0.225	-0.612 to -0.599	-1.180 to -1.168	-1.570 to -1.548	-2.093 to -2.073	--
				Est.	-0.232	-0.601	-1.174	-1.562	2.076	--
	26.95	580	Heuristic	-0.232	-0.606	-1.174	-1.566	-2.083	^c	
			Automated	Range	-0.236 to -0.223	-0.612 to -0.599	-1.180 to -1.168	-1.570 to -1.550	-2.093 to -2.073	--
				Est.	-0.230	-0.603	-1.173	-1.563	2.074	--
Pt	8.98	602	Heuristic	-0.233	-0.606	^d	^c	^c	^c	
			Automated	Range	-0.238 to -0.228	-0.612 to -0.600	--	--	--	--
				Est.	-0.232	-0.604	--	--	--	--
	26.95	552	Heuristic	-0.233	-0.606	^d	^c	^c	^c	
			Automated	Range	-0.238 to -0.228	-0.612 to -0.600	--	--	--	--
				Est.	-0.231	-0.605	--	--	--	--

^aOther Parameters used in the simulations are: $A_{GC} = 8.0 \times 10^{-3} \text{ cm}^2$, $A_{Au} = 8.1 \times 10^{-3} \text{ cm}^2$, $A_{Pt} = 8.0 \times 10^{-3} \text{ cm}^2$, $\Delta E = 80 \text{ mV}$, $D = 6.3 \times 10^{-6} \text{ cm}^2 \text{ s}^{-1}$, $T = 295 \text{ K}$, $v_{GC} = 0.099 \text{ V s}^{-1}$, $v_{Au} = 0.100 \text{ V s}^{-1}$ and $v_{Pt} = 0.057 \text{ V s}^{-1}$, $f_{GC,Au \text{ and } Pt} = 8.98 \text{ and } 26.95 \text{ Hz}$.

^b varies due to slight variability in electrode arrangement ^c process is not observed due to lower negative potential limit ^d poorly defined.

(b) Heterogeneous charge transfer kinetics:

Electrode	f (Hz)	Simulation method	k_{app}^0						
			k_{app1}^0	k_{app2}^0	k_{app3}^0	k_{app4}^0	k_{app5}^0	k_{app6}^0	
			cm s^{-1}						
GC	8.98	Heuristic	≥ 0.19	0.14 ^a	0.058 ^a	0.055	0.031	0.02	
		Automated	Range	0.12 to 0.25	0.090 to 0.165	0.035 to 0.065	0.043 to 0.068	0.023 to 0.042	0.010 to 0.030
			Est.	0.18 ^b	0.11 ^c	0.046 ^c	0.062	0.031	0.018
	26.95	Heuristic	0.18 ^a	0.13 ^a	0.060	0.056	0.034	0.024	
		Automated	Range	0.12 to 0.25	0.090 to 0.165	0.040 to 0.070	0.043 to 0.068	0.023 to 0.042	0.010 to 0.030
			Est.	0.16 ^c	0.11 ^c	0.062	0.062	0.036	0.025
Au	8.98	Heuristic	0.11	0.11 ^a	0.024	0.0018 ^d	0.0003 ^d	^e	
		Automated	Range	0.07 to 0.16	0.07 to 0.16	0.016 to 0.030	0.0007 to 0.005	0.0001 to 0.0008	--
			Est.	0.119	0.087 ^c	0.026	0.0045 ^d	0.0005 ^d	--
	26.95	Heuristic	0.11	0.11	0.020 ^a	0.0018 ^d	0.0003 ^d	^e	
		Automated	Range	0.07 to 0.16	0.07 to 0.16	0.016 to 0.030	0.0007 to 0.005	0.0001 to 0.0008	--
			Est.	0.119	0.10	0.029 ^c	0.0047 ^d	0.00047 ^d	--
Pt	8.98	Heuristic	0.077	0.022 ^a	0.00001 ^f	^e	^e	^e	
		Automated	Range	0.060 to 0.095	0.012 to 0.030	--	--	--	--
			Est.	0.075	0.017 ^c	--	--	--	--
	26.95	Heuristic	0.075	0.021 ^a	0.00001 ^f	^e	^e	^e	
		Automated	Range	0.060 to 0.095	0.012 to 0.030	--	--	--	--
			Est.	0.072	0.016 ^c	--	--	--	--

^a determined from reduction component of data only ^b near reversible limit so uncertainty substantial ^c derived from use of all data even though asymmetry is present in reduction and oxidation components ^d estimated from 1st to 3rd harmonic components ^e process is not observed due to lower negative potential limit ^f poorly defined.

(c) Charge transfer coefficient:

Electrode	f (Hz)	Simulation method	α_{app1}	α_{app2}	α_{app3}	α_{app4}	α_{app5}	α_{app6}
GC	8.98	Heuristic	^a	0.60	0.70	0.64	0.60	0.50
		Automated	Range	0.40 to 0.70				
	Est.		0.64 ^b	0.55	0.60 ^c	0.63	0.57	0.57 ^c
	26.95	Heuristic	0.55	0.58	0.60	0.60	0.60	0.50
		Automated	Range	0.40 to 0.70				
	Est.		0.67 ^c	0.51 ^c	0.49 ^c	0.53 ^c	0.43 ^c	0.53
Au	8.98	Heuristic	0.60	0.60	0.55	0.50 ^d	0.50 ^d	^e
		Automated	Range	0.40 to 0.70				
	Est.		0.57	0.65	0.57	0.42 ^d	0.60 ^d	--
	26.95	Heuristic	0.60	0.60	0.52	0.50 ^d	0.50 ^d	^e
		Automated	Range	0.40 to 0.70				
	Est.		0.64	0.60	0.59	0.41 ^d	0.45 ^d	--
Pt	8.98	Heuristic	0.57	0.50	0.50 ^f	^e	^e	^e
		Automated	Range	0.40 to 0.70	0.44 to 0.60	--	--	--
	Est.		0.60	0.55 ^c	--	--	--	--
	26.95	Heuristic	0.58	0.50	0.50 ^f	^e	^e	^e
		Automated	Range	0.50 to 0.67	0.44 to 0.65	--	--	--
	Est.		0.56	0.52	--	--	--	--

^a too close to reversible limit to be determined ^b near reversible limit so uncertainty substantial ^c all data used ^d estimated from 1st to 3rd harmonic components ^e process is not observed due to lower negative potential limit ^f poorly defined.

Table 5 summarises the thermodynamic and electrode kinetic parameters obtained using the same heuristic and computer supported data optimisation protocols applied above using 0.50 M $[n\text{-Bu}_4\text{N}][\text{PF}_6]$ as the supporting electrolyte cases. Clearly, as expected and as revealed from comparison of data in Tables 3 and 5, the uncompensated resistance has increased with use of the lower 0.10 M supporting electrolyte concentration. There is also a negative shift in E_{app}^0 with 0.10 M of $[n\text{-Bu}_4\text{N}][\text{PF}_6]$, $E_{\text{app1}}^0 = -0.232$, $E_{\text{app2}}^0 = -0.608$, $E_{\text{app3}}^0 = -1.178$, $E_{\text{app4}}^0 = -1.563$ V, $E_{\text{app5}}^0 = -2.046$ and $E_{\text{app6}}^0 = -2.409$ V vs $\text{Fc}^{0/+}$ (versus $E_{\text{app1}}^0 = -0.215$ V, $E_{\text{app2}}^0 = -0.592$ V, $E_{\text{app3}}^0 = -1.156$ V, $E_{\text{app4}}^0 = -1.539$ V, $E_{\text{app5}}^0 = -2.006$ V and $E_{\text{app6}}^0 = -2.344$ V vs $\text{Fc}^{0/+}$ in the case of 0.50 M $[n\text{-Bu}_4\text{N}][\text{PF}_6]$) were used in heuristic simulations. Agreement between simulated and experimental data that correspond to each reduction process also is improved as demonstrated by higher LS values (see Table 4) from automated data optimisation results and visual inspection of heuristic comparison of experimental and simulated data shown Figure 3 versus Figure 4 at the GC electrode. The values of k_{app1}^0 , k_{app2}^0 , k_{app3}^0 , k_{app4}^0 , k_{app5}^0 and k_{app6}^0 generally increase on use of the lower electrolyte concentration. For example, k_{app}^0 values of ≥ 0.10 , 0.080, 0.053, 0.041, 0.012 and 0.002 cm s^{-1} with 0.50 M electrolyte present increase to ≥ 0.19 , 0.14, 0.058, 0.055, 0.031 and 0.02 cm s^{-1} for the six processes detected at the GC electrode according to heuristically derived data at 8.98 Hz (see Tables 3 and 5).

Analogous electrolyte dependence is found at Au (Figures S6 and S7) and Pt electrodes (Figure S8) to that at the GC one. For example, according the heuristic method of data analysis, the k_{app1}^0 , k_{app2}^0 and k_{app3}^0 values increase from 0.053, 0.039 and 0.017 cm s^{-1} to 0.11, 0.11 and 0.024 cm s^{-1} respectively at the Au electrode using data collected at 8.98 Hz on decreasing the supporting electrolyte concentration from 0.50 M to 0.10 M. However, it should be noted that the 4th and 5th processes at this electrode are very slow and display pronounced departures from

Butler- Volmer prediction at both concentrations of $[n\text{-Bu}_4\text{N}][\text{PF}_6]$ in both FTAC and DC voltammetry (Figures S2, S3, S6 and S7).

While decreased, some residual asymmetry remains in the reduction-oxidation components of the higher order AC harmonics (see Figures 4, S5, S6, S7 and S8) obtained with 0.10 M electrolyte concentration. This leads to smaller but nevertheless still detectable systematic differences in electrode kinetic evaluations being detected in heuristic versus automated data optimisation methods.

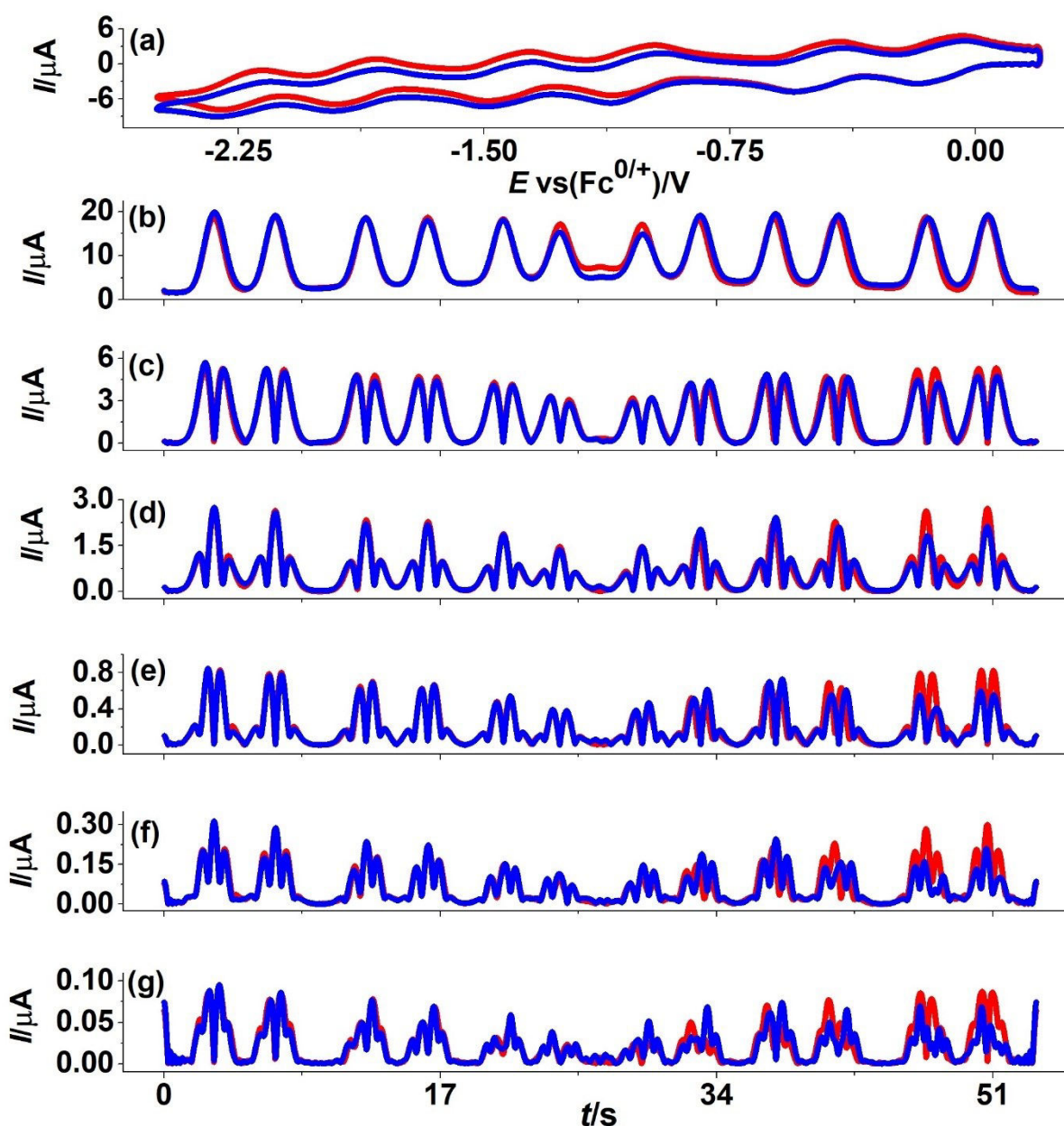


Figure 4. Heuristic comparison of simulated (red line) and experimental (blue line) AC voltammetric data for the α -[S₂W₁₈O₆₂]^{4-/5-/6-/7-/8-/9-/10-} processes obtained with $\Delta E = 80$ mV, $f = 8.98$ Hz and $\nu = 0.099$ V s⁻¹ derived from reduction of 2.5 mM α -[S₂W₁₈O₆₂]⁴⁻ in CH₃CN containing 0.10 M [*n*-Bu₄N][PF₆] at GC electrode. (a) DC component, (b-g) 1st to 6th harmonic components. Other parameters given in Table 5 and text.

3.4. Origin of departures from the Butler- Volmer model of electron transfer

There are a series of observations that emerge from studying the electrode kinetics of up to six well resolved processes that encompass over a 2V potential range when reduction of α -[S₂W₁₈O₆₂]⁴⁻ occurs in CH₃CN containing [n-Bu₄N][PF₆] as the supporting electrolyte. These six one electron processes can be modelled as α -[S₂W₁₈O₆₂]^{4-/5-/6-/7-/8-/9-/10-} electron transfer reactions using the Butler- Volmer relationship. Indeed, it is access to this wide potential reduction range feature involving an overall large change in charge from 4- to 10- that is possible with POMs and also very informative in understanding electrode and electrolyte dependent nuances in the voltammetry that are summarised in points (a) to (e) listed below.

- (a) The heterogeneous charge transfer rate constant decreases as each electron transfer process is encountered at a progressively more negative potentials ($k_{app1}^0 > k_{app2}^0 > k_{app3}^0 > k_{app4}^0 > k_{app5}^0 > k_{app6}^0$). Thus, the [S₂W₁₈O₆₂]^{4-/5-} process is reversible or close to reversible while the α -[S₂W₁₈O₆₂]^{9-/10-} process is kinetically very sluggish.
- (b) Non-conformance to the Butler-Volmer model progressively increases with respect to the process order as in (a). Thus, processes I and II that are close to reversible complying well to predictions of this model, whereas slow processes III to VI that occur at more negative potentials display a significant level of non-ideality. However, interestingly while the α -[S₂W₁₈O₆₂]^{4-/5-/6-} processes conform very well with the Butler-Volmer model when the potential is switched immediately after the α -[S₂W₁₈O₆₂]^{5-/6-} process, the level of agreement decreases somewhat when the potential is switched at very negative potentials after the α -[S₂W₁₈O₆₂]^{9-/10-} process.
- (c) k_{app}^0 increases as the [n-Bu₄N][PF₆] electrolyte concentration is decreased from 0.50 to 0.10 M.

- (d) k_{app}^0 values are highest at GC electrodes, and smallest at Pt, with values at Au being intermediate between GC and Pt. The level of conformance with the Butler-Volmer model also follows the order GC > Au > Pt.
- (e) The non-conformance of data with the Butler-Volmer model translated into apparently data analysis method dependent values of k_{app}^0 .

In principle, the fact that the level of non-conformance to the Butler-Volmer model for all process increases significantly when the voltammetric experiment includes the potential region where $[S_2W_{18}O_{62}]^{7-}$ and further reduced forms are generated suggests that surface accumulation of this reduced POM or a decomposition product may lead to electrode modification that causes electrode blockage. If indeed this does occur, then the resultant mass change during the voltammetry can be measured by the EQCM technique via a change in the oscillation frequency of the quartz crystal working electrode [51]. In this study, the frequency (mass) of a gold quartz crystal working electrode was monitored during the course of a DC cyclic voltammetric experiment ($\nu = 0.050 \text{ V s}^{-1}$) undertaken with 1.0 mM α - $[S_2W_{18}O_{62}]^{4-}$ in CH_3CN (0.50 M $[n\text{-Bu}_4N][PF_6]$) over the potential region where five reduction processes occur at this electrode surface (Figure 5a).

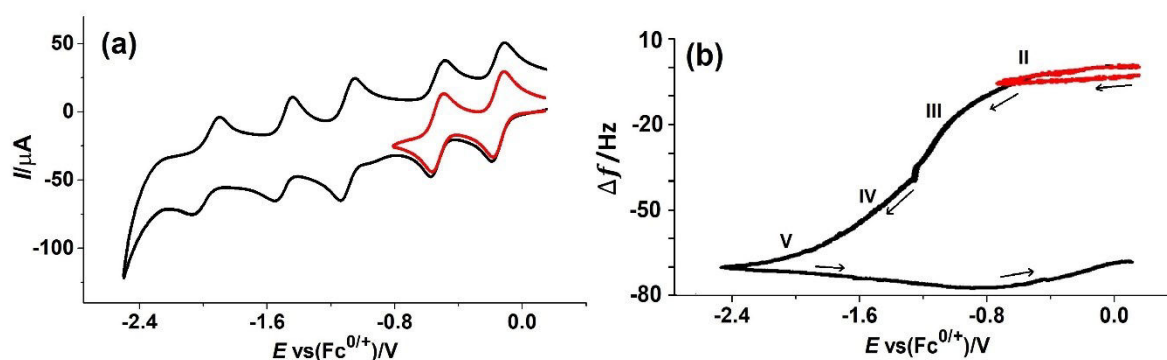


Figure 5. EQCM data obtained for the reduction of 1.0 mM α - $[S_2W_{18}O_{62}]^{4-}$ in CH_3CN (0.50 M $[n\text{-Bu}_4N][PF_6]$) at a scan rate of 0.050 V s^{-1} with an Au quartz crystal electrode over the

potential region where five (black) α -[S₂W₁₈O₆₂]^{4-/5-/6-/7-/8-/9-} and initial two α -[S₂W₁₈O₆₂]^{4-/5-/6-} (red) processes occur. (a) DC cyclic voltammetry (current versus potential) and (b) change frequency (Δf) of the gold quartz crystal versus potential.

As shown in Figure 5b, a negative frequency shift consistent with a mass increase is evident as in the study with [*n*-Bu₄N]₄[PW₁₁O₃₉{Sn(C₆H₄)C≡C(C₆H₄)(N₃C₄H₁₀)}] POM [17]. This mass increase commences at potentials corresponding to the onset of the 2nd α -[S₂W₁₈O₆₂]^{5-/6-} reduction process. The frequency change (mass increase) then continues until the α -[S₂W₁₈O₆₂]^{6-/5-/4-} oxidation processes occur where frequency change a small amount of mass loss is detected. Apparently, accumulation of α -[S₂W₁₈O₆₂]⁷⁻ itself, further reduced forms or their decomposition products occurs at a gold electrode. Probably, the same scenario applies at GC and Pt electrodes, but with electrode dependent characteristics. This surface accumulation phenomenon is not included in the modelling but would explain the asymmetry found in the reduction and oxidation AC components. Since this accumulation continues to increase at potentials where α -[S₂W₁₈O₆₂]⁷⁻ and even higher negative charge containing species are generated, enhanced departures in experimental versus simulated data comparisons are anticipated to progressively increase for the α -[S₂W₁₈O₆₂]^{6-/7-}, α -[S₂W₁₈O₆₂]^{7-/8-}, α -[S₂W₁₈O₆₂]^{8-/9-} and α -[S₂W₁₈O₆₂]^{9-/10-} processes which occur at more negative potentials and longer times after the onset of the α -[S₂W₁₈O₆₂]^{6-/7-} process.

Results of 10 consecutive voltammetric experiments encompassing either reduction processes I and II or I, II and III at GC, Au and Pt electrodes in CH₃CN (0.50 M [*n*-Bu₄N][PF₆]) with 1.0 mM α -[S₂W₁₈O₆₂]⁴⁻ are displayed in Figure 6, without polishing the electrode between experiments. If the potential range is limited to processes I and II, then each cyclic voltammetric experiment 1 to 10 remains essentially unchanged (Figures 6i-a, 6ii-a and 6iii-a).

In contrast, when process III is included (see Figures 6i-b,c, 6ii-b,c and 6iii-b,c) each experiment displays a progressively enhanced level of change from peak (linear diffusion controlled) to sigmoidal shape (radial diffusion controlled) as occurs in the voltammetry of metalloproteins or metalloenzymes [52-54] or with surface active diazonium modified POMs [17] when denaturation/decomposition and consequently surface blocking occur.

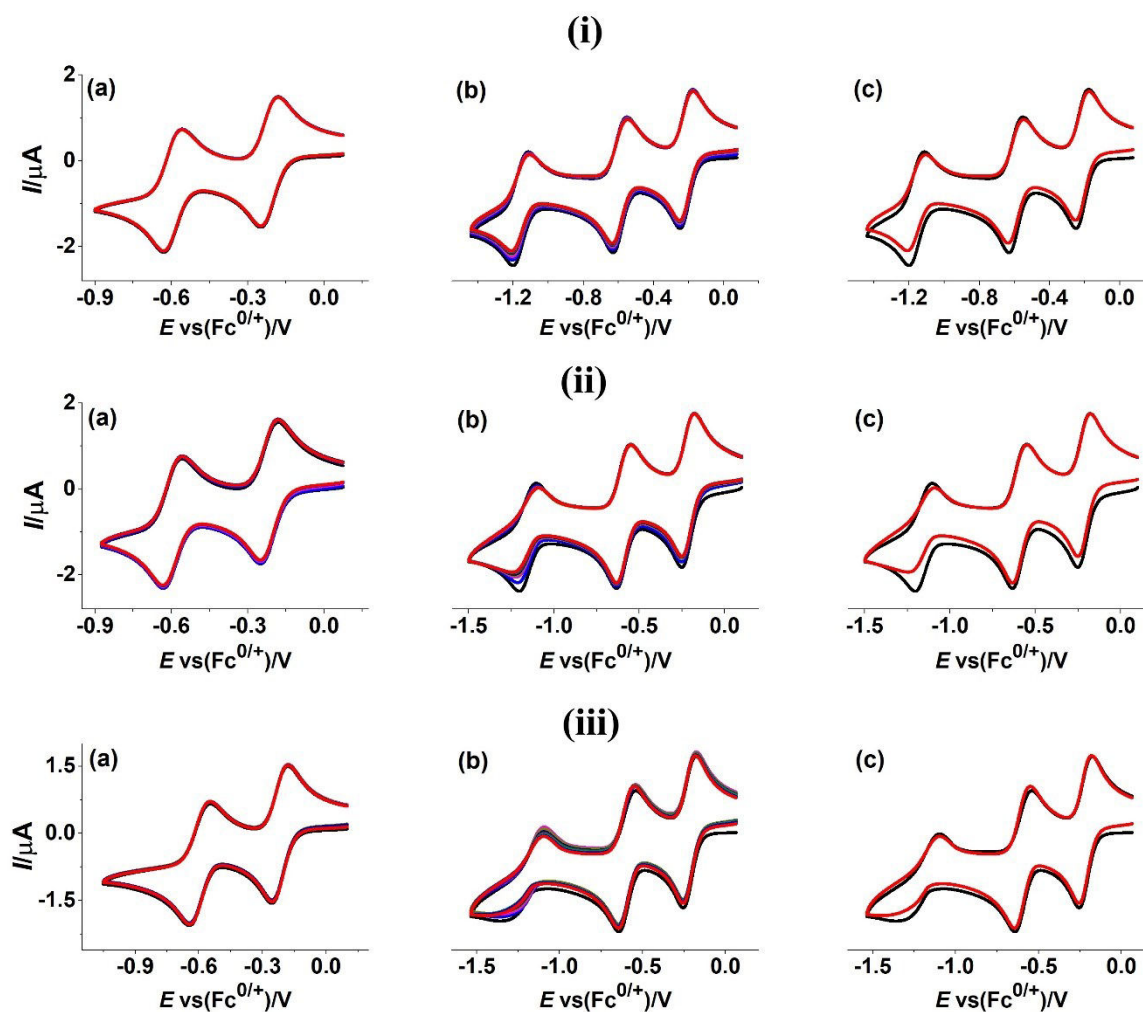


Figure 6. Repetitive cycling of the potential in voltammetry of 1.0 mM α -[S₂W₁₈O₆₂]⁴⁻ in CH₃CN (0.50 M [*n*-Bu₄N][PF₆]) at (i) GC, (ii) Au and (iii) Pt electrodes without polishing the electrode after the first cycle. (a) and (b) represent the first two and three one-electron transfer processes, respectively and (c) represent the 1st and 10th experiments for three one-electron transfer processes.

In a previous study, Richardt et al reported that only two well resolved rotating disc electrode voltammograms were observed at a GC electrode when 1.0 mM γ^* -[S₂W₁₈O₆₂]⁴⁻ is reduced in CH₃CN (0.10 M Bu₄NClO₄) [11]. The absence of processes at a more negative potential was postulated due to surface blocking by accumulation of a product of the 2nd process at the higher current densities associated with rotating disc electrode voltammetry. The 3rd process was detectable with the addition of 5% water which was proposed to suppress the product formation from the 2nd process. In contrast, RDE voltammetry in this work (CH₃CN/0.50 M [*n*-Bu₄N][PF₆]) with a higher electrolyte concentration and a lower POM concentration allow six processes to be detected at a GC electrode (Figure 7a) with half wave potentials of -0.22, -0.61, -1.16, -1.54, -2.02, -2.37 V vs Fc^{0/+} for processes I, II, III, IV, V and VI, respectively. However, electrode blocking is more pronounced at Au and Pt electrodes, resulting in only 4 (Figure 7b) and 2 processes (Figure 7c) instead of the 6 obtained at a GC electrode.

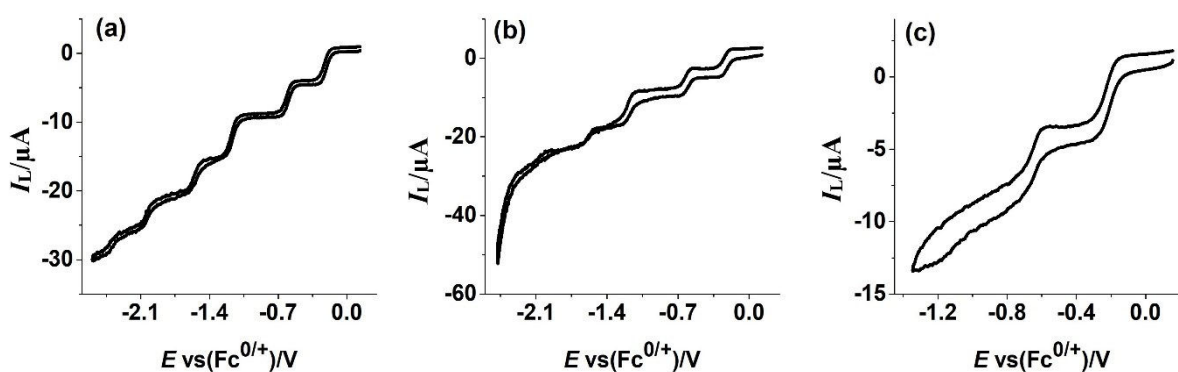


Figure 7. Rotating disk electrode voltammograms for the reduction of 0.25 mM α -[S₂W₁₈O₆₂]⁴⁻ in CH₃CN (0.50 M [*n*-Bu₄N][PF₆]) at (a) GC, (b) Au and (c) Pt electrodes, respectively. $\nu = 0.050$ V s⁻¹, rotation rate 52.4 s⁻¹.

Based on evidence provided from the above DC voltammetric and EQCM experiments, it is apparent that surface accumulation and electrode blockage accompanies generation of the three electron reduced α -[S₂W₁₈O₆₂]⁷⁻ and further reduced forms with the order of impact on the

subsequent voltammetry being Pt > Au > GC. As a consequence of adsorption, well defined Pt electrode electrochemistry is restricted to first two process, with the third process being ill-defined. The voltammetric impact at the Au electrode by surface modification is the introduction of asymmetry in the reduction-oxidation components, which is less extreme at the GC electrode and even more extreme in the case of the Pt electrode.

An understanding that the origin of the asymmetry in some of the voltammograms is based on surface interaction of a product of reduction, advises that undertaking data analysis for estimation of k_{app}^0 on the reduction component of the data set, as was done in the heuristic form of data analysis, is justified. Thus, the experimenter biased method used in this study generates what can be considered to be superior estimates of the electrode kinetic parameters. Based on this conclusion, the automated data optimisation analysis approach could be restricted to only the reduction data set to generate a new set of E_{app}^0 , k_{app}^0 and α_{app} values that as might be anticipated equate almost exactly with those generated via heuristic analysis. The approach we have adopted recently [10] to parameterisation of complex problems in using a heuristic data analysis method prior to implementation automated data optimisation methods is again demonstrated in this study to be highly valuable. The downside is that the heuristic approach is exceptionally tedious and time consuming for the experimenter. The challenge now is to implement artificial intelligence/ machine learning/ pattern recognition into data optimisation methods used in voltammetry that contain knowledge of the experimenter's experience in as has been implemented for simple problems [49, 50].

In POM electrochemistry, the role ion-pairing must be significant. In this study, ion pairing between highly charged oxidised α -[S₂W₁₈O₆₂]⁴⁻ and reduced species α -[S₂W₁₈O₆₂]ⁿ⁻ (n = 5 to 10) and cation ($[n - \text{Bu}_4\text{N}]^+$) of supporting electrolyte ($[n\text{-Bu}_4\text{N}][\text{PF}_6]$) will be enhanced the more negative the charge on the POM. Accordingly, the electron transfer process should

be represented by a square-scheme mechanism which incorporates the coupling of ion-pairing with electron transfer [10, 48]. This mechanism also provides an explanation as to why k_{app}^0 decreases with an increase in supporting electrolyte concentration as the $[n\text{-Bu}_4\text{N}]^+$ concentration is decreased from 0.50 M to 0.10 M. The combination of stronger ion pairing in the reduced relative to oxidised for a very sluggish POM processes as in a square reaction scheme could in its own right explain the asymmetry in reduced and oxidised components of FTAC voltammetric data as noted in reference [10]. However, this study reveals that surface interaction features also contribute to and may even be the dominant contributor to this phenomenon. A positive shift in thermodynamically based E_{app}^0 also is evident (see table 2) with the higher 0.50 M concentration of supporting electrolyte ($[n\text{-Bu}_4\text{N}][\text{PF}_6]$), which is a consequence of enhanced ion-pairing differences between oxidised and reduced forms of each redox couple. Supporting electrolyte concentration dependence of ion pairing also has been established in previous studies of the electrochemistry of POMs [10, 45].

The influence of the double layer region which contains a very high concentration of $[n\text{-Bu}_4\text{N}]^+$ at the very negative potentials where processes V and VI occur also could be an important contributor to the increasingly sluggish electron transfer kinetics found as more electrons and hence negative charges are added to the POM. The electrolyte concentration and potential dependent effect are related to the point of zero charge (PZC) which in turn is electrode material dependent [39]. In this study, k_{app}^0 for all processes at all electrode materials increase when the $[n\text{-Bu}_4\text{N}][\text{PF}_6]$ supporting electrolyte concentration decreased from 0.50 M to 0.10 M, because the diminution of the ion-pairing effect that is probably magnified significantly for all reduction processes that occur at more negative potentials than the PZC.

It has been well established that oxidised forms of negatively charged POMs can adsorb spontaneously at carbon, Au and Pt electrodes [55-59]. The combination of very negative

potentials where $[n\text{-Bu}_4\text{N}]^+$ concentrations in the double layer region are considerably higher than in bulk solution, extensive reduction leads to high charges on the POMs may even provide scenarios where the solubility product is exceeded at the solution-electrode interface leading to precipitation of POM or specific adsorption to give a chemically modified electrode which partially blocks the electrode and alters the mass transport thereby leading to departure from theoretical predictions based Butler-Volmer electrode kinetics and linear diffusion for POM processes occurring at negative potentials as found in this and other studies [17]. Unfortunately, corrections for the double layer effect were not possible as the PZC value at GC, Au and Pt electrodes has not been established, although potentials more negative than the onset of process II should be more negative than the PZC and hence provide conditions favouring of a $[n\text{-Bu}_4\text{N}]^+$ dominated double layer region. Studies by Fawcett et al [23] on double layer at the mercury electrode/acetonitrile interface demonstrated the strong electrolyte cation (tetraalkylammonium, TAA⁺) distribution in the electrode-solution double layer interfacial region at a far cathodic potential which is far from the PZC. As a consequence, large double layer capacitance at more negative potential compared to minimum at or close to PZC was evident. These findings should be relevant to our study, and the $\alpha\text{-[S}_2\text{W}_{18}\text{O}_{62}]^{9-/10-}$ process at negative potential close to the solvent limit should be influenced more by the double layer effect compared to $\alpha\text{-[S}_2\text{W}_{18}\text{O}_{62}]^{4-/5-}$ process near to the PZC resulting the progressive increase in complexity for processes at more negative potential than $\alpha\text{-[S}_2\text{W}_{18}\text{O}_{62}]^{5-/6-}$ process.

5 Conclusion

Electron transfer kinetics for the reduction processes of $\alpha\text{-[S}_2\text{W}_{18}\text{O}_{62}]^{4-}$ were determined by FTAC voltammetry using heuristic and computer-assisted automated data analysis approaches where GC carbon electrode possessed rapid kinetics than the other two metal electrodes (e.g.,

Au and Pt). Increased kinetic values were observed at all electrodes when the concentration of $[n\text{-Bu}_4\text{N}][\text{PF}_6]$ change from 0.50 to 0.10 M, which probably is the result of availability of the more free species ($\alpha\text{-[S}_2\text{W}_{18}\text{O}_{62}]^{4-}$, $\alpha\text{-[S}_2\text{W}_{18}\text{O}_{62}]^{5-}$ or higher negative charge containing reduced species) at lower cation concentration. Increased departure from ideality was observed in the theory-experimental comparison when wide potential used that encompasses all six rather than initial two processes. Ion-pairing between POM ($\alpha\text{-[S}_2\text{W}_{18}\text{O}_{62}]^{4-}$) or reduced POM species ($\alpha\text{-[S}_2\text{W}_{18}\text{O}_{62}]^{n-}$, $n = 5$ to 10) and cation ($[n\text{-Bu}_4\text{N}]^+$) of the supporting electrolyte could be more influential on reduction processes at more negative potential resulting in the progressive asymmetry in reduced and oxidised components of FTAC voltammetric data. Improved agreement between experimental and simulated data was observed with lower concentration of supporting electrolyte ($[n\text{-Bu}_4\text{N}][\text{PF}_6]$), which is a consequence of diminished ion-pairing demonstrated by negative E_{app}^0 shift. Results of EQCM experiments at a gold quartz crystal electrode and 10 consecutive DC cyclic voltammetric experiments at GC, Au and Pt electrodes demonstrate that surface accumulation of reduced species also contributes to and may even be the dominant contributor to these non-idealities. This surface accumulation starts at potential after 2nd process and continues to increase at higher negative charge containing POM species, which can explain the progressive departures in experimental versus simulated data comparison that encounter for the reduction processes at more negative potential. Another driving factor for progressive complexity is double layer capacitance, which would be larger at more negative potential and more influential for $\alpha\text{-[S}_2\text{W}_{18}\text{O}_{62}]^{9-/10-}$ process than $\alpha\text{-[S}_2\text{W}_{18}\text{O}_{62}]^{4-/5-}$ process near to the PZC.

References:

- [1] J. Li, S.-X. Guo, C.L. Bentley, K. Bano, A.M. Bond, J. Zhang, T. Ueda, Electrode material dependence of the electron transfer kinetics associated with the $[\text{SVW}_{11}\text{O}_{40}]^{3-/4-}(\text{V}^{\text{V/IV}})$ and $[\text{SVW}_{11}\text{O}_{40}]^{4-/5-}(\text{W}^{\text{VI/V}})$ processes in dimethylformamide, *Electrochim. Acta* 201 (2016) 45-56.

-
- [2] J.-i. Nambu, T. Ueda, S.-X. Guo, J.F. Boas, A.M. Bond, Detailed voltammetric and EPR study of protonation reactions accompanying the one-electron reduction of Keggin-type polyoxometalates, $[XV^M_{11}O_{40}]^{4-}$ (X= P, As; M= Mo, W) in acetonitrile, *Dalton Trans.* 39(31) (2010) 7364-7373.
- [3] T. Ueda, J.-i. Nambu, J. Lu, S.-X. Guo, Q. Li, J.F. Boas, L.L. Martin, A.M. Bond, Structurally characterised vanadium (v)-substituted Keggin-type heteropolysulfates $[SVM_{11}O_{40}]^{3-}$ (M= Mo, W): voltammetric and spectroscopic studies related to the V(v)/V(iv) redox couple, *Dalton Trans.* 43(14) (2014) 5462-5473.
- [4] X. López, J.J. Carbó, C. Bo, J.M. Poblet, Structure, properties and reactivity of polyoxometalates: a theoretical perspective, *Chem. Soc. Rev.* 41(22) (2012) 7537-7571.
- [5] J.M. Maestre, X. Lopez, C. Bo, J.-M. Poblet, N. Casan-Pastor, Electronic and magnetic properties of α -keggin anions: A DFT Study of $[XM_{12}O_{40}]^{n-}$, (M= W, Mo; X= Al^{III}, Si^{IV}, P^V, Fe^{III}, Co^{II}, Co^{III}) and $[SiM_{11}VO_{40}]^{m-}$ (M= Mo and W), *J. Am. Chem. Soc.* 123(16) (2001) 3749-3758.
- [6] J.M. Poblet, X. López, C. Bo, Ab initio and DFT modelling of complex materials: towards the understanding of electronic and magnetic properties of polyoxometalates, *Chem. Soc. Rev.* 32(5) (2003) 297-308.
- [7] T. Ueda, Electrochemistry of polyoxometalates: from fundamental aspects to applications, *ChemElectroChem* 5(6) (2018) 823-838.
- [8] D.M. Way, A.M. Bond, A.G. Wedd, Multielectron Reduction of α -[S₂Mo₁₈O₆₂] 4- in Aprotic and Protic Media: Voltammetric Studies, *Inorg. Chem.* 36(13) (1997) 2826-2833.
- [9] J. Zhang, A.M. Bond, D.R. MacFarlane, S.A. Forsyth, J.M. Pringle, A.W. Mariotti, A.F. Glowinski, A.G. Wedd, Voltammetric studies on the reduction of polyoxometalate anions in ionic liquids, *Inorg. Chem.* 44(14) (2005) 5123-5132.
- [10] M.A. Rahman, J. Li, S.-X. Guo, G. Kennedy, T. Ueda, A.M. Bond, J. Zhang, Modelling limitations encountered in the thermodynamic and electrode kinetic parameterization of the α -[S₂W₁₈O₆₂]^{4-/5-/6-} processes at glassy carbon and metal electrodes, *J. Electroanal. Chem.* (2019) 113786.
- [11] P.J. Richardt, R.W. Gable, A.M. Bond, A.G. Wedd, Synthesis and Redox Characterization of the Polyoxo Anion, γ^* -[S₂W₁₈O₆₂] 4-: A Unique Fast Oxidation Pathway Determines the Characteristic Reversible Electrochemical Behavior of Polyoxometalate Anions in Acidic Media, *Inorg. Chem.* 40(4) (2001) 703-709.
- [12] J. Zhang, A.M. Bond, P.J. Richardt, A.G. Wedd, Voltammetric Reduction of alpha- and gamma-[S₂W₁₈O₆₂]⁴⁻ and α -, β -, and γ -[SiW₁₂O₄₀]⁴⁻: isomeric dependence of reversible potentials of polyoxometalate anions using data obtained by novel dissolution and conventional solution-phase processes, *Inorg. Chem.* 43(26) (2004) 8263-71.
- [13] H. Hirabaru, D. Kawamoto, M. Ohnishi, H. Ota, M. Sadakane, K. Yanagisawa, T. Hasegawa, T. Ueda, New path for polyoxometalates: Controlled synthesis and characterization of metal - substituted tungstosulphates, *Eur. J. Inorg. Chem.* (2019).
- [14] D. Sawyer, A. Sobkowiak, J. Roberts Jr, *Electrochemistry for Chemists*, ; John Wiley&Sons, 1995.
- [15] A. Bard, M. Mirkin, In *Electroanalytical chemistry*, by AJ Bard, Marcel Dekker, New York 18 (1984) 243.
- [16] Md Anisur Rahman's unpublished work on " Nuances of the electrochemistry of the α -[S₂W₁₈O₆₂]^{4-/5-/6-} processes at boron doped diamond electrodes, (2020).
- [17] Md Anisur Rahman's unpublished work on "Thermodynamics, electrode kinetics and mechanistic nuances associated with the voltammetric reduction of dissolved
-

- [*n*-Bu₄N]₄[PW₁₁O₃₉{Sn(C₆H₄)C ≡ C(C₆H₄)(N₃C₄H₁₀)}] and a surface confined diazonium derivative"., (2020).
- [18] L.B. Fullmer, P.I. Molina, M.R. Antonio, M. Nyman, Contrasting ion-association behaviour of Ta and Nb polyoxometalates, *Dalton Trans.* 43(41) (2014) 15295-15299.
- [19] J. Gómez-Gil, E. Laborda, J. Gonzalez, A. Molina, R. Compton, Electrochemical and Computational Study of Ion Association in the Electroreduction of PW₁₂O₄₀³⁻, *J. Phys. Chem. C* 121(48) (2017) 26751-26763.
- [20] D.J. Sures, S.A. Serapian, K. Kozma, P.I. Molina, C. Bo, M. Nyman, Electronic and relativistic contributions to ion-pairing in polyoxometalate model systems, *PCCP* 19(13) (2017) 8715-8725.
- [21] A.J. Lucio, S.K. Shaw, J. Zhang, A.M. Bond, Large-Amplitude Fourier-Transformed AC Voltammetric Study of the Capacitive Electrochemical Behavior of the 1-Butyl-3-methylimidazolium Tetrafluoroborate–Polycrystalline Gold Electrode Interface, *J. Phys. Chem. C* 121(22) (2017) 12136-12147.
- [22] F. Silva, C. Gomes, M. Figueiredo, R. Costa, A. Martins, C.M. Pereira, The electrical double layer at the [BMIM][PF₆] ionic liquid/electrode interface—Effect of temperature on the differential capacitance, *J. Electroanal. Chem.* 622(2) (2008) 153-160.
- [23] W. Fawcett, R. Loutfy, Double Layer Structure at the Mercury/Acetonitrile Interface, *Can. J. Chem.* 51(2) (1973) 230-236.
- [24] A. Müller, L. Dloczik, E. Diemann, M.T. Pope, A cyclic voltammetric study of manganese (II) undecatungstosilicate: an illustrative example of the reduction, protonation and disproportionation pathways of transition metal substituted heteropolytungstates in aqueous solution, *Inorg. Chim. Acta* 257(2) (1997) 231-239.
- [25] Y.V. Geletii, B. Botar, P. Kögerler, D.A. Hillesheim, D.G. Musaev, C.L. Hill, An all - inorganic, stable, and highly active tetraruthenium homogeneous catalyst for water oxidation, *Angew. Chem. Int. Ed.* 47(21) (2008) 3896-3899.
- [26] S.-X. Guo, Y. Liu, C.-Y. Lee, A.M. Bond, J. Zhang, Y.V. Geletii, C.L. Hill, Graphene-supported [{Ru₄O₄(OH)₂(H₂O)₄}{γ-SiW₁₀O₃₆}₂]¹⁰⁻ for highly efficient electrocatalytic water oxidation, *Energy Environ. Sci.* 6(9) (2013) 2654-2663.
- [27] I.V. Kozhevnikov, Catalysis by heteropoly acids and multicomponent polyoxometalates in liquid-phase reactions, *Chem. Rev.* 98(1) (1998) 171-198.
- [28] N. Mizuno, K. Yamaguchi, K. Kamata, Epoxidation of olefins with hydrogen peroxide catalyzed by polyoxometalates, *Coord. Chem. Rev.* 249(17-18) (2005) 1944-1956.
- [29] C. Venturello, R. D'ALOISIO, J.J. Bart, M. Ricci, A new peroxotungsten heteropoly anion with special oxidizing properties: synthesis and structure of tetrahexylammonium tetra (diperoxotungsto) phosphate (3-), *J. Mol. Catal.* 32(1) (1985) 107-110.
- [30] J.J. Chen, M.D. Symes, S.C. Fan, M.S. Zheng, H.N. Miras, Q.F. Dong, L. Cronin, High - Performance Polyoxometalate - Based Cathode Materials for Rechargeable Lithium - Ion Batteries, *Adv. Mater.* 27(31) (2015) 4649-4654.
- [31] H.D. Pratt III, T.M. Anderson, Mixed addenda polyoxometalate “solutions” for stationary energy storage, *Dalton Trans.* 42(44) (2013) 15650-15655.
- [32] H.D. Pratt III, N.S. Hudak, X. Fang, T.M. Anderson, A polyoxometalate flow battery, *J. Power Sources* 236 (2013) 259-264.
- [33] H.D. Pratt III, W.R. Pratt, X. Fang, N.S. Hudak, T.M. Anderson, Mixed-metal, structural, and substitution effects of polyoxometalates on electrochemical behavior in a redox flow battery, *Electrochim. Acta* 138 (2014) 210-214.

- [34] S. Himeno, H. Tatewaki, M. Hashimoto, Synthesis, Structure, and Characterization of an α -Dawson-type $[S_2W_{18}O_{62}]^{4-}$ Complex, *Bull. Chem. Soc. Jpn.* 74(9) (2001) 1623-1628.
- [35] A.M. Bond, N.W. Duffy, S.-X. Guo, J. Zhang, D. Elton, Changing the look of voltammetry, ACS Publications, 2005.
- [36] A.A. Sher, A.M. Bond, D.J. Gavaghan, K. Harriman, S.W. Feldberg, N.W. Duffy, S.-X. Guo, J. Zhang, Resistance, capacitance, and electrode kinetic effects in fourier-transformed large-amplitude sinusoidal voltammetry: Emergence of powerful and intuitively obvious tools for recognition of patterns of behavior, *Anal. Chem.* 76(21) (2004) 6214-6228.
- [37] J. Zhang, S.-X. Guo, A.M. Bond, F. Marken, Large-amplitude Fourier transformed high-harmonic alternating current cyclic voltammetry: kinetic discrimination of interfering faradaic processes at glassy carbon and at boron-doped diamond electrodes, *Anal. Chem.* 76(13) (2004) 3619-3629.
- [38] G. Gritzner, J. Kuta, Recommendations on reporting electrode potentials in nonaqueous solvents (Recommendations 1983), *Pure and applied chemistry* 56(4) (1984) 461-466.
- [39] A.a.F. Bard, Larry R, *Electrochemical Methods: Fundamentals and applications*, 2nd ed., Wiley, New York, 2001.
- [40] J. Zhang, S.-X. Guo, A.M. Bond, Discrimination and evaluation of the effects of uncompensated resistance and slow electrode kinetics from the higher harmonic components of a Fourier transformed large-amplitude alternating current voltammogram, *Anal. Chem.* 79(6) (2007) 2276-2288.
- [41] G.F. Kennedy, MECSim software package, 2019.
- [42] A.M. Bond, N.W. Duffy, D.M. Elton, B.D. Fleming, Characterization of nonlinear background components in voltammetry by use of large amplitude periodic perturbations and Fourier transform analysis, *Anal. Chem.* 81(21) (2009) 8801-8808.
- [43] Y.P. Liu, S.X. Guo, A.M. Bond, J. Zhang, Y.V. Geletii, C.L. Hill, Voltammetric Determination of the Reversible Potentials for $\{Ru_4O_4(OH)_2 \cdot 4(H_2O)\}(\gamma-SiW_{10}O_{36})(2)^{(10-)}$ over the pH Range of 2-12: Electrolyte Dependence and Implications for Water Oxidation Catalysis, *Inorg. Chem.* 52(20) (2013) 11986-11996.
- [44] S.X. Guo, S.W. Feldberg, A.M. Bond, D.L. Callahan, P.J.S. Richardt, A.G. Wedd, Systematic approach to the quantitative voltammetric analysis of the Fe^{III}/Fe^{II} component of the $\alpha(2)-Fe(OH_2)P_2W_{17}O_{61}^{(7-/8-)}$ reduction process in buffered and unbuffered aqueous media, *J. Phys. Chem. B* 109(43) (2005) 20641-20651.
- [45] J. Li, C.L. Bentley, A.M. Bond, J. Zhang, T. Ueda, Influence of 1-butyl-3-methylimidazolium on the electron transfer kinetics associated with the $[SVW_{11}O_{40}]^{3-/4-}(V^{V/IV})$ and $[SVW_{11}O_{40}]^{4-/5-}(W^{VI/V})$ processes in dimethylformamide, *J. Electroanal. Chem.* 779 (2016) 67-74.
- [46] K. Bano, J. Zhang, A.M. Bond, P.R. Unwin, J.V. Macpherson, Diminished Electron Transfer Kinetics for $[Ru(NH_3)_6]^{3+/2+}$, $[\alpha-SiW_{12}O_{40}]^{4-/5-}$, and $[\alpha-SiW_{12}O_{40}]^{5-/6-}$ Processes at Boron-Doped Diamond Electrodes, *J. Phys. Chem. C* 119(22) (2015) 12464-12472.
- [47] S.-X. Guo, A.M. Bond, J. Zhang, Fourier transformed large amplitude alternating current voltammetry: principles and applications, *Review of Polarography* 61(1) (2015) 21-32.
- [48] J. Li, A.M. Bond, J. Zhang, Probing electrolyte cation effects on the electron transfer kinetics of the $[\alpha-SiW_{12}O_{40}]^{4-/5-}$ and $[\alpha-SiW_{12}O_{40}]^{5-/6-}$ processes using a boron-doped diamond electrode, *Electrochim. Acta* 178 (2015) 631-637.
- [49] S. Marsland, *Machine learning: an algorithmic perspective*, Chapman and Hall/CRC2014.
- [50] M. Stephenson, S. Amarasinghe, M. Martin, U.-M. O'Reilly, Meta optimization: Improving compiler heuristics with machine learning, *ACM sigplan notices* 38(5) (2003) 77-90.

- [51] G. Sauerbrey, The use of quartz oscillators for weighing thin layers and for microweighing, *Z. Phys.* 155 (1959) 206-222.
- [52] V. Bogdanovskaya, M. Tarasevich, R. Hintsche, F. Scheller, Electrochemical transformations of proteins adsorbed at carbon electrodes, *Bioelectrochemistry and Bioenergetics* 19(3) (1988) 581-584.
- [53] D. Pletcher, R. Greff, R. Peat, L. Peter, J. Robinson, *Instrumental methods in electrochemistry*, Elsevier 2001.
- [54] P. Salvatore, D. Zeng, K.K. Karlsen, Q. Chi, J. Wengel, J. Ulstrup, Electrochemistry of Single Metalloprotein and DNA - Based Molecules at Au (111) Electrode Surfaces, *ChemPhysChem* 14(10) (2013) 2101-2111.
- [55] S.-H. Choi, J.-W. Kim, Adsorption properties of Keggin-type polyoxometalates on carbon based electrode surfaces and their electrocatalytic activities, *Bull. Korean Chem. Soc.* 30(4) (2009) 810-816.
- [56] A.Z. Ernst, L. Sun, K. Wiaderek, A. Kolary, S. Zoladek, P.J. Kulesza, J.A. Cox, Synthesis of Polyoxometalate - Protected Gold Nanoparticles by a Ligand - Exchange Method: Application to the Electrocatalytic Reduction of Bromate, *Electroanalysis: An International Journal Devoted to Fundamental and Practical Aspects of Electroanalysis* 19(19 - 20) (2007) 2103-2109.
- [57] Z.P. Guo, D.M. Han, D. Wexler, R. Zeng, H.K. Liu, Polyoxometallate-stabilized platinum catalysts on multi-walled carbon nanotubes for fuel cell applications, *Electrochim. Acta* 53(22) (2008) 6410-6416.
- [58] C. Rong, F.C. Anson, Spontaneous adsorption of heteropolytungstates and heteropolymolybdates on the surfaces of solid electrodes and the electrocatalytic activity of the adsorbed anions, *Inorg. Chim. Acta* 242(1-2) (1996) 11-16.
- [59] B. Wang, S. Dong, Electrochemical study of isopoly- and heteropoly-oxometallates film modified microelectrodes—vi. preparation and redox properties of 12-molybdophosphoric acid and 12-molybdosilicic acid modified carbon fiber microelectrodes, *Electrochim. Acta* 41(6) (1996) 895-902.

Supporting Information

Electrode Material Dependence, Ion-Pairing and the Progressive Increase in Complexity of the α - $[\text{S}_2\text{W}_{18}\text{O}_{62}]^{4-}$ Reduction Processes in Acetonitrile Containing $[n\text{-Bu}_4\text{N}][\text{PF}_6]$ as the Supporting Electrolyte

Md Anisur Rahman^a, Alan M. Bond^{a, b *} and Jie Zhang^{a, b *}

^aSchool of Chemistry, Monash University, Clayton, Victoria 3800, Australia

^bARC Centre of Excellence for Electrochemical Science, Monash University, Clayton, Victoria 3800, Australia

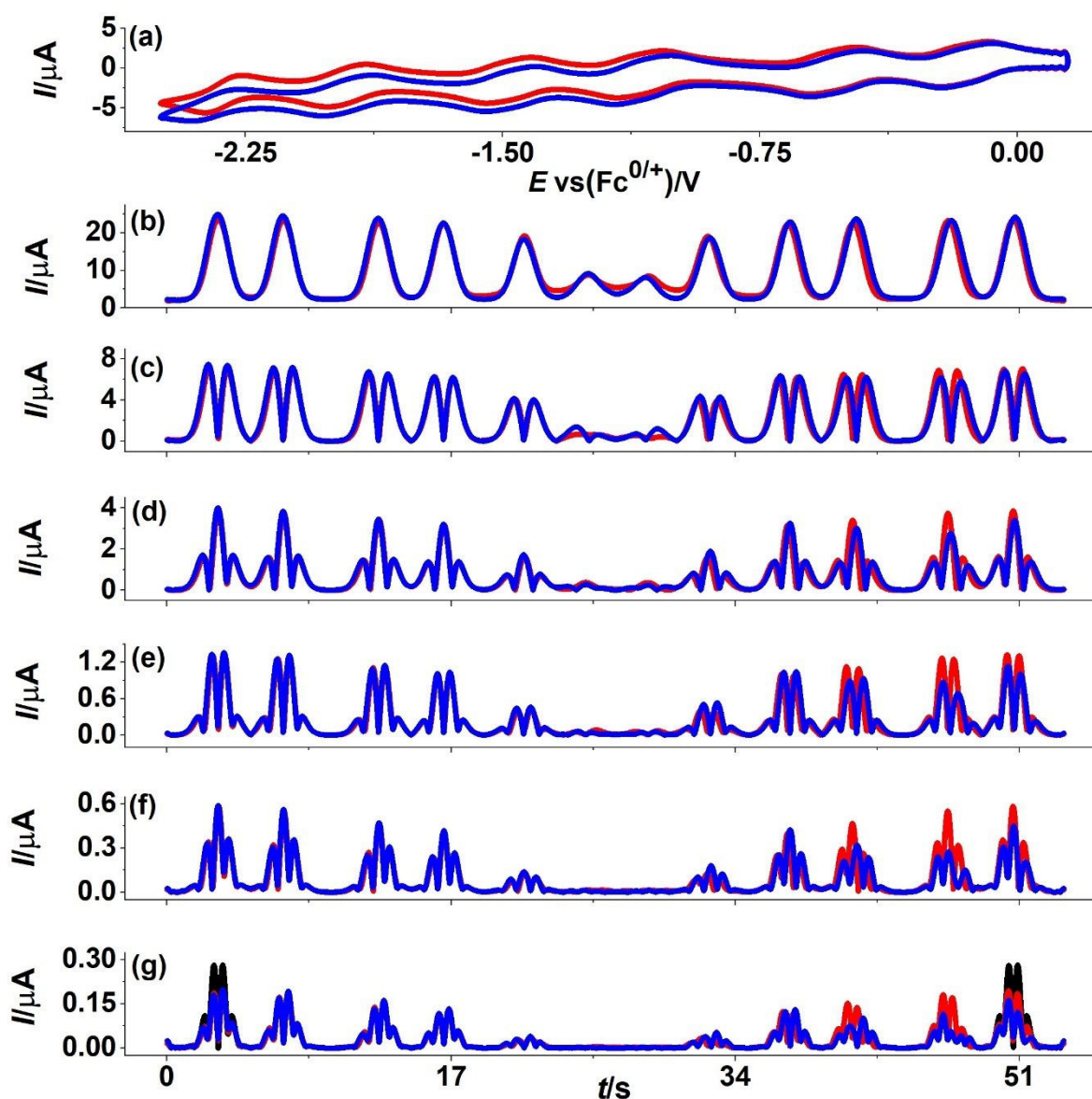


Figure S1. Heuristic comparison of simulated (red line) and experimental (blue line) AC voltammetric data for the α -[S₂W₁₈O₆₂]^{4-/-5-/-6-/-7-/-8-/-9-/-10-} processes obtained with $\Delta E = 80$ mV, $f = 26.95$ Hz and $\nu = 0.099$ V s⁻¹ derived from reduction of 2.5 mM α -[S₂W₁₈O₆₂]⁴⁻ in CH₃CN containing 0.50 M [*n*-Bu₄N][PF₆] at GC electrode. (a) DC component, (b-f) 1st to 5th harmonic components. (g) The 6th harmonic for a reversible process (black line) is also shown for comparison with the experimental one. Other parameters given in Table 3 and text.

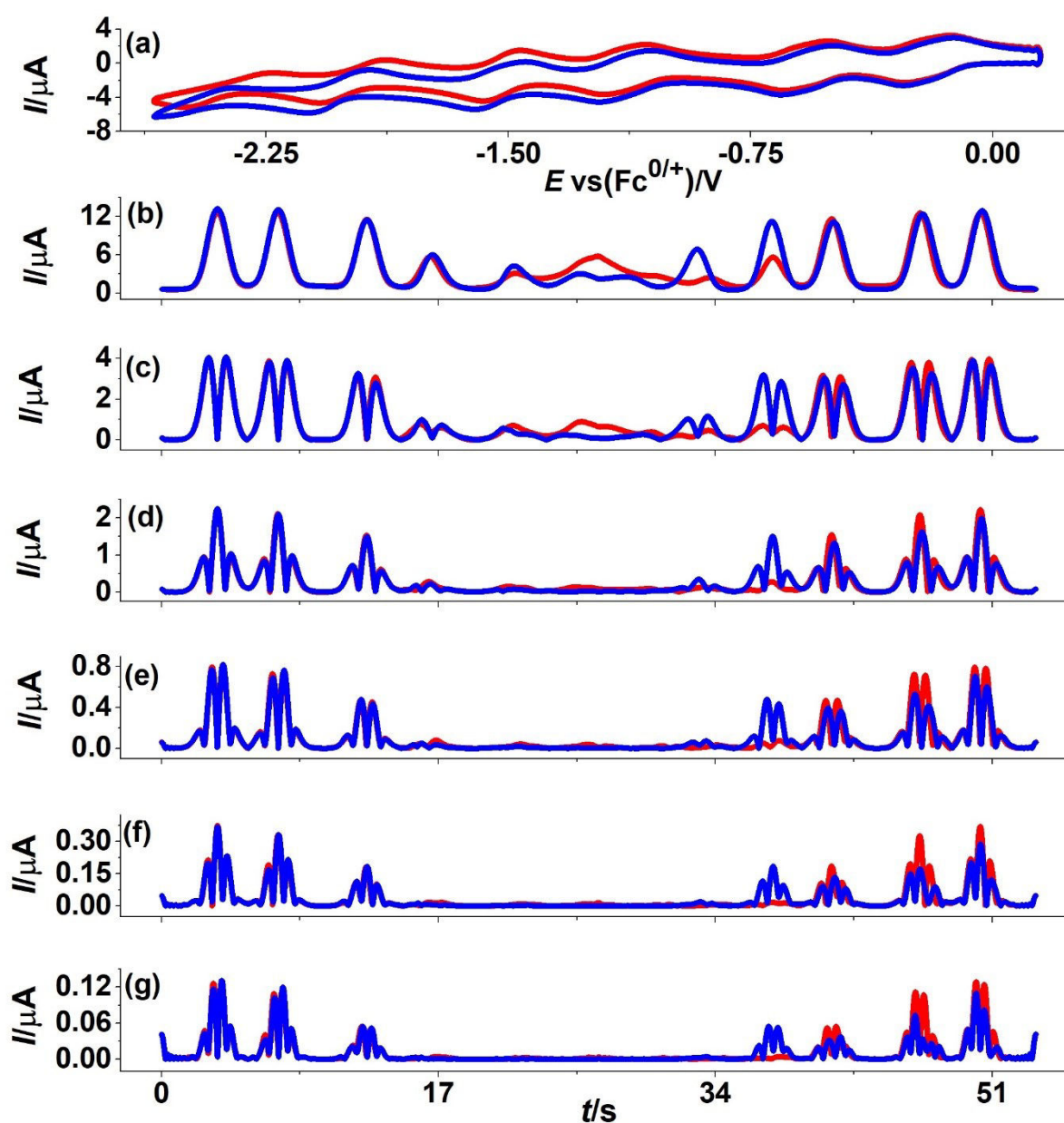


Figure S2. Heuristic comparison of simulated (red line) and experimental (blue line) AC voltammetric data for the α -[S₂W₁₈O₆₂]^{4-/5-/6-/7-/8-/9-} processes obtained with $\Delta E = 80$ mV, $f = 8.98$ Hz and $\nu = 0.100$ V s⁻¹ derived from reduction of 2.5 mM α -[S₂W₁₈O₆₂]⁴⁻ in CH₃CN containing 0.50 M [*n*-Bu₄N][PF₆] at Au electrode. (a) DC component, (b-g) 1st to 6th harmonic components. Other parameters given in Table 3 and text.

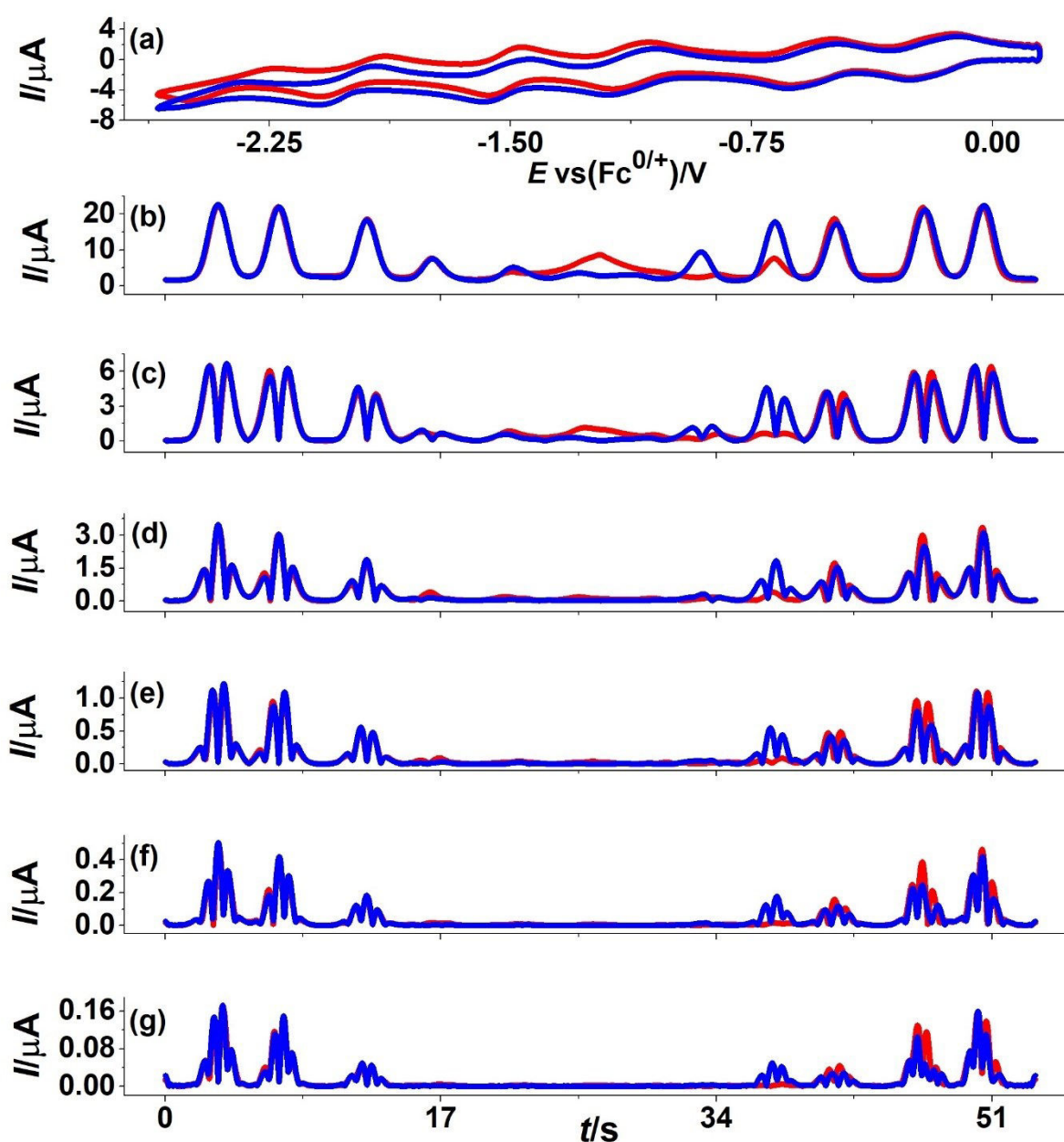


Figure S3. Heuristic comparison of simulated (red line) and experimental (blue line) AC voltammetric data for the α -[S₂W₁₈O₆₂]^{4-/-5-/-6-/-7-/-8-/-9-} processes obtained with $\Delta E = 80$ mV, $f = 26.95$ Hz and $\nu = 0.100$ V s⁻¹ derived from reduction of 2.5 mM α -[S₂W₁₈O₆₂]⁴⁻ in CH₃CN containing 0.50 M [*n*-Bu₄N][PF₆] at Au electrode. (a) DC component, (b-g) 1st to 6th harmonic components. Other parameters given in Table 3 and text.

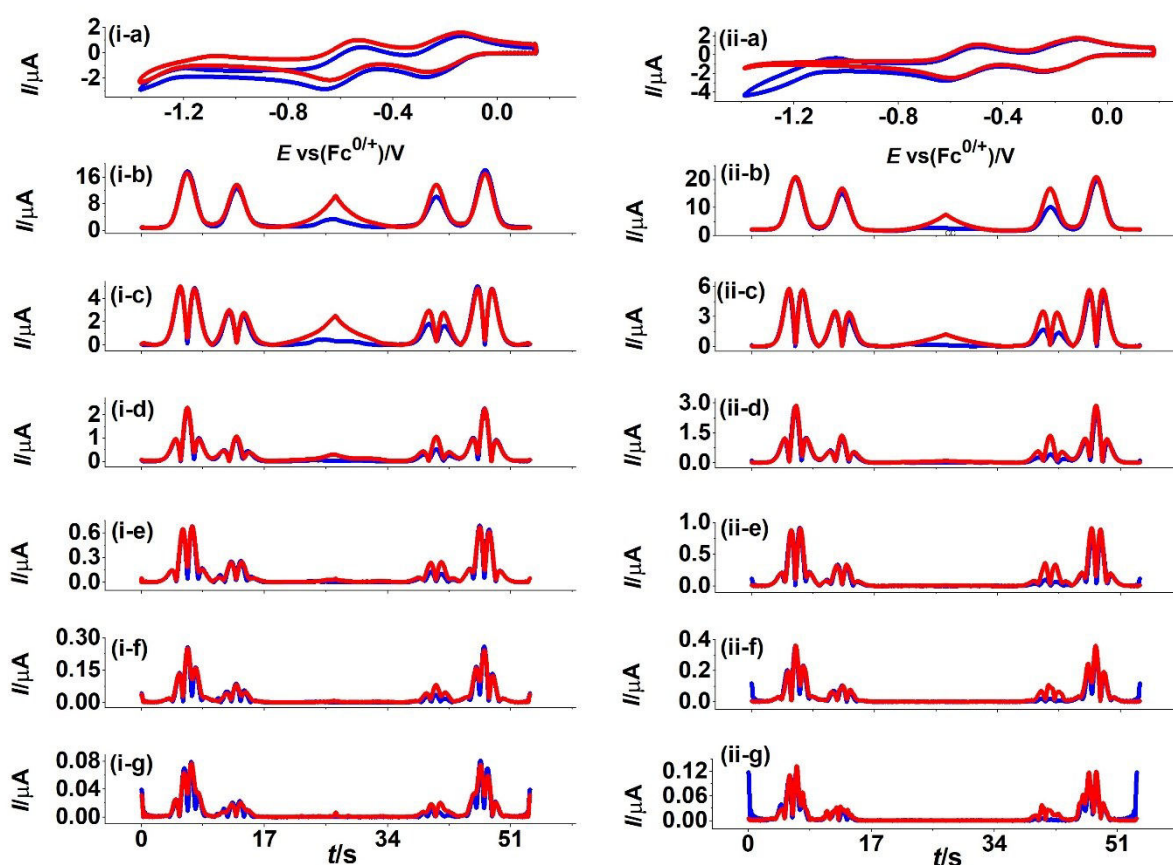


Figure S4. Heuristic comparison of simulated (red line) and experimental (blue line) AC voltammetric data for the α -[S₂W₁₈O₆₂]^{4-/-5-/-6-/-7-} processes obtained with $\Delta E = 80$ mV, f (i) = 8.98 and (ii) = 26.95 Hz and $\nu = 0.057$ V s⁻¹ derived from reduction of 2.5 mM α -[S₂W₁₈O₆₂]⁴⁻ in CH₃CN containing 0.50 M [*n*-Bu₄N][PF₆] at Pt electrode. (a) DC component, (b-g) 1st to 6th harmonic components. Other parameters given in Table 3 and text.

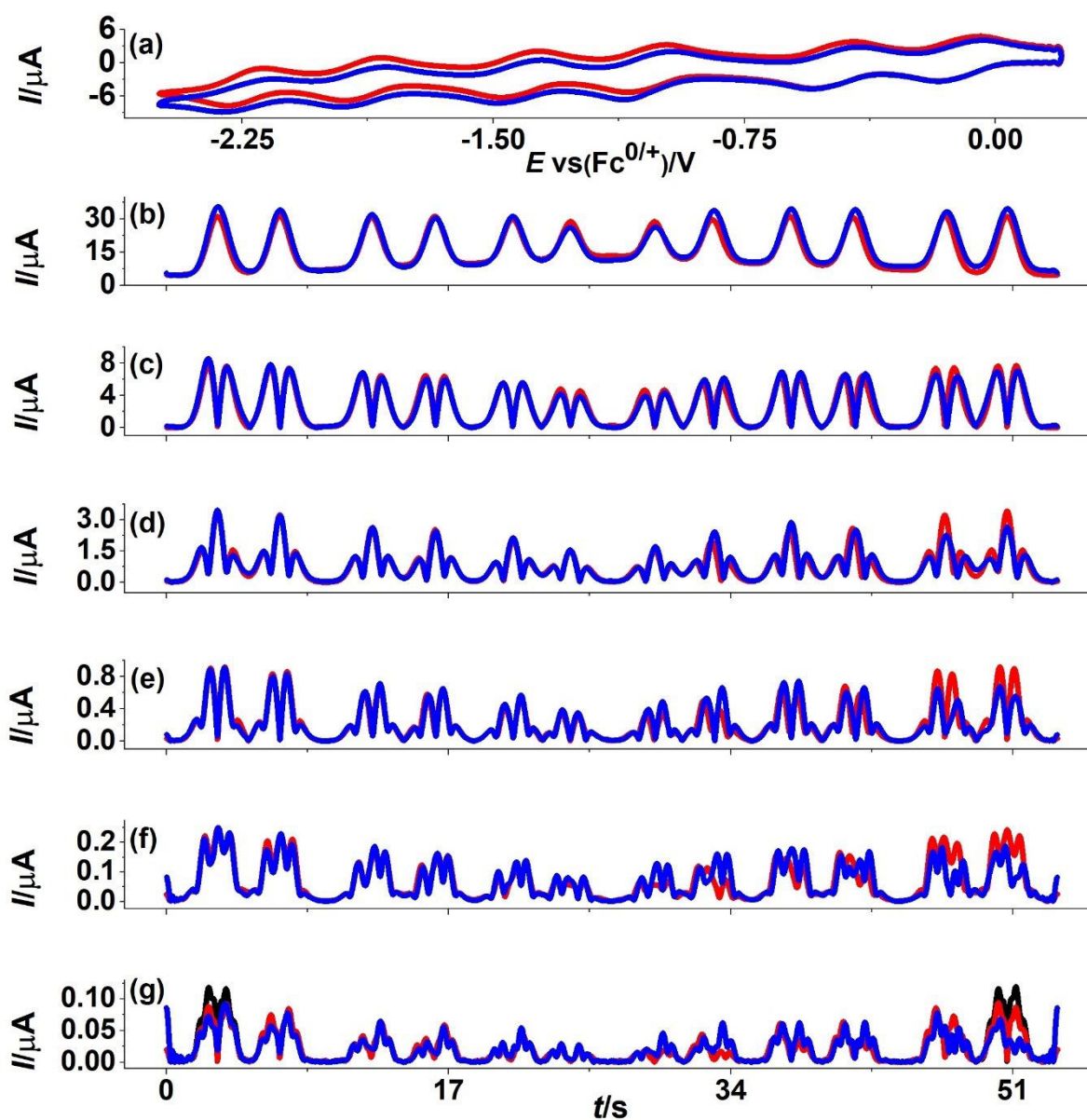


Figure S5. Heuristic comparison of simulated (red line) and experimental (blue line) AC voltammetric data for the α -[S₂W₁₈O₆₂]^{4-/-5-/-6-/-7-/-8-/-9-/-10-} processes obtained with $\Delta E = 80$ mV, $f = 26.95$ Hz and $\nu = 0.099$ V s⁻¹ derived from reduction of 2.5 mM α -[S₂W₁₈O₆₂]⁴⁻ in CH₃CN containing 0.10 M [n-Bu₄N][PF₆] at GC electrode. (a) DC component, (b-f) 1st to 5th harmonic components. (g) The 6th harmonic for a reversible process (black line) is also shown for comparison with the experimental one. Other parameters given in Table 5 and text.

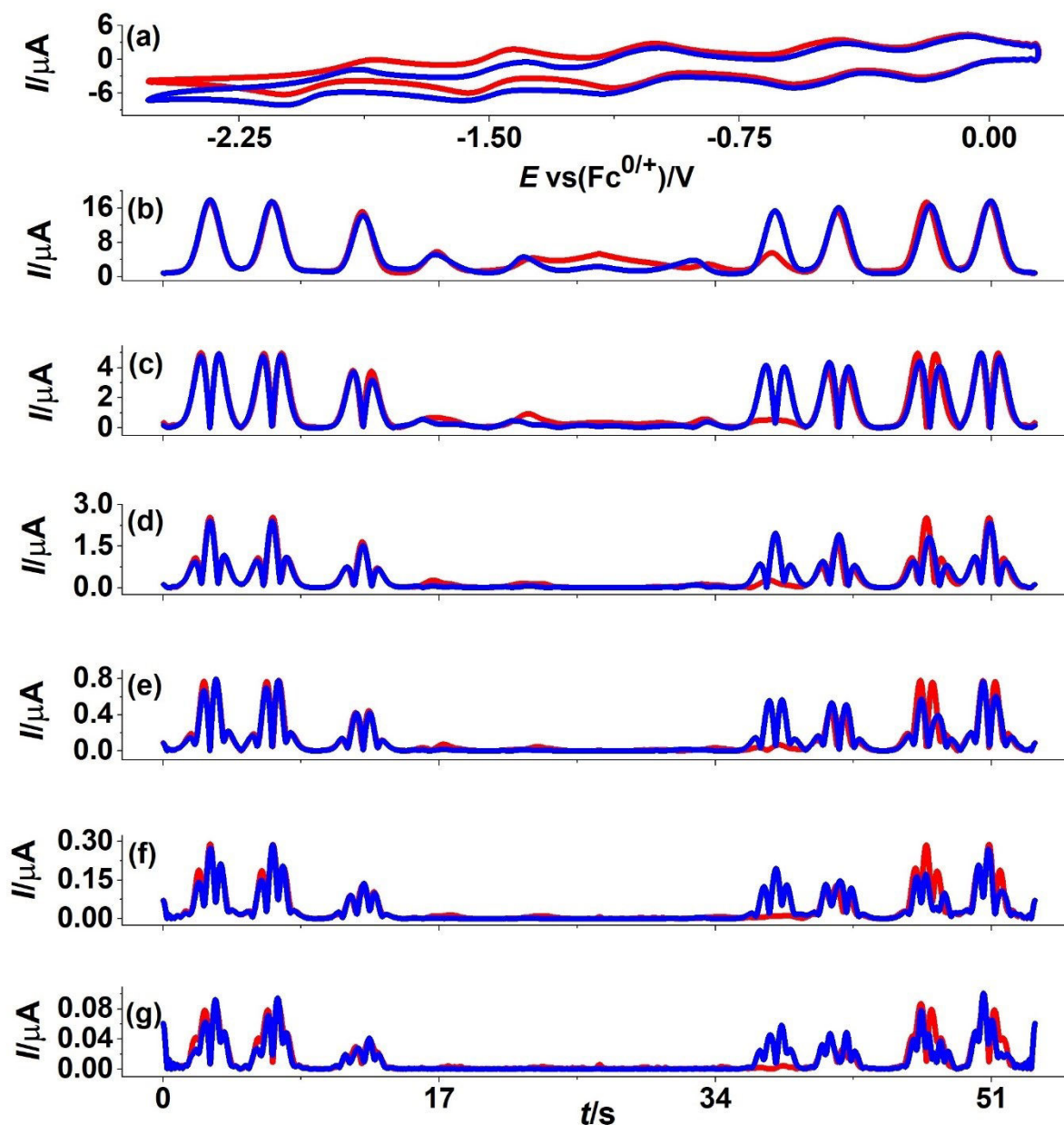


Figure S6. Heuristic comparison of simulated (red line) and experimental (blue line) AC voltammetric data for the α -[S₂W₁₈O₆₂]^{4-/-5-/-6-/-7-/-8-/-9-} processes obtained with $\Delta E = 80$ mV, $f = 8.98$ Hz and $\nu = 0.100$ V s⁻¹ derived from reduction of 2.5 mM α -[S₂W₁₈O₆₂]⁴⁻ in CH₃CN containing 0.10 M [*n*-Bu₄N][PF₆] at Au electrode. (a) DC component, (b-g) 1st to 6th harmonic components. Other parameters given in Table 5 and text.

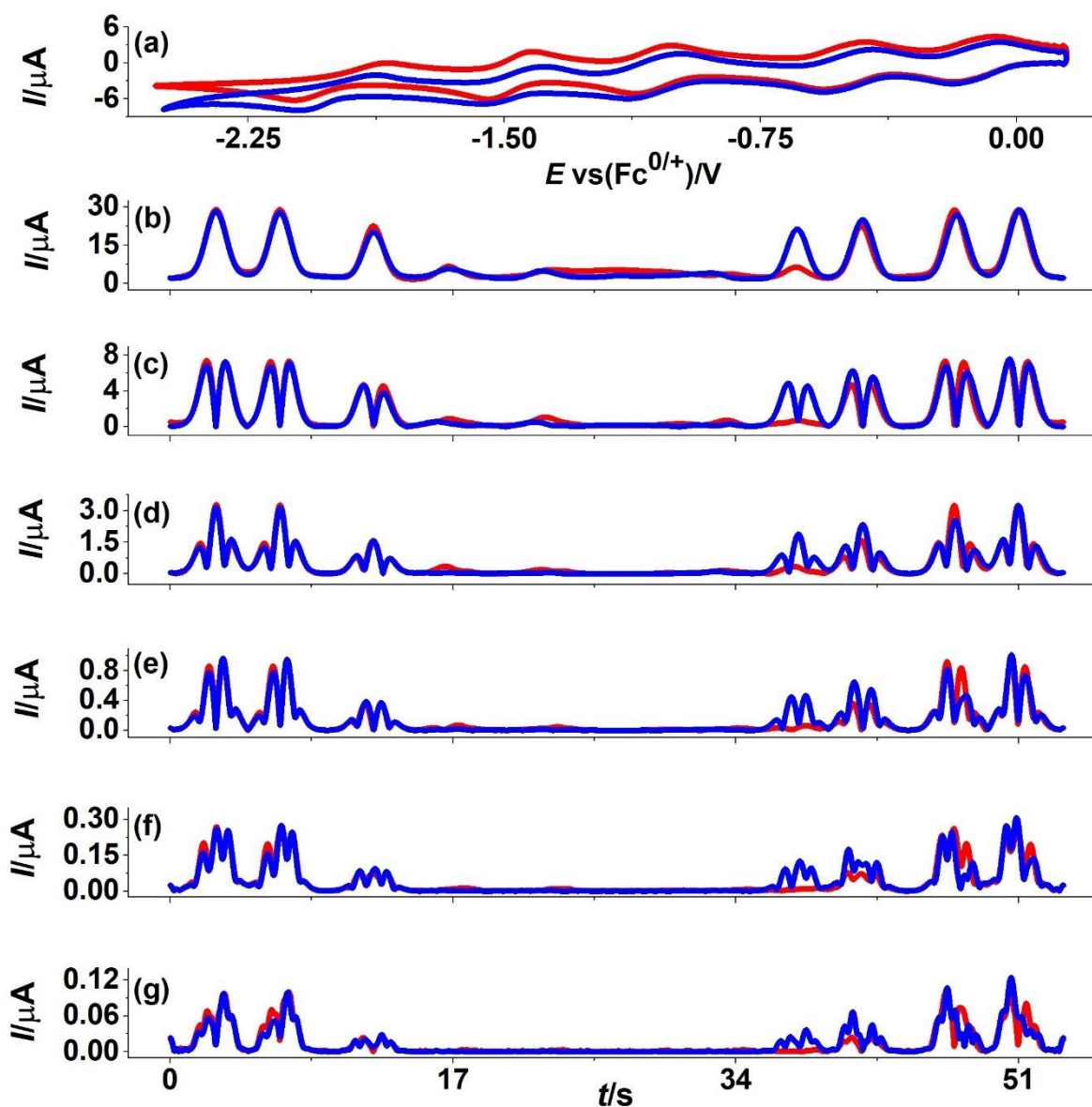


Figure S7. Heuristic comparison of simulated (red line) and experimental (blue line) AC voltammetric data for the α -[S₂W₁₈O₆₂]^{4-/5-/6-/7-/8-/9-} processes obtained with $\Delta E = 80$ mV, $f = 26.95$ Hz and $\nu = 0.100$ V s⁻¹ derived from reduction of 2.5 mM α -[S₂W₁₈O₆₂]⁴⁻ in CH₃CN containing 0.10 M [*n*-Bu₄N][PF₆] at Au electrode. (a) DC component, (b-g) 1st to 6th harmonic components. Other parameters given in Table 5 and text.

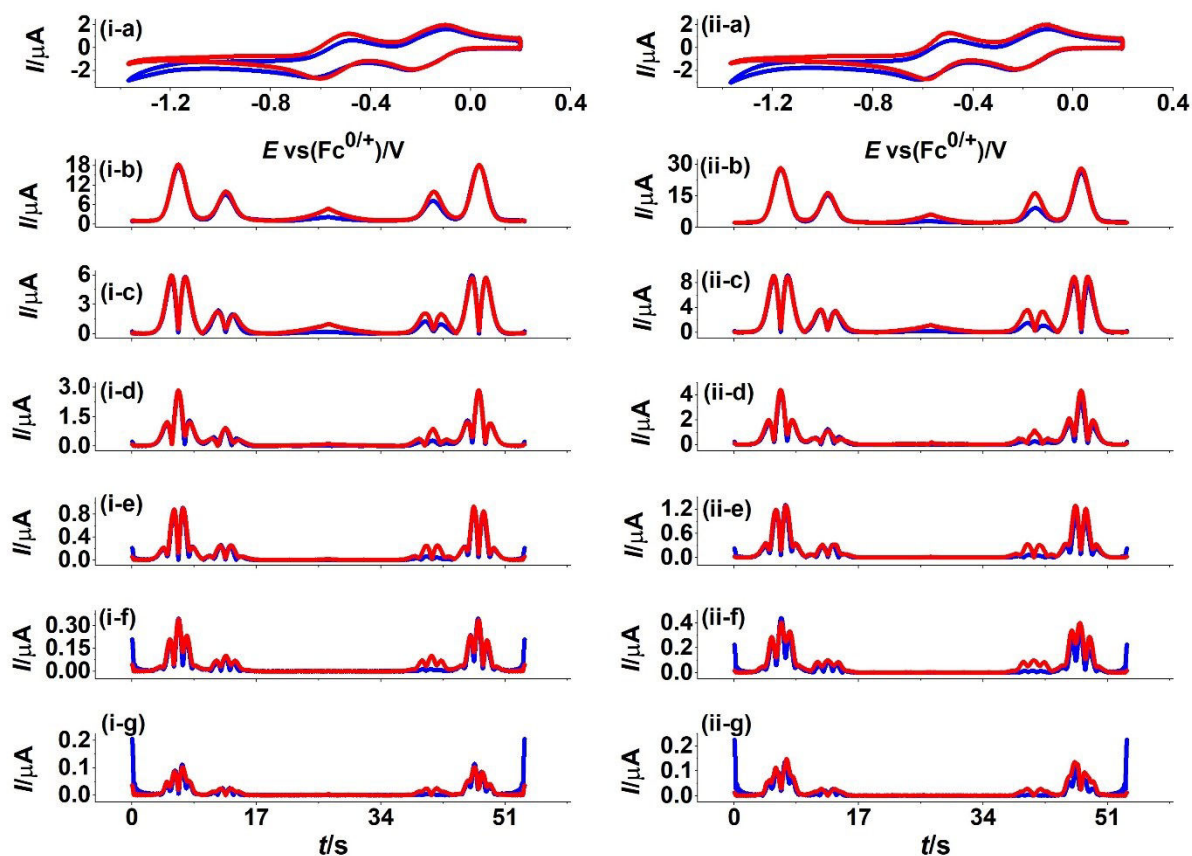


Figure S8. Heuristic comparison of simulated (red line) and experimental (blue line) AC voltammetric data for the α -[S₂W₁₈O₆₂]^{4-/-5-/-6-/-7-} processes obtained with $\Delta E = 80$ mV, f (i) = 8.98 and (ii) = 26.95 Hz and $\nu = 0.057$ V s⁻¹ derived from reduction of 2.5 mM α -[S₂W₁₈O₆₂]⁴⁻ in CH₃CN containing 0.10 M [*n*-Bu₄N][PF₆] at Pt electrode. (a) DC component, (b-g) 1st to 6th harmonic components. Other parameters given in Table 5 and text.

Chapter 5:

Thermodynamics, Electrode Kinetics and Mechanistic Nuances

Associated with the Voltammetric Reduction of Dissolved

$[n\text{-Bu}_4\text{N}]_4[\text{PW}_{11}\text{O}_{39}\{\text{Sn}(\text{C}_6\text{H}_4)\text{C}\equiv\text{C}(\text{C}_6\text{H}_4)(\text{N}_3\text{C}_4\text{H}_{10})\}]$ and a

Surface Confined Diazonium Derivative

Md Anisur Rahman^a, Si-Xuan Guo^{a, b}, Maxime Laurans^c, Guillaume Izzet^c, Anna Proust^{c *},

Alan M. Bond^{a, b *} and Jie Zhang^{a, b *}

^a School of Chemistry, Monash University, Clayton, Victoria 3800, Australia

^b ARC Centre of Excellence for Electrochemical Science, Monash University, Clayton,
Victoria 3800, Australia

^c Sorbonne Université, CNRS, Institut Parisien de Chimie Moléculaire, IPCM, 4 Place
Jussieu, F-75005 Paris, France

ABSTRACT

The power of Fourier transformed large amplitude alternating current voltammetry (FTACV) has been applied to parameterise the reduction of the phospho-tungstate $[\text{PW}_{11}\text{O}_{39}\{\text{Sn}(\text{C}_6\text{H}_4)\text{C}\equiv\text{C}(\text{C}_6\text{H}_4)(\text{N}_3\text{C}_4\text{H}_{10})\}]^{4-}$ polyoxometalate ($\text{K}_{\text{Sn}}^{\text{W}}[\text{N}_3\text{C}_4\text{H}_{10}]^{4-/5-/6-}$ processes) at glassy carbon (GC), gold (Au) and platinum (Pt) electrodes in acetonitrile (0.10 M $[n\text{-Bu}_4\text{N}][\text{PF}_6]$). Same data analysis protocol also has been applied to parameterise the surface confined processes of $\text{K}_{\text{Sn}}^{\text{W}}[-]^{4-}$ -grafted diazonium derivative at GC electrode. The thermodynamics (E^0) and heterogeneous electron-transfer kinetics (k^0 and α) were estimated using the Butler-Volmer relationship. FTACV provides access to significantly more detailed mechanistic information related to non-conformance to the theory than widely used DC voltammetric methods, especially with the more intricate surface confined electrochemistry. Parameterisation, the level of agreement and systematic variations between experimental and simulated data were established by both an experimenter controlled heuristic method and by a computationally efficient data optimisation approach that employed parameter space searches restricted in scope by knowledge of the heuristically based estimations. The first electron transfer process for both acetonitrile soluble $\text{K}_{\text{Sn}}^{\text{W}}[\text{N}_3\text{C}_4\text{H}_{10}]^{4-}$ and surface confined $\text{K}_{\text{Sn}}^{\text{W}}[-]^{4-}$ is always significantly faster than the second. The electrode dependence order is $k_{\text{GC}}^0 > k_{\text{Au}}^0 > k_{\text{Pt}}^0$ for the $\text{K}_{\text{Sn}}^{\text{W}}[\text{N}_3\text{C}_4\text{H}_{10}]^{4-/5-}$ process. The relatively slower electrode kinetics found for reduction of $\text{K}_{\text{Sn}}^{\text{W}}[\text{N}_3\text{C}_4\text{H}_{10}]^{4-}$ as compared to some other monomeric Keggin POMs may be due to the long organic chain hindering the approach of the POM to the electrode surface, although differences in ion-pairing and other factors also may play a role. Subtle, but systematic differences identified in comparisons of experimental and simulated voltammetry give rise to apparently data analysis method dependent parameterisation and are discussed in terms of nuances not accommodated in the modelling. In the solution phase voltammetry, data obtained by electrochemical quartz crystal microbalance and other techniques are consistent with solid

adhering to and modifying the electrode surface following reduction of $\text{K}^{\text{W}}_{\text{Sn}}[\text{N}_3\text{C}_4\text{H}_{10}]^{4-}$ to $\text{K}^{\text{W}}_{\text{Sn}}[\text{N}_3\text{C}_4\text{H}_{10}]^{5-}$. Kinetic and thermodynamic dispersion present in the heterogeneous $\text{K}^{\text{W}}_{\text{Sn}}[-]^{4-}$ -grafted electrode are probable causes of non-ideality detected in the surface confined voltammetry of this material. Thus, FTACV gives valuable insights into what is needed to provide a more realistic description of the polyoxometalate/electrode interface in polyoxometalate electrochemistry by revealing subtle nuances that are often overlooked.

Keywords: Polyoxometalate electrochemistry, electrografting, Fourier transformed alternating current voltammetry, electrode kinetics and thermodynamics, parameterisation, mechanistic nuances.

1. Introduction

Nano-sized metal oxoanions, known as polyoxometalates (POMs), are an important class of inorganic clusters that are usually constructed from early transition metals. Their ability to undergo an extensive series of electron transfer reactions when dissolved in solution or attached to electrode surfaces¹⁻⁴ has made these anions valuable in applications of electrochemistry in diverse fields such as electrocatalysis⁵⁻⁷, electrosynthesis⁸, biosensing⁹⁻¹⁰ and energy storage¹¹⁻¹². Glassy carbon (GC) has been available as an electrode material^{2, 13-15} for over half a century. Much of the recent solution phase and surface confined POM electrochemistry has been reported at this electrode surface to improve selectivity in electroanalysis or to overcome slow electron-transfer kinetics found with use of conventional metal electrodes¹⁶⁻¹⁷. The main techniques for electrode modification are largely based on electrostatic¹⁸⁻²⁰ or covalent attachment^{2-3, 21-22}.

The electrode kinetics of POMs with Keggin and Dawson structures have been reported in studies in solution phase²³⁻²⁵ and with spontaneously adsorbed forms²⁶⁻²⁸. Relevant to this study, functionalization of POMs has recently been introduced to provide a reactive terminal diazonium group that facilitates surface anchoring to the electrode^{2-3, 22, 29}. In the present study, the thermodynamics (reversible formal potentials, E^0 values) and electrode kinetics (heterogeneous charge transfer rate constant k^0 at E^0 and charge transfer coefficient, α values) of the solution soluble Keggin POM functionalized with a protected diazonium, [*n*-Bu₄N]₄[PW₁₁O₃₉{Sn(C₆H₄)C≡C(C₆H₄)(N₃C₄H₁₀)}] ([*n*-Bu₄N]₄K^W_{Sn}[N₃C₄H₁₀], Figure 1a) is initially explored via modelling based on the reactions given in Eqns. 1 and 2. This precursor is then converted to the diazonium derivative [*n*-Bu₄N]₃[PW₁₁O₃₉{Sn(C₆H₄)C≡C(C₆H₄)N₂⁺}] ([*n*-Bu₄N]₃K^W_{Sn}[N₂⁺], (Figure 1b) which is then subsequently grafted onto the GC electrode as K^W_{Sn}[⁻]⁴⁻-grafted (Figure S1). Thus, the thermodynamics and electrode kinetics for reduction

of $K_{Sn}^W[-]^{4-}$ is evaluated according to Eqns. 3 and 4 using modelling relevant to this surface confined material.

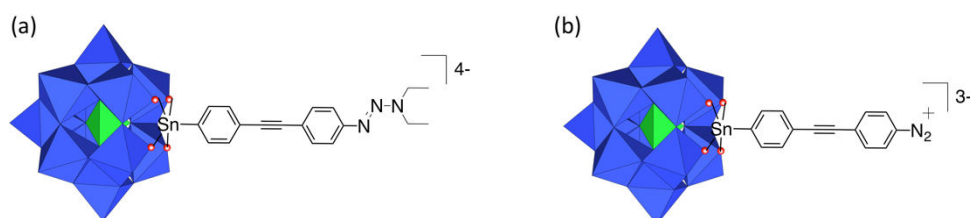
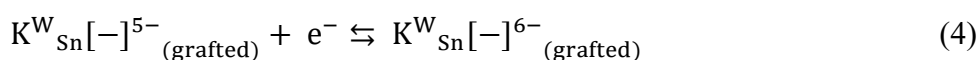
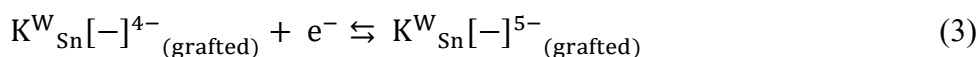


Figure 1. Structural representation of (a) the precursor functionalized phosphotungstate POM $K_{Sn}^W[N_3C_4H_{10}]^{4-}$ used in solution phase electrochemical studies and (b) $K_{Sn}^W[N_2^+]^{3-}$ used for grafting to a GC electrode via the terminal diazonium group.

Electrografting of the related diazonium functionalized POMs $[PMo_{11}O_{39}\{Sn(C_6H_4)C\equiv C(C_6H_4)N_2^+\}]^{3-}$ ² and $[PW_{11}O_{39}\{Ge(C_6H_4)C\equiv C(C_6H_4)N_2^+\}]^{3-}$ ³ has been used to prepare chemically modified GC or silicon surfaces. Studies of the electron transfer kinetics of the functionalized POM grafted onto GC or silicon have been reported by traditional DC cyclic voltammetry ^{3,22} using the separation in the peak reduction and oxidation potentials for the first one electron reduction process as a function of scan rate with reference to Laviron theory ³⁰ used for quantification. Electrode kinetic studies with the solution soluble $[PW_{11}O_{39}\{Ge(C_6H_4)C\equiv C(C_6H_4)(N_3C_4H_{10})\}]^{4-}$ ($K_{Ge}^W[N_3C_4H_{10}]^{4-}$) also have been undertaken by linear sweep voltammetry which are based on comparison of the dependence of the reduction peak potential on scan rate ³¹. Thus, parameterisation in these studies with solution

soluble and surface confined POMs is derived from analysis of peak potentials. This very restricted use of only one or two data points selected from the extensive current-potential profile collected experimentally, means that information related to the shape of the voltammogram does not form part of the quantitative data analysis protocol, which minimises prospects for identifying nuances or non-idealities associated with the voltammetry.

In this study, the more sophisticated technique of Fourier transformed alternating current voltammetry (FTACV) is introduced to characterize the reduction of $K_{Sn}^W[N_3C_4H_{10}]^{4-}$ in the solution phase at GC, Au and Pt electrodes and $K_{Sn}^W[-]^{4-}$ grafted onto a GC electrode. This method allows all data in very extensive sets collected in the experiments to be used in the parameterisation exercise, thereby allowing subtle departures from the theory predicted using the Butler-Volmer electron transfer model to be more readily detected. The thermodynamic and electrode kinetic parameters associated with reduction of $K_{Sn}^W[N_3C_4H_{10}]^{4-}$ in solution and surface confined $K_{Sn}^W[-]^{4-}$ are estimated with FTACV by comparing theoretical predictions based on MECSim³² software derived simulated data with experimental data using both experimenter based heuristic and computationally supported data optimisation methods. Manual comparisons of simulated and experimental data are undertaken in the heuristic approach and the decision as to when the best fit data has been achieved is made by the experimenters on the basis of their expertise in voltammetry and data analysis. Knowledge from the tedious heuristic approach helps establish the range of variables that have to be searched in the computer assisted data optimisation approach³³⁻³⁴. Unlike the outcome of the heuristic approach, parameters derived from the data optimised analysis approach are independent of experimenter bias. However, an experienced electrochemist may more readily detect systematic departures of experimental data from theoretical predictions than by routinely implemented automated computational assessment as indeed applies in this study.

2. Experimental Section

2.1. Reagents and solvents. The functionalized Keggin POM, $[n\text{-Bu}_4\text{N}]_4[\text{PW}_{11}\text{O}_{39}\{\text{Sn}(\text{C}_6\text{H}_4)\text{C}\equiv\text{C}(\text{C}_6\text{H}_4)(\text{N}_3\text{C}_4\text{H}_{10})\}]$ ($[n\text{-Bu}_4\text{N}]_4\text{K}^{\text{W}}_{\text{Sn}}[\text{N}_3\text{C}_4\text{H}_{10}]$) was prepared by a literature method³⁵. Ferrocene (Fc, 98%, Sigma-Aldrich), Al_2O_3 (Buehler), trifluoroacetic acid (Sigma-Aldrich), diethylether (Merch-KGaA, Germany, 99.5%), dimethylformamide (DMF) and ethanol (96%, Merck) were used as provided by the manufacturer. Acetonitrile (CH_3CN , 99.9%, Sigma-Aldrich) was dried over molecular sieves. Tetrabutylammonium hexafluorophosphate ($[n\text{-Bu}_4\text{N}][\text{PF}_6]$, 98%, Sigma-Aldrich) and tetrabutylammonium bromide (Bu_4NBr , 98%, Sigma-Aldrich) were recrystallized from hot ethanol³⁶ and isopropanol ($\text{C}_3\text{H}_8\text{O}$, 99.5% Merck), respectively.

2.2. Synthesis of $[n\text{-Bu}_4\text{N}]_3[\text{PW}_{11}\text{O}_{39}\{\text{Sn}(\text{C}_6\text{H}_4)\text{C}\equiv\text{C}(\text{C}_6\text{H}_4)(\text{N}_2^+)\}]$ ($[n\text{-Bu}_4\text{N}]_3\text{K}^{\text{W}}_{\text{Sn}}[\text{N}_2^+]$). 40.9 mg of $[n\text{-Bu}_4\text{N}]_4\text{K}^{\text{W}}_{\text{Sn}}[\text{N}_3\text{C}_4\text{H}_{10}]$ (0.010 mmol) was dissolved in 2 mL of dried acetonitrile. 3.8 μL of trifluoroacetic acid ($\text{C}_2\text{HF}_3\text{O}_2$, 0.050 mmol) was then added with stirring at room temperature for 10 minutes. A brown solid was removed by filtration of the yellow solution and 64.5 mg of Bu_4NBr was added to the filtrate. The required product was precipitated by mixing the filtrate with diethyl ether and collected, dried and stored under vacuum.

2.3. Electrochemical instrumentation and procedures. CH Instruments 700E and home built FTACV³⁷ electrochemical workstations were used to undertake DC cyclic and FTAC voltammetric experiments, respectively. In the FTACV, a sinusoidal wave having an amplitude ($\Delta E = 80$ mV) and frequency (f) of 9.02 Hz was superimposed onto the DC ramp. Resolution of the AC current-time data into aperiodic DC and AC harmonics was undertaken using Fourier transform based mathematical tools as described elsewhere³⁷. All voltammetric experiments were carried out in a standard 3-electrode electrochemical cell at $22 \pm 2^\circ$ C under

an inert environment achieved by conducting the experiments inside a dry box. Before grafting and prior to each electrochemical experiment, the GC electrode was polished on a polishing pad with an aqueous aluminium oxide (Al_2O_3 , 0.3 μm) slurry, washed sequentially with water and acetone, and then dried under N_2 . The same pre-treatment procedure also was applied to the Au and Pt electrodes. Pt wire and Pt wire inside a capillary tube were employed as counter and quasi-reference electrodes, respectively.

The electroactive areas (A) of the bare electrodes with a nominal diameter of 1.0 mm were estimated from the dependence of the peak current (I_p^{ox}) for the reversible $\text{Fc}^{0/+}$ oxidation process on scan rate using a 1.0 mM Fc solution in CH_3CN (0.10 M [$n\text{-Bu}_4\text{N}$][PF_6]) and the Randles-Sevcik equation (Eq. 5) ³⁸ with a known diffusion coefficient ($D = 2.4 \times 10^{-5} \text{ cm}^2 \text{ s}^{-1}$) for ferrocene ³⁹. That is, values of parameters such as number of electrons transferred (n), A , scan rate (ν), D , bulk concentration (C), temperature (T), Faraday's constant (F) and the universal gas constant (R) contained in Eq. 5 were assumed to be known and with mass transport occurring by liner diffusion ⁴⁰. On this basis, $A = 8.0 \times 10^{-3} \text{ cm}^2$ for GC, $A = 8.1 \times 10^{-3} \text{ cm}^2$ for Au and, $A = 8.0 \times 10^{-3} \text{ cm}^2$ for Pt.

$$I_p = 0.4463nFA(nFD\nu/RT)^{1/2}C \quad (5)$$

The value of diffusion coefficient of $\text{K}_{\text{Sn}}^{\text{W}}[\text{N}_3\text{C}_4\text{H}_{10}]^{4-}$ of $6.3 \times 10^{-6} \text{ cm}^2 \text{ s}^{-1}$ was calculated from the dependence of the peak current (I_p^{red}) on ν and use of the Randles-Sevcik equation ³⁸ for reduction of a 0.50 mM POM solution in CH_3CN containing 0.10 M [$n\text{-Bu}_4\text{N}$][PF_6] as the supporting electrolyte.

In order to establish if spontaneous adsorption of $\text{K}_{\text{Sn}}^{\text{W}}[\text{N}_3\text{C}_4\text{H}_{10}]^{4-}$ occurs and may be the origin of some discrepancies detected between simulated and experimental solution phase voltammetric data, freshly polished GC, Au and Pt electrodes were dipped into an acetonitrile

solution containing 0.50 mM $\text{K}_{\text{Sn}}^{\text{W}}[\text{N}_3\text{C}_4\text{H}_{10}]^{4-}$ and 0.10 M $[\textit{n}\text{-Bu}_4\text{N}][\text{PF}_6]$ for at least five minutes. Electrodes were removed from the solution, sonicated in acetonitrile, rinsed carefully with acetone and dried under a nitrogen flow. Voltammetric experiments were then undertaken with these electrodes placed in CH_3CN containing only 0.10 M $[\textit{n}\text{-Bu}_4\text{N}][\text{PF}_6]$ electrolyte to detect the possible presence of surface attached POMs that had been adsorbed at open circuit potential. Analogous experiments were undertaken after the potential of the electrodes had been held at a value between the two $\text{K}_{\text{Sn}}^{\text{W}}[\text{N}_3\text{C}_4\text{H}_{10}]^{4-/5-/6-}$ processes for 0, 60, 120 or 180 s to ascertain if POM surface confinement occurred after reduction of $\text{K}_{\text{Sn}}^{\text{W}}[\text{N}_3\text{C}_4\text{H}_{10}]^{4-}$ to $\text{K}_{\text{Sn}}^{\text{W}}[\text{N}_3\text{C}_4\text{H}_{10}]^{5-}$.

Electrochemical quartz crystal microbalance (EQCM) experiments used to detect mass changes accompanying the voltammetry were undertaken with a 13.7 mm diameter ($A = 0.205 \text{ cm}^2$) gold coated quartz crystal (oscillation frequency = 8.0 MHz) electrode using a CH Instruments 400B electrochemical workstation that supports EQCM experiments. The reference and counter electrodes in the EQCM measurements were again Pt wires.

Calibration of the potential of the Pt quasi-reference electrode was undertaken by reference to the IUPAC recommended $\text{Fc}^{0/+}$ process⁴¹ under conditions of cyclic voltammetry and assuming its reversible potential is equal to the mid-point potential (average of oxidation and reduction peak potentials).

2.4. Electrografting of GC electrode surface. Grafting of the diazonium derivative² to the GC electrode surface was achieved via cyclic voltammetry (see Figure S2) of 1.0 mM of $\text{K}_{\text{Sn}}^{\text{W}}[\text{N}_2^+]^{3-}$ in CH_3CN (0.10 M $[\textit{n}\text{-Bu}_4\text{N}][\text{PF}_6]$) on a freshly polished GC electrodes over the potential range of -0.3 and -1.050 V vs $\text{Fc}^{0/+}$ with a scan rate of 0.100 V s^{-1} . Six cycles of potential were used to achieve close to a monolayer coverage. The grafted electrode was ultrasonicated in DMF and then CH_3CN (5 min each) to remove loosely attached material and

dried under nitrogen. This surface grafted electrode was then used as the working electrode in subsequent voltammetric experiments in CH₃CN with 0.10 M of [*n*-Bu₄N][PF₆] present as the supporting electrolyte.

2.5. Theoretical analysis of AC voltammetry. All simulations were undertaken with the Monash University Simulation package MECSim³². Details of the theory used for simulation of solution phase FTAC voltammetry with mass transport by linear diffusion as applies to Eqns. 1 and 2 are available in the literature⁴². Simulation of the diffusionless surface confined voltammetry of the grafted POM was undertaken as described in the literature⁴³⁻⁴⁴. In both scenarios, the Butler-Volmer model of electron transfer applied to a quasi-reversible process was used. This requires the incorporation of three (E^0, k^0, α) parameters for each electron transfer step, with units of k^0 being cm s⁻¹ and s⁻¹ for the solution soluble and grafted cases respectively. Neither thermodynamic nor kinetic dispersion that can occur with surface confined reactions⁴⁵⁻⁴⁶ were included in the simulation.

Ion-pairing chemistry reactions coupled to electron transfer were assumed to be diffusion controlled and hence reversible and subject to a solely thermodynamic description. On this basis, the unknown ion-pairing equilibrium constants effectively have been combined with the E^0 which implies that reported E^0, k^0, α values represent only apparent or E_{app}^0, k_{app}^0 and α_{app} values. No double layer correction was applied to the electrode kinetics.

For the surface confined process, the Langmuir adsorption isotherm model was used. This adsorption isotherm implies that all surface confined grafted POM moieties present in monolayer or sub-monolayer coverage are electrochemically identical in their behaviour and act independently of each other. Use of the Langmuir relationship also requires that no dissolution of surface bound POM occurs during the course of the voltammetric experiment.

The surface concentration (Γ) of $\text{K}^{\text{W}}_{\text{Sn}}[-]^{4-}$ in moles cm^{-2} was calculated from the charge Q in coulomb transferred during the first surface confined reduction process as given by Eqn. 6.

$$\Gamma = N/A = Q/nFA \quad (6)$$

where N is number of moles of the electroactive species.

Modelling uncompensated resistance (R_u) via Ohm's law required the inclusion of this parameter in the simulations. The value of R_u used assumes a simple $R_u C_{\text{dl}}$ time constant applies at potentials prior to the onset of POM reduction. Other parameters present in the simulation model such as AC amplitude, frequency, DC scan rate, electrode area, temperature were assumed to be accurately known.

Double layer capacitance (C_{dl}) was evaluated from the background current in the potential region of the fundamental harmonic of the FTACV response (Figure S3) where faradaic current is absent. A non-linear model was used to model the potential dependence of C_{dl} as in Eqn. 7⁴⁷

$$C_{\text{dl}}(t) = c_0 + c_1 E(t) + c_2 E(t)^2 + c_3 E(t)^3 + c_4 E(t)^4 \quad (7)$$

In this equation, the nonlinearity of the capacitor is defined by the coefficients c_0 , c_1 , c_2 , c_3 , and c_4 and the time dependant potential is designated by $E(t)$. However, it will emerge that the background current, particularly at the POM modified electrode, exhibits even more complicated behaviour than predicted by this model, although conveniently, second and higher order AC harmonics are essentially devoid of background current, as predicted by the model.

As in previous papers⁴⁸⁻⁴⁹, automated computationally supported comparison of experimental and simulated data in the data optimisation exercises were undertaken using a least squares (LS) function (Eqn. 8) to estimate E^0 , k^0 and α values obtained with the best fit

of theory to experimental data. Here, only the 2nd to 6th harmonics were employed for optimisation so the influence of background current present in the aperiodic DC and fundamental harmonic could be ignored in the optimisation exercise.

$$LS = \left[1 - \left(\sum_{h=2}^6 \sqrt{\frac{\sum_{i=1}^N [(f_h^{\text{exp}}(t_i) - f_h^{\text{sim}}(t_i))^2]}{\sum_{i=1}^N f_h^{\text{exp}}(t_i)^2}} \right) / 5 \right] \times 100\% \quad (8)$$

where $f^{\text{exp}}(t_i)$ and $f^{\text{sim}}(t_i)$ characterize the experimental and simulated functions, respectively, h is the order of an individual AC harmonic component and N is the number of data points.

3. RESULT AND DISCUSSION

3.1. DC cyclic voltammetric studies for the solution soluble and surface confined POMs.

Figure 2 shows a DC cyclic voltammogram at a GC electrode for reduction of $\text{K}_{\text{Sn}}^{\text{W}}[\text{N}_3\text{C}_4\text{H}_{10}]^{4-}$ over the potential range of about -0.1 to -1.7 V vs $\text{Fc}^{0/+}$. No reduction response associated with the side chain is evident prior to the $\text{K}_{\text{Sn}}^{\text{W}}[\text{N}_3\text{C}_4\text{H}_{10}]^{4-/5-}$ process observed at about -1.4 V vs $\text{Fc}^{0/+}$.

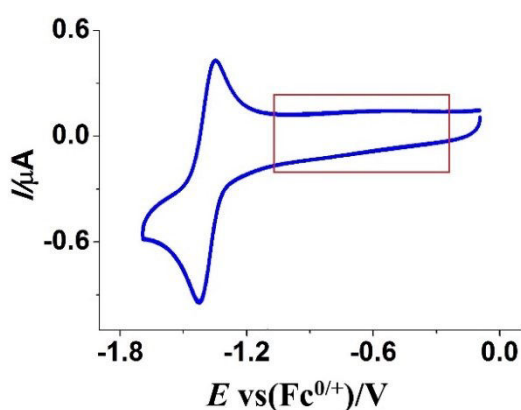


Figure 2. DC Cyclic voltammetry of $\text{K}_{\text{Sn}}^{\text{W}}[\text{N}_3\text{C}_4\text{H}_{10}]^{4-}$ in CH_3CN (0.10 M $[\text{n-Bu}_4\text{N}][\text{PF}_6]$) at a scan rate of 0.100 V s^{-1} with a GC electrode over the potential range of about -0.10 to -1.7 V

vs $\text{Fc}^{0/+}$ which covers the region where grafting with the diazonium derivative (red marked area) and the first $\text{K}^{\text{W}}_{\text{Sn}}[\text{N}_3\text{C}_4\text{H}_{10}]^{4-/5-}$ process occur.

DC Cyclic voltammograms for a 0.50 mM $\text{K}^{\text{W}}_{\text{Sn}}[\text{N}_3\text{C}_4\text{H}_{10}]^{4-}$ solution and the surface confined grafted $\text{K}^{\text{W}}_{\text{Sn}}[-]^{4-}$ at a GC electrode recorded over a wider potential range than in Figure 2 are provided in Figure 3. In the former case, three reduction processes are observed at a GC electrode (Figure 3i-a). The first two, which are assigned to $\text{K}^{\text{W}}_{\text{Sn}}[\text{N}_3\text{C}_4\text{H}_{10}]^{4-/5-}$ and $\text{K}^{\text{W}}_{\text{Sn}}[\text{N}_3\text{C}_4\text{H}_{10}]^{5-/6-}$ processes and are of interest in this study, are well defined and chemically reversible since the magnitudes of the ratios of the reduction to oxidation peak currents are close to unity. Consequently, their mid-point potentials, $(E_{\text{ox}}^{\text{p}} + E_{\text{red}}^{\text{p}})/2$, can be equated to the reversible potential, E^0 , values of -1.390 and -1.843 V vs $\text{Fc}^{0/+}$, respectively. These processes also can be classified as essentially reversible or close to reversible in the electrochemical sense since their peak-to-peak separation ($E_{\text{p}}^{\text{red}} - E_{\text{p}}^{\text{ox}}$) values of ~60 mV, uncorrected for IR_u drop, are close to the theoretically predicted value of 56.4 mV for a reversible one-electron transfer process at 22° C³⁸. The third most negative process at about -2.4 V vs $\text{Fc}^{0/+}$ at the GC electrode is chemically irreversible and not considered further.

Interestingly, the shapes of the processes for reduction of $\text{K}^{\text{W}}_{\text{Sn}}[\text{N}_3\text{C}_4\text{H}_{10}]^{4-}$ detected at Au (Figure 3ii) and Pt (figure 3iii) electrodes differ significantly from those at the GC electrode. The first process at these metal electrodes is assigned as quasi-reversible by traditional forms of analysis of DC cyclic voltammograms on the basis of their much larger ($E_{\text{p}}^{\text{red}} - E_{\text{p}}^{\text{ox}}$) separations but identical mid-point potentials relative to values of these parameters at the GC electrode. In contrast, the second $\text{K}^{\text{W}}_{\text{Sn}}[\text{N}_3\text{C}_4\text{H}_{10}]^{5-/6-}$ process at the Au electrode is observed at a significantly more negative potential (mid-point potential approximately -1.94 V) than at the GC electrode while this process is ill-defined at Pt, indicating additional complexity relative

the quasi-reversible assignment scenario. Thus, modelling these processes with the Butler-Volmer relationship will not be appropriate.

With the grafted GC electrode, the cyclic voltammetry (Figure 3i-b), contains $\text{K}^{\text{W}}_{\text{Sn}}[-]^{4-/5-}$ and $\text{K}^{\text{W}}_{\text{Sn}}[-]^{5-/6-}$ reduction processes with mid-point potentials of -1.450 V and -1.922 vs $\text{Fc}^{0/+}$, respectively. The shapes of both these diffusionless processes are symmetrical unlike those for the diffusion-controlled solution phase reactions, as expected theoretically. The germanium analogue of the tungsten, $\text{K}^{\text{W}}_{\text{Ge}}[-]^{4-3}$ grafted GC electrode also exhibits two well resolved symmetrically shaped reduction processes.

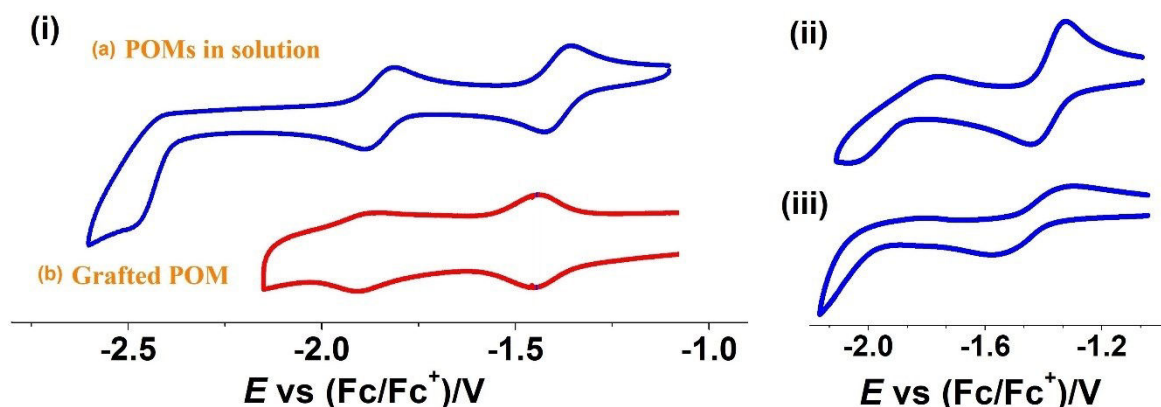


Figure 3. DC cyclic voltammetry of $\text{K}^{\text{W}}_{\text{Sn}}[\text{N}_3\text{C}_4\text{H}_{10}]^{4-}$ at a bare (i-a) GC, (ii) Au and (iii) Pt electrodes and (i-b) at a $\text{K}^{\text{W}}_{\text{Sn}}[-]^{4-}$ -grafted GC electrode at a scan rate of 0.100 V s^{-1} in CH_3CN ($0.10 \text{ M } [n\text{-Bu}_4\text{N}][\text{PF}_6]$).

A summary of $\Delta E_p (E_{\text{ox}}^p - E_{\text{red}}^p)$ and E^0 values determined by DC cyclic voltammetry for dissolved $\text{K}^{\text{W}}_{\text{Sn}}[\text{N}_3\text{C}_4\text{H}_{10}]^{4-}$ and grafted $\text{K}^{\text{W}}_{\text{Sn}}[-]^{4-}$ are provided in Table 1 and compared with those for related polyoxomolybdate $[\text{PMo}_{11}\text{O}_{39}\{\text{Sn}(\text{C}_6\text{H}_4)\text{C}\equiv\text{C}(\text{C}_6\text{H}_4)(\text{N}_3\text{C}_4\text{H}_{10})\}]^{4-}$ ($\text{K}^{\text{Mo}}_{\text{Sn}}[\text{N}_3\text{C}_4\text{H}_{10}]^{4-}$)² and polyoxotungstate $\text{K}^{\text{W}}_{\text{Ge}}[\text{N}_3\text{C}_4\text{H}_{10}]^{4-3}$ compounds.

Table 1. Summary of DC cyclic voltammetric data obtained at a scan rate of 0.100 V s⁻¹ in CH₃CN (0.10 M [*n*-Bu₄N][PF₆]).

POM type	Electrode	E_{app1}^0	E_{app2}^0	E_{app1}^0	E_{app2}^0	ΔE_{p1}	ΔE_{p2}
		V vs SCE		V vs Fc ^{0/+ a}		mV	
K ^W _{Sn} [N ₃ C ₄ H ₁₀] ⁴⁻	Bare-GC			-1.390	-1.843	63	67
	Bare-Au			-1.400	-1.94 ^b	103	310 ^c
	Bare-Pt			-1.400 ^c	^d	310 ^c	^d
	Grafted-GC (K ^W _{Sn} [-] ⁴⁻)			-1.450	-1.922	13	37
K ^W _{Ge} [N ₃ C ₄ H ₁₀] ⁴⁻	Bare-GC	-0.990	-1.460	-1.300	-1.770	65±5	65±5
	Grafted-GC (K ^W _{Ge} [-] ⁴⁻)	-1.010	-1.500	-1.310	-1.800	30	60
K ^{Mo} _{Sn} [N ₃ C ₄ H ₁₀] ⁴⁻	Bare-GC	-0.500	-0.920	-0.810	-1.230	--	--
	Grafted-GC (K ^{Mo} _{Sn} [-] ⁴⁻)	-0.550	^d	-0.860	^d	72 ^e	^d

^a Converted to Fc^{0/+} scale ^{38, 50} when required

^b Well-removed from GC value (see text for further details)

^c Approximate value

^d Ill defined

^e $\nu < 0.3 \text{ V s}^{-1}$

In terms of electrode kinetics, the following qualitative conclusions might be made from data in Table 1. The ΔE_{p1} value of $63 \pm 2 \text{ mV}$ at a GC electrode for the K^W_{Sn}[N₃C₄H₁₀]^{4-/5-} reduction processes in solution phase at a scan rate of 0.100 V s⁻¹ approaches the theoretically predicted value for ΔE_p of 56.4 mV for a reversible one-electron process. The difference may be attributed to the presence of a small amount of Ohmic IR_u drop, so that on this DC time scale this process may be regarded as reversible, within experimental error. ΔE_{p2} is slightly larger for the second process ($\Delta E_{p2} = 67 \pm 2 \text{ mV}$) implying that $k_1^0 > k_2^0$ and that the second process is quasi-reversible rather than reversible. The much larger ΔE_p values for the K^W_{Sn}[-]^{4-/5-} process at Au and Pt than at GC electrodes implies that $k_{GC}^0 > k_{Au}^0 > k_{Pt}^0$.

The D value of $6.3 \times 10^{-6} \text{ cm}^2 \text{ s}^{-1}$ for $[\text{K}^{\text{W}}_{\text{Sn}}[\text{N}_3\text{C}_4\text{H}_{10}]^{4-}]$ was estimated from the DC voltammetric peak reduction current for the $\text{K}^{\text{W}}_{\text{Sn}}[\text{N}_3\text{C}_4\text{H}_{10}]^{4-/5-}$ process at a GC electrode as described in the Experimental Section. The D value for the germanium analogue in CH_3CN is reported to be $9.3 \times 10^{-6} \text{ cm}^2 \text{ s}^{-1}$ ³.

The first reduction process at the $\text{K}^{\text{W}}_{\text{Sn}}[-]^{4-}$ -grafted GC electrode in contact with CH_3CN (0.10 M $[n\text{-Bu}_4\text{N}][\text{PF}_6]$) has a $\Delta E_{\text{p}1}$ value of $13 \pm 2 \text{ mV}$ at a scan rate of 0.100 V s^{-1} which differs slightly from the value of zero predicted theoretically for a reversible process ⁵¹. On the other hand, the much larger value of $\Delta E_{\text{p}2}$ of $37 \pm 2 \text{ mV}$ is well removed from that predicted for the reversible value implying a much slower electron transfer rate for this process, relative electrode to the first one.

The E^0 values ² $\text{K}^{\text{Mo}}_{\text{Sn}}[\text{N}_3\text{C}_4\text{H}_{10}]^{4-}$ in solution phase and for the $\text{K}^{\text{Mo}}_{\text{Sn}}[-]^{4-}$ grafted-GC and are considerably less negative than for the W derivatives studied in this paper (Table 1). This is usually the case in POM electrochemistry and is attributed to the significantly lower position of the LUMO energy for a Mo based POM compared to its W analogue, also noting that the HOMO-LUMO gap is $\sim 2 \text{ eV}$ for molybdates which is smaller than $\sim 2.8 \text{ eV}$ for tungstates ⁵². The potentials for the germanium analogues of the tin derivatives in both solution and surface confined (grafted electrode) phases are considered to be similar when uncertainties in conversion of literature data reported vs SCE to the $\text{Fc}^{0/+}$ scale are taken into account. This reflects the fact that this change of a single side chain atom is less significant in terms of redox thermodynamics than when all W are replaced by all Mo in the polyoxometalate core framework. Differences in values of E_1^0 and E_2^0 are very similar for all compounds in both solution soluble and grafted cases, again as might be expected.

In three experiments undertaken in this study, the POM surface coverage, Γ , was estimated from the charge calculated from DC voltammetric experiments to be 6.2×10^{-11} , 8.8×10^{-11} and 10×10^{-11} mol cm⁻² which approaches the value estimated for a monolayer of immobilized polyoxomolybdate analogue, $K^{Mo}_{Sn}[-]^{4-}$ on a GC electrode, although it is noted that multilayer formation could arise by aryl radicals reacting with already grafted aryls

53.

3.2. FTACV voltammetric characterization of the $K^{W}_{Sn}[N_3C_4H_{10}]^{4-/5-/6-}$ processes.

E^0 , k^0 and α values were quantified by comparison of experimental and simulated FTACV data modelled by use of the Butler Volmer relationship, although from now on they will be referred to as E^0_{app} , k^0_{app} and α_{app} since they neglect ion-pairing and are regarded as apparent values (see above).

The k^0_{app} , and α_{app} values associated with the $K^{W}_{Sn}[N_3C_4H_{10}]^{4-/5-}$ process in acetonitrile containing 0.10 M $[n-Bu_4N][PF_6]$ at the bare GC electrode were initially determined using heuristic form of data analysis of the FTACV data obtained with 0.20 mM $K^{W}_{Sn}[N_3C_4H_{10}]^{4-}$. In this exercise, $E^0_{app} = -1.390$ V, derived from the mid-point potential in DC cyclic voltammetry (see above), was employed as a known rather than estimated parameter value. Simulated data containing variable combinations of k^0_{app} , and α_{app} were compared with experimental data and adjustments to simulated data constantly undertaken until the experimenter decided that the “best fit” had been achieved. Parameters reported by this tedious and subjective method are included in Table 2.

A comparison of the FTACV experimental voltammetry for 0.20 mM $K^{W}_{Sn}[N_3C_4H_{10}]^{4-}$ at a GC electrode and the simulated voltammetry achieved heuristically as the “best fit” in this work is shown in Figure 4i. Good, but not perfect agreement between experimental and

simulated data for the third and higher order AC harmonics is evident in this outcome of the data analysis exercise undertaken by the experimenter. Clearly the background current is not perfectly matched in either the DC, or fundamental or second harmonic AC responses. Additionally, the experimental faradaic responses are not quite as symmetrical with respect to reduction and oxidation components as the ones simulated using the Butler-Volmer model. In the heuristic form of data analysis, and to address this asymmetry issue, matching of reduction component was chosen in the simulation-experimental comparisons to obtain the “best fit” and enumerate the k_{app}^0 , and α_{app} parameters. This achieved an almost perfect fit of this set of data for all the higher order harmonics based on visual inspection. The assumption made by the experimentalist in choosing this *modus operandi* is that non-ideality in the modelling is negligible in the data derived at short times from the reduction component of the experiment with features not accommodated in the model having a small impact at longer experimental times relevant to data collected in the oxidation component. Support for implementing data analysis based on this hypothesis is provided below, but clearly a different experimentalist may have chosen to undertake a different approach in the heuristic method and generate apparently different values of k_{app}^0 , and α_{app} .

The values of k_{app}^0 and α_{app} must be regarded as unreliable when determined by FTACV or any other method when they lie at or very close to the reversible limit where Nernstian rather than Butler-Volmer theory may be more appropriate. With 0.20 mM $K_{Sn}^W[N_3C_4H_{10}]^{4-}$, the heuristically estimated k_{app}^0 value of 0.058 cm s⁻¹ and α_{app} of 0.50 at 9.02 Hz are derived from good agreement of experimental results with simulated data that lie well below that predicted for a simulated reversible process (Figure 4i) so modelling on the basis of a kinetically controlled quasi-reversible reaction is concluded to be appropriate.

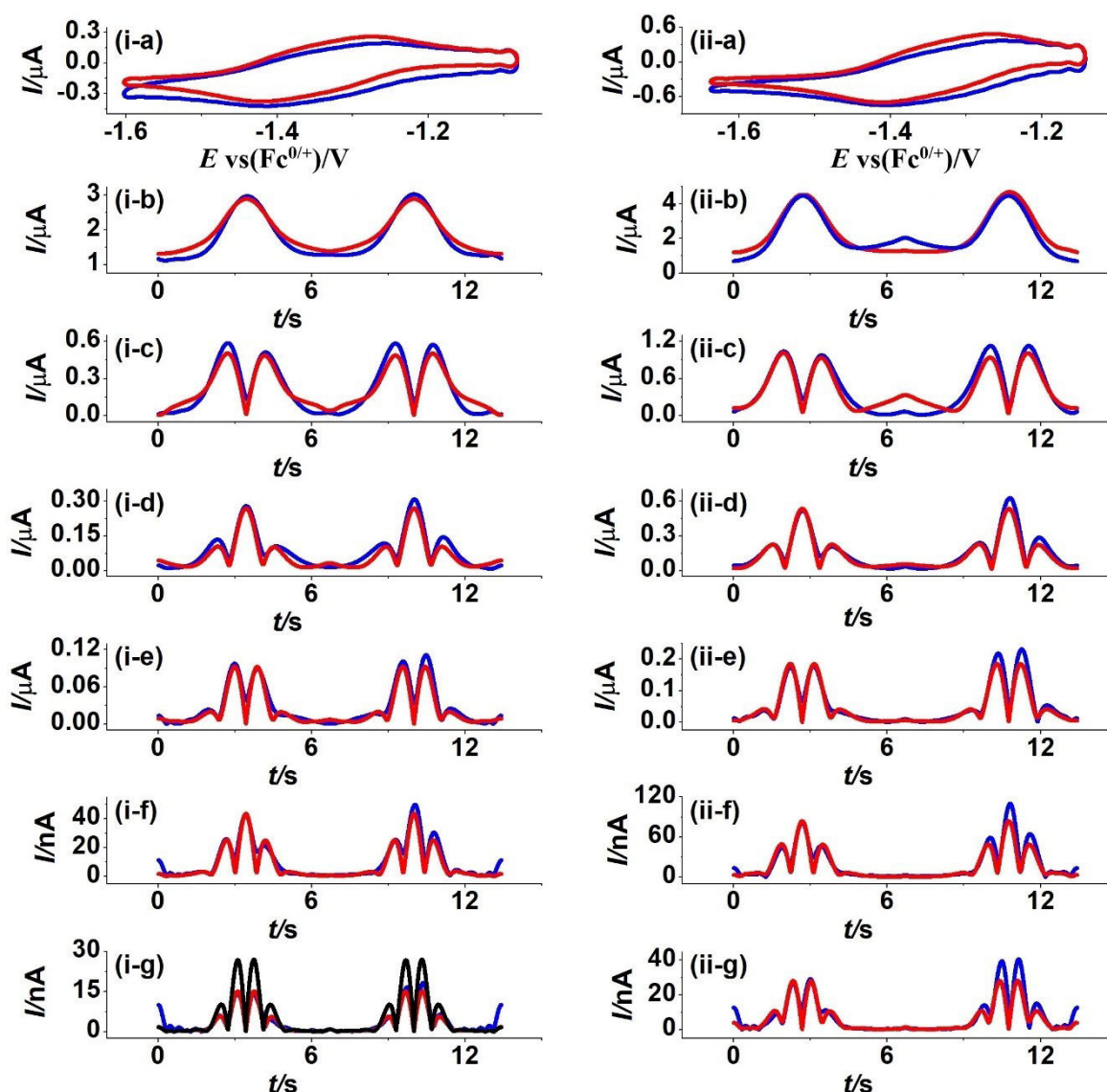


Figure 4. Heuristic comparison of simulated (red) and experimental (blue) FTAC voltammetric data for the $\text{K}^{\text{W}}_{\text{Sn}}[\text{N}_3\text{C}_4\text{H}_{10}]^{4-/5-}$ process, obtained with (i) 0.20 and (ii) 0.50 mM $\text{K}^{\text{W}}_{\text{Sn}}[\text{N}_3\text{C}_4\text{H}_{10}]^{4-}$ in CH_3CN (0.10 M $[n\text{-Bu}_4\text{N}][\text{PF}_6]$) at a bare GC electrode. $\Delta E = 80$ mV, $f = 9.02$ Hz and $v_{0.20\text{ mM}} = 0.078$ V s $^{-1}$ and $v_{0.50\text{ mM}} = 0.075$ V s $^{-1}$. (a) DC component, (b to g) 1st to 6th harmonic components where parameters used in the simulations are given in Table 2, (i-g) comparison of experimental data with that for the 6th harmonic component simulated for a reversible process (black).

Heuristic electrode kinetic parameterisation using a higher concentration (0.50 mM) of $K^w_{an} [N_3C_4H_{10}]^{4-}$ also was investigated by the FTACV technique as shown in Figure 4ii, and again emphasising the reduction component of the data. Discrepancies associated with modelling of the background current are now relatively less important at the higher POM concentration, but asymmetry not predicted in the faradaic reduction and oxidation components is slightly more pronounced than with the lower 0.20 mM POM concentration. Nevertheless, results presented in Table 2 on the basis of heuristic analysis with incorporation of judgemental input from an experienced electrochemist show that as theoretically required, the electrode kinetic parameters are concentration independent as theoretically predicted. This outcome also implies that IR_u drop has been correctly modelled.

Table 2. Electrode kinetic parameters^a derived from heuristic and computer-based comparison of simulated and experimental FTACV data at 9.02 Hz at a bare GC, Au and Pt electrode for the $K^w_{an}[N_3C_4H_{10}]^{4-/5-}$ process in CH_3CN (0.10 M [*n*-Bu₄N][PF₆]).

Electrode	Conc (mM)	Simulation method	R_u (Ω) ^b	E_{app}^0 V vs Fc ^{0/+}	k_{app}^0 (cm s ⁻¹)	α_{app}	LS %	
GC	0.20	Heuristic	510	-1.390	0.058 ^c	0.50		
		Automated		Range	-1.395 to -1.385	0.040 to 0.095	0.40 to 0.70	
			Estimated	-1.390	0.075 ^d	0.42	84	
	0.50	Heuristic	599	-1.390	0.056 ^c	0.50		
Automated		Range		-1.397 to -1.385	0.045 to 0.095	0.40 to 0.70		
		Estimated	-1.391	0.075 ^d	0.42	87		
Au	0.20	Heuristic	521	-1.390	0.016	0.50		
		Automated		Range	-1.396 to -1.387	0.005 to 0.030	0.40 to 0.70	
		Estimated		-1.394	0.014	0.43	75	
Pt	0.20	Heuristic	511	-1.390	0.009 to 0.031 ^c	0.43		
		Automated		Range	-1.395 to -1.386	0.002 to 0.040	0.40 to 0.70	
		Estimated		-1.394	0.022	0.43	69	

^a Other parameters used in the simulations are: $A_{GC} = 8.0 \times 10^{-3} \text{ cm}^2$, $A_{Au} = 8.1 \times 10^{-3} \text{ cm}^2$, $A_{Pt} = 8.0 \times 10^{-3} \text{ cm}^2$, $\Delta E = 80 \text{ mV}$, $D = 6.3 \times 10^{-6} \text{ cm}^2 \text{ s}^{-1}$, $T = 295 \text{ K}$, $v_{0.20 \text{ mM}} = 0.078 \text{ V s}^{-1}$ and $v_{0.50 \text{ mM}} = 0.075 \text{ V s}^{-1}$ with GC electrode, $v_{Au \text{ and Pt}} = 0.078 \text{ V s}^{-1}$, $f = 9.02 \text{ Hz}$.

^b vary due to slight difference in electrode arrangement in cell.

^c determined from analysis of the reduction component of data only.

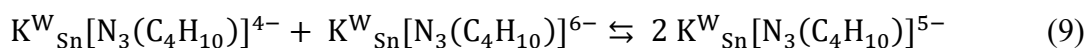
^d derived from use of all data even though asymmetry is present in reduction and oxidation components.

^e apparently harmonic dependent kinetics.

Parameter values estimated from the heuristic data analysis exercise allow the search of parameter space to be constrained efficiently and sensibly so as to minimise the computational time required in automated data optimisation analysis. Thus, $E_{app}^0 = -1.395$ to -1.385 V, $k_{app}^0 = 0.040$ to 0.095 cm s⁻¹, $\alpha_{app} = 0.40$ to 0.70 ranges were used for example in simulations undertaken in the computer aided data optimisation procedure for the first reduction process with 0.20 mM $K_{Sn}^W[N_3C_4H_{10}]^{4-}$ obtained by FTACV at a frequency of 9.02 Hz. The ranges of parameters and resolution used for all simulations are included in Table 2. In this data optimisation exercise, least squares comparison of the experimental and simulated voltammograms, as was the case with the heuristic method, was restricted to the 2nd to 6th harmonics that contain negligible influence from the background current. Normally, the automated method, unless trained to be an intelligent expert system, would find the “best fit” based on least squares outcomes using all data. Best fit values for E_{app}^0 , k_{app}^0 and α_{app} parameters found via this automated computer assisted method using all data and not just data for the reduction component as used in the heuristic method of analysis are summarised in Table 2. While agreement between simulated and experimental FTAC voltammetry is again excellent, close inspection confirms that the small level of asymmetry is still not accommodated by theory. Variation in how the asymmetry is accommodated in the modelling lead to the data analysis dependent electrode kinetic parameters contained in Table 2. In particular, the data optimisation method using all data produces an α_{app} value of about 0.42 which is a result of the attempting to mimic the asymmetry, whereas an α_{app} value of 0.50 is

deduced via heuristic analysis by confining data analysis solely to the reduction component. Furthermore, the automated method provides a slightly larger value of k_{app}^0 of around 0.075 relative to the value of 0.058 cm s⁻¹ obtained via the heuristic approach. Significantly, restricting the data optimisation analysis to just the reduction component generates parameter values almost identical to those reported heuristically. It will emerge from studies described below, that weighting data analysis in this manner can be justified and indeed having α_{app} value of close to 0.50 via this approach is intrinsically satisfying for the $K_{Sn}^W[N_3C_4H_{10}]^{4-/5-}$ process which should not involve significant structural change. This study illustrates the value of initially using heuristic approaches to enhance prospects of detecting potential modelling imperfections.

Both of the $K_{Sn}^W[N_3C_4H_{10}]^{4-/5-/6-}$ processes at GC electrode in solution phase also were parameterised using experimental data collected over a potential range that is sufficiently large to accommodate both reactions (Figure 5). Values derived from both heuristic (reduction component only) and automated data optimisation (all data used with parameter space ranges selected from heuristic results) from 0.20 and 0.50 mM solutions of $K_{Sn}^W[N_3C_4H_{10}]^{4-}$ are summarized in Table 3. Any influence of the cross redox reaction given in eqn. 9 was neglected in this modelling since this reaction adds complication in the simulation unless artificial intelligent include in the modelling.



Clearly, the second $K_{Sn}^W[N_3C_4H_{10}]^{5-/6-}$ process is kinetically slower than first $K_{Sn}^W[N_3C_4H_{10}]^{4-/5-}$ process (e.g. $k_{app1}^0 = 0.056$ cm s⁻¹ versus $k_{app2}^0 = 0.020$ cm s⁻¹ for heuristic analysis for 0.20 mM POM data). This outcome is consistent with the suggestion based on the larger DC cyclic voltammetric peak-to-peak separations for the second process, where $\Delta E_{P2} =$

67 mV > $\Delta E_{p1} = 63$ mV (see Table 1). As would be anticipated, the asymmetry not predicted by theory again leads to data analysis method dependent elected kinetic parameter values. However, parameter estimates for the first process are independent of whether the data are collected independently of the second process or simultaneously with the second process.

k_{app}^0 for the solution soluble Ge analogue of the Sn derivative at a GC electrode in CH₃CN has been reported ³ to be 0.064 cm s⁻¹ (α_{app} assumed to be 0.50) for the K^W_{Ge}[N₃C₄H₁₀]^{4-/5-} process via analysis of a plot of reduction peak potential versus scan rate obtained under conditions of linear sweep voltammetry ⁵⁴ and hence similar to that for the K^W_{Sn}[N₃C₄H₁₀]^{4-/5-} process.

The k_{app}^0 value for the K^W_{Sn}[N₃C₄H₁₀]^{4-/5-} process is about three times slower than that for the α -[S₂W₁₈O₆₂]^{4-/5-} process at a GC electrode under the same conditions ⁵⁵. The long diazonium chain in the structure of K^W_{Sn}[N₃C₄H₁₀]⁴⁻ may influence the rate of electron transfer kinetics by restricting the distance of closest approach of the POM to the electrode surface and lead to slower electrode kinetic than for the fully symmetrical α -[S₂W₁₈O₆₂]⁴⁻ POM, although differences in ion-pairing and other factors also may play a role.

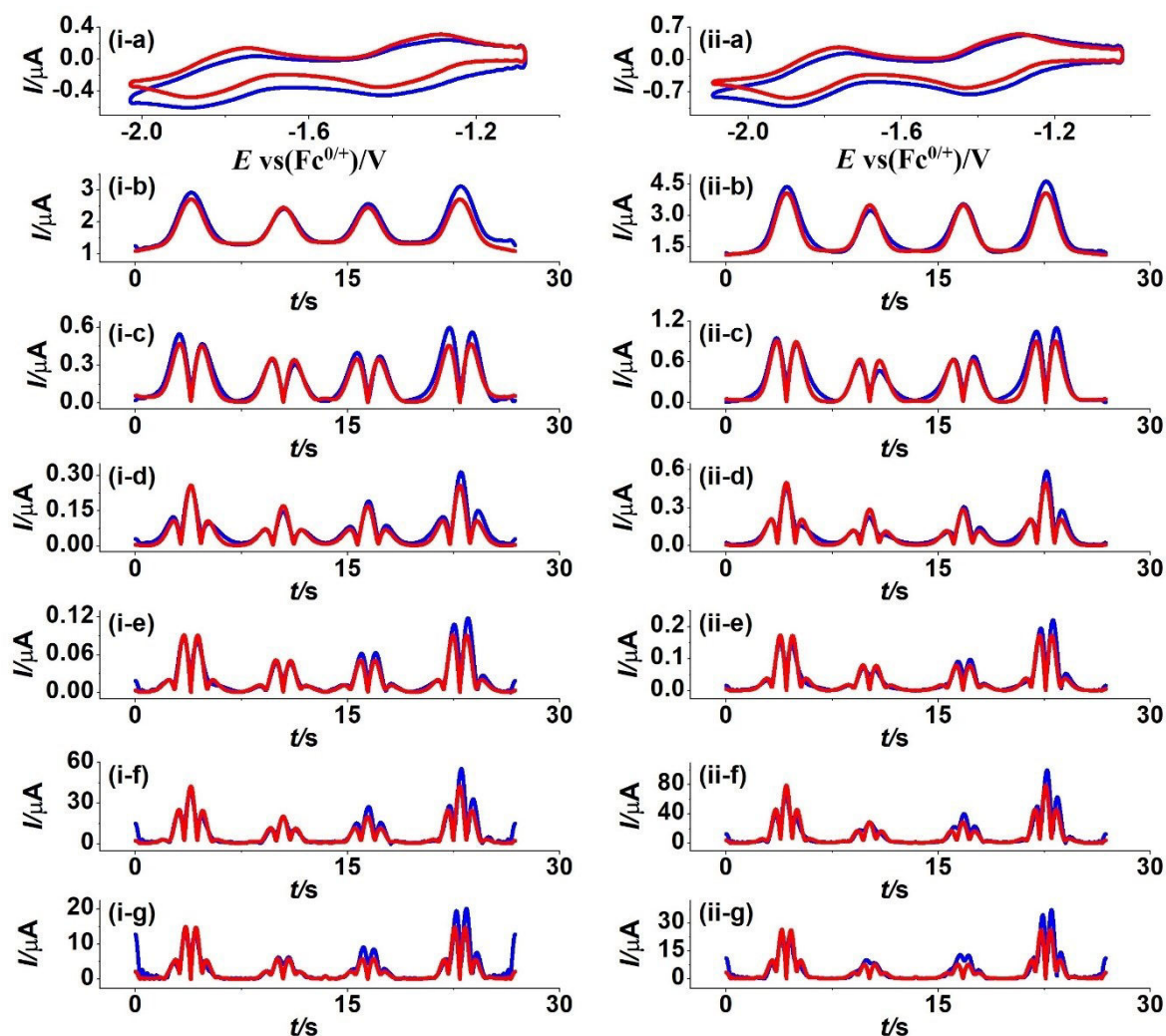


Figure 5. Heuristic comparison of simulated (red line) and experimental (blue line) AC voltammetric data for the $\text{K}^{\text{W}}_{\text{Sn}}[\text{N}_3\text{C}_4\text{H}_{10}]^{4-/5-/6-}$ process, obtained with (i) 0.20 mM and (ii) 0.50 mM $\text{K}^{\text{W}}_{\text{Sn}}[\text{N}_3\text{C}_4\text{H}_{10}]^{4-}$ in CH_3CN (0.10 M $[\text{n-Bu}_4\text{N}][\text{PF}_6]$) at a bare GC electrode. $\Delta E = 80$ mV, $f = 9.02$ Hz and $\nu_{0.20 \text{ mM}} = 0.071$ V s^{-1} and $\nu_{0.50 \text{ mM}} = 0.080$ V s^{-1} . (a) DC component, (b-g) 1st to 6th harmonic components.

Table 3. Electrode kinetic parameters^a derived from the heuristic and computer-based comparison of simulated and experimental FTACV data at 9.02 Hz at a bare GC electrode for the $\text{K}^{\text{W}}_{\text{Sn}}[\text{N}_3\text{C}_4\text{H}_{10}]^{4-/5-}$ and $\text{K}^{\text{W}}_{\text{Sn}}[\text{N}_3\text{C}_4\text{H}_{10}]^{5-/6-}$ processes in CH_3CN (0.10 M $[n\text{-Bu}_4\text{N}][\text{PF}_6]$).

Conc (mM)	Simulation method	R_u (Ω) ^b	E_{app1}^0 E_{app2}^0		k_{app1}^0 k_{app2}^0		α_{app1}	α_{app2}	LS %	
			V vs $\text{Fc}^{0/+}$		cm s^{-1}					
0.20	Heuristic	510	-1.390	-1.843	0.056 ^c	0.020 ^c	0.50	0.50		
	Automated		Range	-1.395	-1.847	0.040	0.005	0.40	0.40	
				to -	to -	to	to	to	to	
			Estimated	1.386	1.840	0.095	0.045	0.70	0.70	
			-1.387	-1.845	0.071^d	0.023^d	0.42	0.42	81	
0.50	Heuristic	599	-1.390	-1.843	0.056 ^c	0.016 ^c	0.50	0.50		
	Automated		Range	-1.395	-1.847	0.040	0.005	0.40	0.40	
				to -	to -	to	to	to	to	
			Estimated	1.386	1.839	0.085	0.045	0.70	0.70	
			-1.387	-1.846	0.072^d	0.018^d	0.43	0.43	80	

^a Other parameters used in the simulations are: $A_{GC} = 8.0 \times 10^{-3} \text{ cm}^2$, $\Delta E = 80 \text{ mV}$, $D = 6.3 \times 10^{-6} \text{ cm}^2 \text{ s}^{-1}$

¹, $T = 295 \text{ K}$, $\nu_{0.20 \text{ mM}} = 0.071 \text{ V s}^{-1}$, $\nu_{0.50 \text{ mM}} = 0.080 \text{ V s}^{-1}$, $f = 9.02 \text{ Hz}$.

^b vary due to slight differences in the electrode arrangement.

^c determined from reduction component of data only

^d derived from use of all data.

FTACV studies on the $\text{K}^{\text{W}}_{\text{Sn}}[\text{N}_3(\text{C}_4\text{H}_{10})]^{4-/5-}$ process at Au and Pt metal electrodes also were undertaken. As stated above, the electrode material dependence predicted on basis of peak-to-peak separations obtained in DC cyclic voltammetry (Table 1) is $k_{GC}^0 > k_{Au}^0 > k_{Pt}^0$, as reported with other POMs²⁵. However, as at GC, FTACV data analysis of the voltammetry at the metal electrodes reveals nuances in the mechanisms relative to predictions based on a simple one-electron quasi-reversible process. Comparisons of simulated and experimental data for FTACV based on heuristic analysis are provided in Figure S5 for Au and Figure S6 for Pt, while parameters that are obtained from the heuristic and computer supported forms of data analysis used in this study are summarised in Table 2. Clearly, agreement between

experimental and simulated data at Au and Pt are poorer than at the GC electrode. Furthermore, electrode kinetic parameters are even more strongly dependent on the method of data analysis.

Assuming the Butler-Volmer model is valid, the kinetics at GC ($k_{app1}^0 = 0.058 \text{ cm s}^{-1}$) are faster than at Au ($k_{app1}^0 = 0.016 \text{ cm s}^{-1}$) based on the heuristic approach and use of only the reduction component. However, there is significant uncertainty as to whether this model is even appropriate for analysis of data obtained with the Pt electrode. With Au, and unlike theoretical predictions, the oxidation current component is larger than reduction one as for GC case, but even more pronounced and a mismatch in background current in DC and fundamental harmonic components is evident. In the case of Pt, excellent agreement between experiment and theory is provided for the third harmonic ($k_{app1}^0 = 0.013 \text{ cm s}^{-1}$) in Figure S6ii based on heuristic estimation, but use of this same rate constant to model lower and higher harmonics respectively overestimates and underestimates the current magnitudes significantly. That is, apparently harmonic dependant kinetics in the range of 0.0095 to 0.031 cm s^{-1} are observed at the Pt electrode (shown in Figure S6i) when best fits applied consecutively to fundamental to sixth harmonic AC data. Theoretically, of course, the rate constant should be harmonic independent. Modelling with Marcus-Hush theory as an alternative to the Butler-Volmer model was considered but did not produce superior fits to data. At Pt, the background current in DC aperiodic and fundamental harmonic components predicted theoretically also differ from that determined experimentally. Harmonic dependent location of potentials of peaks also are evident in theory-experiment comparisons. Finally, it is noted that even the shape of a conventional DC cyclic voltammogram at the Pt electrode does perfectly match theoretical predictions as also noted with the $\text{Fc}^{0/+}$ process at boron diamond electrodes when sp^2 graphite impurity provided complexity in the response⁴⁸. Differences in experimental and theoretical data based on the Butler-Volmer model with mass transport by linear diffusion at Pt are so

profound that parameterisation on this basis is not highly significant. Clearly, the voltammetry of $K_{Sn}^W[N_3(C_4H_{10})]^{4-/5-}$ and $K_{Sn}^W[N_3(C_4H_{10})]^{5-/6-}$ processes are more complex than predicted at all electrodes used, with the extent of non-ideality being in the order $Pt > Au > GC$.

3.3. Origin of discrepancies of experimental data and predictions based on Butler-Volmer electrode kinetic model. Variable levels of non-conformance to the Butler-Volmer model of electron transfer were detected in the solution phase FTAC voltammetry of $K_{Sn}^W[N_3C_4H_{10}]^{4-}$ at GC, Au and Pt electrodes. One possible explanation for the anomalous behaviour is that reduction of $K_{Sn}^W[N_3C_4H_{10}]^{4-}$ to $K_{Sn}^W[N_3C_4H_{10}]^{5-}$ leads to modification of the electrode surface which could alter the shape and other characteristics of the voltammetry in a time or potential dependent manner not accommodated by the theory.

In principle, surface interaction of $K_{Sn}^W[N_3C_4H_{10}]^{4-}$ or $K_{Sn}^W[N_3C_4H_{10}]^{5-}$ with the electrode surface should lead to a mass change during the course of the voltammetry which can be detected by the EQCM method via a change in the oscillation frequency of an Au coated quartz crystal electrode⁵⁶. Accordingly, the frequency (mass) change of a gold crystal working electrode was monitored during DC cyclic voltammetry undertaken in CH_3CN (0.10 M [*n*-Bu₄N][PF₆]) with and without 0.50 mM $K_{Sn}^W[N_3(C_4H_{10})]^{4-}$ at a scan rate of 0.050 V s⁻¹ over the potential range covering the region where grafting (Figure 6i-b) occurs with the diazonium derivative $K_{Sn}^W[N_2^+]^{3-}$ at a GC electrode (see above) as well as the first $K_{Sn}^W[N_3(C_4H_{10})]^{4-/5-}$ process (Figure 6i-a). Although we have not prepared a grafted Au electrode in this study, Gooding et al⁵⁷⁻⁵⁹ for example have shown that Au also provides an excellent surface for diazonium grafting.

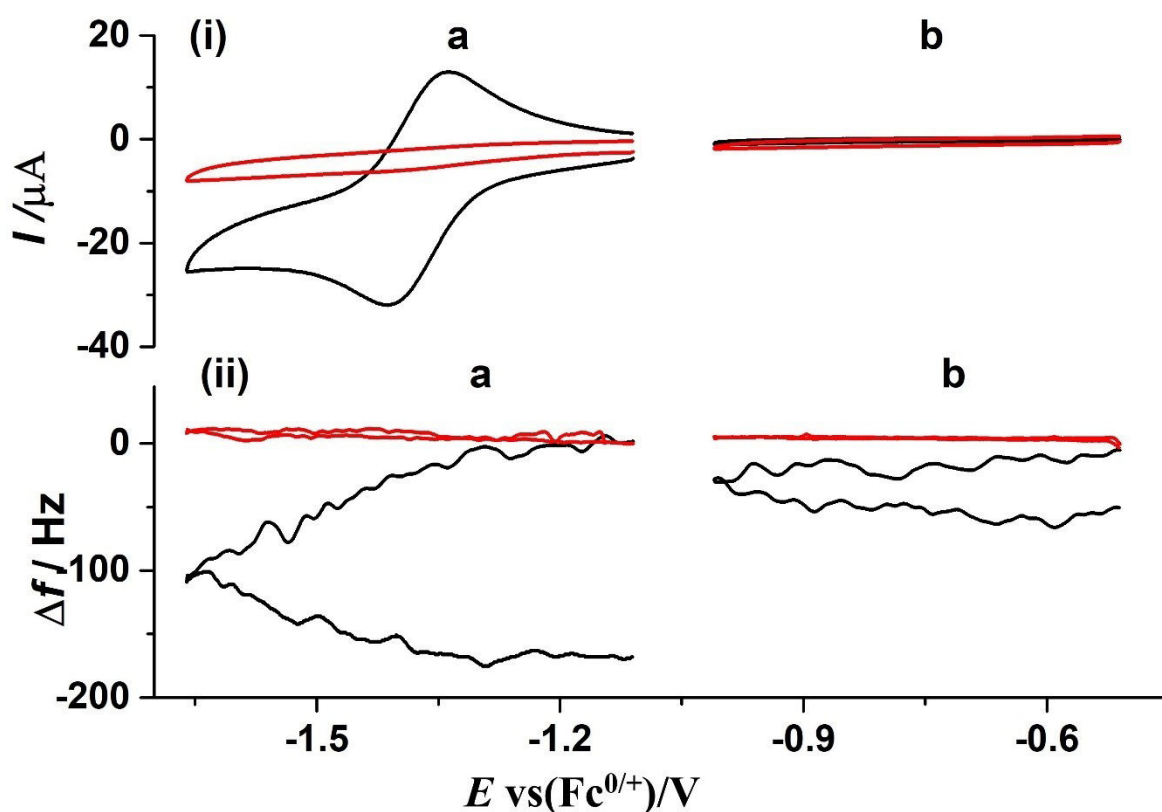


Figure 6. EQCM data obtained for 0.50 mM $\text{K}_{\text{Sn}}^{\text{W}}[\text{N}_3\text{C}_4\text{H}_{10}]^{4+}$ at a scan rate of 0.050 V s^{-1} with an Au quartz crystal electrode over the potential range covering the region where grafting (b) occurs with diazonium derivative and the first $\text{K}_{\text{Sn}}^{\text{W}}[\text{N}_3\text{C}_4\text{H}_{10}]^{4+/5-}$ process (a) occurs. (i) cyclic voltammetry (current versus potential) and (ii) frequency versus potential. (----) 0.50 mM $\text{K}_{\text{Sn}}^{\text{W}}[\text{N}_3\text{C}_4\text{H}_{10}]^{4+}$ in CH_3CN (0.10 M $[n\text{-Bu}_4\text{N}][\text{PF}_6]$). (----) 0.10 M $[n\text{-Bu}_4\text{N}][\text{PF}_6]$. Δf = gold quartz crystal frequency change.

Figure 6 displays the EQCM (i) current and (ii) frequency responses as a function of potential for an Au coated quartz crystal electrode in contact with CH_3CN (0.10 M $[n\text{-Bu}_4\text{N}][\text{PF}_6]$) in the presence and absence of 0.50 mM of $\text{K}_{\text{Sn}}^{\text{W}}[\text{N}_3\text{C}_4\text{H}_{10}]^{4+}$. As shown in Figure 6ii, the frequency of oscillation of the Au coated quartz crystal remains constant in the absence of $\text{K}_{\text{Sn}}^{\text{W}}[\text{N}_3\text{C}_4\text{H}_{10}]^{4+}$. In contrast, with 0.50 mM $\text{K}_{\text{Sn}}^{\text{W}}[\text{N}_3\text{C}_4\text{H}_{10}]^{4+}$ present, and as shown in Figure 6ii-a the frequency decreased (mass increased) significantly at potentials more negative

than the onset of the $\text{K}_{\text{Sn}}^{\text{W}}[\text{N}_3\text{C}_4\text{H}_{10}]^{4-/5-}$ process and continued to decrease upon reversing the scan direction until reduction of $\text{K}_{\text{Sn}}^{\text{W}}[\text{N}_3\text{C}_4\text{H}_{10}]^{4-}$ ceased. Prior to the onset of reduction of $\text{K}_{\text{Sn}}^{\text{W}}[\text{N}_3\text{C}_4\text{H}_{10}]^{4-}$ minimal frequency (mass) change is detected (Figure 6ii-b). Clearly, irreversible surface attachment of a $\text{K}_{\text{Sn}}^{\text{W}}[\text{N}_3\text{C}_4\text{H}_{10}]^{4-}$ reduction product occurs at a gold electrode and presumably also at GC and Pt electrodes, but to differing extents. This surface modification phenomenon is not present in the modelling, but since it is derived from a $\text{K}_{\text{Sn}}^{\text{W}}[\text{N}_3\text{C}_4\text{H}_{10}]^{5-}$ reduction product, larger departures in simulated data are expected the more negative the potential or the longer the time since the onset of the $\text{K}_{\text{Sn}}^{\text{W}}[\text{N}_3\text{C}_4\text{H}_{10}]^{4-/5-}$ process. Use of only the reduction component of data to achieve superior conformance to the simulated data with GC and Au electrodes as implemented in the heuristic form of FTACV data analysis is consistent with this concept.

Spontaneous, electrostatically induced adsorption of POMs often occurs at carbon and metal electrodes⁶⁰. This phenomenon can be detected by so called dipping experiments. Figure S7 shows the results obtained by dipping GC, Au and Pt electrodes in a 0.50 mM solution of $\text{K}_{\text{Sn}}^{\text{W}}[\text{N}_3\text{C}_4\text{H}_{10}]^{4-}$ for at least 5 minutes, removing the electrodes from the solution, sonicating in CH_3CN , drying and placing the electrode in fresh CH_3CN electrolyte (0.10 M [*n*-Bu₄N][PF₆]) solution. No well-defined, surface confined symmetrically shaped, diffusionless voltammetry of adsorbed $\text{K}_{\text{Sn}}^{\text{W}}[\text{N}_3\text{C}_4\text{H}_{10}]^{4-}$ is evident, as occurs with other POMs⁶¹, nor is there evidence of a grafted POM derivative (see below). However, substantial modification of the background charging current response is evident at Au and Pt electrodes, indicating their electrode surfaces have been modified, but not by attachment of $\text{K}_{\text{Sn}}^{\text{W}}[\text{N}_3\text{C}_4\text{H}_{10}]^{4-}$.

In order to seek evidence for product interaction with the surface, the electrode potential for a 0.50 mM $\text{K}_{\text{Sn}}^{\text{W}}[\text{N}_3\text{C}_4\text{H}_{10}]^{4-}$ solution was held at -1.750 V vs $\text{Fc}^{0/+}$ for 0, 60, 120, and 180 seconds at the GC, Au and Pt electrodes before commencing cyclic voltammetry. At this

potential $\text{K}^{\text{W}}_{\text{Sn}}[\text{N}_3\text{C}_4\text{H}_{10}]^{4-}$ is reduced to $\text{K}^{\text{W}}_{\text{Sn}}[\text{N}_3\text{C}_4\text{H}_{10}]^{5-}$ under bulk electrolysis conditions. If surface confined $\text{K}^{\text{W}}_{\text{Sn}}[\text{N}_3\text{C}_4\text{H}_{10}]^{5-}$ accumulated then stripping current would be expected as occurs in stripping voltammetry⁶². However as shown in Figure 7, no stripping oxidative responses are found at any electrode surface.

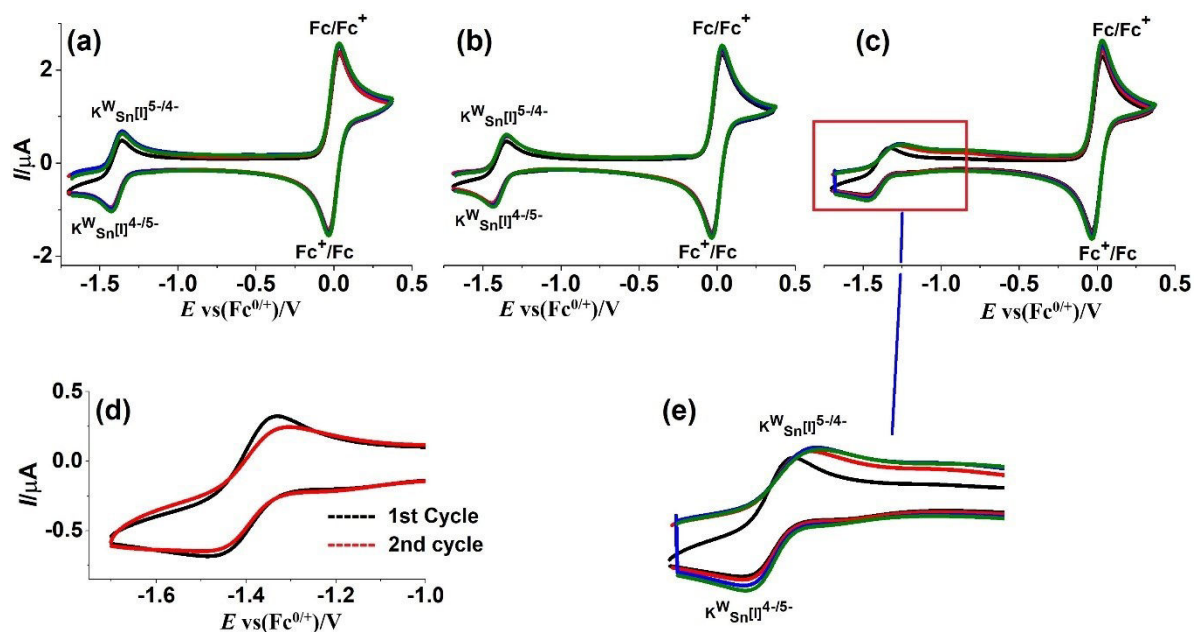


Figure 7. Cyclic voltammetry of 0.50 mM $\text{K}^{\text{W}}_{\text{Sn}}[\text{N}_3\text{C}_4\text{H}_{10}]^{4-}$ in CH_3CN (0.10 M $[\text{n-Bu}_4\text{N}][\text{PF}_6]$) at a scan rate of 0.050 V s^{-1} with (a) GC, (b) Au and (c) Pt electrode ((e) magnified CV of $\text{K}^{\text{W}}_{\text{Sn}}[\text{N}_3\text{C}_4\text{H}_{10}]^{4-/5-}$ process) when hold the potential at -1.750 V for 0 (black), 60 (red), 120 (blue) and 180 (green) s, respectively. (d) first 2 cycles with Pt electrode without hold time.

However, at the Pt electrode (Figure 7c) and (e) it is particularly noticeable that the peak-to-peak separation increases with each cycle of potential ($\Delta E_{0 \text{ sec}} = 156 \text{ mV}$, $\Delta E_{60 \text{ sec}} = 200 \text{ mV}$, $\Delta E_{120 \text{ sec}} = 219 \text{ mV}$ and $\Delta E_{180 \text{ sec}} = 221 \text{ mV}$), the mid-point potential shifts positively ($E_{0 \text{ sec}}^m = -1.408$, $E_{60 \text{ sec}}^m = -1.382$, $E_{120 \text{ sec}}^m = -1.370$ and $E_{180 \text{ sec}}^m = -1.363 \text{ V}$). Furthermore, the shape of the $\text{K}^{\text{W}}_{\text{Sn}}[\text{N}_3\text{C}_4\text{H}_{10}]^{4-/5-}$ process changes to a more sigmoidal one and the background or charging current increases significantly. The $\text{K}^{\text{W}}_{\text{Sn}}[\text{N}_3\text{C}_4\text{H}_{10}]^{4-/5-}$ process was

less effected in these extended electrolysis experiments at GC and Au electrodes. Clearly, electrode fouling which is most severe with the Pt electrode occurred during the $K_{Sn}^W[N_3C_4H_{10}]^{4-/5-}$ process.

Results of 10 consecutive voltammetric experiments (Figure 8) at each of the GC, Au and Pt electrodes, with no electrode polishing in between each cycle show even more clearly how surface accumulation of a $K_{Sn}^W[N_3C_4H_{10}]^{5-}$ decomposition product gradually facilitates transition from a peak to a sigmoidal shaped response. This change in shape is fully analogous to what happens in the voltammetry of metalloproteins or metalloenzymes upon denaturation⁶³⁻⁶⁵. Progressive electrode blockage by denatured electroinactive metalloprotein, generates an expanding array of electroactive sites while electrochemistry from residual intact metalloprotein occurs predominantly by radial (sigmoidal shape response) than by linear diffusion (peak shaped response). In the case of the POM used in this study, accumulation of an unknown surface confined product accompanies the initial one-electron reduction, with the impact order being Pt > Au > GC. It is plausible that reduction to $K_{Sn}^W[N_3C_4H_{10}]^{5-}$ lowers the stability of the organic side chain which becomes detached from the POM and provides a pathway for formation of an array of electroinactive sites of unknown composition. Apparently, degradation is more rapid at the Au and Pt electrodes than at GC. Once the electrode is surface modified, the capacitance and other characteristics change progressively with time to give array electrode type behaviour. This nuance implies that the second $K_{Sn}^W[N_3C_4H_{10}]^{5-/6-}$ process at Au and Pt electrodes in particular are far more distorted than the initial $K_{Sn}^W[N_3C_4H_{10}]^{4-/5-}$ process. Thus, accordingly, electrode kinetic FTACV data analysed via the Butler-Volmer model assuming linear diffusion for mass transport should indeed coincide most closely with the modelled data when applied solely to the initial reduction component of the data rather than when using all data that includes the more distorted oxidation component. Effectively, the mass transport model is changing from linear to radial diffusion

during the course of the FTACV experiment when fully linear diffusion is assumed throughout in the modelling. However, it should be noted that as expected, repolishing the electrode after 10 experiments restores the voltammetric characteristics shown for the initial one.

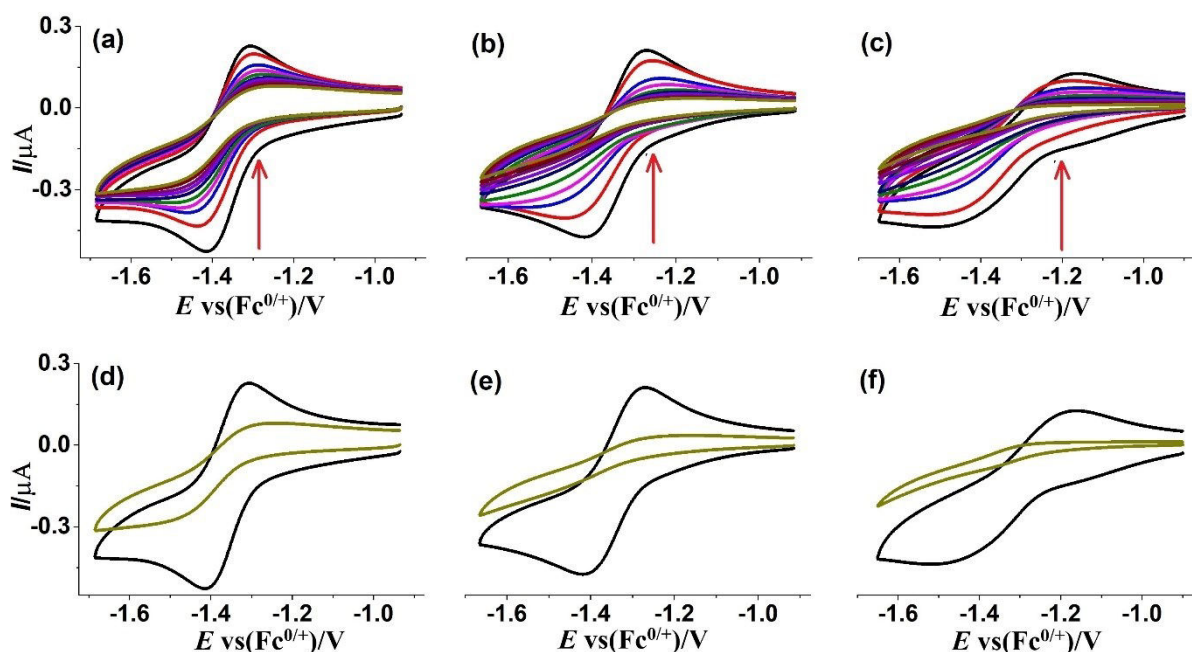


Figure 8. Ten consecutive DC cyclic voltammetric experiments at (a) GC, (b) Au and (c) Pt electrodes without polishing the electrode after each experiment. (d), (e) and (f) represent the 1st and 10th experiments at GC, Au and Pt electrodes, respectively.

3.4. FTACV voltammetric characterization of the grafted $\text{K}^{\text{W}}_{\text{Sn}}[-]^{4-/5-/6-}$ processes at a GC modified electrode in CH_3CN . Thermodynamic and kinetic parameterisation based on FTAC voltammetry with a sinusoidal perturbation having an amplitude of 80 mV, a frequency of 9.02 Hz and an underlying DC scan rate of (0.052 to 0.086 V s^{-1}) also was applied to FTACV data obtained with the $\text{K}^{\text{W}}_{\text{Sn}}[-]^{4-}$ modified GC electrode. As in the solution phase exercise described above, more detailed information was expected to emerge than from analysis with the widely used DC voltammetric method^{39, 43, 66-69}. The initial simulations used to mimic experimental data for the first reduction process obtained with a $\text{K}^{\text{W}}_{\text{Sn}}[-]^{4-}$ -grafted GC

electrode in contact with CH₃CN (0.10 M [*n*-Bu₄N][PF₆]) solution via heuristic data analysis assumed the values of $E_{app}^0 = -1.450$ V (mid-point potential of DC experiment), with $R_u = 518$ Ω and $\Gamma = 8.8 \times 10^{-11}$ mol cm⁻² being known parameters. The outcome of this exercise is shown in Figure 9i. As for the solution phase studies with $K_{Sn}^W[N_3C_4H_{10}]^{4-}$, simulation-experiment agreement with the second and higher harmonics is good, but background current estimation for the DC is poor. Values for k_{app}^0 and α_{app} estimated heuristically with this close to monolayer surface coverage were 40 s⁻¹ and 0.46 respectively for this first $K_{Sn}^W[-]^{4-/5-}$ process. As for the solution soluble scenario described above, estimated k_{app}^0 and α_{app} values are regarded as reliable in the sense that they are derived from simulated data that lie well below that predicted for a reversible process simulated with a very large value of k_{app}^0 and an α_{app} value of 0.50 (Figure 9i-g).

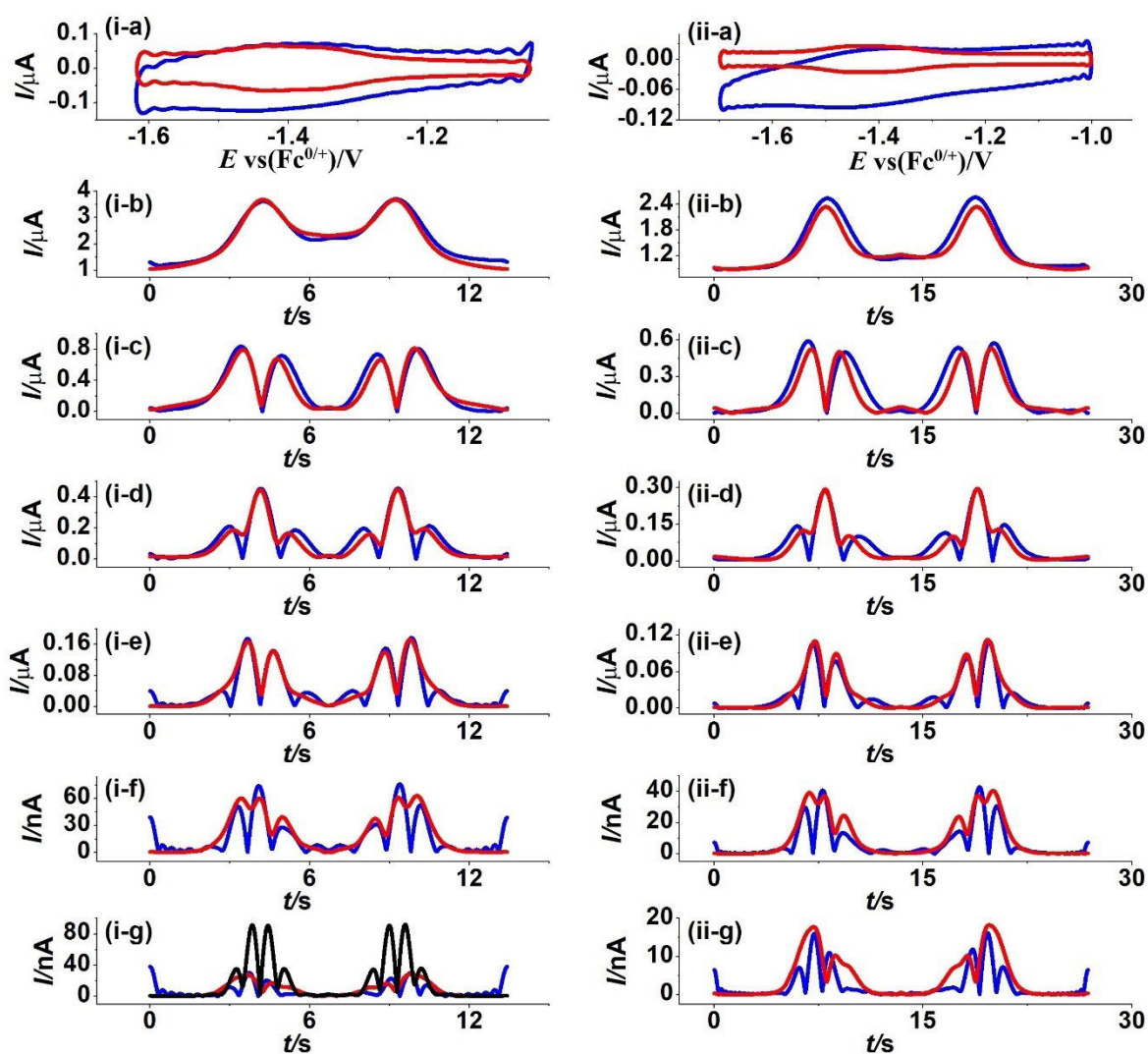


Figure 9. “Best fit” heuristic comparison of simulated (red) and experimental (blue) FTAC voltammetric data obtained for the first reduction process at a $\text{K}^{\text{W}}_{\text{Sn}}[-]^{4-}$ -grafted GC electrode in contact with CH_3CN (0.10 M $[n\text{-Bu}_4\text{N}][\text{PF}_6]$). (i) $\Gamma = 8.8 \times 10^{-11} \text{ mol cm}^{-2}$ and (ii) $\Gamma = 6.2 \times 10^{-11} \text{ mol cm}^{-2}$, $\Delta E = 80 \text{ mV}$, $f = 9.02 \text{ Hz}$, $v_i = 0.082 \text{ V s}^{-1}$ and $v_{ii} = 0.052 \text{ V s}^{-1}$. (a) DC component, (b-g) 1st to 6th harmonic components. Other Parameters used in simulations are given in Table 4. Figure (i-g) is comparison of experimental data with that for the sixth harmonic component simulated for a reversible process (black).

The outcome from a second experiment- simulation exercise with a lower, presumably sub-monolayer coverage, ($\Gamma = 6.2 \times 10^{-11} \text{ mol cm}^{-2}$) is displayed in Figure 9ii and gave

heuristically estimated values of $k_{app}^0 = 38 \text{ s}^{-1}$ and $\alpha_{app} = 0.46$. Again, good theory-experiment agreement was achieved for the second and higher harmonic components that are essentially devoid of background current^{68, 70} with relatively poorer agreement for the DC component again attributed to limitations in modelling of the background current for a $\text{K}_{\text{Sn}}^{\text{W}}[-]^{4-}$ -grafted GC electrode. Many POMs⁷¹⁻⁷⁵, including those mixed with carbon materials form supercapacitors. Hence, pseudo-capacitance arising from this origin and not accommodated in the model used to mimic the background plausibly is present.

Computer aided data analysis was also applied to parameterise the experimental data for the FTAC voltammetry of $\text{K}_{\text{Sn}}^{\text{W}}[-]^{4-}$ -grafted GC electrode in CH_3CN (0.10 M [*n*-Bu₄N][PF₆]). In this data optimisation approach, and as with solution phase studies with $\text{K}_{\text{Sn}}^{\text{W}}[\text{N}_3\text{C}_4\text{H}_{10}]^{4-}$, E_{app}^0 now was assumed to be an unknown rather than known parameter. Also, electrode kinetic values determined heuristically again were used to select and constrain the parameter space range surveyed. Examination of results of parameterisation by both heuristic and automated methods are summarised in Table 4 and are in excellent agreement.

Table 4. Parameters^a derived from the heuristic and computer-based comparison of simulated and experimental FTACV data at 9.02 Hz at $\text{K}_{\text{Sn}}^{\text{W}}[-]^{4-}$ -grafted GC electrode for the $\text{K}_{\text{Sn}}^{\text{W}}[-]^{4-/5-}$ process in CH_3CN (0.10 M [*n*-Bu₄N][PF₆]).

Γ ($\times 10^{-11} \text{ mol cm}^{-2}$)	Simulation method	R_u (Ω) ^b	E_{app}^0 V vs Fc ^{0/+}	k_{app}^0 (s^{-1})	α_{app}	LS %	
8.8 ⁱ	Heuristic	518	-1.450	40	0.46		
	Automated		Range	-1.455 to -1.446	25 to 50	0.40 to 0.70	
			Estimated	-1.451	41	0.48	82
6.2 ⁱⁱ	Heuristic	585	-1.450	38	0.46		
	Automated		Range	-1.455 to -1.446	25 to 45	0.40 to 0.65	
			Estimated	-1.448	35	0.48	84

^aOther parameters used in the simulations are: $A_{GC} = 8.0 \times 10^{-3} \text{ cm}^2$, $\Delta E = 80 \text{ mV}$, $T = 295 \text{ K}$, $v_i = 0.082 \text{ V s}^{-1}$, $v_{ii} = 0.052 \text{ V s}^{-1}$ and $f = 9.02 \text{ Hz}$. ^bvary due to slight difference in electrode arrangement in cell.

Analysis of both the first and second processes at the $\text{K}_{\text{Sn}}^{\text{W}}[-]^4$ -grafted GC electrode simultaneously in one experiment and with $\Gamma = 10 \times 10^{-11} \text{ mol cm}^{-2}$, (see Figure 10) gave the results summarized in Table 5. The second process ($k_{\text{app}2}^0 = 18 \text{ s}^{-1}$) is kinetically slower than first ($k_{\text{app}1}^0 = 37 \text{ s}^{-1}$) according to this analysis of the FTAC voltammetric data. This conclusion is consistent with the greater separation in DC cyclic voltammetric peak-to-peak values for the two processes where $\Delta E_{P2} = 37 \text{ mV} > \Delta E_{P1} = 13 \text{ mV}$ (Table 1).

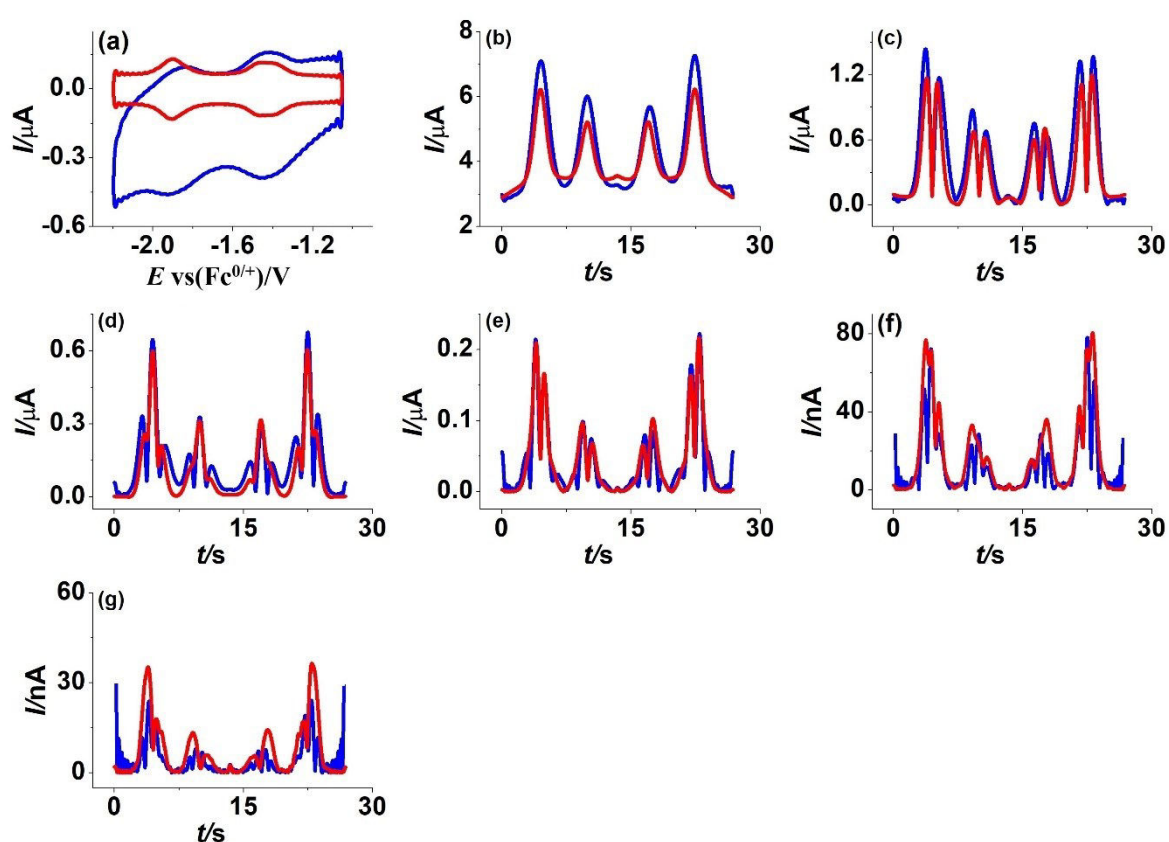


Figure 10. “Best fit” heuristic comparison of simulated (red) and experimental (blue) FTAC voltammetric data for the reduction of a $\text{K}_{\text{Sn}}^{\text{W}}[-]^4$ -grafted GC electrode in contact with CH_3CN ($0.10 \text{ M } [n\text{-Bu}_4\text{N}][\text{PF}_6]$). $\Gamma = 10 \times 10^{-11} \text{ mol cm}^{-2}$, $\Delta E = 80 \text{ mV}$, $f = 9.02 \text{ Hz}$ and $v = 0.086 \text{ V s}^{-1}$. (a) DC component, (b-g). Other parameters used in simulations are given in Table 5.

Table 5: Parameters^a derived from the heuristic and computer based comparison of simulated and experimental FTACV data at 9.02 Hz at $\text{K}^{\text{W}}_{\text{Sn}}[-]^{4-}$ -grafted ($\Gamma = 10 \times 10^{-11}$ mol cm^{-2}) GC electrode for the $\text{K}^{\text{W}}_{\text{Sn}}[-]^{4-/5-}$ and $\text{K}^{\text{W}}_{\text{Sn}}[-]^{5-/6-}$ processes in CH_3CN (0.10 M $[n\text{-Bu}_4\text{N}][\text{PF}_6]$).

Simulation method	E_{app1}^0	E_{app2}^0	k_{app1}^0	k_{app2}^0	α_{app1}	α_{app2}	LS %
	V vs $\text{Fc}^{0/+}$		s^{-1}				
Heuristic	-1.450	-1.920	37	18	0.45	0.46	
Automated	Range	Range	Range	Range	Range	Range	
	-1.454 to -1.445	-1.924 to -1.914	10 to 60	5 to 35	0.40 to 0.70	0.40 to 0.70	
	Estimated	Estimated	Estimated	Estimated	Estimated	Estimated	Estimated
	-1.447	-1.915	40	16	0.48	0.49	77

^a Other parameters used in the simulations are: $A_{\text{GC}} = 8.0 \times 10^{-3}$ cm^2 , $\Delta E = 80$ mV, $T = 295$ K, $\nu = 0.086$ V s^{-1} , $f = 9.02$ Hz.

There are again discrepancies between experimental and simulated faradaic current data, this time mainly due non-idealities arising from the presence a highly heterogeneous rather than uniform homogeneous grafted electrode. The cartoon in Figure S8a displays all grafted POMs in a fully uniform configuration. However, it is well known that all grafted POM moieties need not be located at the same angle to the flat surface. Furthermore, as in Figure S8b, grafting of aryl radicals to already grafted arrays leading to multi-layer formation cannot be excluded, nor can interactions with non-grafted POMs. In accordance with probability of non-ideality, it is noted that simulated AC voltammograms have very sharp valleys and peaks with current in between approaching zero. In contrast, in the experimental data the current does not approach close to zero in between these valley and peak features. Rather, the experimental response in all harmonics is more smeared out than in simulated data. This is indicative of thermodynamic and/or kinetic dispersion with a range E_{app}^0 , k_{app}^0 and α_{app} existing and associated with variability of the distances of the POM redox active framework from the GC surface^{46, 76}.

In a DC cyclic voltammetric studies of $\text{K}^{\text{W}}_{\text{Ge}}[-]^{4-}$ and $\text{K}^{\text{Mo}}_{\text{Sn}}[-]^{4-}$ to a GC electrode, Proust and Kanoufi et al²⁻³ used the Laviron method³¹ derived from so-called trumpet plots of the reduction and oxidation peak potentials in DC as a function of scan rate to probe the electrode kinetics of these POMs. In their work, considerable departure from theory also was noted, with the goodness of fit to the theory being scan rate dependent. For example, analysis of data in selected scan rate regimes, gave k_{app1}^0 values of 800 ($\text{K}^{\text{W}}_{\text{Ge}}[-]^{4-/5-}$) and 500 s^{-1} ($\text{K}^{\text{Mo}}_{\text{Sn}}[-]^{4-/5-}$). The second process in these studies was even more anomalous having DC cyclic voltammetric peak currents very much smaller than the first process, with a dependence on residual water and adsorption of loosely bound as well as grafted material being reported. Under the very dry conditions used in this study and with heavily sonicated grafted electrodes, the second process for reduction for grafted $\text{K}^{\text{W}}_{\text{Sn}}[-]^{4-}$ mimics behaviour expected for a quasi-reversible process with k_{app}^0 slightly less than about 20 s^{-1} which again is well below the anticipated value for reversible process (Figure 9i-g). In the studies based on DC cyclic voltammetry with related compounds²⁻³, only the experimental peak potential data were compared with theoretical predictions. In this work, slow scan rate data are reported to be independent of potential and hence consistent with a fast reversible process on these relatively long time scales. However, these slow scan rate data are anomalous relative to the model in the context that oxidation and reduction branches are separated by well in excess of 10 mV, which is a characteristic on quasi-reversibility or other non-ideality. In this FTACV study, the entire shape and current magnitudes is considered and evidence for kinetic and/or thermodynamic dispersion is reported.

Modification of theory⁷⁷ to accommodate interaction between surface confined redox active moieties sometimes is introduced by employing a Frumkin type isotherm as an alternative to Langmuir one used in this study. In this way interactions between surface confined moieties are modelled. Clearly quantitative studies with surface confined POMs

grafted to an electrode are fraught with difficulty. In principle, thermodynamic and kinetic dispersion could have been included in the modelling undertaken in this study along with use of a Frumkin isotherm and indeed are probably needed. However, this introduces another problem in that containing a unique mathematical solution now becomes daunting with so many extra parameters to be evaluated. Heuristically, the inverse problem would be intractable and data optimisation plagued with lengthy computational times with prospects for numerous localised minima and over- or under-parametrisation being high. Thus, we have used the simplest possible model and note that uncertainties are present in reporting electrode kinetic parameter values by either FTACV or DC voltammetric methods. Nevertheless, it is apparent that use of all data rather than just peak potentials is in principle superior in a statistical sense in terms of undertaking experiment-theory comparisons with a pre-selected model. In particular, with grafted moieties present or potentially present from precursors and with substantial POM ion-pairing not included in the model, it is now evident that not only do all the parameters such as E_{app}^0 , k_{app}^0 and α_{app} estimated as well as the model itself will usually contain unknown levels of uncertainty. Ultimately, sophisticated forms of Bayesian (⁷⁸ and references cited therein) or other forms of statistics applied to even more extensive data sets than collected in this FTACV study will be needed to determine which model or models actually provide the best fit to the data; a far from trivial task.

4. Conclusion

The thermodynamics and electron transfer kinetic parameters associated with the reduction of dissolved $K_{Sn}^W[N_3C_4H_{10}]^{4-}$ at GC, Au and Pt electrodes and the surface confined diazonium derivative $K_{Sn}^W[-]^{4-}$ grafted onto a GC electrode have been derived from FTACV experiments in CH_3CN containing 0.10 M of $[n-Bu_4N][PF_6]$ as the supporting electrolyte. Both experimenter-based heuristic and computer aided data optimisation approaches have been used

to compare experimental and simulated data to provide additional knowledge than could be gleaned by sole use of either method. Discrepancies in experimental and theoretical electrode kinetic data derived using the Butler-Volmer relationship are detected and explained for both dissolved and grafted examples. In solution phase voltammetry, anomalies in the shape of the $K_{Sn}^W[N_3(C_4H_{10})]^{4-/5-}$ process relative to theoretical predictions are evident in the oxidative scan of potential. EQCM experiments at a gold quartz crystal electrode and other experiments at conventional GC, Au and Pt electrodes are indicative of the origin of the non-ideality being accumulation of an unknown surface confined product that accompanies the initial one-electron reduction, with the order in impact being Pt > Au > GC. Confining data analysis to just the reduction component of the FTACV data set minimises the impact of the introduction of radial diffusion and array like behaviour that are not accommodated in the modelling and establishes that E_{app}^0 values for the $K_{Sn}^W[N_3C_4H_{10}]^{4-/5-}$ process are independent of electrode material as required theoretically and that $k_{appGC}^0 > k_{appAu}^0 > k_{appPt}^0$ with α being close to 0.50 at all electrodes. The same electrode material dependency on k_{app}^0 has been reported for other POMs such as α -[S₂W₁₈O₆₂]⁴⁻⁴⁹ and [SVW₁₁O₄₀]³⁻²⁵. The impact of accumulated material from decomposition of $K_{Sn}^W[N_3C_4H_{10}]^{5-}$ following the initial electron transfer step has such a profound effect on the second $K_{Sn}^W[N_3C_4H_{10}]^{5-/6-}$ process that parameterisation of Au and Pt electrode data was not attempted. However, at GC, parameterisation remained viable and revealed that k_{app2}^0 for the second process is significantly less than k_{app1}^0 for the first. This same order, $k_{app1}^0 > k_{app2}^0$, also applies to reduction of grafted $K_{Sn}^W[-]^{4-}$. However, discrepancies in experimental and simulated FTACV data with this surface confined POM are attributed predominantly to the presence of thermodynamic and kinetic dispersion arising from heterogeneity in the grafted GC surface. The relatively sluggish electrode kinetics encountered in the dynamic electrochemistry of $K_{Sn}^W[N_3C_4H_{10}]^{4-}$ may be due to the long organic chain

hindering the approach of the POM to the electrode surface, although differences in ion-pairing and other factors also may play a role.

As might be anticipated, E^0 values for both solution soluble $\text{K}^{\text{W}}_{\text{Sn}}[\text{N}_3\text{C}_4\text{H}_{10}]^{4-}$ and the surface confined $\text{K}^{\text{W}}_{\text{Sn}}[-]^{4-}$ derivative are similar. The thermodynamics for the POMs are mostly controlled by the transition metal in the core framework. Thus, very similar E_{app}^0 values are found when either Sn or Ge side chains are attached to W based frameworks while much less negative E_{app}^0 values are found with Mo-functionalized POMs.

ASSOCIATED CONTENT

Supporting Information

Figure S1. Schematic representation of electrochemical grafting of $\text{K}^{\text{W}}_{\text{Sn}}[\text{N}_2^+]^{4-}$ onto a GC electrode. **Figure S2.** method for grafting of $\text{K}^{\text{W}}_{\text{Sn}}[\text{N}_2^+]^{4-}$ onto a GC electrode. **Figure S3.** Estimation of background capacitance current from fundamental harmonic of the FTACV. **Figure S4 to Figure S6.** Comparison of simulated and experimental FTACV data for the solution phase $\text{K}^{\text{W}}_{\text{Sn}}[\text{N}_3\text{C}_4\text{H}_{10}]^{4-/5-/6-}$ processes at GC, Au and Pt electrode. **Figure S7.** Representation of the dipping experiments with $\text{K}^{\text{W}}_{\text{Sn}}[\text{N}_3\text{C}_4\text{H}_{10}]^{4-}$ in CH_3CN (0.10 M [*n*-Bu₄N][PF₆]) at GC, Au and Pt electrodes. **Figure S8.** Graphical representation of grafted $\text{K}^{\text{W}}_{\text{Sn}}[-]^{4-}$ ideal monolayer and multilayer on a GC electrode.

AUTHOR INFORMATION

Corresponding Authors

Anna Proust - Sorbonne Université, CNRS, Institut Parisien de Chimie Moléculaire, IPCM, 4 Place Jussieu, F-75005 Paris, France ; ORCID: orcid.org/0000-0002-0903-6507; Email: anna.proust@upmc.fr

Alan M. Bond - School of Chemistry and ARC Centre of Excellence for Electrochemical Science, Monash University, Clayton, Victoria 3800, Australia; ORCID: orcid.org/0000-0002-1113-5205; Email: alan.bond@monash.edu

Jie Zhang - School of Chemistry and ARC Centre of Excellence for Electrochemical Science, Monash University, Clayton, Victoria 3800, Australia; ORCID: orcid.org/0000-0003-2493-5209; Email: jie.zhang@monash.edu

Authors

Md Anisur Rahman - School of Chemistry, Monash University, Clayton, Victoria 3800, Australia

Si-Xuan Guo - School of Chemistry and ARC Centre of Excellence for Electrochemical Science, Monash University, Clayton, Victoria 3800, Australia

Maxime Laurans - Sorbonne Université, CNRS, Institut Parisien de Chimie Moléculaire, IPCM, 4 Place Jussieu, F-75005 Paris, France

Guillaume Izzet - Sorbonne Université, CNRS, Institut Parisien de Chimie Moléculaire, IPCM, 4 Place Jussieu, F-75005 Paris, France

ACKNOWLEDGEMENTS

The authors would like to thank the Australian Research Council for financial assistance through a Discovery Project grant.

REFERENCES:

- (1) Kuhn, A.; Mano, N.; Vidal, C. Polyoxometalate modified electrodes: from a monolayer to multilayer structures. *J. Electroanal. Chem.* **1999**, *462* (2), 187-194, DOI: [https://doi.org/10.1016/S0022-0728\(98\)00410-0](https://doi.org/10.1016/S0022-0728(98)00410-0).
- (2) Rinfray, C.; Brasiliense, V.; Izzet, G.; Volatron, F.; Alves, S.; Combellas, C.; Kanoufi, F.; Proust, A. Electron Transfer to a Phosphomolybdate Monolayer on Glassy Carbon: Ambivalent Effect of Protonation. *Inorg. Chem.* **2016**, *55* (14), 6929-6937, DOI: <https://doi.org/10.1021/acs.inorgchem.6b00485>.
- (3) Rinfray, C.; Izzet, G.; Pinson, J.; Gam Derouich, S.; Ganem, J. J.; Combellas, C.; Kanoufi, F.; Proust, A. Electrografting of diazonium-functionalized polyoxometalates: synthesis, immobilisation and electron-transfer characterisation from glassy carbon. *Chem. (Weinheim an der Bergstrasse, Germany)* **2013**, *19* (41), 13838-46, DOI: <https://doi.org/10.1002/chem.201302304>.
- (4) Sadakane, M.; Steckhan, E. Electrochemical Properties of Polyoxometalates as Electrocatalysts. *Chem. Rev.* **1998**, *98* (1), 219-238, DOI: <https://doi.org/10.1021/cr960403a>.
- (5) Han, Z.; Zhao, Y.; Peng, J.; Liu, Q.; Wang, E. Inorganic-organic hybrid polyoxometalate containing supramolecular helical chains: Preparation, characterization and application in chemically bulk-modified electrode. *Electrochim. Acta* **2005**, *51* (2), 218-224, DOI: <https://doi.org/10.1016/j.electacta.2005.04.016>.
- (6) Song, W.; Liu, Y.; Lu, N.; Xu, H.; Sun, C. Application of the sol-gel technique to polyoxometalates: towards a new chemically modified electrode. *Electrochim. Acta* **2000**, *45* (10), 1639-1644, DOI: [https://doi.org/10.1016/S0013-4686\(99\)00326-6](https://doi.org/10.1016/S0013-4686(99)00326-6).
- (7) Toma, F. M.; Sartorel, A.; Iurlo, M.; Carraro, M.; Parisse, P.; Maccato, C.; Rapino, S.; Gonzalez, B. R.; Amenitsch, H.; Da Ros, T. Efficient water oxidation at carbon nanotube-polyoxometalate electrocatalytic interfaces. *Nat. Chem.* **2010**, *2* (10), 826, DOI: <https://doi.org/10.1038/NCHEM.761>.
- (8) Bonastre, J.; Lapuente, R.; Garcés, P.; Cases, F. Electrochemical and chemical characterization of polypyrrole/phosphotungstate coatings electrosynthesized on carbon steel electrodes in acetonitrile medium. *Synth. Met.* **2009**, *159* (17-18), 1723-1730, DOI: <https://doi.org/10.1016/j.synthmet.2009.05.016>.
- (9) Liu, S.; Tian, J.; Wang, L.; Zhang, Y.; Luo, Y.; Li, H.; Asiri, A. M.; Al-Youbi, A. O.; Sun, X. Fast and sensitive colorimetric detection of H₂O₂ and glucose: a strategy based on polyoxometalate clusters. *ChemPlusChem* **2012**, *77* (7), 541-544, DOI: <https://doi.org/10.1002/cplu.201200051>.
- (10) Mercier, D.; Haddada, M. B.; Huebner, M.; Knopp, D.; Niessner, R.; Salmain, M.; Proust, A.; Boujday, S. Polyoxometalate nanostructured gold surfaces for sensitive biosensing of benzo [a] pyrene. *Sensor Actuat. B: Chem.* **2015**, *209*, 770-774, DOI: <https://doi.org/10.1016/j.snb.2014.12.015>.
- (11) Chen, J.-J.; Symes, M. D.; Cronin, L. Highly reduced and protonated aqueous solutions of [P₂W₁₈O₆₂]⁶⁻ for on-demand hydrogen generation and energy storage. *Nat. Chem.* **2018**, *10* (10), 1042-1047, DOI: <https://doi.org/10.1038/s41557-018-0109-5>.
- (12) Nishimoto, Y.; Yokogawa, D.; Yoshikawa, H.; Awaga, K.; Irle, S. Super-reduced polyoxometalates: excellent molecular cluster battery components and semipermeable molecular capacitors. *J. Am. Chem. Soc.* **2014**, *136* (25), 9042-9052, DOI: <https://doi.org/10.1021/ja5032369>.
- (13) Kinoshita, K. Carbon: electrochemical and physicochemical properties. **1988**.

-
- (14) McCreery, R. L. Carbon electrodes: structural effects on electron transfer kinetics. *Electroanal. Chem.* **1991**, *17*, 221-374.
- (15) Zhang, W.; Zhu, S.; Luque, R.; Han, S.; Hu, L.; Xu, G. Recent development of carbon electrode materials and their bioanalytical and environmental applications. *Chem. Soc. Rev.* **2016**, *45* (3), 715-752, DOI: <https://doi.org/10.1039/c5cs00297d>.
- (16) Liu, H.; He, P.; Li, Z.; Sun, C.; Shi, L.; Liu, Y.; Zhu, G.; Li, J. An ionic liquid-type carbon paste electrode and its polyoxometalate-modified properties. *Electrochem. Commun.* **2005**, *7* (12), 1357-1363, DOI: <https://doi.org/10.1016/j.elecom.2005.09.018>.
- (17) Zhou, M.; Guo, L.-p.; Lin, F.-y.; Liu, H.-x. Electrochemistry and electrocatalysis of polyoxometalate-ordered mesoporous carbon modified electrode. *Anal. Chim. Acta* **2007**, *587* (1), 124-131, DOI: <https://doi.org/10.1016/j.aca.2007.01.017>.
- (18) Sung, H.; So, H.; Paik, W.-k. Polypyrrole doped with heteropolytungstate anions. *Electrochim. Acta* **1994**, *39* (5), 645-650, DOI: [https://doi.org/10.1016/0013-4686\(94\)80005-7](https://doi.org/10.1016/0013-4686(94)80005-7).
- (19) Cheng, L.; Cox, J. A. Nanocomposite Multilayer Film of a Ruthenium Metallodendrimer and a Dawson-Type Polyoxometalate as a Bifunctional Electrocatalyst. *Chem. Mat.* **2002**, *14* (1), 6-8, DOI: <https://doi.org/10.1021/cm010854y>.
- (20) Martel, D.; Kuhn, A. Electrocatalytic reduction of H₂O₂ at [P₂Mo₁₈O₆₂]⁶⁻ modified glassy carbon, 2000; Vol. 45, p 1829-1836.
- (21) Proust, A.; Matt, B.; Villanneau, R.; Guillemot, G.; Gouzerh, P.; Izzet, G. Functionalization and post-functionalization: a step towards polyoxometalate-based materials. *Chem. Soc. Rev.* **2012**, *41* (22), 7605-7622, DOI: <https://doi.org/10.1039/C2CS35119F>.
- (22) Volatron, F.; Noël, J.-M.; Rinfray, C.; Decorse, P.; Combellas, C.; Kanoufi, F.; Proust, A. Electron transfer properties of a monolayer of hybrid polyoxometalates on silicon. *J. Mater. Chem. C* **2015**, *3* (24), 6266-6275, DOI: <https://doi.org/10.1039/C5TC00074B>.
- (23) Li, J.; Bentley, C. L.; Bond, A. M.; Zhang, J.; Ueda, T. Influence of 1-butyl-3-methylimidazolium on the electron transfer kinetics associated with the [SVW₁₁O₄₀]^{3-/4-}(V^{V/IV}) and [SVW₁₁O₄₀]^{4-/5-}(W^{VI/V}) processes in dimethylformamide. *J. Electroanal. Chem.* **2016**, *779*, 67-74, DOI: <https://doi.org/10.1016/j.jelechem.2016.04.050>.
- (24) Li, J.; Bond, A. M.; Zhang, J. Probing electrolyte cation effects on the electron transfer kinetics of the [α-SiW₁₂O₄₀]^{4-/5-} and [α-SiW₁₂O₄₀]^{5-/6-} processes using a boron-doped diamond electrode. *Electrochim. Acta* **2015**, *178*, 631-637, DOI: <https://doi.org/10.1016/j.electacta.2015.08.049>.
- (25) Li, J.; Guo, S.-X.; Bentley, C. L.; Bano, K.; Bond, A. M.; Zhang, J.; Ueda, T. Electrode material dependence of the electron transfer kinetics associated with the [SVW₁₁O₄₀]^{3-/4-}(V^{V/IV}) and [SVW₁₁O₄₀]^{4-/5-}(W^{VI/V}) processes in dimethylformamide. *Electrochim. Acta* **2016**, *201*, 45-56, DOI: <https://doi.org/10.1016/j.electacta.2016.03.107>.
- (26) Choi, S.-H.; Kim, J.-W. Adsorption properties of Keggin-type polyoxometalates on carbon based electrode surfaces and their electrocatalytic activities. *Bull. Korean Chem. Soc.* **2009**, *30* (4), 810-816, DOI: <https://doi.org/10.5012/bkcs.2009.30.4.810>.
- (27) Fleming, B. D.; Bond, A. M. DC and AC voltammetry of a free-base porphyrin adsorbed onto basal-plane graphite under acidic conditions: An example of a close to ideal reversible two-electron surface-confined redox process at sub-monolayer coverages. *Electrochim. Acta* **2009**, *54* (10), 2713-2719, DOI: <https://doi.org/10.1016/j.electacta.2008.11.042>.
-

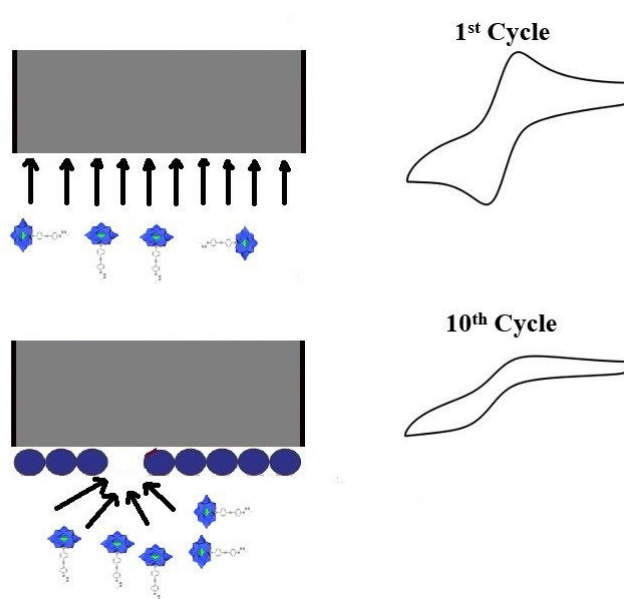
-
- (28) Guziejewski, D.; Mirceski, V.; Jadresko, D. Measuring the electrode kinetics of surface confined electrode reactions at a constant scan rate. *Electroanalysis* **2015**, *27* (1), 67-73, DOI: <https://doi.org/10.1002/elan.201400349>.
- (29) Huder, L.; Rinfray, C.; Rouchon, D.; Benayad, A.; Baraket, M.; Izzet, G.; Lipp-Bregolin, F.; Lapertot, G. r.; Dubois, L.; Proust, A. Evidence for charge transfer at the interface between hybrid phosphomolybdate and epitaxial graphene. *Langmuir* **2016**, *32* (19), 4774-4783, DOI: <https://doi.org/10.1021/acs.langmuir.6b00870>.
- (30) Laviron, E.; Roullier, L.; Degrand, C. A multilayer model for the study of space distributed redox modified electrodes: Part II. Theory and application of linear potential sweep voltammetry for a simple reaction. *J. Electroanal. Chem. and Interf. Electrochem.* **1980**, *112* (1), 11-23, DOI: [https://doi.org/10.1016/S0022-0728\(80\)80003-9](https://doi.org/10.1016/S0022-0728(80)80003-9).
- (31) Laviron, E. General expression of the linear potential sweep voltammogram in the case of diffusionless electrochemical systems. *J. Electroanal. Chem. and Interf. Electrochem.* **1979**, *101* (1), 19-28, DOI: [https://doi.org/10.1016/S0022-0728\(79\)80075-3](https://doi.org/10.1016/S0022-0728(79)80075-3).
- (32) Kennedy, G. F., MECSim software package. 2020.
- (33) Kennedy, G. F.; Bond, A. M.; Simonov, A. N. Modelling ac voltammetry with MECSim: facilitating simulation–experiment comparisons. *Curr. Opin. Electrochem.* **2017**, *1* (1), 140-147, DOI: <https://doi.org/10.1016/j.coelec.2016.12.001>.
- (34) Morris, G. P.; Simonov, A. N.; Mashkina, E. A.; Bordas, R.; Gillow, K.; Baker, R. E.; Gavaghan, D. J.; Bond, A. M. A comparison of fully automated methods of data analysis and computer assisted heuristic methods in an electrode kinetic study of the pathologically variable $[\text{Fe}(\text{CN})_6]^{3-/4-}$ process by AC voltammetry. *Anal. Chem.* **2013**, *85* (24), 11780-11787, DOI: <https://doi.org/10.1021/ac4022105>.
- (35) Laurans, M.; Dalla Francesca, K.; Volatron, F.; Izzet, G.; Guerin, D.; Vuillaume, D.; Lenfant, S.; Proust, A. Molecular signature of polyoxometalates in electron transport of silicon-based molecular junctions. *Nanoscale* **2018**, *10* (36), 17156-17165, DOI: <https://doi.org/10.1039/c8nr04946g>.
- (36) Sawyer, D.; Sobkowiak, A.; Roberts Jr, J. *Electrochemistry for Chemists*, ; John Wiley&Sons, 1995.
- (37) Bond, A. M.; Duffy, N. W.; Guo, S.-X.; Zhang, J.; Elton, D., Changing the look of voltammetry. ACS Publications: 2005.
- (38) Bard, A. a. F., Larry R. *Electrochemical Methods: Fundamentals and applications*, 2nd ed.; Wiley: New York, 2001.
- (39) Zhang, J.; Guo, S.-X.; Bond, A. M. Discrimination and evaluation of the effects of uncompensated resistance and slow electrode kinetics from the higher harmonic components of a Fourier transformed large-amplitude alternating current voltammogram. *Anal. Chem.* **2007**, *79* (6), 2276-2288, <https://doi.org/10.1021/ac061859n>
- (40) Bond, A. M.; Bano, K.; Adeel, S.; Martin, L. L.; Zhang, J. Fourier-Transformed Large-Amplitude AC Voltammetric Study of Tetrathiafulvalene (TTF): Electrode Kinetics of the $\text{TTF}^0/\text{TTF}^+$ and $\text{TTF}^-/\text{TTF}^{2+}$ Processes. *ChemElectroChem* **2014**, *1* (1), 99-107, DOI: <https://doi.org/10.1002/celec.201300129>.
- (41) Gritzner, G.; Kuta, J. Recommendations on reporting electrode potentials in nonaqueous solvents (Recommendations 1983). *Pure Appl. Chem.* **1984**, *56* (4), 461-466, DOI: <https://doi.org/10.1351/pac198456040461>.
- (42) Rudolph, M.; Reddy, D. P.; Feldberg, S. W. A simulator for cyclic voltammetric responses. *Anal. Chem.* **1994**, *66* (10), 589A-600A, DOI: <https://doi.org/10.1021/ac00082a725>.
-

-
- (43) Guo, S.; Zhang, J.; Elton, D. M.; Bond, A. M. Fourier transform large-amplitude alternating current cyclic voltammetry of surface-bound azurin. *Anal. Chem.* **2004**, *76* (1), 166-177, DOI: <https://doi.org/10.1021/ac034901c>.
- (44) Zhang, J.; Guo, S.-X.; Bond, A. M.; Honeychurch, M. J.; Oldham, K. B. Novel kinetic and background current selectivity in the even harmonic components of Fourier transformed square-wave voltammograms of surface-confined azurin. *J. Phys. Chem. B* **2005**, *109* (18), 8935-8947, DOI: <https://doi.org/10.1021/jp044614s>.
- (45) Fourmond, V.; Léger, C. Modelling the voltammetry of adsorbed enzymes and molecular catalysts. *Curr. Opin. Electrochem.* **2017**, *1* (1), 110-120, DOI: <https://doi.org/10.1016/j.coelec.2016.11.002>.
- (46) Morris, G. P.; Baker, R. E.; Gillow, K.; Davis, J. J.; Gavaghan, D. J.; Bond, A. M. Theoretical analysis of the relative significance of thermodynamic and kinetic dispersion in the dc and ac voltammetry of surface-confined molecules. *Langmuir* **2015**, *31* (17), 4996-5004, DOI: <https://doi.org/10.1021/la5042635>.
- (47) Bond, A. M.; Duffy, N. W.; Elton, D. M.; Fleming, B. D. Characterization of nonlinear background components in voltammetry by use of large amplitude periodic perturbations and Fourier transform analysis. *Anal. Chem.* **2009**, *81* (21), 8801-8808, DOI: <https://doi.org/10.1021/ac901318r>.
- (48) Li, J.; Bentley, C. L.; Tan, S. Y.; Mosali, V. S.; Rahman, M. A.; Cobb, S. J.; Guo, S.-X.; Macpherson, J. V.; Unwin, P. R.; Bond, A. M. Impact of sp² Carbon Edge Effects on the Electron Transfer Kinetics of the Ferrocene/Ferricenium Process at a Boron Doped Diamond Electrode in an Ionic Liquid. *J. Phys. Chem. C* **2019**, DOI: <https://doi.org/10.1021/acs.jpcc.9b04519>.
- (49) Rahman, M. A.; Li, J.; Guo, S.-X.; Kennedy, G.; Ueda, T.; Bond, A. M.; Zhang, J. Modelling limitations encountered in the thermodynamic and electrode kinetic parameterization of the α -[S₂W₁₈O₆₂]^{4-/5-/6-} processes at glassy carbon and metal electrodes. *J. Electroanal. Chem.* **2019**, 113786, DOI: <https://doi.org/10.1016/j.jelechem.2019.113786>.
- (50) Bard, A.; Parsons, R.; Jordan, J. *Standard Potentials in Aqueous Solution 1985*, Marcel Dekker: New York, 1985.
- (51) Laviron, E. Adsorption, autoinhibition and autocatalysis in polarography and in linear potential sweep voltammetry. *J. Electroanal. Chem. Interf. Electrochem.* **1974**, *52* (3), 355-393, DOI: [https://doi.org/10.1016/S0022-0728\(74\)80448-1](https://doi.org/10.1016/S0022-0728(74)80448-1).
- (52) Poblet, J. M.; López, X.; Bo, C. Ab initio and DFT modelling of complex materials: towards the understanding of electronic and magnetic properties of polyoxometalates. *Chem. Soc. Rev.* **2003**, *32* (5), 297-308, DOI: <https://doi.org/10.1039/b109928k>.
- (53) Hinrichs, K.; Roodenko, K.; Rappich, J.; Chehimi, M. M.; Pinson, J. Analytical methods for the characterization of aryl layers, Wiley-VCH Verlag GmbH & Co. KGaA: Weinheim: 2012.
- (54) Nicholson, R. S. Theory and application of cyclic voltammetry for measurement of electrode reaction kinetics. *Anal. Chem.* **1965**, *37* (11), 1351-1355, DOI: <https://doi.org/10.1021/ac60230a016>.
- (55) Md Anisur Rahman's unpublished work. **2020**.
- (56) Sauerbrey, G. The use of quartz oscillators for weighing thin layers and for microweighing. *Z. Phys.* **1959**, *155*, 206-222.
- (57) Gooding, J. J. Advances in interfacial design for electrochemical biosensors and sensors: aryl diazonium salts for modifying carbon and metal electrodes. *Electroanalysis: An International Journal Devoted to Fundamental and Practical Aspects of Electroanalysis* **2008**, *20* (6), 573-582, DOI: <https://doi.org/10.1002/elan.200704124>.
-

-
- (58) Liu, G.; Böcking, T.; Gooding, J. J. Diazonium salts: Stable monolayers on gold electrodes for sensing applications. *J. Electroanal. Chem.* **2007**, *600* (2), 335-344, DOI: <https://doi.org/10.1016/j.jelechem.2006.09.012>.
- (59) Liu, G.; Chockalingham, M.; Khor, S. M.; Gui, A. L.; Gooding, J. J. A comparative study of the modification of gold and glassy carbon surfaces with mixed layers of in situ generated aryl diazonium compounds. *Electroanalysis: An International Journal Devoted to Fundamental and Practical Aspects of Electroanalysis* **2010**, *22* (9), 918-926, DOI: <https://doi.org/10.1002/elan.200900539>.
- (60) Liu, S.; Tang, Z.; Shi, Z.; Niu, L.; Wang, E.; Dong, S. Electrochemical preparation and characterization of silicotungstic heteropolyanion monolayer electrostatically linked aminophenyl on carbon electrode surface. *Langmuir* **1999**, *15* (21), 7268-7275, DOI: <https://doi.org/10.1021/la981641z>.
- (61) Robinson, M.; Ounnunkad, K.; Zhang, J.; Gavaghan, D.; Bond, A. M. Models and Their Limitations in the Voltammetric Parameterization of the Six-Electron Surface-Confined Reduction of $[\text{PMo}_{12}\text{O}_{40}]^{3-}$ at Glassy Carbon and Boron-Doped Diamond Electrodes. *ChemElectroChem* **2019**, *6* (21), 5499-5510, DOI: <https://doi.org/10.1002/celec.201901415>.
- (62) Choi, S. M.; Seo, M. H.; Kim, H. J.; Lim, E. J.; Kim, W. B. Effect of polyoxometalate amount deposited on Pt/C electrocatalysts for CO tolerant electrooxidation of H_2 in polymer electrolyte fuel cells. *Int. J. Hydrogen Energ.* **2010**, *35* (13), 6853-6862, DOI: <https://doi.org/10.1016/j.ijhydene.2010.04.020>.
- (63) Bogdanovskaya, V.; Tarasevich, M.; Hintsche, R.; Scheller, F. Electrochemical transformations of proteins adsorbed at carbon electrodes. *Bioelectrochem. Bioenerg.* **1988**, *19* (3), 581-584, DOI: [https://doi.org/10.1016/0302-4598\(88\)80036-9](https://doi.org/10.1016/0302-4598(88)80036-9).
- (64) Pletcher, D.; Greff, R.; Peat, R.; Peter, L.; Robinson, J. *Instrumental methods in electrochemistry*, Elsevier: 2001.
- (65) Salvatore, P.; Zeng, D.; Karlsen, K. K.; Chi, Q.; Wengel, J.; Ulstrup, J. Electrochemistry of Single Metalloprotein and DNA-Based Molecules at Au (111) Electrode Surfaces. *ChemPhysChem* **2013**, *14* (10), 2101-2111, DOI: <https://doi.org/10.1002/cphc.201300299>.
- (66) Fleming, B. D.; Zhang, J.; Bond, A. M.; Bell, S. G.; Wong, L.-L. Separation of electron-transfer and coupled chemical reaction components of biocatalytic processes using Fourier transform ac voltammetry. *Anal. Chem.* **2005**, *77* (11), 3502-3510, DOI: <https://doi.org/10.1021/ac048151y>.
- (67) Fleming, B. D.; Zhang, J.; Elton, D.; Bond, A. M. Detailed analysis of the electron-transfer properties of azurin adsorbed on graphite electrodes using dc and large-amplitude Fourier transformed ac voltammetry. *Anal. Chem.* **2007**, *79* (17), 6515-6526, DOI: <https://doi.org/10.1021/ac070448j>.
- (68) O'Mullane, A. P.; Zhang, J.; Brajter-Toth, A.; Bond, A. M. Higher harmonic large-amplitude fourier transformed alternating current voltammetry: analytical attributes derived from studies of the oxidation of ferrocenemethanol and uric acid at a glassy carbon electrode. *Anal. Chem.* **2008**, *80* (12), 4614-4626, DOI: <https://doi.org/10.1021/ac0715221>.
- (69) Sher, A. A.; Bond, A. M.; Gavaghan, D. J.; Harriman, K.; Feldberg, S. W.; Duffy, N. W.; Guo, S.-X.; Zhang, J. Resistance, capacitance, and electrode kinetic effects in fourier-transformed large-amplitude sinusoidal voltammetry: Emergence of powerful and intuitively obvious tools for recognition of patterns of behavior. *Anal. Chem.* **2004**, *76* (21), 6214-6228, DOI: <https://doi.org/10.1021/ac0495337>.
-

-
- (70) Zhang, J.; Guo, S.-X.; Bond, A. M.; Marken, F. Large-amplitude Fourier transformed high-harmonic alternating current cyclic voltammetry: kinetic discrimination of interfering faradaic processes at glassy carbon and at boron-doped diamond electrodes. *Anal. Chem.* **2004**, *76* (13), 3619-3629, DOI: <https://doi.org/10.1021/ac049744b>.
- (71) Brousse, T.; Crosnier, O.; Bélanger, D.; Long, J. W. Capacitive and pseudocapacitive electrodes for electrochemical capacitors and hybrid devices. In *Metal Oxides in Supercapacitors*; Elsevier: 2017; pp 1-24.
- (72) Dubal, D. P.; Gómez-Romero, P.; Korotcenkov, G. *Metal oxides in supercapacitors*, Elsevier: 2017.
- (73) Genovese, M.; Lian, K. Polyoxometalate modified inorganic–organic nanocomposite materials for energy storage applications: A review. *Curr. Opin. Solid State Mater. Sci.* **2015**, *19* (2), 126-137, DOI: <https://doi.org/10.1016/j.cossms.2014.12.002>.
- (74) Hu, C.; Zhao, E.; Nitta, N.; Magasinski, A.; Berdichevsky, G.; Yushin, G. Aqueous solutions of acidic ionic liquids for enhanced stability of polyoxometalate-carbon supercapacitor electrodes. *J. Power Sources* **2016**, *326*, 569-574, DOI: <https://doi.org/10.1016/j.jpowsour.2016.04.036>.
- (75) Ruiz, V.; Suárez-Guevara, J.; Gomez-Romero, P. Hybrid electrodes based on polyoxometalate–carbon materials for electrochemical supercapacitors. *Electrochem. Commun.* **2012**, *24*, 35-38, DOI: <https://doi.org/10.1016/j.elecom.2012.08.003>.
- (76) Rowe, G. K.; Carter, M. T.; Richardson, J. N.; Murray, R. W. Consequences of kinetic dispersion on the electrochemistry of an adsorbed redox-active monolayer. *Langmuir* **1995**, *11* (5), 1797-1806, DOI: <https://doi.org/10.1021/la00005a059>.
- (77) Laviron, E.; Roullier, L. General expression of the linear potential sweep voltammogram for a surface redox reaction with interactions between the adsorbed molecules: applications to modified electrodes. *J. Electroanal. Chem. Interf. Electrochem.* **1980**, *115* (1), 65-74, DOI: [https://doi.org/10.1016/S0022-0728\(80\)80496-7](https://doi.org/10.1016/S0022-0728(80)80496-7).
- (78) Lambert, B. *A student's guide to Bayesian statistics*, Sage: 2018.

TOC:



Supporting Information

Thermodynamics, Electrode Kinetics and Mechanistic Nuances

Associated with the Voltammetric Reduction of Dissolved

$[n\text{-Bu}_4\text{N}]_4[\text{PW}_{11}\text{O}_{39}\{\text{Sn}(\text{C}_6\text{H}_4)\text{C}\equiv\text{C}(\text{C}_6\text{H}_4)(\text{N}_3\text{C}_4\text{H}_{10})\}]$ and a

Surface Confined Diazonium Derivative

Md Anisur Rahman^a, Si-Xuan Guo^{a,b}, Maxime Laurans^c, Guillaume Izzet^c, Anna Proust^{c,*},

Alan M. Bond^{a,b,*} and Jie Zhang^{a,b,*}

^a School of Chemistry, Monash University, Clayton, Victoria 3800, Australia

^b ARC Centre of Excellence for Electrochemical Science, Monash University, Clayton,
Victoria 3800, Australia

^c Sorbonne Université, CNRS, Institut Parisien de Chimie Moléculaire, IPCM, 4 Place
Jussieu, F-75005 Paris, France.

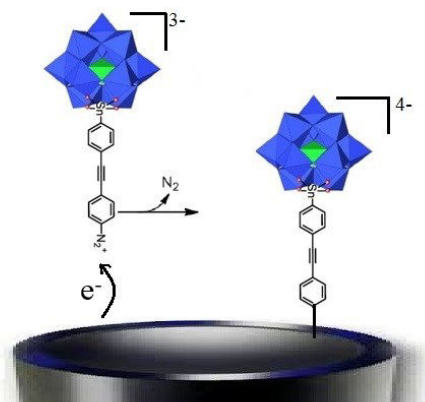


Figure S1. Schematic representation of electrochemical grafting of $\text{K}^{\text{W}}_{\text{Sn}}[\text{N}_2^+]^{4-}$ onto a GC electrode.

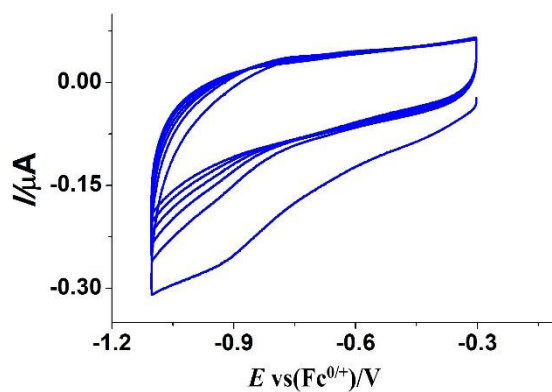


Figure S2. Grafting of $\text{K}^{\text{W}}_{\text{Sn}}[\text{N}_2^+]^{4-}$ onto a GC electrode by cyclic voltammetry in CH_3CN containing 0.10 M $[\text{n-Bu}_4\text{N}][\text{PF}_6]$. $v = 0.100 \text{ V s}^{-1}$.

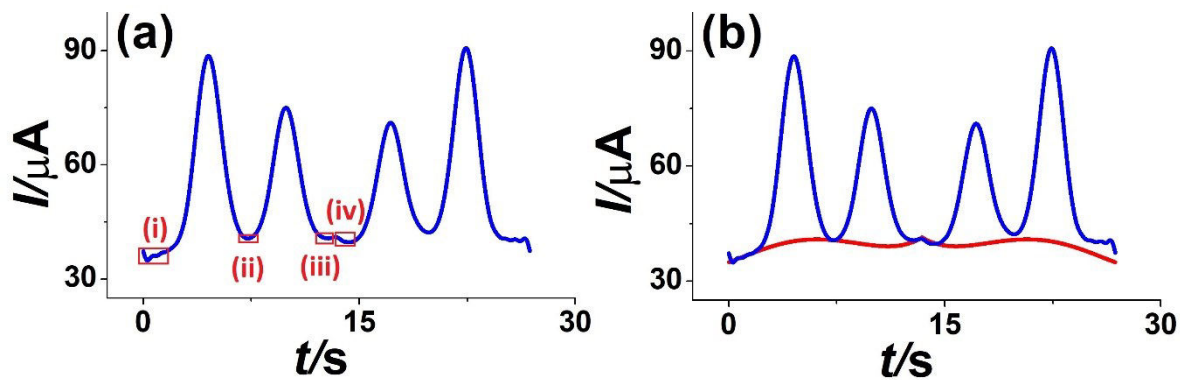


Figure S3. Estimation of background capacitance current from fundamental harmonic of the FTACV experiment. (a) Selection of points (i, ii, iii and iv) where no faradaic current is present. (b) background current estimated by fourth order polynomial fit.

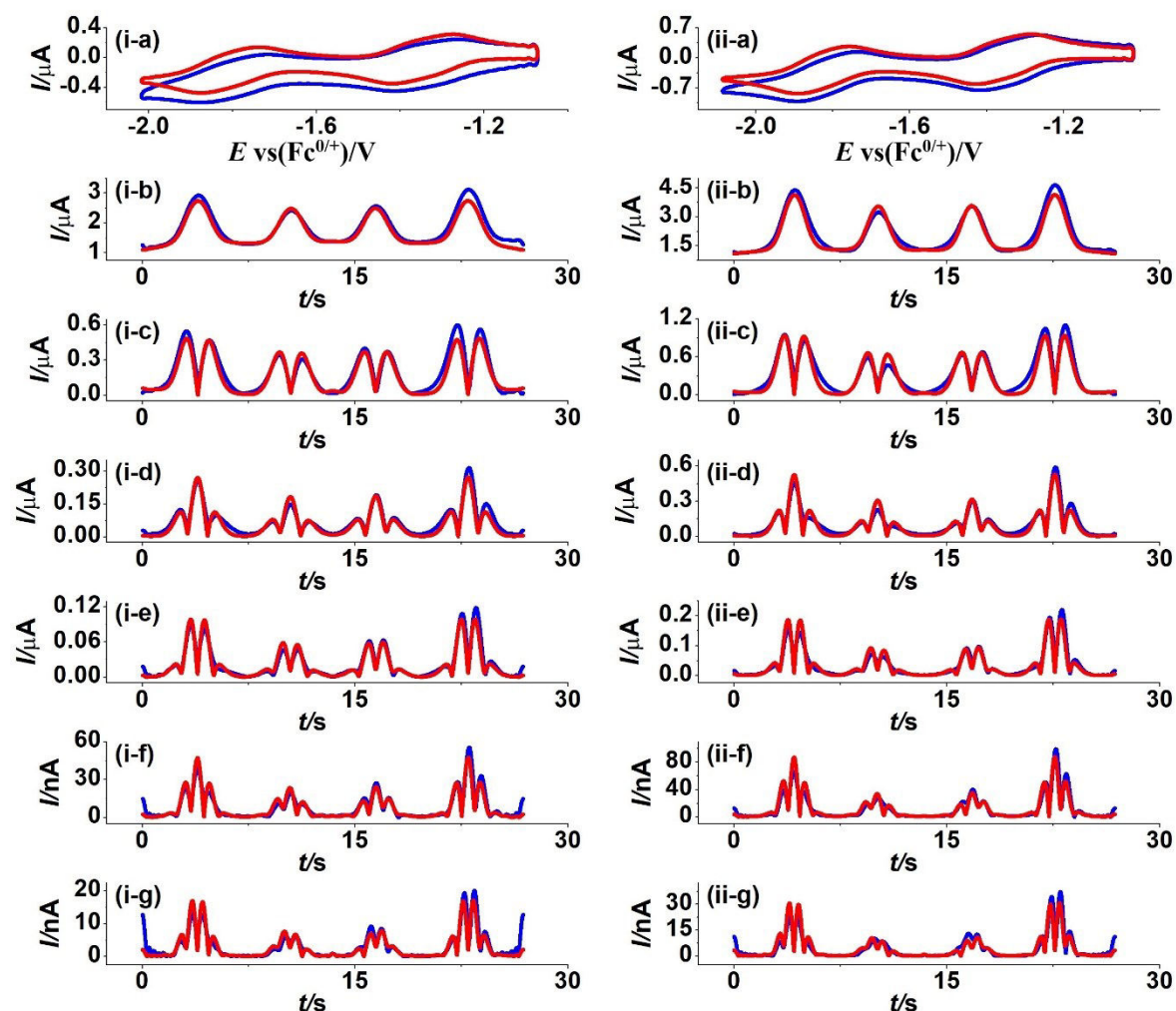


Figure S4. Comparison of simulated (red) data obtained using parameters deduced from automated data optimisation and experimental (blue) FTAC voltammetric data for the $\text{K}_{\text{Sn}}^{\text{W}}[\text{N}_3\text{C}_4\text{H}_{10}]^{4-}$ processes, obtained with (i) 0.20 mM and (ii) 0.50 mM $\text{K}_{\text{Sn}}^{\text{W}}[\text{N}_3\text{C}_4\text{H}_{10}]^{4-}$ in CH_3CN (0.10 M $[\text{n-Bu}_4\text{N}][\text{PF}_6]$) at a bare GC electrode. $\Delta E = 80$ mV, $f = 9.02$ Hz and $\nu_{0.20 \text{ mM}} = 0.071$ V s^{-1} , $\nu_{0.50 \text{ mM}} = 0.080$ V s^{-1} . (a) DC component, (b-g) 1st to 6th harmonic components.

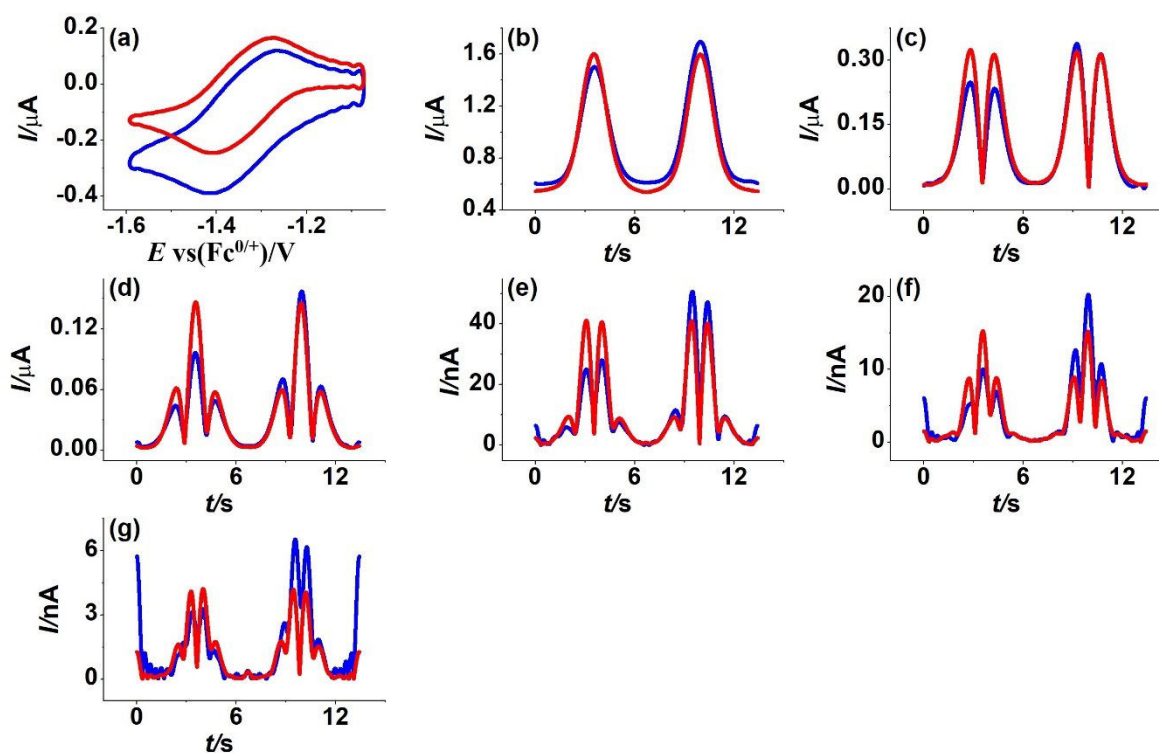


Figure S5. Heuristic comparison of simulated (red) and experimental (blue) FTAC voltammetric data for the $\text{K}^{\text{W}}_{\text{Sn}}[\text{N}_3\text{C}_4\text{H}_{10}]^{4-/5-}$ process obtained with 0.20 mM $\text{K}^{\text{W}}_{\text{Sn}}[\text{N}_3\text{C}_4\text{H}_{10}]^{4-}$ in CH_3CN (0.10 M $[n\text{-Bu}_4\text{N}][\text{PF}_6]$) at an Au electrode. $\Delta E = 80$ mV, $f = 9.02$ Hz and $\nu = 0.078$ V s^{-1} . (a) DC component, (b-g) 1st to 6th harmonic components.

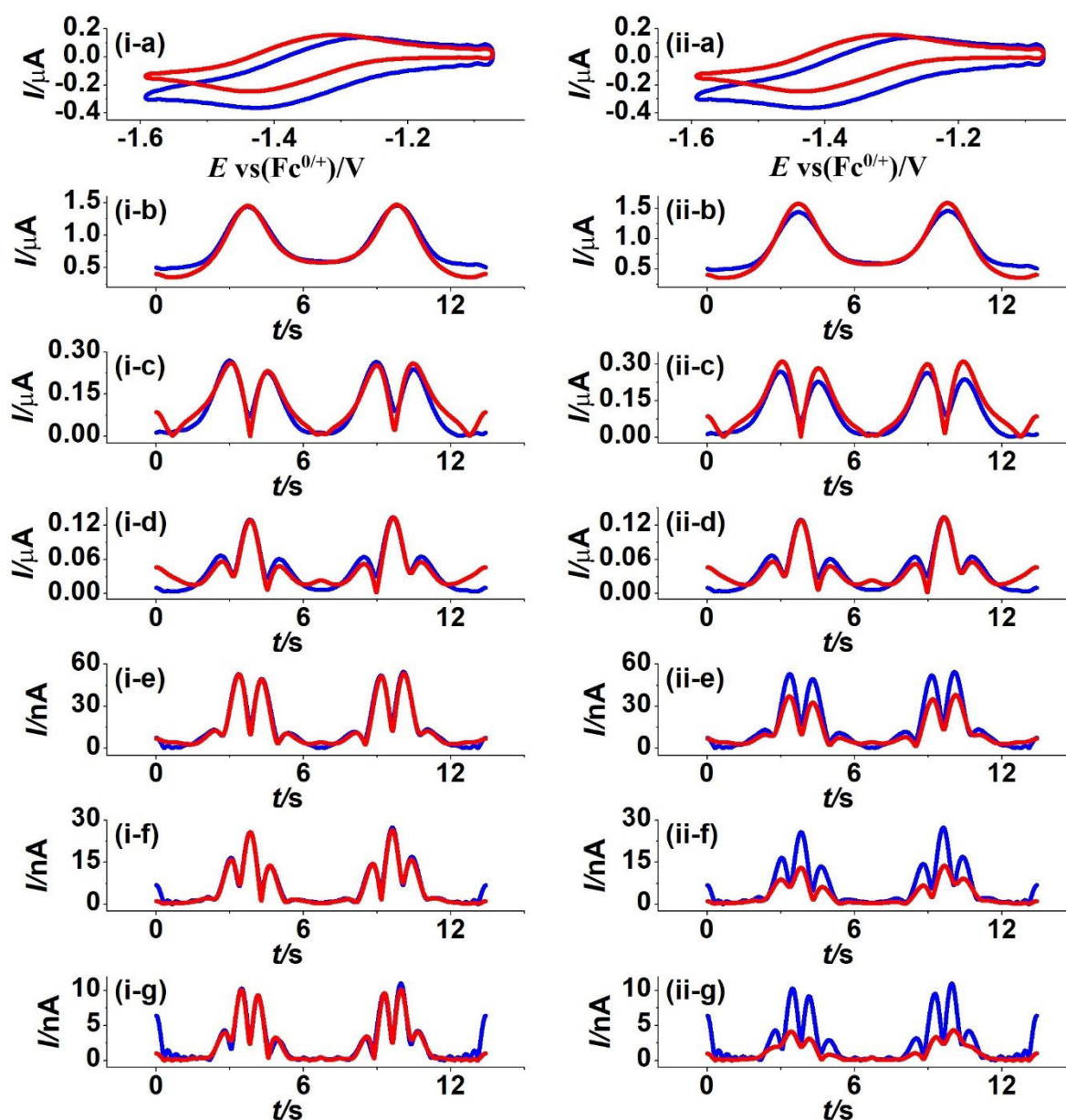


Figure S6. Heuristic comparison of simulated (red) and experimental (blue) AC voltammetric data for the $\text{K}^{\text{W}}_{\text{Sn}}[\text{N}_3\text{C}_4\text{H}_{10}]^{4-/5-}$ process, obtained with 0.20 mM $\text{K}^{\text{W}}_{\text{Sn}}[\text{N}_3\text{C}_4\text{H}_{10}]^4$ in CH_3CN (0.10 M $[n\text{-Bu}_4\text{N}][\text{PF}_6]$) at a Pt electrode. $\Delta E = 80$ mV, $f = 9.02$ Hz and $\nu = 0.078$ V s $^{-1}$. (a) DC component, (b-g) 1st to 6th harmonic components. In this data analysis exercise, in (i), use of apparently harmonic dependent kinetics provides excellent fits ($k_{\text{har}1}^0 = 0.095$, $k_{\text{har}2}^0 = 0.010$, $k_{\text{har}3}^0 = 0.013$, $k_{\text{har}4}^0 = 0.020$, $k_{\text{har}5}^0 = 0.026$ and $k_{\text{har}6}^0 = 0.031$) and in (ii) an excellent fit of the 3rd harmonic but not other harmonics is achieved with $k^0 = 0.013$ cm s $^{-1}$.

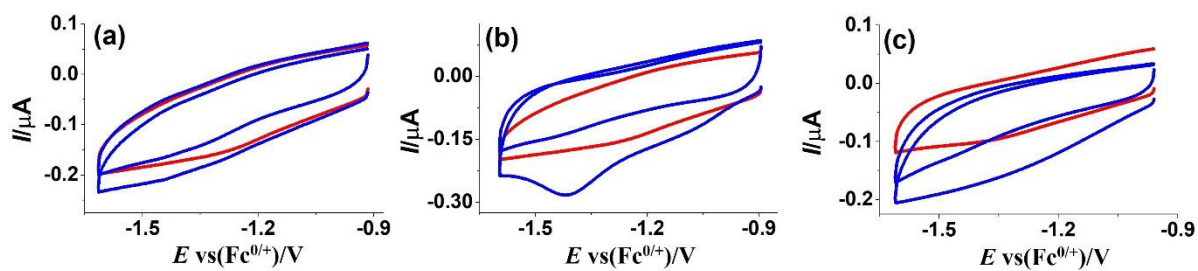


Figure S7. Cyclic voltammetry at a scan rate of 0.100 V s^{-1} in CH_3CN ($0.10 \text{ M } [n\text{-Bu}_4\text{N}][\text{PF}_6]$) following dipping experiments with $\text{K}^{\text{W}}_{\text{Sn}}[\text{N}_3\text{C}_4\text{H}_{10}]^{4-}$ using (a) GC, (b) Au and (c) Pt electrodes (see text for details). (----) plots represent dipping experiments with $\text{K}^{\text{W}}_{\text{Sn}}[\text{N}_3\text{C}_4\text{H}_{10}]^{4-}$. (----) plots are for electrolyte only.

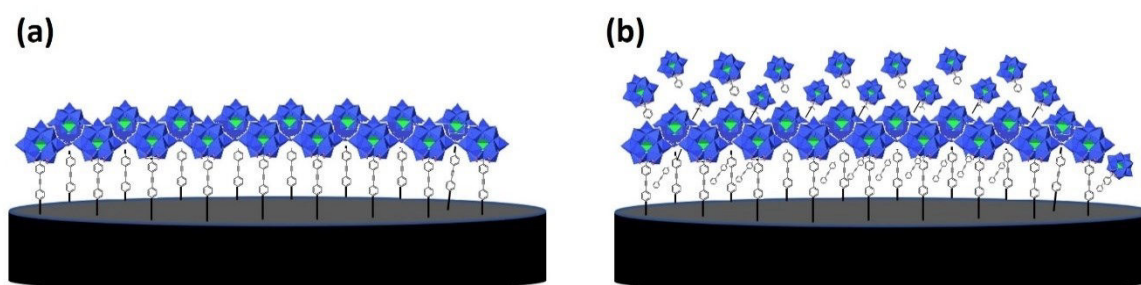


Figure S8. Grafted $\text{K}^{\text{W}}_{\text{Sn}}[-]^{4-}$ ideal monolayer (a) and multilayer (b) on a GC electrode surface.

Chapter 6:

Electrochemical and EPR Spectroscopic Characterisation of Two Electron Reduced Fe(III) and One Electron Reduced Zn(II), Cu(II) and Co(II) Functionalized Vanadium Polyoxometalates

Md Anisur Rahman^a, Stephen Best^b, John F. Boas^c, Alan M. Bond^{a, d*} and Jie Zhang^{a, d*}

^a School of Chemistry, Monash University, Clayton, Victoria 3800, Australia

^b School of Chemistry, The University of Melbourne, Victoria 3010, Australia

^c School of Physics and Astronomy, Monash University, Clayton, Victoria 3800, Australia

^d ARC Centre of Excellence for Electrochemical Science, Monash University, Clayton,
Victoria 3800, Australia

*Corresponding authors: jie.zhang@monash.edu, alan.bond@monash.edu

ABSTRACT

One electron reduced $[\text{Zn}^{\text{II}}\text{ClV}^{\text{V}}_{12}\text{O}_{32}\text{Cl}]^{4-}$, $[\text{Cu}^{\text{II}}(\text{MeCN})\text{V}^{\text{V}}_{12}\text{O}_{32}\text{Cl}]^{3-}$, $[\text{Co}^{\text{II}}(\text{MeCN})\text{V}^{\text{V}}_{12}\text{O}_{32}\text{Cl}]^{3-}$ and two electron reduced $[\text{Fe}^{\text{III}}\text{ClV}^{\text{V}}_{12}\text{O}_{32}\text{Cl}]^{4-}$ were characterized by electrochemistry and electron paramagnetic resonance (EPR) and visible-near infrared (Vis-NIR) spectroscopy. Controlled potential reductive bulk electrolysis has been used to generate the one electron reduced species of $[\text{Zn}^{\text{II}}\text{ClV}^{\text{V}}_{12}\text{O}_{32}\text{Cl}]^{4-}$, $[\text{Cu}^{\text{II}}(\text{MeCN})\text{V}^{\text{V}}_{12}\text{O}_{32}\text{Cl}]^{3-}$ and $[\text{Co}^{\text{II}}(\text{MeCN})\text{V}^{\text{V}}_{12}\text{O}_{32}\text{Cl}]^{3-}$ and the two electron reduced species of $[\text{Fe}^{\text{III}}\text{ClV}^{\text{V}}_{12}\text{O}_{32}\text{Cl}]^{4-}$ in high yield which were confirmed by RDE voltammetry at a GC electrode and insitu Vis-NIR spectroscopy. EPR data obtained at liquid nitrogen temperature of frozen glasses suggest that electron density of two electron reduced $[\text{Fe}^{\text{III}}\text{ClV}^{\text{V}}_{12}\text{O}_{32}\text{Cl}]^{4-}$ and one electron reduced $[\text{Cu}^{\text{II}}(\text{MeCN})\text{V}^{\text{V}}_{12}\text{O}_{32}\text{Cl}]^{3-}$ resides on the Fe and Cu in $\text{Fe}^{\text{III/II}}$ and $\text{Fe}^{\text{II/I}}$ and $\text{Cu}^{\text{II/I}}$ based process, respectively. On the other hand, the electron is delocalised onto the V framework upon one electron reduction of $[\text{Zn}^{\text{II}}\text{ClV}^{\text{V}}_{12}\text{O}_{32}\text{Cl}]^{4-}$. In the case of $[\text{Co}^{\text{II}}(\text{MeCN})\text{V}^{\text{V}}_{12}\text{O}_{32}\text{Cl}]^{3-}$, at least some of the added electron resides on V, but requires EPR spectrum at liquid helium (4 K) temperature to clarify if electron density also resides on the Co atom.

Keywords: Transition metal functionalized polyoxometalates, bulk electrolysis, spectroelectrochemistry, electron paramagnetic resonance.

1. Introduction:

The electrochemistry of the metal oxygen clusters known as polyoxometalates (POMs) is exceptionally rich and has been investigated [1-6] extensively in the field of both fundamental and applied science [1, 7-9] due to their extensive range of redox potentials [10, 11] and the higher degree of electronic adaptability. Reduced species are also of fundamental and applied interest as they can act as reductive electro-catalysts [12-15]. The so-called Keggin POM [16] represented by the formula $[XM_{12}O_{40}]^{n-}$ where M and X represent addenda atom and heteroatom, respectively is widely found with vanadium (V), molybdenum (VI), and tungsten (VI) addenda atoms and phosphorus, sulphur and halide heteroatoms [17-19]. Different orientations of the $\{M_3O_{13}\}$ building blocks in the Keggin structure (see Figure 1a) give the five different Keggin isomers [20] designated as α , β , γ , δ and ϵ forms. Furthermore, numerous structural variations leading to significant changes in redox chemistry, catalytic activity and other properties have been achieved by replacing one or more addenda atoms with another metal [21, 22]. In voltammetric experiments, POMs based on V^V , Mo^{VI} or W^{VI} almost invariably contain a series of well-defined usually reversible reduction ($V^{V/IV}$, $Mo^{VI/V}$, $W^{VI/V}$). If the replacement metal atom (e.g., Fe^{III}) in a vanadium POM framework is redox active, then ambiguity may exist when reduction occurs, as to whether the Fe^{III} or V^V metal atoms are reduced to Fe^{II} or V^{IV} respectively. Alternatively, of course the electron could be delocalised over all or part of the POM framework, making specific assignment of redox levels of particular metal atoms inappropriate.

The issue of assignment of redox levels in POM electrochemistry has arisen in a recent debate related to reduction of an $Fe(III)$ functionalized vanadium based Keggin type POM. In their initial report, it was proposed [23] on the basis of experimental voltammetric and EPR evidence and density functional theory (DFT) support that the two initial reversible one electron

reduction processes were iron based. Sproules then suggested that this results should be reinterpreted [24]. He proposed both these processes were vanadium rather than iron based, a conclusion that was challenged [25] on the basis that there were imperfections in the version of DFT he relied upon for his assignments and misunderstanding in his re-analysis of the EPR data.

In the conclusion of the rejoinder to Sproules publication [24], it was concluded that additional work was still needed to provide improved clarity on the assignment of the reduction processes with respect to changes in metal redox levels. In order to achieve this goal, attention is now given to voltammetric and EPR studies on related vanadate POMs, where metal atoms that are either electroinactive (e.g. Zn(II)) or electroactive (Cu(II)) are substituted into the vanadium Keggin POM. The concept behind this new study is for example that it is implausible that Zn(II) could be reduced to Zn(I) implying that the initial reduction process for this substituted POM should be vanadium based. In contrast, Cu(II) can be easily reduced to Cu(I), implying initial reduction for this POM is more likely to be associated with Cu^{II/I} rather than V^{V/IV} electrochemistry.

The $[n\text{-Bu}_4\text{N}]^+$ salt of the dodecavanadate chloride-templated cluster, $(\text{DMA})_2[\text{V}_{12}\text{O}_{32}\text{Cl}]^{3-}$ represented as $\{\text{V}_{12}^{\text{V}}\}$ (Figure 1a) (DMA= dimethylamonium $[(\text{CH}_3)_2\text{NH}_2]^+$) acts as precursor for the synthesis of a family of vanadium POMs substituted by a transition metal. Two metal binding sites in this cluster are selectively blocked by DMA placeholder cations [22]. The mono-functionalized vanadate oxide cluster $[n\text{-Bu}_4\text{N}]_n(\text{DMA})[\{\text{TM}(\text{L})\}\text{V}_{12}\text{O}_{32}\text{Cl}]$ (L = ligand; Cl or CH₃CN) (Figure 1) again as $[n\text{-Bu}_4\text{N}]^+$ salts are obtained [22] by replacing only one of the DMA cations from the dodecavanadate cluster. Selective incorporation of Zn(II) or Fe(III) into the dodecavanadate [21], $(\text{DMA})_2[\text{V}_{12}\text{O}_{32}\text{Cl}]^{3-}$ structure occurs by replacing one DMA placeholder cation to give the zinc(II) and iron(III) functionalized species [23] $[n\text{-}$

$\text{Bu}_4\text{N}]_3(\text{DMA})[\text{Zn}^{\text{II}}\text{ClV}^{\text{V}}_{12}\text{O}_{32}\text{Cl}] \quad \{\text{Zn}^{\text{II}}\text{V}^{\text{V}}_{12}\}$ and $[\textit{n}\text{-Bu}_4\text{N}]_3(\text{DMA})[\text{Fe}^{\text{III}}\text{ClV}^{\text{V}}_{12}\text{O}_{32}\text{Cl}] \quad \{\text{Fe}^{\text{III}}\text{V}^{\text{V}}_{12}\}$, respectively (Figure 1b) where chloride acts as a ligand. Analogously, replacement of one DMA placeholder cation with Cu(II) and Co(II) gives $[\textit{n}\text{-Bu}_4\text{N}]_2(\text{DMA})[\text{Cu}^{\text{II}}(\text{MeCN})\text{V}^{\text{V}}_{12}\text{O}_{32}\text{Cl}] \quad \{\text{Cu}^{\text{II}}\text{V}^{\text{V}}_{12}\}$, $[\textit{n}\text{-Bu}_4\text{N}]_2(\text{DMA})[\text{Co}^{\text{II}}(\text{MeCN})\text{V}^{\text{V}}_{12}\text{O}_{32}\text{Cl}] \quad \{\text{Co}^{\text{II}}\text{V}^{\text{V}}_{12}\}$, (Figures 1c and d), respectively, where acetonitrile (MeCN) acts as a ligand.

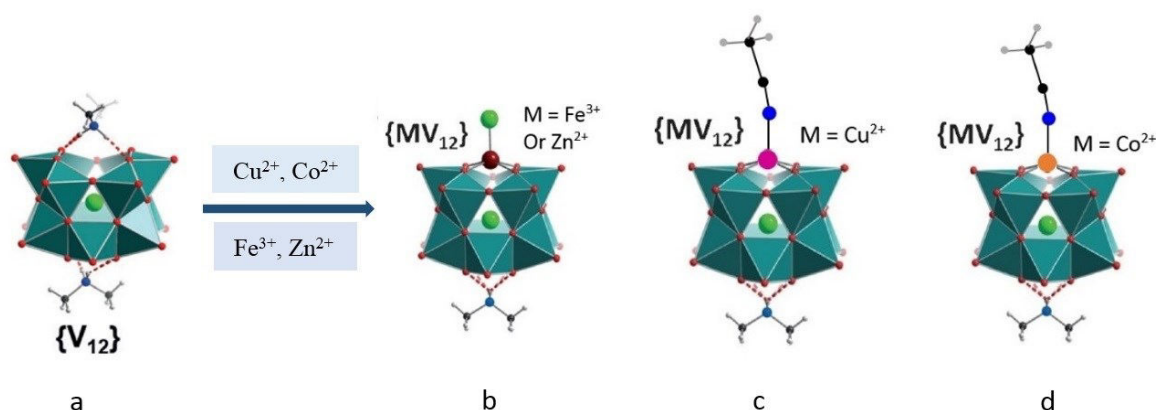


Figure 1. The metal-functionalized vanadates $\{(\text{TM})\text{V}^{\text{V}}_{12}\}$ (TM= Cu(II), Co(II), Fe(III), Zn(II)) obtained by replacing one DMA cation in (a) $\{\text{V}^{\text{V}}_{12}\}$ with a transition-metal cation TM, giving $\{\text{Fe}^{\text{III}}\text{V}^{\text{V}}_{12}$ and $\text{Zn}^{\text{II}}\text{V}^{\text{V}}_{12}$ (b)} (b, ligand Cl⁻), $\{\text{Cu}^{\text{II}}\text{V}^{\text{V}}_{12}$ (c)} and $\{\text{Co}^{\text{II}}\text{V}^{\text{V}}_{12}$ (d)} (c and d, ligand CH₃CN). Colour Scheme; V teal, O red, Cl large green, N blue, C small black, H small light grey, Cu large magenta, Co large yellow, Fe and Zn large maroon.

The group of transition metal (e.g., Cu, Co, Zn) functionalized vanadium POMs synthesized from the precursor, $(\text{DMA})_2[\text{V}^{\text{V}}_{12}\text{O}_{32}\text{Cl}]^{3-}$ are now subjected to electrochemical experiments using transient cyclic and steady state voltammetry along with bulk electrolysis to generate one-electron reduced species for Zn(II), Cu(II) and Co(II) and two-electron reduced species for Fe(III) functionalized vanadium POM accompanied by visible-near infrared (Vis-NIR) and

electron paramagnetic resonance (EPR) spectroscopic characterisation. Cyclic voltammetry [26] was used to establish the reversible potentials of the electron transfer processes undertaken in the reduction of $[\text{V}^{\text{V}}_{12}\text{O}_{32}\text{Cl}]^{5-}$, $[\text{Cu}^{\text{II}}(\text{MeCN})\text{V}^{\text{V}}_{12}\text{O}_{32}\text{Cl}]^{3-}$, $[\text{Co}^{\text{II}}(\text{MeCN})\text{V}^{\text{V}}_{12}\text{O}_{32}\text{Cl}]^{3-}$ and $[\text{Zn}^{\text{II}}\text{ClV}^{\text{V}}_{12}\text{O}_{32}\text{Cl}]^{4-}$ in acetonitrile (0.10 M $[\text{n-Bu}_4][\text{PF}_6]$) where the charges provided by the DMA^+ placeholder cation is removed so charges on the POM framework are readily compared. Steady-state voltammetry at a rotating disc electrode (RDE) was introduced to establish yields of the reduced species produced by bulk electrolysis. Vis-NIR and EPR spectroscopic characterization before and after the one electron reduction of Zn^{2+} , Cu^{2+} and Co^{2+} functionalized vanadium POMs by bulk electrolysis was used to examine the degree of delocalization of the electron on the reduced transition metal functionalized POM framework. Studies with the Fe(III) derivative $[\text{n-Bu}_4\text{N}]_3(\text{DMA})[\text{Fe}^{\text{III}}\text{ClV}^{\text{V}}_{12}\text{O}_{32}\text{Cl}]$, or with the placeholder cation removed to reveal the charge on the framework represented as $[\text{Fe}^{\text{III}}\text{ClV}^{\text{V}}_{12}\text{O}_{32}\text{Cl}]^{4-}$, have also been repeated to confirm that previous findings [23] are reproducible with a newly synthesised sample.

2. Experimental section:

2.1. Reagents and Solvents

$[\text{n-Bu}_4\text{N}]_3(\text{DMA})_2[\text{V}^{\text{V}}_{12}\text{O}_{32}\text{Cl}]$, $[\text{n-Bu}_4\text{N}]_3(\text{DMA})[\text{Zn}^{\text{II}}\text{ClV}^{\text{V}}_{12}\text{O}_{32}\text{Cl}]$, $[\text{n-Bu}_4\text{N}]_3(\text{DMA})[\text{Fe}^{\text{III}}\text{ClV}^{\text{V}}_{12}\text{O}_{32}\text{Cl}]$, $[\text{n-Bu}_4\text{N}]_2(\text{DMA})[\text{Cu}^{\text{II}}(\text{MeCN})\text{V}^{\text{V}}_{12}\text{O}_{32}\text{Cl}]$ and $[\text{n-Bu}_4\text{N}]_2(\text{DMA})[\text{Co}^{\text{II}}(\text{MeCN})\text{V}^{\text{V}}_{12}\text{O}_{32}\text{Cl}]$ were synthesised according to literature methods [21, 22] and provided by Professor Carsten Streb (Ulm University, Germany). Ferrocene (Fc, 98%, Sigma-Aldrich), Al_2O_3 (Buehler), acetonitrile (CH_3CN , 99.9%, Sigma-Aldrich) and ethanol (99%, Merck) were used as received from the manufacturer. Tetrabutylammonium hexafluorophosphate ($[\text{n-Bu}_4][\text{PF}_6]$) was purchased from Sigma-Aldrich and recrystallized from hot ethanol [27].

2.2. Electrochemical Instrumentation

Cyclic voltammetric experiments were undertaken with a CHI 760E electrochemical workstation. All experiments were executed at $22 \pm 2^\circ \text{C}$ in a 3-electrode electrochemical cell (1.5 ml Eppendorf centrifuge tube). Oxygen was removed by purging with N_2 for at least 10 minutes before each measurement. A glassy carbon (GC) disk with a nominal diameter of 1.0 mm, (eDAQ) was employed as the working electrode and was polished with an aqueous Al_2O_3 slurry (0.3 μm), rinsed sequentially with water and acetone, and then dried under N_2 , prior to use. Platinum (Pt) wires were used as both the reference and auxiliary electrode. The effective electroactive areas (A) of the macrodisk working electrode was determined from the peak current for oxidation of 1.0 mM Fc to Fc^+ in CH_3CN (0.10 M [$n\text{-Bu}_4$][PF_6]) and use of Randles-Sevcik relationship [26] (see Eqn. 1) with a known diffusion coefficient (D) of $2.4 \times 10^{-5} \text{ cm}^2 \text{ s}^{-1}$ for Fc under the conditions used [28].

$$I_p = 0.4463nFA(nFDv/RT)^{1/2}C \quad (1)$$

In this Equation, I_p , n , C , and A denote the oxidation peak current, number of electrons transferred ($n = 1$), bulk solution concentration, and electrode area, respectively. The determined area of the GC electrode was $8.0 \times 10^{-3} \text{ cm}^2$.

2.2.1 Bulk electrolysis:

One electron reduced $[\text{Zn}^{\text{II}}\text{ClV}^{\text{V}}_{12}\text{O}_{32}\text{Cl}]^{4-}$, $[\text{Cu}^{\text{II}}(\text{MeCN})\text{V}^{\text{V}}_{12}\text{O}_{32}\text{Cl}]^{3-}$ and $[\text{Co}^{\text{II}}(\text{MeCN})\text{V}^{\text{V}}_{12}\text{O}_{32}\text{Cl}]^{3-}$ and two electron reduced $[\text{Fe}^{\text{III}}\text{ClV}^{\text{V}}_{12}\text{O}_{32}\text{Cl}]^{4-}$ species were obtained by bulk electrolysis of 10 mL of 1.0 mM solutions of the POM in CH_3CN (0.10M [$n\text{-Bu}_4$][PF_6]) in an H-shaped electrolysis cell with coulometric monitoring using the same instrumentation as for the voltammetry. Large surface area glassy carbon (GC) plate and Pt-gauze were used as the working and auxiliary electrodes respectively and separated from each other by a fine

porosity glass frit in the H-Cell. Ag wire in contact with CH₃CN (0.10 M [*n*-Bu₄][PF₆]) contained in a salt bridge was used as the reference electrode and placed in the same compartment as the working electrode.

2.2.2 Steady State Voltammetry:

Both the parent transition metal functionalized POMs and the one electron reduced species were studied by steady state voltammetry at a GC (3mm diameter) rotating disk electrode. Rotation rates of 52.4, 105, 157, 209, 262 and 314 s⁻¹ were maintained by the BAS-M 1005 electrode rotator and experiments undertaken in conjunction with the electrochemical workstation as for the transient voltammetry. Ag wire in a glass frit containing 0.10 M [*n*-Bu₄][PF₆] in CH₃CN was used as reference electrode and Pt wire as the counter electrode. This form voltammetry is independent of potential and scan direction and so can readily differentiate between reduction and oxidation process which is difficult to achieve by transient cyclic voltammetry [29].

2.2.3 Vis-NIR Spectroelectrochemistry:

The in situ Vis-NIR spectroelectrochemistry was performed in an Oriel Instaspec II linear diode array detector (LDA) in combination with the CHI 760E electrochemical workstation used in other electrochemically based experiments. In most visible-near infrared spectroelectrochemical experiments, Visible-near infrared light passes through the solution. In these experiments, light reflected from a platinum disk working electrode (3 mm diameter) surface was detected as shown in the schematic representation displayed in Figure 2. Ag wire (2 mm diameter) and a platinum ring were used as pseudo-reference and counter electrodes, respectively, and experiments conducted in an airtight SEC cell (details described in reference [30]) where nitrogen pressure can be easily maintained.

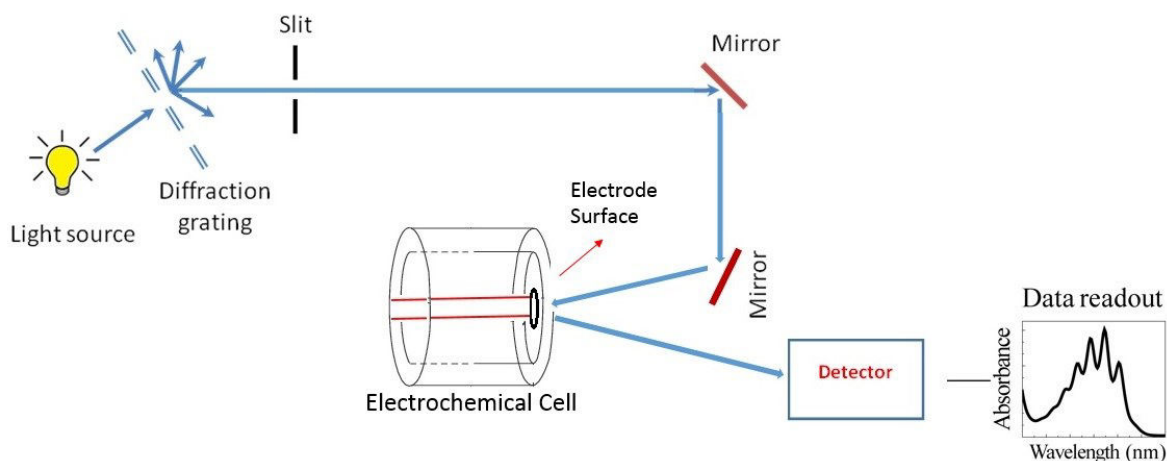


Figure 2. Schematic representation of the experimental arrangement used for Visible-near infrared spectroelectrochemical experiments. Concept taken from reference. [26]

2.2.4 EPR spectroscopy:

EPR spectra were measured with a Bruker EleXys E 500 continuous wave X band spectrometer controlled by Linux-based XEPR software and use of a standard cylindrical cavity (ER 4102ST). Liquid nitrogen was used to maintain the sample temperature at 77 K. Samples were frozen to liquid nitrogen temperature in the EPR sample tube before it was inserted into the EPR cavity. A microwave frequency counter (EIP 548A) was used to measure the microwave frequency. The g -values were estimated by calibration with reference to the F^+ line in CaO ($g = 2.0001 \pm 0.0001$) [31]. Spectra were detected as the absorption and simulated with the Sophe-Xepr View software [32]. Uncertainties in the g -values calculation were assessed as ± 0.002 . One electron reduced $[Zn^{II}ClV^{V}_{12}O_{32}Cl]^{4-}$, $[Cu^{II}(MeCN)V^{V}_{12}O_{32}Cl]^{3-}$, $[Co^{II}(MeCN)V^{V}_{12}O_{32}Cl]^{3-}$ and two electron reduced $[Fe^{III}ClV^{V}_{12}O_{32}Cl]^{4-}$ species were prepared by controlled potential bulk electrolysis.

3. Results and Discussion:

3.1 Cyclic voltammetry of transition metal functionalized vanadium POMs:

Figure 3 displays DC cyclic voltammograms for the one electron reduction of 0.5 mM $[\text{V}^{\text{V}}_{12}\text{O}_{32}\text{Cl}]^{5-}$, $[\text{Fe}^{\text{III}}\text{ClV}^{\text{V}}_{12}\text{O}_{32}\text{Cl}]^{4-}$, $[\text{Zn}^{\text{II}}\text{ClV}^{\text{V}}_{12}\text{O}_{32}\text{Cl}]^{4-}$, $[\text{Cu}^{\text{II}}(\text{MeCN})\text{V}^{\text{V}}_{12}\text{O}_{32}\text{Cl}]^{3-}$ and $[\text{Co}^{\text{II}}(\text{MeCN})\text{V}^{\text{V}}_{12}\text{O}_{32}\text{Cl}]^{3-}$ in CH_3CN (0.10 M $[\text{n-Bu}_4][\text{PF}_6]$) obtained at a GC electrode using a scan rate of 0.100 V s^{-1} . For the all vanadium POM, this reduction has to be vanadium based. Thus the initial well-defined process shown in Figure 3a with a mid-point potential, E_m of -0.542 V vs $\text{Fc}^{0/+}$ calculated from the average of the reduction and oxidation peak potentials, $(E_p^{\text{red}} + E_p^{\text{ox}})/2$, and equated to the reversible formal potential, E^0 , must involve reduction of V^{V} . The peak-to-peak separation ($E_p^{\text{red}} - E_p^{\text{ox}}$) or ΔE_p value of 78 mV and the unity magnitude ratio of reduction and oxidation peak currents imply that this is a chemically and electrochemically reversible one electron $\text{V}^{\text{V/IV}}$ reduction process (Eqn. 2).

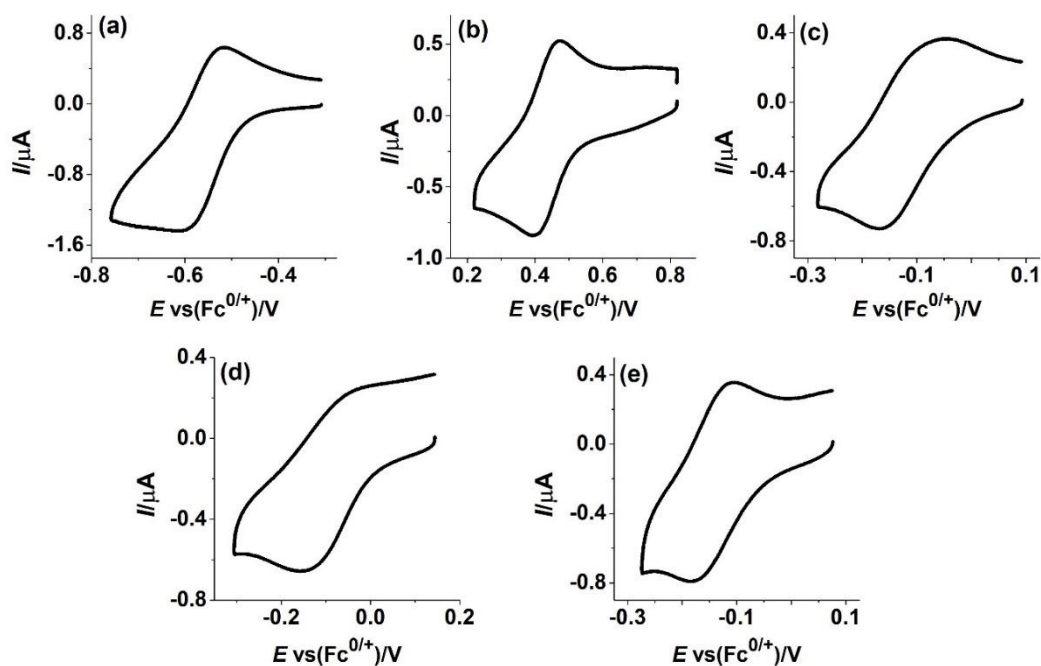


Figure 3. Cyclic voltammograms obtained at a scan rate of 0.100 V s^{-1} for the first one electron reduction of 0.5 mM (a) $[\text{V}^{\text{V}}_{12}\text{O}_{32}\text{Cl}]^{5-}$, (b) $[\text{Fe}^{\text{III}}\text{ClV}^{\text{V}}_{12}\text{O}_{32}\text{Cl}]^{4-}$, (c) $[\text{Zn}^{\text{II}}\text{ClV}^{\text{V}}_{12}\text{O}_{32}\text{Cl}]^{4-}$, (d) $[\text{Cu}^{\text{II}}(\text{MeCN})\text{V}^{\text{V}}_{12}\text{O}_{32}\text{Cl}]^{3-}$ and (e) $[\text{Co}^{\text{II}}(\text{MeCN})\text{V}^{\text{V}}_{12}\text{O}_{32}\text{Cl}]^{3-}$ in CH_3CN (0.10 M $[\text{n-Bu}_4][\text{PF}_6]$) at GC electrode.

Figure 3b shows that the cyclic voltammogram for the one-electron reduction of $[\text{Fe}^{\text{III}}\text{ClV}^{\text{V}}_{12}\text{O}_{32}\text{Cl}]^{4-}$ is well-defined and chemically reversible with $E_1^0 = 0.44 \text{ V}$ and $\Delta E_{p1} = 75 \text{ mV}$. According to the previous work from this laboratory, this reaction converts Fe(III) to Fe(II) to give the analogues of the Zn(II), Cu(II) and Co(II) POMs. A further two one electron transfer process are observed at more negative potentials (Figure S1a) as reported in reference [23].

$[\text{ZnClV}_{12}\text{O}_{32}\text{Cl}]^{4-}$ in principle also provides an example of a POM where it is anticipated that any initial reversible one electron reduction process should be $\text{V}^{\text{V/IV}}$ based. It is highly unlikely that Zn^{II} can be reduced to Zn^{I} . Reduction to the zinc metallic state is difficult and, in any case, would give rise to a two electron rather than one electron reduction process.

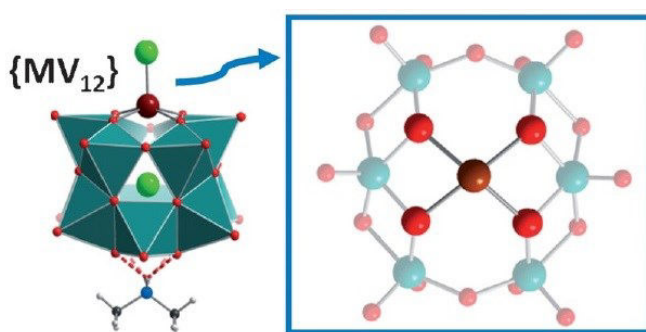


Figure 4. Structure of zinc functionalized vanadium $[\text{Zn}^{\text{II}}\text{ClV}^{\text{V}}_{12}\text{O}_{32}\text{Cl}]^{4-}$ POM with a DMA^+ placeholder [21] (left) and representation of location of Zn relative to POM framework (right). Zinc is coloured deep brown, Oxygen red and Vanadium teal.

As shown in the Figure 4, in the structure of $[\text{Zn}^{\text{II}}\text{ClIV}^{\text{V}}_{12}\text{O}_{32}\text{Cl}]^{4-}$, the centrally situated heteroatom Zn has four surroundings oxygen ligands. The chloride ligand sits above a POM cage framework constructed from 12 octahedral MO_6 -units linked to one another by neighbouring oxygen atoms with the placeholder located below the POM framework. The Zn^{2+} functionalized POM differs from the Cu^{2+} and Co^{2+} functionalized POMs considered below because chloride acts as ligand rather than MeCN. This means that the charge on the Zn^{2+} POM is more negative by one unit than for the $[\text{Cu}^{\text{II}}(\text{MeCN})\text{V}^{\text{V}}_{12}\text{O}_{32}\text{Cl}]^{3-}$ and $[\text{Co}^{\text{II}}(\text{MeCN})\text{V}^{\text{V}}_{12}\text{O}_{32}\text{Cl}]^{3-}$ POMs, but not as negatively charged as $[\text{V}^{\text{V}}_{12}\text{O}_{32}\text{Cl}]^{5-}$. The charge can have a significant impact on the E^0 value.

The cyclic voltammogram (Figure 3c), as for $[\text{Fe}^{\text{III}}\text{ClIV}^{\text{V}}_{12}\text{O}_{32}\text{Cl}]^{4-}$ gives a well-defined chemically reversible process with an E^0 value of -0.123 V vs $\text{Fc}^{0/+}$ derived from $(E_{\text{p}}^{\text{red}} + E_{\text{p}}^{\text{ox}})/2$. The ΔE_{p} value of 93 mV is consistent with a quasi-reversible one-electron reduction process. Scanning the potential to more negative values reveals a second one-electron reduction process (see Figure S1b) with E^0 and ΔE_{p} values of -0.67 V vs $\text{Fc}^{0/+}$ and 105 mV respectively. A series of complex processes are evident at even more negative potentials.

In the case of $[\text{Cu}^{\text{II}}(\text{MeCN})\text{V}^{\text{V}}_{12}\text{O}_{32}\text{Cl}]^{3-}$, both the Cu^{II} and V^{V} metal centres are in principle electroactive and could be reduced to Cu^{I} or Cu(metal) and V^{IV} respectively. In contrast with $[\text{Zn}^{\text{II}}\text{ClIV}^{\text{V}}_{12}\text{O}_{32}\text{Cl}]^{4-}$, $[\text{Cu}^{\text{II}}(\text{MeCN})\text{V}^{\text{V}}_{12}\text{O}_{32}\text{Cl}]^{3-}$ has a lower charge, which is likely to facilitate reduction. Figure 3d displays a cyclic voltammogram for $[\text{Cu}^{\text{II}}(\text{MeCN})\text{V}^{\text{V}}_{12}\text{O}_{32}\text{Cl}]^{3-}$ for the initial well-defined quasi-reversible one electron process with E^0 and ΔE_{p} values of -0.101 V vs $\text{Fc}^{0/+}$ and 81 mV (scan rate of 100 mV s^{-1}), respectively.

The current magnitude of the 2nd process (Figure S1c) is slightly smaller than the first which followed by a series of more complex processes in the very negative potential region as applies

for all POMs. The voltammetry of $[\text{Cu}^{\text{II}}(\text{MeCN})\text{V}^{\text{V}}_{12}\text{O}_{32}\text{Cl}]^{3-}$ does not define the redox level of the Cu and V metals in the reduced forms.

$[\text{Co}^{\text{II}}(\text{MeCN})\text{V}^{\text{V}}_{12}\text{O}_{32}\text{Cl}]^{3-}$ has the same formal charge and a similar structure to that $[\text{Cu}^{\text{II}}(\text{MeCN})\text{V}^{\text{V}}_{12}\text{O}_{32}\text{Cl}]^{3-}$. However, while Co(I) is a known redox state [33], it is far less accessible electrochemically than Cu^{I} so a $\text{V}^{\text{V/IV}}$ process is more likely than $\text{Co}^{\text{II/I}}$. The cyclic voltammogram for $[\text{Co}^{\text{II}}(\text{MeCN})\text{V}^{\text{V}}_{12}\text{O}_{32}\text{Cl}]^{3-}$ shown in Figure 3e exhibits the now familiar initial well-defined quasi-reversible one electron reduction process which in this case has an E^0 value of $-0.144 \text{ V vs Fc}^{0/+}$ ($\Delta E_p = 78 \text{ mV}$), along with a series of complex reduction processes at more negative potentials.

In summary, under conditions of cyclic voltammetry at a GC electrode, all POMs examined showed chemically reversible one electron charge transfer processes at a GC electrode with a scan rate of 100 mV s^{-1} . At more negative potentials, the degree of complexity varies with the identity of the POM. The peak currents for first process for all POMs are linearly dependent with $v^{1/2}$ over the scan rate range of 0.05 to 1.0 V s^{-1} (Figure S2), indicating that the mass transport process is diffusion control. D values calculated from the slopes of these linear plots and use of the Randles-Sevcik equation (see Eqn. 1) are 4.0×10^{-6} , 3.1×10^{-6} , 4.0×10^{-6} , 5.7×10^{-6} and 6.0×10^{-6} for $[\text{V}^{\text{V}}_{12}\text{O}_{32}\text{Cl}]^{5-}$, $[\text{Fe}^{\text{III}}\text{ClIV}^{\text{V}}_{12}\text{O}_{32}\text{Cl}]^{4-}$, $[\text{Zn}^{\text{II}}\text{ClIV}^{\text{V}}_{12}\text{O}_{32}\text{Cl}]^{4-/5-}$, $[\text{Cu}^{\text{II}}(\text{MeCN})\text{V}^{\text{V}}_{12}\text{O}_{32}\text{Cl}]^{3-/4-}$ and $[\text{Co}^{\text{II}}(\text{MeCN})\text{V}^{\text{V}}_{12}\text{O}_{32}\text{Cl}]^{3-/4-}$, respectively. However, this equation strictly only applies to a reversible process rather than quasi-reversible ones as found for the POMs of interest in this study. Accordingly, D values are probably slightly underestimated. Table 1 summarises the voltammetric data for all compounds.

Table 1. Summary of voltammetric parameters obtained from the reduction of 0.5 mM $[\text{V}^{\text{V}}_{12}\text{O}_{32}\text{Cl}]^{5-}$, $[\text{Fe}^{\text{III}}\text{ClV}^{\text{V}}_{12}\text{O}_{32}\text{Cl}]^{4-}$, $[\text{Zn}^{\text{II}}\text{ClV}^{\text{V}}_{12}\text{O}_{32}\text{Cl}]^{4-}$, $[\text{Cu}^{\text{II}}(\text{MeCN})\text{V}^{\text{V}}_{12}\text{O}_{32}\text{Cl}]^{3-}$ and $[\text{Co}^{\text{II}}(\text{MeCN})\text{V}^{\text{V}}_{12}\text{O}_{32}\text{Cl}]^{3-}$ in CH_3CN (0.10 M $[n\text{-Bu}_4][\text{PF}_6]$) at a scan rate of 0.100 V s^{-1} .

POM	$E_{app}^0(1^{\text{st}}, 2^{\text{nd}} \dots n^{\text{th}})$	$\Delta E_p(1^{\text{st}}, 2^{\text{nd}} \dots n^{\text{th}})$	D^{d}
	V^{a} vs $\text{Fc}^{0/+}$	mV^{b}	$\text{cm}^2 \text{ s}^{-1}$
$[\text{V}^{\text{V}}_{12}\text{O}_{32}\text{Cl}]^{5-}$	-0.542, ^c	78, ^c	4.0×10^{-6}
$[\text{Fe}^{\text{III}}\text{ClV}^{\text{V}}_{12}\text{O}_{32}\text{Cl}]^{4-}$	0.44, 0.02, ^c	75, 83, ^c	3.1×10^{-6}
$[\text{Zn}^{\text{II}}\text{ClV}^{\text{V}}_{12}\text{O}_{32}\text{Cl}]^{4-}$	-0.123, -0.670 ^c	93, 105, ^c	4.0×10^{-6}
$[\text{Cu}^{\text{II}}(\text{MeCN})\text{V}^{\text{V}}_{12}\text{O}_{32}\text{Cl}]^{3-}$	-0.101, ^c	81, ^c	5.7×10^{-6}
$[\text{Co}^{\text{II}}(\text{MeCN})\text{V}^{\text{V}}_{12}\text{O}_{32}\text{Cl}]^{3-}$	-0.144, ^c	78, ^c	6.0×10^{-6}

^a Uncertainty in E_{app}^0 is $\pm 5 \text{ mV}$

^b Uncertainty in ΔE_p is $\pm 2 \text{ mV}$

^c further processes present at more negative potentials region

^d calculated from the from the slop of the graph ($I/\mu\text{A}$ vs $\nu^{1/2}$, see Figure S2) by using Randles-Sevcik equation

3.2 Bulk electrolysis for the one electron $[\text{Zn}^{\text{II}}\text{ClV}^{\text{V}}_{12}\text{O}_{32}\text{Cl}]^{4-}$, $[\text{Cu}^{\text{II}}(\text{MeCN})\text{V}^{\text{V}}_{12}\text{O}_{32}\text{Cl}]^{3-}$ and $[\text{Co}^{\text{II}}(\text{MeCN})\text{V}^{\text{V}}_{12}\text{O}_{32}\text{Cl}]^{3-}$ and two one electron $[\text{Fe}^{\text{III}}\text{ClV}^{\text{V}}_{12}\text{O}_{32}\text{Cl}]^{4-}$ reduction processes:

Whilst, the initial one electron reduction processes are chemically reversible on the cyclic voltammetric timescale, this may not be the case under the much longer experimental times used in exhaustive controlled potential electrolysis undertaken to obtain bulk concentrations of the one electron reduced transition metal functionalized vanadium POMs. Constant potentials of -0.25, -0.20 and -0.23 V vs $\text{Fc}^{0/+}$ and 0.15 V vs $\text{Fc}^{0/+}$ were applied to synthesize the one electron reduced $[\text{Zn}^{\text{II}}\text{ClV}^{\text{V}}_{12}\text{O}_{32}\text{Cl}]^{4-}$, $[\text{Cu}^{\text{II}}(\text{MeCN})\text{V}^{\text{V}}_{12}\text{O}_{32}\text{Cl}]^{3-}$ and $[\text{Co}^{\text{II}}(\text{MeCN})\text{V}^{\text{V}}_{12}\text{O}_{32}\text{Cl}]^{3-}$ and two electron reduced $[\text{Fe}^{\text{III}}\text{ClV}^{\text{V}}_{12}\text{O}_{32}\text{Cl}]^{4-}$, respectively. In all cases, the charge calculated by coulometric analysis [34] of the current-time data and use of

Faraday's law was 0.95 ± 0.05 C and hence close to the theoretical value predicted for a one electron reduction process. The solution colour changed from initially light yellow to yellowish green, deep yellow to yellowish green and yellow to yellowish green at the conclusion of exhaustive reductive bulk electrolysis of $[\text{Zn}^{\text{II}}\text{ClV}^{\text{V}}_{12}\text{O}_{32}\text{Cl}]^{4-}$, $[\text{Cu}^{\text{II}}(\text{MeCN})\text{V}^{\text{V}}_{12}\text{O}_{32}\text{Cl}]^{3-}$ and $[\text{Co}^{\text{II}}(\text{MeCN})\text{V}^{\text{V}}_{12}\text{O}_{32}\text{Cl}]^{3-}$ respectively.

3.3 Rotating disc electrode voltammograms of POMs before and after bulk electrolysis:

Figure 5 shows the steady state voltammograms obtained at a GC rotating disc electrode (RDE) using a rotation rate of 157.08 s^{-1} for 0.10 mM $[\text{Zn}^{\text{II}}\text{ClV}^{\text{V}}_{12}\text{O}_{32}\text{Cl}]^{4-}$, $[\text{Cu}^{\text{II}}(\text{MeCN})\text{V}^{\text{V}}_{12}\text{O}_{32}\text{Cl}]^{3-}$ and $[\text{Co}^{\text{II}}(\text{MeCN})\text{V}^{\text{V}}_{12}\text{O}_{32}\text{Cl}]^{3-}$ in CH_3CN (0.10 M $[n\text{-Bu}_4][\text{PF}_6]$) before and after one electron bulk electrolysis. For, $[\text{Zn}^{\text{II}}\text{ClV}^{\text{V}}_{12}\text{O}_{32}\text{Cl}]^{4-}$ and $[\text{Co}^{\text{II}}(\text{MeCN})\text{V}^{\text{V}}_{12}\text{O}_{32}\text{Cl}]^{3-}$ almost full chemical reversibility is achieved on the bulk electrolysis timescale as the limiting current magnitudes for reduction, I_L , which is negative before bulk electrolysis and that for oxidation current which is positive after bulk electrolysis are almost the same ($\geq 90\%$). Furthermore, the potentials at $I_L/2$ or so called half-wave potentials, $E_{1/2}$, are similar for oxidation after and reduction before bulk electrolysis as expected for a close to reversible process. In the case of $[\text{Cu}^{\text{II}}(\text{MeCN})\text{V}^{\text{V}}_{12}\text{O}_{32}\text{Cl}]^{3-}$ only about 63% of product is stable on this timescale as noted by the magnitude of the I_L value after bulk electrolysis being only about half that before bulk electrolysis. Consistent with this conclusion, essentially 100% of both $[\text{Zn}^{\text{II}}\text{ClV}^{\text{V}}_{12}\text{O}_{32}\text{Cl}]^{4-}$ and $[\text{Co}^{\text{II}}(\text{MeCN})\text{V}^{\text{V}}_{12}\text{O}_{32}\text{Cl}]^{3-}$ could be recovered by bulk oxidative electrolysis of the initially one-electron reduced POM, but only about 60% of $[\text{Cu}^{\text{II}}(\text{MeCN})\text{V}^{\text{V}}_{12}\text{O}_{32}\text{Cl}]^{3-}$.

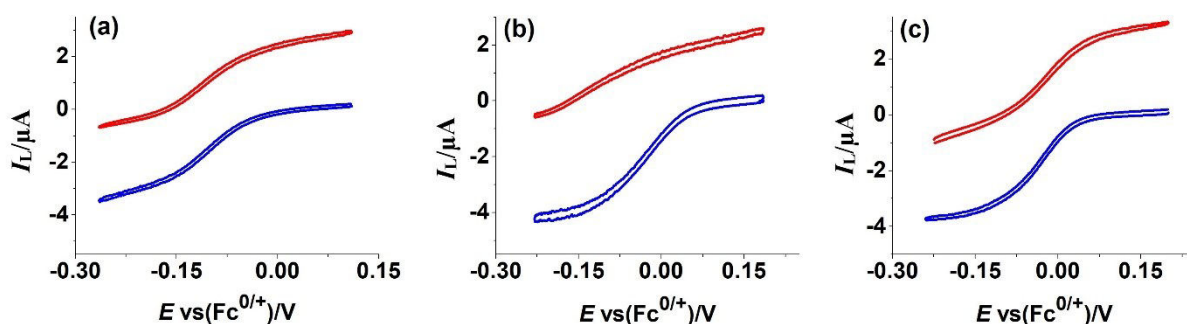


Figure 5. Steady state voltammogram obtained by rotating disc electrode voltammetry prior to (blue) and after one electron bulk reductive electrolysis of (a) $[\text{Zn}^{\text{II}}\text{Cl}^{\text{IV}}\text{V}_{12}\text{O}_{32}\text{Cl}]^{4-}$, (b) $[\text{Cu}^{\text{II}}(\text{MeCN})\text{V}^{\text{V}}_{12}\text{O}_{32}\text{Cl}]^{3-}$ and (c) $[\text{Co}^{\text{II}}(\text{MeCN})\text{V}^{\text{V}}_{12}\text{O}_{32}\text{Cl}]^{3-}$. Scan rate = 0.02 V. Rotation rate = 157.08 s^{-1} , POM concentration = 0.1 mM.

Plots of I_L vs $\omega^{1/2}$ for the reduction of all POMs were linear over the rotation rate range of 52–314 s^{-1} as predicted by the Levich equation [28] confirming mass transport-controlled reactions are occurring in the limiting current region [29]. The slopes of these plots and use of the Levich equation gave diffusion coefficient values of 4.5×10^{-6} , 5.5×10^{-6} and 6.1×10^{-6} (see Table 2) for $[\text{Zn}^{\text{II}}\text{Cl}^{\text{IV}}\text{V}_{12}\text{O}_{32}\text{Cl}]^{4-/5-}$, $[\text{Cu}^{\text{II}}(\text{MeCN})\text{V}^{\text{V}}_{12}\text{O}_{32}\text{Cl}]^{3-/4-}$ and $[\text{Co}^{\text{II}}(\text{MeCN})\text{V}^{\text{V}}_{12}\text{O}_{32}\text{Cl}]^{3-/4-}$, respectively which are consistent with the values that obtained by linear sweep voltammetry and Randles-Sevcik equation. The RDE data are summarised in Table 2.

Table 2. Summary of RDE voltammetric data obtained from reduction of 0.1 mM $[\text{Zn}^{\text{II}}\text{Cl}^{\text{IV}}\text{V}_{12}\text{O}_{32}\text{Cl}]^{4-}$, $[\text{Cu}^{\text{II}}(\text{MeCN})\text{V}^{\text{V}}_{12}\text{O}_{32}\text{Cl}]^{3-}$ and $[\text{Co}^{\text{II}}(\text{MeCN})\text{V}^{\text{V}}_{12}\text{O}_{32}\text{Cl}]^{3-}$ in CH_3CN (0.10 M $[\text{n-Bu}_4][\text{PF}_6]$) at a scan rate of 0.02 V s^{-1} and rotation rate of 157.08 s^{-1} .

POM	$E_{1/2}(\text{red})$	$E_{1/2}(\text{ox})$	$I_L(\text{red})$	$I_L(\text{ox})$	$(I_L(\text{ox})/I_L(\text{red}))$	D^b
	V ^a vs $\text{Fc}^{0/+}$		μA		% recovery	$\text{cm}^2\text{ s}^{-1}$
$[\text{Zn}^{\text{II}}\text{Cl}^{\text{IV}}\text{V}_{12}\text{O}_{32}\text{Cl}]^{4-}$	-0.115	-0.11	-3.5	3.1	88	4.5×10^{-6}
$[\text{Cu}^{\text{II}}(\text{MeCN})\text{V}^{\text{V}}_{12}\text{O}_{32}\text{Cl}]^{3-}$	-0.09	-0.09	-4.1	2.6	63	5.5×10^{-6}
$[\text{Co}^{\text{II}}(\text{MeCN})\text{V}^{\text{V}}_{12}\text{O}_{32}\text{Cl}]^{3-}$	-0.135	-0.13	-3.8	3.4	93	6.1×10^{-6}

^a Uncertainty in $E_{1/2}$ is ± 5 mV

^b calculated from the from the slop of a plot of $I_L/\mu\text{A}$ vs $\omega^{1/2}$ (see Figure S3) and use Levich equation

3.4 In situ Visible-near infra-red (Vis-NIR) spectroelectrochemistry of the one electron reduction of $[\text{Zn}^{\text{II}}\text{Cl}^{\text{V}}_{12}\text{O}_{32}\text{Cl}]^{4-}$, $[\text{Cu}^{\text{II}}(\text{MeCN})\text{V}^{\text{V}}_{12}\text{O}_{32}\text{Cl}]^{3-}$ and $[\text{Co}^{\text{II}}(\text{MeCN})\text{V}^{\text{V}}_{12}\text{O}_{32}\text{Cl}]^{3-}$:

The Vis-NIR spectral changes observed during the electrochemical reduction of the transition metal functionalized POMs are shown in Figure 6. As noted in the bulk electrolysis section presented above, colour changes accompanying the one electron reduction detected visually were minor. Consequently, and as expected, absorbances in the visible region of the spectrum are small as are changes accompanying reductions. In case of $[\text{Zn}^{\text{II}}\text{Cl}^{\text{V}}_{12}\text{O}_{32}\text{Cl}]^{4-/5-}$, absorption in the visible and near infrared region (Figure 6a) increases slightly due to enhanced d-d metal to ligand transition [35]. The spectral changes accompanying reduction of $[\text{Cu}^{\text{II}}(\text{MeCN})\text{V}^{\text{V}}_{12}\text{O}_{32}\text{Cl}]^{3-}$ and $[\text{Co}^{\text{II}}(\text{MeCN})\text{V}^{\text{V}}_{12}\text{O}_{32}\text{Cl}]^{3-}$ are far more substantial. One electron reduction of $[\text{Cu}^{\text{II}}(\text{MeCN})\text{V}^{\text{V}}_{12}\text{O}_{32}\text{Cl}]^{3-}$ generates a band in the visible region at 622 nm (Figure 6b) and one in the near infra-red region at 1060 nm (with a shoulder at lower wavelengths). All bands diminish/increase in intensity during the course of the one electron reduction, with an isosbestic points detected at 646 and 960 nm. Reduction of $[\text{Co}^{\text{II}}(\text{MeCN})\text{V}^{\text{V}}_{12}\text{O}_{32}\text{Cl}]^{3-}$ also generates a band in the near infrared region of 1060 nm as with $[\text{Cu}^{\text{II}}(\text{MeCN})\text{V}^{\text{V}}_{12}\text{O}_{32}\text{Cl}]^{3-}$ and again a shoulder is present at lower wavelengths as are isosbestic points at 658 and 937 nm. In all cases, changes are reversible as when the potential is switched to oxidation, original spectrum of the POM is recovered.

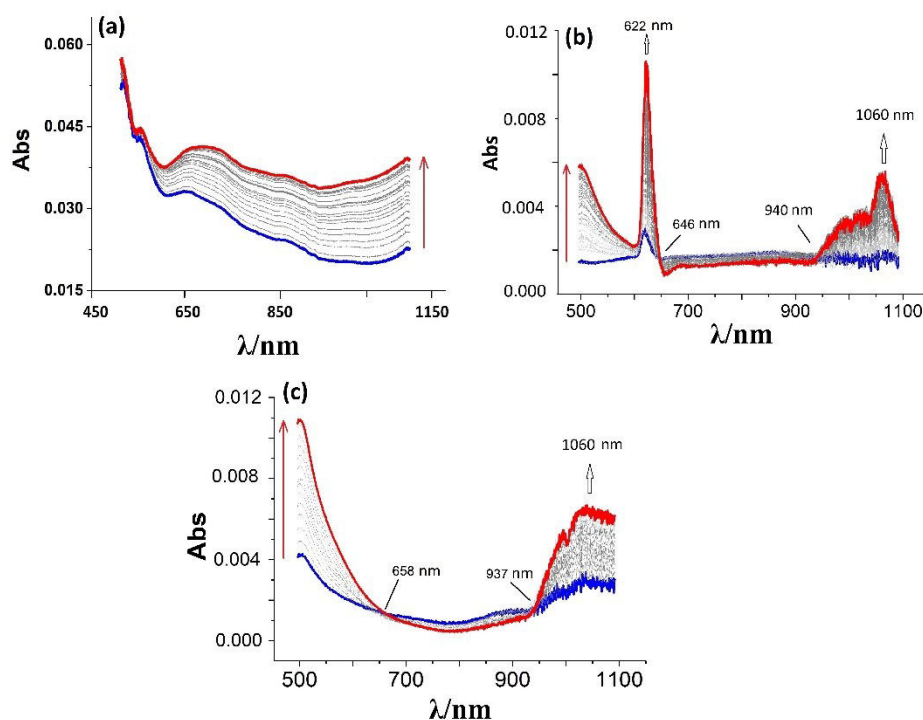


Figure 6. In situ spectroelectrochemical experiments displaying the Vis-NIR spectral changes accompanying the one electron reduction of 1.0 mM (a) $[\text{Zn}^{\text{II}}\text{CIV}^{\text{V}}_{12}\text{O}_{32}\text{Cl}]^{4-}$, $[\text{Cu}^{\text{II}}(\text{MeCN})\text{V}^{\text{V}}_{12}\text{O}_{32}\text{Cl}]^{3-}$ and $[\text{Co}^{\text{II}}(\text{MeCN})\text{V}^{\text{V}}_{12}\text{O}_{32}\text{Cl}]^{3-}$ in CH_3CN (0.10 M $[\textit{n}\text{-Bu}_4][\text{PF}_6]$). Blue (---) and red (---) represent the initial and last absorption spectrum, respectively. Arrow sign stand for the direction of absorption band.

3.5 EPR spectroscopic characterization of the one electron reduced $[\text{Zn}^{\text{II}}\text{CIV}^{\text{V}}_{12}\text{O}_{32}\text{Cl}]^{4-}$, $[\text{Cu}^{\text{II}}(\text{MeCN})\text{V}^{\text{V}}_{12}\text{O}_{32}\text{Cl}]^{3-}$ and $[\text{Co}^{\text{II}}(\text{MeCN})\text{V}^{\text{V}}_{12}\text{O}_{32}\text{Cl}]^{3-}$ and two electron reduced $[\text{Fe}^{\text{III}}\text{CIV}^{\text{V}}_{12}\text{O}_{32}\text{Cl}]^{4-}$ POMs:

EPR spectra were obtained on one and two electron reduced POMs prepared as in the bulk electrolysis experiments at a GC electrode in CH_3CN (0.1M $[\textit{n}\text{-Bu}_4][\text{PF}_6]$) described above. However, these solutions were transferred to an EPR tube and then frozen in liquid nitrogen. Hence, the EPR spectra were recorded on glass samples at 77K rather than in solution phase at 22 °C used for other measurements. In principle, analysis of the EPR spectra may provide knowledge as to where the electron resides on the reduced POM.

The EPR spectra obtained at 77 K from frozen glasses of the two electron reduced $[\text{Fe}^{\text{III}}\text{ClV}^{\text{V}}_{12}\text{O}_{32}\text{Cl}]^{4-}$ and one electron reduced $[\text{Zn}^{\text{II}}\text{ClV}^{\text{V}}_{12}\text{O}_{32}\text{Cl}]^{4-}$, $[\text{Cu}^{\text{II}}(\text{MeCN})\text{V}^{\text{V}}_{12}\text{O}_{32}\text{Cl}]^{3-}$ and $[\text{Co}^{\text{II}}(\text{MeCN})\text{V}^{\text{V}}_{12}\text{O}_{32}\text{Cl}]^{3-}$ are shown in Figures 7-10, respectively.

The EPR spectra of the parent and two electrons reduced $[\text{Fe}^{\text{III}}\text{ClV}^{\text{V}}_{12}\text{O}_{32}\text{Cl}]^{4-}$ are similar to that reported in previous work [23] (see Figure 7) which were associated to the electrons being localized on to Fe atom rather than V framework to give Fe^{II} and then Fe^{I} centres.

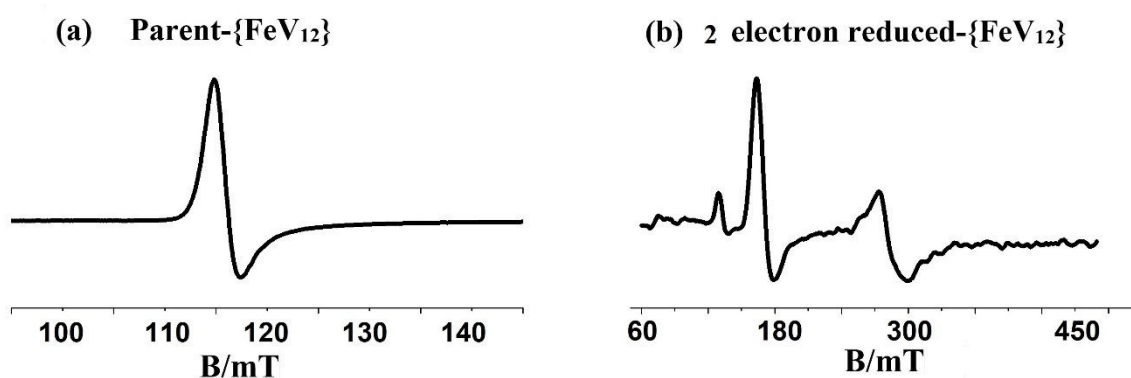


Figure 7. EPR spectrum of (a) 1 mM parent $[\text{Fe}^{\text{III}}\text{ClV}^{\text{V}}_{12}\text{O}_{32}\text{Cl}]^{4-}$ and (c) two electron reduced $[\text{Fe}^{\text{III}}\text{ClV}^{\text{V}}_{12}\text{O}_{32}\text{Cl}]^{4-}$ in frozen CH_3CN (0.10 M $[n\text{-Bu}_4][\text{PF}_6]$) solution at 77 K. **Spectrometer settings:** microwave frequency 9.4473 and 9.4501 GHz for parent and two electron reduced species; microwave power 5.024 mW; modulation amplitude 0.4 mT.

The EPR spectrum of one electron reduced all vanadium POM $[\text{V}^{\text{V}}_{12}\text{O}_{32}\text{Cl}]^{5-}$ has been reported [23] and also is included in Figure 8. This POM has a high degree of symmetry with DMA^+ groups in both capping positions (see Figure 1a). Furthermore, this POM reduction process has to be a $\text{V}^{\text{V}/\text{IV}}$ one and hence provides a reference EPR spectrum for assignment in reduced transition metal substituted POMs that are of interest in this publication. However, the electron need not be, and probably is not localised on just a one of the twelve vanadium sites available in this POM framework. The experimental EPR spectrum of the one-electron reduced

$[\text{V}^{\text{V}}_{12}\text{O}_{32}\text{Cl}]^{5-}$ POM (Figure 8a), now conveniently represented as $[\text{V}^{\text{V}}_{11}\text{V}^{\text{IV}}\text{O}_{32}\text{Cl}]^{6-}$ is described in reference [23] as a single broad V^{IV} resonance at *ca.* 345 mT ($g = 1.963$). Hyperfine features would be expected to be generated from the hyperfine structure as a result of the interaction between unpaired electron and ^{51}V nucleus ($I = 7/2$; 99.2 % abundance), but this is not observed. The lack of hyperfine was postulated in reference [23] to be indicative of the possible delocalization of unpaired electron which resides on a number of V sites. Moreover, parameters that used in the simulation shown in Figure 8a, especially isotropic hyperfine interaction is comparable with $84 \times 10^{-4} \text{ cm}^{-1}$ that assessed for the V^{IV} ion in the $[\text{PVMo}_{11}\text{O}_{40}]^{4-}$, which suggest that delocalization of unpaired electron occurs over about three V sites. [36].

Reduction of $[\text{Zn}^{\text{II}}\text{ClV}^{\text{V}}_{12}\text{O}_{32}\text{Cl}]^{4-}$, as for $[\text{V}^{\text{V}}_{12}\text{O}_{32}\text{Cl}]^{5-}$ should be vanadium based, to give what could be described as $[\text{Zn}^{\text{II}}\text{ClV}^{\text{V}}_{11}\text{V}^{\text{IV}}\text{O}_{32}\text{Cl}]^{5-}$. However, this POM has a significantly lower level of symmetry than for the all vanadium POM. Now, a zinc atom coordinated to oxygen and chloride lies in one capping position and a DMA⁺ in the other. From a purely electrostatic perspective, the electron could on average reside near the Zn^{2+} positively charged region. Thus, the presence of the Zn^{2+} metal could perturb the EPR spectrum, even though the electron remains fully located on the vanadium POM framework. A different distribution over the V framework is indicated as the g -value is 1.974 compared to the 1.963 for the 1-electron reduced $[\text{V}^{\text{V}}_{12}\text{O}_{32}\text{Cl}]^{5-}$. A presented radical type signal also is superimposed on the broad line which have a g -value close to 2.003 [37]. However, this signal with a very narrow line width only represents around 1 % of the unpaired spins generated by reduction of $[\text{Zn}^{\text{II}}\text{ClV}^{\text{V}}_{12}\text{O}_{32}\text{Cl}]^{4-}$ and probably represents an impurity.

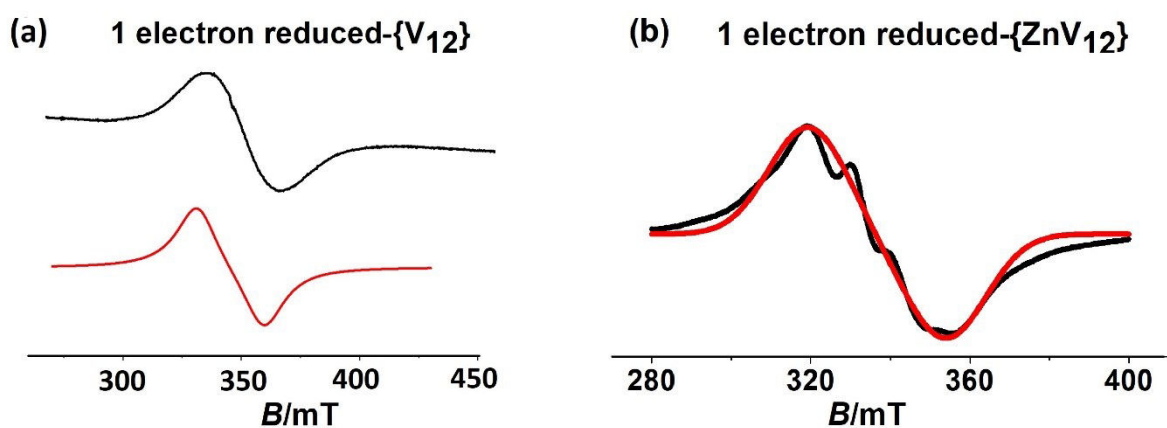


Figure 8. EPR spectrum of one electron reduced (a) $[\text{V}^{\text{V}}_{12}\text{O}_{32}\text{Cl}]^{5-}$ and (b) $[\text{Zn}^{\text{II}}\text{Cl}^{\text{V}}\text{V}_{12}\text{O}_{32}\text{Cl}]^{4-}$ POM in frozen CH_3CN (0.10 M $[\text{n-Bu}_4][\text{PF}_6]$) at 77 K. **Experimental spectrum (black):** (a) microwave frequency 9.4905 GHz; microwave power 5.024 mW; modulation amplitude 0.5 mT and (b) microwave frequency 9.3241 GHz; microwave power 1.002 mW; modulation amplitude 0.4 mT. **Simulated spectrum (red):** (a) g -factor 1.978; (b) Lorentzian line shape width $100 \times 10^{-4} \text{ cm}^{-1}$; isotropic g -factor 1.963; isotropic hyperfine interaction $32 \times 10^{-4} \text{ cm}^{-1}$.

In the case of $[\text{Cu}^{\text{II}}(\text{MeCN})\text{V}^{\text{V}}_{12}\text{O}_{32}\text{Cl}]^{3-}$, the one-electron reduction process could be associated with $\text{Cu}^{\text{III/I}}$ or $\text{V}^{\text{V/IV}}$ redox chemistry. EPR simulations are of course dependent on the model used to mimic the experimental data. Thus, it is noted that while reasonably good agreement between experimental and simulated EPR data could be obtained by modelling with a single $[\text{Cu}^{\text{II}}(\text{MeCN})\text{V}^{\text{V}}_{12}\text{O}_{32}\text{Cl}]^{3-}$ species, significantly superior agreement was achieved by assuming the presence of Cu^{II} in two structurally similar sites of POM in an axial environment. The two g -values provided for this POM in the Table 3 prior to reduction correspond to the Cu^{II} in two sites. A comparison of the EPR spectrum obtained from of a 1.0 mM solution of $[\text{Cu}^{\text{II}}(\text{MeCN})\text{V}^{\text{V}}_{12}\text{O}_{32}\text{Cl}]^{3-}$ in CH_3CN (0.10 M $[\text{n-Bu}_4][\text{PF}_6]$) frozen to 77 K with simulated EPR

spectra based on the presence of two similar Cu^{II} sites is displayed in Figure 9. Simulations of the EPR spectra gave the spin Hamiltonian parameters listed in Table 3.

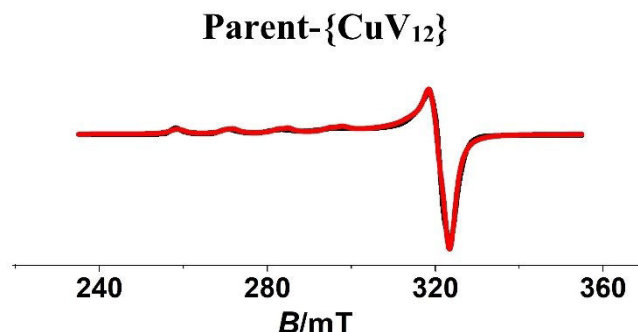


Figure 9. EPR spectrum of 1 mM parent $[\text{Cu}^{\text{II}}(\text{MeCN})\text{V}_{12}\text{O}_{32}\text{Cl}]^{3-}$ in frozen CH_3CN (0.10 M $[n\text{-Bu}_4][\text{PF}_6]$) solution at 77 K. **Experimental spectrum (black):** microwave frequency 9.3277 GHz; microwave power 1.002 mW; modulation amplitude 0.4 mT. **Simulated spectrum (red):** simulation parameters provided in the table 3.

Table 3. Cu^{II} Spin Hamiltonian parameters obtained for 1.0 mM $[\text{Cu}^{\text{II}}(\text{MeCN})\text{V}_{12}\text{O}_{32}\text{Cl}]^{3-}$ frozen solution in CH_3CN (0.10 M $[n\text{-Bu}_4][\text{PF}_6]$). Hyperfine interaction parameters (A) are $\times 10^{-4} \text{ cm}^{-1}$; linewidths (σ) in G.

Species	g_{\parallel}	g_{\perp}	A_{\parallel}	A_{\perp}	σ
$[\text{Cu}^{\text{II}}(\text{MeCN})\text{V}_{12}\text{O}_{32}\text{Cl}]^{3-}$ (site-1)	2.400	2.070	140	10	30
$[\text{Cu}^{\text{II}}(\text{MeCN})\text{V}_{12}\text{O}_{32}\text{Cl}]^{3-}$ (site-2)	2.415	2.070	118	10	30

The values of g_{\parallel} and A_{\parallel} are consistent with coordination by four oxygen atoms [38]. The relative concentration of site 1 was estimated to be 20% greater than that of site 2.

The EPR spectrum of the 1.0 mM solution of $[\text{Cu}^{\text{II}}(\text{MeCN})\text{V}_{12}\text{O}_{32}\text{Cl}]^{3-}$ in CH_3CN , when frozen to 77 K after a one-electron reduction, also exhibited a weak resonance at $g = 2.070$, attributable to the perpendicular features of the same Cu^{II} spectrum as exhibited by the

unreduced solution. However, this resonance only had 3% of the intensity of that observed with the unreduced solution. This spectrum is consistent with a residual concentration of $[\text{Cu}^{\text{II}}(\text{MeCN})\text{V}^{\text{V}}_{12}\text{O}_{32}\text{Cl}]^{3-}$ remaining from slightly incomplete bulk electrolysis. Significantly, there was no evidence for an EPR resonance attributable to V^{IV} as was observed with frozen solutions of one-electron reduced $[\text{Zn}^{\text{II}}\text{ClV}^{\text{V}}_{12}\text{O}_{32}\text{Cl}]^{4-}$.

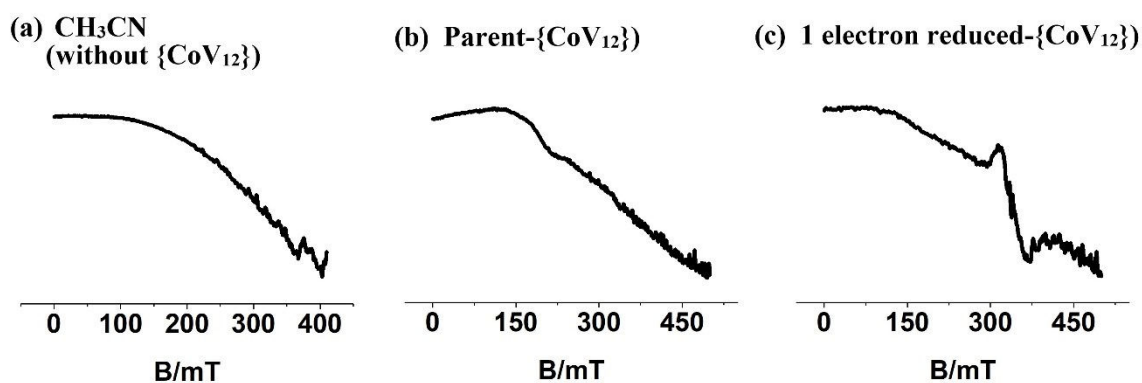


Figure 10. EPR spectrum of (a) CH_3CN (b) 1 mM $[\text{Co}^{\text{II}}(\text{MeCN})\text{V}^{\text{V}}_{12}\text{O}_{32}\text{Cl}]^{3-}$ and (c) one electron reduced $[\text{Co}^{\text{II}}(\text{MeCN})\text{V}^{\text{V}}_{12}\text{O}_{32}\text{Cl}]^{3-}$ in frozen CH_3CN (0.10 M $[\text{n-Bu}_4][\text{PF}_6]$) solution at 77 K. **Spectrometer settings:** microwave frequency 9.451 GHz; microwave power 5.024 mW; modulation amplitude 0.4 mT.

With one electron reduction of $[\text{Co}^{\text{II}}(\text{MeCN})\text{V}^{\text{V}}_{12}\text{O}_{32}\text{Cl}]^{3-}$ it is possible that a formally Co^{III} reduction process occurs, but it is far more likely that the process will be $\text{V}^{\text{V/IV}}$. The EPR spectrum is shown in Figure 10c. Frozen solutions of unreduced 1.0 mM $[\text{Co}^{\text{II}}(\text{MeCN})\text{V}^{\text{V}}_{12}\text{O}_{32}\text{Cl}]^{3-}$ at 77 K gave the EPR spectrum shown in Figure 10b which are similar to that for the cavity with CH_3CN (0.1 M $[\text{n-Bu}_4\text{N}][\text{PF}_6]$) given in Figure 10a. This response implies that $[\text{Co}^{\text{II}}(\text{MeCN})\text{V}^{\text{V}}_{12}\text{O}_{32}\text{Cl}]^{3-}$ is EPR silent at 77 K. In principle, an EPR feature for high spin $\text{Co}(\text{II})$ could be present, but typically, this requires much lower temperatures than 77K for detection [39]. For the one electron reduced $[\text{Co}^{\text{II}}(\text{MeCN})\text{V}^{\text{V}}_{12}\text{O}_{32}\text{Cl}]^{3-}$ a broad resonance, with a g -value of 1.961 is found, which lies close

to that of $g = 1.963$ found for the one-electron reduced $[\text{V}^{\text{V}}_{12}\text{O}_{32}\text{Cl}]^{5-}$ [23]. Interestingly, the intensity of this EPR signal is very weak and just above the cavity background signal (Figure 10a) obtained for CH_3CN (0.10 M $[n\text{-Bu}_4][\text{PF}_6]$). It is also of much lower intensity compared to the V^{IV} EPR spectra obtained from one electron reduced $[\text{V}^{\text{V}}_{12}\text{O}_{32}\text{Cl}]^{5-}$ or $[\text{Zn}^{\text{II}}\text{ClIV}_{12}\text{O}_{32}\text{Cl}]^{4-}$ noting that at least 90% of the one electron reduced $[\text{Co}^{\text{II}}(\text{MeCN})\text{V}^{\text{V}}_{12}\text{O}_{32}\text{Cl}]^{3-}$ was formed by bulk electrolysis prior to freezing to 77 K for EPR experiments. However, while there is evidence for a V^{IV} EPR resonance at 77 K, also resonances attributable to Co^{II} or Co^{I} was detected. Experiments at liquid helium (4 K) temperatures are needed to clarify the interpretation of the EPR spectrum for one electron reduced $[\text{Co}^{\text{II}}(\text{Men})\text{V}^{\text{V}}_{12}\text{O}_{32}\text{Cl}]^{3-}$.

4. Conclusion:

Under transient voltammetric conditions (scan rate of 100 mV s^{-1}) the transition metal functionalised vanadium POMs, $[\text{Fe}^{\text{III}}\text{ClIV}_{12}\text{O}_{32}\text{Cl}]^{4-}$, $[\text{Zn}^{\text{II}}\text{ClIV}_{12}\text{O}_{32}\text{Cl}]^{4-}$, $[\text{Cu}^{\text{II}}(\text{MeCN})\text{V}^{\text{V}}_{12}\text{O}_{32}\text{Cl}]^{3-}$ and $[\text{Co}^{\text{II}}(\text{MeCN})\text{V}^{\text{V}}_{12}\text{O}_{32}\text{Cl}]^{3-}$ give well-defined quasi-reversible one-electron reduction reactions at a GC electrode in CH_3CN (0.10 M $[n\text{-Bu}_4][\text{PF}_6]$) can be reduced in a series of steps. The fact that these initial processes are all well separated from those at more negative potential allows the generation of the one electron reduced species of these POMs by controlled potential bulk electrolysis yields are $\geq 90\%$ for Zn and Co containing POMs and 63% for the Cu one as confirmed by RDE voltammetry at a GC electrode. In situ Vis-NIR Spectroelectrochemistry shows simple change upon reduction of $[\text{Zn}^{\text{II}}\text{ClIV}_{12}\text{O}_{32}\text{Cl}]^{4-}$ and $[\text{Cu}^{\text{II}}(\text{MeCN})\text{V}^{\text{V}}_{12}\text{O}_{32}\text{Cl}]^{3-}$ and formation of intervalence basis with reduction of $[\text{Co}^{\text{II}}(\text{MeCN})\text{V}^{\text{V}}_{12}\text{O}_{32}\text{Cl}]^{3-}$. EPR spectra also were obtained from oxidized and one electron reduced form of $[\text{Zn}^{\text{II}}\text{ClIV}_{12}\text{O}_{32}\text{Cl}]^{4-}$, $[\text{Cu}^{\text{II}}(\text{MeCN})\text{V}^{\text{V}}_{12}\text{O}_{32}\text{Cl}]^{3-}$ and $[\text{Co}^{\text{II}}(\text{MeCN})\text{V}^{\text{V}}_{12}\text{O}_{32}\text{Cl}]^{3-}$ and two electron reduced $[\text{Fe}^{\text{III}}\text{ClIV}_{12}\text{O}_{32}\text{Cl}]^{4-}$ generated by bulk electrolysis in CH_3CN (0.10 M $[n\text{-Bu}_4][\text{PF}_6]$) and then frozen to the glass state at 77 K. EPR

spectrum of the two electron reduced $[\text{Fe}^{\text{III}}\text{ClIV}^{\text{V}}_{12}\text{O}_{32}\text{Cl}]^{4-}$ implies that Fe^{III} is reduced sequentially to Fe^{II} and then to Fe^{I} . The EPR data suggest that the electron on reduced $[\text{Cu}^{\text{II}}(\text{MeCN})\text{V}^{\text{V}}_{12}\text{O}_{32}\text{Cl}]^{3-}$ resides on Cu in this $\text{Cu}^{\text{II/I}}$ based process. In contrast, the electron is delocalised onto the V framework following the one electron reduction of $[\text{Zn}^{\text{II}}\text{ClIV}^{\text{V}}_{12}\text{O}_{32}\text{Cl}]^{4-}$ as it must with one electron reduced $[\text{V}^{\text{V}}_{12}\text{O}_{32}\text{Cl}]^{5-}$. In the case of the one-electron reduced $[\text{Co}^{\text{II}}(\text{MeCN})\text{V}^{\text{V}}_{12}\text{O}_{32}\text{Cl}]^{3-}$, EPR data imply that some of the electron density is located on the V framework. However, the intensity of the EPR signal is much suppressed relative to one electron reduced $[\text{Zn}^{\text{II}}\text{ClIV}^{\text{V}}_{12}\text{O}_{32}\text{Cl}]^{4-}$ and $[\text{V}^{\text{V}}_{12}\text{O}_{32}\text{Cl}]^{5-}$ POMs for similar concentrations. EPR spectra at liquid helium (4 K) temperature are needed for further clarification.

References:

- [1] C.L. Hill, C.M. Prosser-McCartha, Homogeneous catalysis by transition metal oxygen anion clusters, *Coord. Chem. Rev.* 143 (1995) 407.
- [2] M. Misono, N. Nojiri, Recent progress in catalytic technology in Japan, *Appl. Catal.* 64 (1990) 1-30.
- [3] K. Na, T. Okuhara, M. Misono, Catalysis by Heteropoly Compounds, *J. Catal.* 170(1) (1997) 96-107.
- [4] T. Okuhara, A. Kasai, N. Hayakawa, M. Misono, Y. Yoneda, The Important Role of the Bulk of 12-Tungstophosphoric Acid in the Catalytic Dehydration of Alcohols to Olefins, *Chem. Lett.* 10(3) (1981) 391-394.
- [5] J.T. Rhule, C.L. Hill, D.A. Judd, R.F. Schinazi, Polyoxometalates in Medicine, *Chem. Rev.* 98(1) (1998) 327-358.
- [6] K. Unoura, N. Tanaka, Comparative study of the electrode reactions of 12-molybdosilicate and 12-molybdophosphate, *Inorg. Chem.* 22(20) (1983) 2963-2964.
- [7] *Chem. Rev.* 98 (1998) 1.
- [8] M.T. Pope, *Heteropoly and isopoly oxometalates*, Springer-Verlag (1983).
- [9] M.T. Pope, A. Müller, *Polyoxometalate Chemistry: An Old Field with New Dimensions in Several Disciplines*, *Angew. Chem., Int. Ed. Engl.* 30 (1991) 34.
- [10] D.L. Long, R. Tsunashima, L. Cronin, *Polyoxometalates: building blocks for functional nanoscale systems*, *Angew. Chem. Int. Ed. Engl.* 49(10) (2010) 1736-58.
- [11] A. Proust, R. Thouvenot, P. Gouzerh, *Functionalization of polyoxometalates: towards advanced applications in catalysis and materials science*, *Chem Commun (Camb)* (16) (2008) 1837-52.
- [12] S. Dong, X. Xi, M. Tian, *Study of the electrocatalytic reduction of nitrite with silicotungstic heteropolyanion*, *J. Electroanal. Chem.* 385(2) (1995) 227-233.

-
- [13] B. Keita, L. Nadjo, New aspects of the electrochemistry of heteropolyacids: Part II. Coupled electron and proton transfers in the reduction of silicongstic species, *J. Electroanal. Chem. Interf. Electrochem.* 217(2) (1987) 287-304.
- [14] B. Keita, L. Nadjo, New aspects of the electrochemistry of heteropolyacids: Part IV. Acidity dependent cyclic voltammetric behaviour of phosphotungstic and silicotungstic heteropolyanions in water and N,N-dimethylformamide, *J. Electroanal. Chem. Interf. Electrochem.* 227(1) (1987) 77-98.
- [15] B. Keita, L. Nadjo, J.P. Haeussler, Distribution of oxometalates on polymer-covered electrodes: Compared catalytic activity of these new polymers and the corresponding oxometalates in solution, *J. Electroanal. Chem. Interf. Electrochem.* 243(2) (1988) 481-491.
- [16] G. Li, Y. Ding, J. Wang, X. Wang, J. Suo, New progress of Keggin and Wells–Dawson type polyoxometalates catalyze acid and oxidative reactions, *J. Mol. Catal. A: Chem.* 262(1) (2007) 67-76.
- [17] J.J. Berzelius, Beitrag zur näheren Kenntniss des Molybdäns, *Annalen der Physik* 82(4) (1826) 369-392.
- [18] J.F. Keggin, Structure of the Crystals of 12-Phosphotungstic Acid, *Nature* 132 (1933) 351.
- [19] K. Yamamura, Y. Sasaki, Crystal structure of the β -12-tungstosilicate anion, *J. Chem. Soc., Chem. Commun.* (18) (1973) 648-649.
- [20] A. Bijelic, A. Rompel, The use of polyoxometalates in protein crystallography - An attempt to widen a well-known bottleneck, *Coord. Chem. Rev.* 299 (2015) 22-38.
- [21] K. Kastner, J. Forster, H. Ida, G.N. Newton, H. Oshio, C. Streb, Controlled Reactivity Tuning of Metal-Functionalized Vanadium Oxide Clusters, *Chemistry – A European Journal* 21(21) (2015) 7686-7689.
- [22] K. Kastner, J.T. Margraf, T. Clark, C. Streb, A Molecular Placeholder Strategy To Access a Family of Transition - Metal - Functionalized Vanadium Oxide Clusters, *Chemistry – A European Journal* 20(38) (2014) 12269-12273.
- [23] M.H. Anjass, K. Kastner, F. Nägele, M. Ringenberg, J.F. Boas, J. Zhang, A.M. Bond, T. Jacob, C. Streb, Stabilization of Low-Valent Iron(II) in a High-Valent Vanadium(V) Oxide Cluster, *Angew. Chem. Int. Ed.* 56(46) (2017) 14749-14752.
- [24] S. Sproules, Comment on “Stabilization of Low - Valent Iron (II) in a High - Valent Vanadium (V) Oxide Cluster”, *Angew. Chem. Int. Ed.* 58(30) (2019) 10043-10047.
- [25] M.H. Anjass, K. Kastner, F. Nägele, M. Ringenberg, J.F. Boas, J. Zhang, A. Bond, T. Jacob, C. Streb, Reply to Comment on Stabilization of Low - Valent Iron (II) in a High - Valent Vanadium (V) Oxide Cluster, *Angew. Chem. Int. Ed.* 58(30) (2019) 10048-10050.
- [26] A.a.F. Bard, Larry R, *Electrochemical Methods: Fundamentals and applications*, 2nd ed., Wiley, New York, 2001.
- [27] D. Sawyer, A. Sobkowiak, J. Roberts Jr, *Electrochemistry for Chemists*, ; John Wiley&Sons, 1995.
- [28] J. Zhang, S.-X. Guo, A.M. Bond, Discrimination and evaluation of the effects of uncompensated resistance and slow electrode kinetics from the higher harmonic components of a fourier transformed large-amplitude alternating current voltammogram, *Anal. Chem.* 79(6) (2007) 2276-2288.
- [29] B.D. Fleming, J. Zhang, D. Elton, A.M. Bond, Detailed Analysis of the Electron-Transfer Properties of Azurin Adsorbed on Graphite Electrodes Using dc and Large-Amplitude Fourier Transformed ac Voltammetry, *Anal. Chem.* 79(17) (2007) 6515-6526.
-

-
- [30] S.J. Borg, S.P. Best, Spectroelectrochemical cell for the study of interactions between redox-activated species and moderate pressures of gaseous substrates, *J. Electroanal. Chem.* 535(1-2) (2002) 57-64.
- [31] J.E. Wertz, J.W. Orton, P. Auzins, Electron spin resonance studies of radiation effects in inorganic solids, *Discuss. Faraday. Soc.* 31(0) (1961) 140-150.
- [32] G.R. Hanson, K.E. Gates, C.J. Noble, M. Griffin, A. Mitchell, S. Benson, XSope-Sophe-XeprView®. A computer simulation software suite (v. 1.1. 3) for the analysis of continuous wave EPR spectra, *J. Inorg. Biochem.* 98(5) (2004) 903-916.
- [33] N.N. Greenwood, A. Earnshaw, *Chemistry of the Elements*, Elsevier 2012.
- [34] A. Abu-Surrah, M. Kettunen, *Platinum Group Antitumor Chemistry: Design and development of New Anticancer Drugs Complementary to Cisplatin*, 2006.
- [35] S. Záliš, C. Consani, A. El Nahhas, A. Cannizzo, M. Chergui, F. Hartl, A. Vlček Jr, Origin of electronic absorption spectra of MLCT-excited and one-electron reduced 2, 2'-bipyridine and 1, 10-phenanthroline complexes, *Inorg. Chim. Acta* 374(1) (2011) 578-585.
- [36] J.-i. Nambu, T. Ueda, S.-X. Guo, J.F. Boas, A.M. Bond, Detailed voltammetric and EPR study of protonation reactions accompanying the one-electron reduction of Keggin-type polyoxometalates, $[XV^M_{11}O_{40}]^{4-}$ (X= P, As; M= Mo, W) in acetonitrile, *Dalton Trans.* 39(31) (2010) 7364-7373.
- [37] R.W. Holmberg, ESR Study of H $\dot{C}O$ in Single Crystals of Formic Acid at 77° K, *J. Chem. Phys.* 51(8) (1969) 3255-3260.
- [38] J. Peisach, W.E. Blumberg, Structural implications derived from the analysis of electron paramagnetic resonance spectra of natural and artificial copper proteins, *Arch. Biochem. Biophys.* 165(2) (1974) 691-708.
- [39] S.K. Misra, S. Diehl, D. Tipikin, J.H. Freed, A multifrequency EPR study of Fe²⁺ and Mn²⁺ ions in a ZnSiF₆· 6H₂O single crystal at liquid-helium temperatures, *J. Magn. Reson.* 205(1) (2010) 14-22.

Supporting Information

Electrochemical and EPR Spectroscopic Characterisation of Two Electron Reduced Fe(III) and One Electron Reduced Zn(II), Cu(II) and Co(II) Functionalized Vanadium Polyoxometalates

Md Anisur Rahman^a, Stephen Best^b, John F. Boas^c, Alan M. Bond^{a, d*} and Jie Zhang^{a, d*}

^a School of Chemistry, Monash University, Clayton, Victoria 3800, Australia

^b School of Chemistry, The University of Melbourne, Victoria 3010, Australia

^c School of Physics and Astronomy, Monash University, Clayton, Victoria 3800, Australia

^d ARC Centre of Excellence for Electrochemical Science, Monash University, Clayton,
Victoria 3800, Australia

*Corresponding authors: jie.zhang@monash.edu, alan.bond@monash.edu

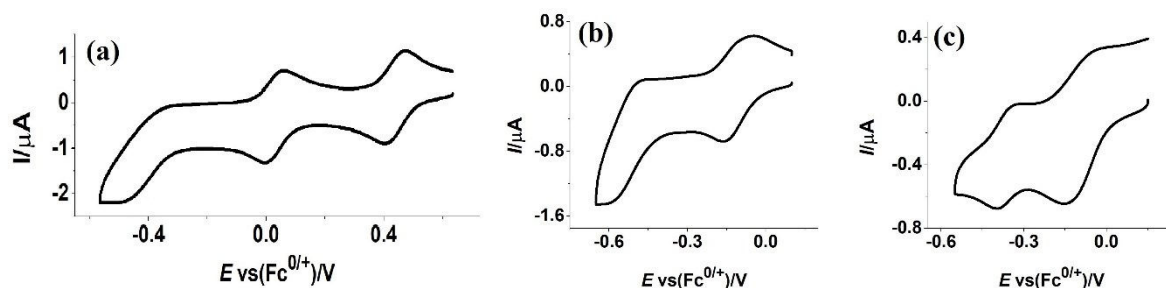


Figure S1. Cyclic voltammograms obtained at a scan rate of 0.100 V s^{-1} for the reduction processes of 0.5 mM (a) $[\text{Fe}^{\text{III}}\text{ClIV}^{\text{V}}_{12}\text{O}_{32}\text{Cl}]^{4-}$ (b) $[\text{Zn}^{\text{II}}\text{ClIV}^{\text{V}}_{12}\text{O}_{32}\text{Cl}]^{4-}$ and (c) $[\text{Cu}^{\text{II}}(\text{MeCN})\text{V}^{\text{V}}_{12}\text{O}_{32}\text{Cl}]^{3-}$ in CH_3CN (0.10 M $[\text{n-Bu}_4][\text{PF}_6]$) at GC electrode.

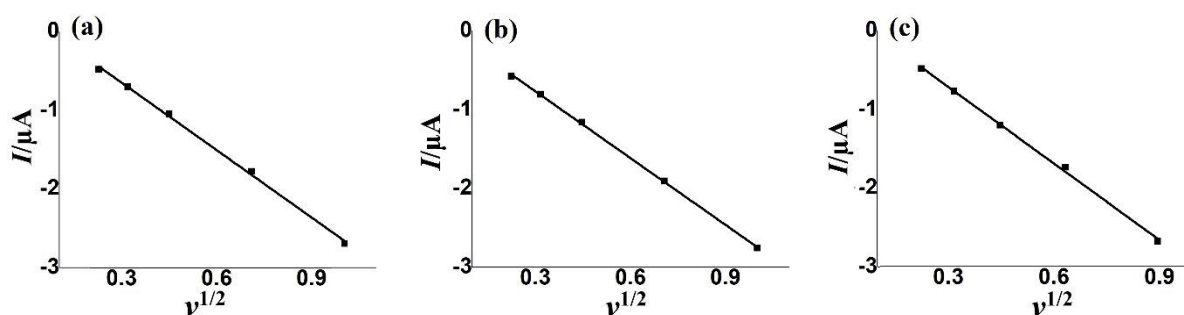


Figure S2. Linear plot of peak reduction current versus square root of scan rate ($v^{1/2}$) for the reduction of (a) $[\text{Zn}^{\text{II}}\text{ClIV}^{\text{V}}_{12}\text{O}_{32}\text{Cl}]^{4-}$, (b) $[\text{Cu}^{\text{II}}(\text{MeCN})\text{V}^{\text{V}}_{12}\text{O}_{32}\text{Cl}]^{3-}$ and (c) $[\text{Co}^{\text{II}}(\text{MeCN})\text{V}^{\text{V}}_{12}\text{O}_{32}\text{Cl}]^{3-}$. Experimental data point (■) and linear regression fit (—).

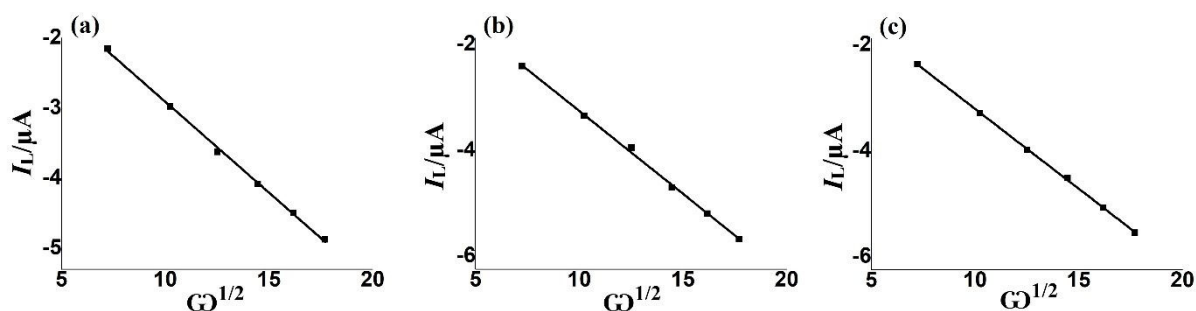


Figure S3. Linear plot of RDE limiting current (I_L) versus square root of rotation rate ($\omega^{1/2}$) for reduction of (a) $[\text{Zn}^{\text{II}}\text{ClIV}^{\text{V}}_{12}\text{O}_{32}\text{Cl}]^{4-}$, (b) $[\text{Cu}^{\text{II}}(\text{MeCN})\text{V}^{\text{V}}_{12}\text{O}_{32}\text{Cl}]^{3-}$ and (c) $[\text{Co}^{\text{II}}(\text{MeCN})\text{V}^{\text{V}}_{12}\text{O}_{32}\text{Cl}]^{3-}$. Experimental data point (■) and linear regression fit (—).

Chapter 7

Conclusions and Future Work

7.1 Conclusions

Nanosized oxoanion POM clusters constructed from high valent transition metals (e.g. vanadium, tungsten and molybdenum) are used in various fields such as materials science, capacitors, medicine, solar energy and catalysis. Access to quantitative electrochemical POM studies that enhance the understanding of electron transfer kinetics can facilitate further practical POM uses. In this study, the electron transfer kinetics associated with several Dawson and Keggin POMs have been examined by DC, FTAC voltammetry as well as other methods. Results in combination with EPR, Vis-NIR and EQCM experiments helped to clarify nuances in the kinetic findings.

Features such as enhanced ability to resolve the impact of electrode kinetics and uncompensated resistant (R_u) and higher kinetic sensitivity make the FTACV technique superior to the widely used DC voltammetry in quantitative electrode kinetics POM studies.

FTAC voltammetric experimental data have been compared with simulated data to determine the electrode kinetic parameters. Initial estimates of kinetic parameters (E^0 , k^0 and α) by a heuristic approach could introduce experimenter bias as simulation parameters are changed manually with the best fit decided by the experimenter. However, these manual estimates help to set the ranges of variables that are used in the computer-assisted data optimisation approach and provide parameters that are free of experimenter bias. In general, kinetic parameters obtained by both approaches are similar unless there are departures from the ideality in theory-experiment comparisons. Findings suggest that electron transfer kinetics at GC electrode is faster than with Au and Pt metal electrodes, and the rate of the first α -[S₂W₁₈O₆₂]^{4-/5-} process

is always faster than that of the second α -[S₂W₁₈O₆₂]^{5-/6-} process in CH₃CN (0.50 M [n-Bu₄N][PF₆]).

Without great care, the automated data analysis approach can provide false parameter values, such as where the kinetic estimation nears the reversible limit. In other cases where reduction and oxidation components are not symmetrical, which is readily detected in the heuristic method, automated estimates can be substantially different from the heuristic estimates as these are derived solely from the reduction component. Non-conformance with the Butler-Volmer model of electron transfer arises in the electrode kinetic parameterisation of the α -[S₂W₁₈O₆₂]^{4-/5-/6-} process especially at Pt electrodes. This can be explained by the combination of slow electrode kinetics and ion-pairing between the electrolyte cation and highly negatively charged POMs, α -[S₂W₁₈O₆₂]⁴⁻ or reduced species α -[S₂W₁₈O₆₂]⁵⁻. Surface modification also may account for this anomalistic behaviour.

Several electrode kinetic nuances were detected when a BDD electrode also was employed to parameterise the thermodynamics and electrode kinetics associated with the α -[S₂W₁₈O₆₂]^{4-/5-/6-} processes. An unusual kinetic pattern where the second α -[S₂W₁₈O₆₂]^{5-/6-} process is apparently kinetically faster than the first α -[S₂W₁₈O₆₂]^{4-/5-} process and harmonic dependent kinetics also are revealed with BDD. These non-idealities are removed upon removal of the sp² carbon-rich exposed edge of the BDD electrode. On the other hand, concentration dependent electrode kinetics at BDD electrode is attributed to the limited charge carrier density associated with BDD.

α -[S₂W₁₈O₆₂]^{6-/7-/8-/9-/10-} at a more negative potentials also have been parameterised, and again departures from the theoretical predictions of the Butler-Volmer model of electron transfer are detected; this may be the consequence of the enhanced impact of ion-pairing and electrode

material dependent surface interactions. Additionally, the influence of a double layer on processes at very negative potentials was more substantial.

The electrochemistry of dissolved $K^W_{Sn}[N_3C_4H_{10}]^{4-}$ along with its surface confined diazonium derivative $K^W_{Sn}[-]^{4-}$ and non-idealities associated with parameterisation also have been detected by FTAC voltammetry. The relatively slow electron transfer kinetics associated with $K^W_{Sn}[N_3C_4H_{10}]^{4-/5-/6-}$ processes compared to $\alpha-[S_2W_{18}O_{62}]^{4-/5-/6-}$ processes in the solution phase ($CH_3CN/0.10\text{ M }[n\text{-Bu}_4N][PF_6]$) may be due to the extended diazonium chain that restrains the approach of the active monomeric POM to the electrode surface. A series of conventional DC voltammetric experiments without polishing the electrode and EQCM measurements at a gold quartz crystal electrode reveal that the source of non-ideality may originate from the electrode surface accumulation of an unidentified product that accompanies the first $K^W_{Sn}[N_3C_4H_{10}]^{4-/5-}$ reduction process. Nuances associated with surface-confined voltammetry may arise due to thermodynamic and kinetic dispersion resulting from heterogeneity in the grafted GC electrode surface.

EPR and visible-near IR spectroscopy combined with conventional DC cyclic voltammetry have been used to characterise the one-electron reduced Zn(II), Cu(II) and Co(II) functionalized vanadium POMs as well as the two electron reduced Fe^{III} derivatives. EPR data suggest that electrons added to $[Fe^{III}ClV^V_{12}O_{32}Cl]^{4-}$ and $[Cu^{II}(MeCN)V^V_{12}O_{32}Cl]^{3-}$ reside on the Fe and Cu^{II} centre, respectively. On the other hand, the reduction of the Zn derivative leads to electron transfer on the V framework. The very similar g-value of 1.961 for one-electron reduced $[Co^{II}(MeCN)V^V_{12}O_{32}Cl]^{3-}$ compared to g-value = 1.963 reported³ for the one-electron reduced $[V^V_{12}O_{32}Cl]^{5-}$ suggests that at least some of the electron density resides on the V framework. However, the intensity of the EPR signal is much lower than for the one electron

reduced $[\text{Zn}^{\text{II}}\text{ClV}^{\text{V}}_{12}\text{O}_{32}\text{Cl}]^{4-}$ and $[\text{V}^{\text{V}}_{12}\text{O}_{32}\text{Cl}]^{5-}$ POMs; hence, some electron density may also reside on Co as well.

7.2 Future Work

In Chapters 2 to 5, the MECSim simulation software package has been used to analyse the FTAC voltammetric data by adopting the Butler-Volmer model for the electron transfer processes. However, departures from theory are detected. Therefore, including ion-pairing phenomena into the theoretical data analysis, may qualitatively express the asymmetry in reduction and oxidation AC components, as POM may adsorb on the electrode surface specifically with $\text{K}^{\text{W}}_{\text{Sn}}[\text{N}_3\text{C}_4\text{H}_{10}]^{4-}$. This better modelling explains the non-conformance to the Butler-Volmer model and can provide a better understanding of thermodynamics, electrode kinetics, and mechanistic nuances associated with POM electrochemistry.

In FTAC voltammetric data analysis, both experimenter-based heuristic and computer-assisted automated data analysis approaches have been used to parameterise the electrode kinetics and ensure chemically sensible values are reported. The automated method can unknowingly generate physically unreliable parameter values when for example a process is near a reversible limit. A future challenge is to avoid over parameterisation by the introduction of Bayesian interference or any other more sophisticated statistical method.

In Chapter 6, absorption spectroscopy covering the visible-near infrared region was employed in conjunction with insitu bulk electrolysis of Fe(III), Zn(II), Cu(II) and Co(II) functionalized vanadium POMs. Further experiments are needed in the ultra-violet (UV) region where other absorption bands may be present. EPR spectroscopic measurements of one electron reduced $[\text{Co}^{\text{II}}(\text{Men})\text{V}^{\text{V}}_{12}\text{O}_{32}\text{Cl}]^{3-}$ at liquid helium (4 K) temperature may also clarify where the added electrons reside in this POM.